Study of the neutralino sector and analysis of the muon response of a highly granular hadron calorimeter at the International Linear Collider

Dissertation
zur Erlangung des Doktorgrades
des Department Physik
der Universität Hamburg

vorgelegt von

Nicola D'Ascenzo

aus Lamezia Terme

Hamburg
2009

Gutachter der Dissertation:	Dr. E. Garutti Prof. Dr. J. Mnich
Gutachter der Disputation:	Prof. Dr. P. Schleper JProf. Dr. J. Haller
Datum der Disputation:	14. Januar 2009
Vorsitzender des Prüfungausschusses:	Prof. Dr. C. Hagner
Vorsitzender des Promotionsausschusses:	Prof. Dr. R. Klanner
Dekan der MIN-Fakultät:	Prof. Dr. A. Frühwald

Abstract

The studies presented in this thesis concern the physics potential and the detector R&D program of the International Linear Collider (ILC), an e^+e^- collider with a centre of mass energy extendible up to 1 TeV.

The first part of the thesis presents the study of the neutralino system in the SPS1a$'$ SUSY scenario. The process $e^+e^- \rightarrow \tilde{\mu}_L\tilde{\mu}_L \rightarrow \mu\chi^0_1\mu\chi^0_1$ is proposed for the analysis of the χ^0_1. From the kinematic edges of the energy distribution of the muons in the final state the mass of the χ^0_1 (97.71 GeV) can be estimated with a relative statistical uncertainty of 1.09%. The mass of the $\tilde{\mu}_L$ (189.87 GeV) can be estimated with a relative statistical uncertainty of 0.21%. The cross section of this process (54.32 fb) can be estimated with a relative statistical uncertainty of 2.47% at 68% C.L. The χ^0_2 is investigated in the process $e^+e^- \rightarrow \chi^0_2\chi^0_1 \rightarrow \tilde{\mu}_R\mu \rightarrow \chi^0_1\mu\mu\chi^0_1$. The mass of the χ^0_2 (183.89 GeV) is estimated with a relative statistical uncertainty of 0.75% from the detection of the kinematic edge of the di-muon invariant mass. The cross section of the process (4.2 fb) can be determined within the confidence band $(3.75, 5.57)$ fb, at 95% C.L.

The second part of the thesis reports the analysis of the experimental data collected in the test beam of the prototype of a highly granular hadronic calorimeter (AHCAL) build by the CALICE collaboration. The aim of the analysis is to measure the response of the hadronic calorimeter to muons with momentum ranging between 6 GeV and 120 GeV and incidence angle up to $28.3^\circ \pm 0.1^\circ$. The energy and angular dependence of the muon response are found in agreement with the Monte Carlo. The effects of the higher order electromagnetic interaction of muons in the detector are studied; the high granularity of the hadronic calorimeter allows to identify and measure the δ-rays produced by a 120 GeV muon. A correlation function between the energy deposited in the scintillator and in the absorber based on these higher order effects is found in order to reconstruct the total energy deposited by a 120 GeV muon in the AHCAL. The e/mip ratio of the AHCAL is extracted from the muon response as $0.897 \pm 0.001_{stat} \pm 0.057_{syst}$. With a combined analysis of the information of the AHCAL and the Muon Tracker Tail Catcher the probability (P_μ) of muon emission from a shower of a pion with energy E_π is found to be $P_\mu = (0.9 \pm 0.4_{stat} \pm 0.1_{syst}) \cdot 10^{-5} \times E_\pi$.

Zusammenfassung

Die Untersuchungen, die in dieser Arbeit vorgestellt werden, behandeln die Möglichkeiten für die Physik und das Detector-R&D-Programm des Internationalen Linearcolliders (ILC), eines e$^+$e$^-$-Colliders mit einer Schwerpunktsenergie von bis zu 1 TeV.

Der erste Teil der Arbeit präsentiert die Untersuchung des Neutralino-Systems im SPS1a$'$-SUSY-Szenario. Der Prozess $e^+e^- \rightarrow \tilde{\mu}_L\tilde{\mu}_L \rightarrow \mu\chi^0_1\mu\chi^0_1$ wird zur Analyse des χ^0_1 verwendet. Aus den kinematischen Schranken der Energieverteilung der Myonen im Endzustand wird die Masse des χ^0_1 (97.71 GeV) mit einem relativen statistischen Fehler von 1.09% abgeschätzt. Die Masse des $\tilde{\mu}_L$ (189.86 GeV) wird mit einem relativen statistischen Fehler von 0.21% abgeschätzt. Der Wirkungsquerschnitt des Prozesses (54.32 fb) wird mit einem relativen statistischen Fehler von 2.47% mit einem Konfidenzniveau von 68% abgeschätzt. Das χ^0_2 wird im Prozess $e^+e^- \rightarrow \chi^0_2\chi^0_1 \rightarrow \tilde{\mu}\mu \rightarrow \chi^0_1\mu\mu\chi^0_1$ untersucht. Die Masse des χ^0_2 (183.89 GeV) kann mit einem relativen statistischen Fehler von 0.75% durch die Ermittlung der kinematischen Schranken der invarianten Masse der zwei Myonen abgeschätzt werden. Außerdem kann für den Wirkungsquerschnitt des Prozesses (4.2 fb) das Konfidenzintervall (3.75, 5.57) fb bei einem Konfidenzniveau von 95% angegeben werden.

Der zweite Teil der Arbeit beschreibt die Analyse der experimentellen Daten, die beim Teststrahl des von der CALICE-Kollaboration gebauten Prototyps eines highly granular hadronic calorimeters (AHCAL) gesammelt wurden. Das Ziel der Analyse ist die Messung der Response des hadronischen Kalorimeters auf Myonen mit einem Impuls zwischen 6 GeV und 120 GeV sowie einem Einfallswinkel bis $28.3° \pm 0.1°$. Dabei wurde festgestellt, dass die Energie und die Winkelabhängigkeit der Myonen-Response mit der Monte-Carlo-Simulation übereinstimmen. Ferner werden die Effekte der elektromagnetischen Wechselwirkung höherer Ordnung im Detektor untersucht; die hohe Granularität des hadronischen Kalorimeters erlaubt es, die von einem 120-GeV-Myon produzierten d-Strahlen zu identifizieren und zu messen. Es wird eine auf diesen Effekten höherer Ordnung basierende Korrelationsfunktion zwischen der im Szintillator und im Absorber deponierten Energie aufgestellt, um die Gesamtenergie zu rekonstruieren, die von einem 120-GeV-Myon im AHCAL deponiert wird. Aus der Myon-Response kann für das e/mip-Verhältnis des AHCAL der Wert $0.897 \pm 0.001_{stat} \pm 0.057_{syst}$ gewonnen werden. Abschließend kann man aus einer kombinierten Analyse der Informationen aus dem AHCAL und dem Muon Tracker Tail Catcher für die Wahrscheinlichkeit (P_μ) einer Myonenemission aus dem Schauer eines Pions mit der Energie E_π den Wert $P_\mu = (0.9 \pm 0.4_{stat} \pm 0.1_{syst})10^{-5}E_\pi$ angeben.

Contents

“Once upon a time, in the magic forest,
where the blue Moonflowers grow up around lakes and rivers,
Prince Semola and Princess Camomilla
were keeping safe the heart and the beauty of each other.”
— from *The adventures of Prince Semola and Princess Camomilla*

S.T.D.

Chapter 1

Introduction

"Our story begins long ago,
Semola was a toad and Camomilla a little ladybird.
If you have the patience and the wish,
just follow your poet along these pages."
— From the adventures of Prince Semola and Princess Camomilla

The studies presented in this thesis are performed in the framework of the International Linear Collider (ILC). This experiment is still in the design phase and there are two main research streams which are conducted and are represented in this work. The first is the analysis of the physics case at ILC; the potential of the ILC in the discovery and determination of the neutralino system is investigated. The second is the design and *R&D* of a detector for ILC; the analysis of the experimental data collected in a test beam of the prototype of highly granular hadronic calorimeter for ILC is proposed.

The physics case of the International Linear Collider

The International Linear Collider (ILC) is a proposed linear e^+e^- machine with a centre of mass energy of 500 GeV extendible up to 1 TeV [1–3]. High-luminosity options at the Z^0 resonance and at the W^+W^- threshold are also foreseen. The main feature of the ILC is the precise measurement of the initial state; both the centre of mass energy and the polarization of the beams can be determined with accuracy. The current design consists of two 11 Km long linacs. The high energy of the centre of mass is achieved with the innovative RF cavities which can reach a gradient up to 35 MeV/m.

The physics motivations of such experiment have their roots in the great success and limits of the Standard Model. This theory describes the electroweak and strong forces between fermions within the gauge group $SU(2)_L \otimes U(1)_Y \otimes SU(3)_C$. On one side the observation of the neutral electro-weak currents at the Gargamelle experiment in 1973-74 [4] and the discovery of the three associated gauge bosons (Z^0, $W^\pm$) at the UA2 [5] and LEP [6] experiments provided an experimental evidence of the $SU(2)_L \otimes U(1)_Y$ electroweak theory. On the other side QCD-based experiments, as electron-proton scattering at HERA, gave a proof of the validity of the $SU(3)_C$ strong force [7, 8].

However, the SM leaves many open questions. A key-point is that a spin-0 field — the Higgs Boson — is introduced in the theory in order to explain the mass generation mechanism [9, 10]; yet there is no experimental proof of this particle. Moreover astrophysics observations have a clear evidence of non-baryonic cold *dark matter* in the universe, which is not foreseen by the SM [11–13]. Last but not least the *grand unification theorem* postulates that the three fundamental forces unify at the Planck scale; the unification of the coupling constants is excluded at about 7 sigma's within the SM [14]. On the theoretical point of view, the main limitation of the SM is the instability of the mass of the Higgs Boson, which is affected by divergent loop corrections — hierarchy problem [15]. Moreover, the gravity is not described by the SM at all.

One of the most favourite possible extensions of the SM is the Supersymmetry (SUSY) [16, 17]. It consists of a symmetry between fermions and bosons. This theory proposes that a supersymmetric partner of the SM particles exists; in the minimal supersymmetric extension of the SM (MSSM) it is postulated a supersymmetric boson field partner for every SM fermion field, and vice-versa. SUSY would provide an elegant solution to most of the problem of the SM. First the symmetry between fermions and bosons cures the loop divergences of the mass of the Higgs. Second the lightest SUSY particle (LSP) is one of the favourite dark matter candidates. Third it provides the unification of the gauge coupling constants at the Plank scale. Fourth gravity enters the SUSY breaking mechanism, being hence included in the full theory.

As a matter of fact, the key-challenges of the contemporary high energy physics are the understanding of the mechanism of the mass generation and the exploitation of the new physics beyond the Standard Model. SUSY is one of the favoured models but its nice features have to contrast the complete lack of any experimental evidence. However, new physics phenomena are expected to appear at a scale of about 1 TeV, according to the constrain of unitarity of the electroweak gauge bosons scattering [18]. This is the energy scale which has to be explored by future experiments.

At the present the most energetic operating collider is the Tevatron, at Fermilab. It is a $\overline{p}p$ collider with 1.96 TeV centre of mass energy [19]. Searches of Higgs Boson are being performed in the two experiments CDF and D0 with a total luminosity of about 3 fb^{-1} of data for each experiment [20]. In 2009 LHC, a 14 TeV pp collider, will start to take data. Many Monte Carlo studies demonstrated that this experiment has a high discovery potential of the Higgs Boson and of the physics beyond the Standard Model [21, 22].

However, a big limit of the hadron machine is the undetermination of the partonic initial state. Protons are in fact composed of quarks and gluons, which are the real particles involved in the interaction. The energy distribution of each sub-component is known, on average, but not at each event. The International Linear Collider is a lepton machine, providing a very clean and determined initial state; it is hence suitable for the high precision measurement of the physics mechanism within and beyond the SM.

Many theoretical and experimental studies are performed in order to investigate the physics potential of ILC [23]. This machine will provide an unique set of precision measurements which will complete the information extracted at other colliders. The mass, coupling constants and branching ratios of the SM Higgs Boson can be determined with a relative statistical uncertainty of about 1%. Moreover the ILC will provide a precise measurement of the properties of the SM. The top quark mass can be determined with a precision of about 100 MeV; the high-luminosity option at the W^+W^- threshold will provide a sub per-mille level determination of the WW self-coupling, finally establishing the non-abelian gauge symmetry of the electroweak forces.

The ILC will be a precision tool also for the precision measurement of the features of SUSY. In case this theory is broken at the TeV scale, a part of the SUSY spectrum can be observed at ILC. The masses of the super-partners can be determined with a statistical uncertainty of 0.05% up to 1%. Furthermore the polarization of the beams provides an unique tool for the construction of CP-even and CP-odd azimuthal asymmetries, which give access to determine CP-violating phases in a broad range of the MSSM parameter space [24].

The study of the neutralino system at ILC

In this work the potential of the Linear Collider is investigated in the specific case of the determination of the properties of the neutralino sector (χ_i^0). The neutralino's are the four mass eigenstates of the neutral super-partners of the higgs and gauge vector boson fields. There are two main motivations of this study.

A first motivation is based on recent theoretical studies which showed that the neutralino mixing matrix is related to the SUSY fundamental parameters at a tree level [25, 26]; the measurement of the mass of the χ_1^0, of the χ_2^0 and of the $\sigma(\chi_1^0\chi_2^0)$ would provide a determination of the supersymmetric gauge boson mass scale M_1. Moreover, it was evidenced that the χ_i^0 sector has a relevant role in CP and lepton flavour violating scenarios [27, 28].

A second motivation is based on the investigation of a possible method to constrain the SUSY lagrangian parameters using the full information of the collider measurements. This study is a part of a more extended research program aiming at a determination of all the possible SUSY observables at ILC and LHC, performed in the mSUGRA SUSY scenario at the SPS1a$'$ parameter space point [29]. In this specific model, the total number of parameters of the lagrangian is reduced to 19; it is shown that a combination of the experimental observables of the two experiments would provide an excellent understanding of the SUSY breaking mechanism which determines the parameters of the Lagrangian.

In the $SPS1a'$ point only the χ_1^0 and the χ_2^0 are reachable at a 500 GeV linear collider. The physics channels proposed in this study are characterized by two muons and missing energy in the final state. The χ_1^0 is studied in the chain $e^+e^- \to \tilde{\mu}_L\tilde{\mu}_L \to \mu\chi_1^0\mu\chi_1^0$ and the χ_2^0 in the process $e^+e^- \to \chi_2^0\chi_1^0 \to \tilde{\mu}_R\mu \to \chi_1^0\mu\mu\chi_1^0$.

The analysis is performed with the Monte Carlo model of the LDC$'$ detector, one of the possible detector designs proposed for the ILC. This detector is characterized by a high muon detection efficiency and a precise measurement of the momentum of charged particles in the tracking system ($\delta p/p \approx 10^{-5}$). An important scope of this study is to verify that this detector design is capable to contrast the physic challenges of the International Linear Collider.

The key-point of this analysis is the determination of the properties of the χ_1^0 and of the χ_2^0 directly in the 500 GeV continuum operation. While this is the traditional method proposed for the χ_1^0, there are currently no published studies about the χ_2^0. The threshold scan of the $\chi_2^0\chi_2^0$ pair production is usually proposed for the determination of the mass of the χ_2^0. The possibility of the observation of the χ_2^0 signal in the invariant mass spectrum of the di-muon final state is hence the core-result of this analysis and underlines the powerful physics potential of the International Linear Collider.

The muon response of a highly granular hadronic calorimeter

The second part of the thesis focuses on a specific sub-detector designed within the *R&D* for the International Linear Collider. The analysis of experimental data collected during the test beam of a prototype of a highly granular analog hadronic calorimeter is presented. This detector is developed by the CALICE collaboration in the framework of the LDC/ILD detector design (CALICE AHCAL). The topic of the analysis is the quantification of the response of the hadronic calorimeter to muons.

The main function of the hadronic calorimeter is the measurement of the response to hadrons. At ILC many interesting physics channels will provide dense multi-jet final states. An important case is offered by the $e^+e^- \rightarrow H^0H^0Z^0$ process which is the key-mechanism to measure the Higgs self-coupling constant and to have a unique insight of the Higgs potential; also the identification of the Z^0 and $W^\pm$ boson in their hadronic decay is essential in the SUSY scenario which allows the decay $\chi_2^0 \rightarrow Z^0\chi_1^0$ and $\chi_1^\pm \rightarrow W^\pm\chi_1^0$. The particle flow [30–33] is the technique proposed for the improvement of the energy resolution of the jets at ILC; it aims at a reconstruction of the mass of the vector bosons with a precision equivalent to their natural decay width. It consists of the measurement of the four-momentum of each particle within the jet. The measured energy of the jets is the sum of the energy of each single particle. According to this method the hadronic calorimeter has to provide the measurement of the energy of neutral hadrons and the identification of charged hadrons, whose momentum is then measured in the tracker. The identification of the charged hadrons in the hadronic calorimeter consists of the geometrical identification of the energy deposited by these particles in the detector. The main requirement of the particle flow to hadronic calorimetry is hence the high granularity and segmentation; charged hadrons interact with this detector generating complicated hadronic showers whose topological reconstruction requires a system with extremely good imaging performance.

The CALICE AHCAL prototype is designed specifically for the particle flow. It consists of a sandwich scintillator/steel detector, alternating a 0.5 cm thick sensitive layer with a 2 cm thick steel absorber layer. Each sensitive layer is segmented in square tiles, whose size is as low as 3×3 cm^2 in the core of the detector. Each scintillator tile is read-out by a Silicon photomultiplier [34–36]. This innovative silicon photo-detector has a sensitive area of 1×1 mm^2 and is very easy to operate. It can be installed directly in the scintillator tile and is the technological key-ingredient of the high granularity.

The motivations of the study of the response of the AHCAL to muons range from the experimental determination of the calorimeter features which affect the particle flow performance to the measurement of some characterization parameters of this detector.

First muons deposit energy in the detector mainly through ionization. The measurement of the response of the sensitivity of the AHCAL to the muon signal investigates hence the possibility of the detection of the ionization energy level. The ionization is the basic mechanism of propagation of hadronic shower in the matter. The hadronic shower can be effectively described as a net of ionization tracks — the charged hadrons — connecting electromagnetic dense deposits. Moreover in the hadronic shower muons are generated from the decay of $\pi^\pm$ and $K^\pm$ mesons. The topological identification of the ionization tracks is the first step of the geometrical reconstruction of hadronic shower in the AHCAL, according to the particle flow technique. In the analysis proposed in this study the response of the CALICE AHCAL to muons with energy ranging between 6 GeV and 120 GeV and impinging the detector at an incidence angle up to $28.3° \pm 0.1°$ is proposed to investigate the sensitivity of the detector to the energy measurement at the ionization level. Moreover it is exploited the measurement of the probability of muon emission in pion showers, which provides an experimental proof of the possibility of the identification of ionization tracks in the more complicated hadronic shower environment.

Second the most probable value of the ionization energy level of the muon signal is proposed as reference for the absolute calibration scale of the visible energy signal of the CALICE AHCAL. Any systematic uncertainty of the determination of the muon signal reflects to the quality of the analysis of the AHCAL response to hadrons.

Third the e/mip ratio of the CALICE AHCAL can be measured analysing the muon response at the electromagnetic energy scale. This parameter plays an essential role in the determination of the e/h ratio, affecting the energy resolution of the hadronic calorimeter [37].

Last but not least, the information of the hadronic calorimeter is essential for the identification of muons in the LDC/ILD detector concept. In the analysis of the neutralino system proposed in this thesis the imaging performance of the AHCAL is used in order to merge the track identified in the tracker and in the muon chamber. The experimental proof of the possibility of the measurement and identification of ionization tracks is hence important.

Although many analysis of muon response of hadronic calorimeters are published [38–42], it is the first time that such studies are presented for a highly granular calorimeter. The key-point of this study is the possibility of a topological and geometric reconstruction of the energy deposited by muons in the AHCAL. On one side muons are identified as tracks in the detector and the energy associated to the tracks is measured. On the other side, the δ-rays produced by muons can be identified along the tracks; the measurement of their energy distribution and the comparison with the theoretical expectation is proposed.

Outline of the thesis

The first part of the thesis presents the general framework of the study; in chapter 1 the theoretical and experimental motivations of SUSY as extension of the SM are treated and in chapter 2 the challenges of the design of the International Linear Collider are outlined. The study of the neutralino system is hence presented in chapter 3. In the last part of the thesis it is presented the R&D program for the CALICE AHCAL; in chapter 4 the fundamental ideas of the design of the CALICE AHCAL are defined and in chapter

5 the analysis of experimental data is presented. Finally conclusions and outlook are discussed.

Chapter 2

Theoretical Background

"A ladybird was flitting from flower to flower,
with the elegance of the pretty princess of a tale,
two old spinster ladybirds were her bridesmaids,
mystery and beauty in her blue eyes."
— ibidem

Introduction

The Standard Model (SM) of particles and their interactions [19] is a solid theory which is in successful agreement with the experimental observations of the last three decades. However this theory is not totally satisfactory. Among the problems which feature the model, three are more important. First the Higgs mechanism [9, 10], which explains the origin of the mass of the particles, has not been yet experimentally proven. Second the stabilization of the mass scale of the Higgs particle is not possible at a loop level [15, 43]. Third the cosmological observations show strong evidence of non-baryonic matter in the universe, which is not included in the Standard Model [11–13].

Many attempts were done in order to extend the Standard Model [44–46]. Supersymmetry [47–49] (SUSY) is nowadays one of the most convincing and complete theories beyond the SM. It postulates an additional symmetry between fermions and bosons. Although an experimental evidence of this theory has not been found up to now, it is believed that the next high energy collider experiments will provide clear SUSY signatures.

The aim of this chapter is to show the validity of supersymmetry as possible extension of the standard model. The basic features of the SM are shown with the support of a selection of recent experimental results. A particular emphasis is given to the limits and the current problems of the SM. The concepts of SUSY are then introduced. The full theoretical description of SUSY would have been outside the scope of this thesis. It was chosen hence to clarify the basic mechanism of symmetry between fermions and bosons with the clear quantum mechanics example of the *supersymmetric harmonic oscillator*.

Only the phenomenological aspects of the Supersymmetry as a Quantum Field Theory are then shown, in the framework of the Minimal Supersymmetric extension of the Standard Model (MSSM). Finally a study of the neutralino system is presented, which is the main topic of investigation of this thesis.

2.1 The discovery of four forces

The 20^{th} century was an exciting time for particle physics. Most of the experimental and theoretical efforts aimed at a deeper understanding of the basic components of the matter. The new and surprising observations were described with the leading theory of the Quantum Mechanics (QM). A first theoretical description was done by M. Plank in 1900. He proposed a quantized energy in order to explain the radiation spectrum of a black body [50]. Few years later (1905), A. Einstein, following Plank's hypothesis, postulated the existence of radiation quanta in order to describe the emission of electrons from materials irradiated with light [51]. The experimental evidence of a radiation quantum was obtained by A.H.Compton in 1923 [52]. He measured the wavelength of the light scattered from a fixed charged particle. He observed that the scattered light was shifted in wavelength following the same law of the relativistic scattering of a massless particle with energy $E = h\nu$, where ν was the frequency of the wave. It was hence experimentally established that the electromagnetic force was mediated by an energy quantum, the *photon*.

Further information about the structure of the matter came with the experimental study of the atoms. Rutherford's scattering experiment provided a good evidence of the existence of nuclei. He called *proton* the nucleus of hydrogen, the lightest atom. Chadwick discovered the *neutron* ten years later, in 1932. Developing a theory of nuclei, the existence of a force which bounds protons and neutrons in the nucleus was postulated. This *strong force* has a small range, of the order of 1 fm, just the typical size of the nucleus.

A new piece of the puzzle was clarified by Fermi in 1934. The neutron had recently been discovered and Pauli postulated the existence of a *neutrino* some years before (1930). With this information, Fermi described the nuclear β decay as a decay of the neutron into a proton, an electron and a neutrino. The interaction which causes the decay was supposed to be *weak*. Twenty years later the discovery of the K^+ added a new ingredient in the understanding of this new force. The K^+ can decay both into $\pi^\pm\pi^0$ and into $\pi^+\pi^+\pi^-$. In principle it was supposed that there were two different particles with mass approximately equal to the mass of the K^+. This was the so-called $\tau - \theta$ puzzle. T.D. Lee and C.N. Yang proposed that a solution could be the violation of the parity [53]. This hypothesis was experimentally confirmed by C.S Wu, E. Ambler, R.W. Hayward, D.D. Hoppes and R.P. Hudson in 1957 [54]. They discovered that parity is indeed violated even in the β decay. As both nuclear interactions and electromagnetic interactions conserve the parity, this was a struggling evidence of a new force.

Only the formulation of the electroweak theory by Glashow, Weinberg and Salam [55–57] brought light to the fundamental mechanisms of the weak and electromagnetic interactions. They postulated that this interaction is mediated by the vector bosons $W^\pm$ and

Z^0, whose evidence was experimentally established in the neutral electro-weak currents observation at the Gargamelle experiment in 1973-74 [4]; the discovery of the three associated gauge bosons (Z^0, $W^{\pm}$) was finally obtained at the UA2 [5, 58] and LEP [6] experiments.

The classical physics developed in the 19th century found hence a more advanced description in the Quantum Mechanics in the 20th century. However an older observation have been confusing the scientists all along the 20th century until today, without any solution. The gravity, the force which binds massive particles and rules the motion of planets, has been known since the 17th century but it has not found yet a good explanation in the framework of QM [19].

2.2 The Standard Model

The *strong*, *weak* and *electromagnetic* interactions were understood to be *gauge theories* [19] in which the symmetry of fields causes the existence of force-carrying particles. This is the basic idea of the Standard Model (SM) of elementary particles and of their interactions.

2.2.1 Theory and experimental validation

Elementary particles are the point-like constituents of the matter with no known substructure down to the present limit of $10^{-18} - 10^{-19}$ m. Two classes of elementary particles are observed in nature. First the building blocks of the matter are fermions and have spin 1/2. Second the interactions between fermions are mediated by bosons, i.e. particles with integer spin.

More precisely, the SM is a gauge theory based on the $SU(3)_C \otimes SU(2)_L \otimes U(1)_Y$ gauge group. The field components and their quantum numbers under the gauge group are [59]:

Gauge sector: spin 1. The gauge bosons belong to the adjoint representation of the Standard Model gauge group. They mediate the interactions between matter particles. In the following list their definition, the quantum numbers under their symmetry gauge group[1], the gauge sub-group to which they belong and the associated coupling constant are reported:

$$\begin{array}{rrlcc} \textit{gluons} & G^a_\mu: & (\underline{8}, \underline{1}, 0) & SU(3)_C & g_s \\ \textit{weak} & W^i_\mu: & (\underline{1}, \underline{3}, 0) & SU(2)_L & g \\ \textit{abelian} & B_\mu: & (\underline{1}, \underline{1}, 0) & U(1)_Y & g' \end{array} \tag{2.1}$$

Gluons are physical states, corresponding to real massless particles, and mediate the strong force ($SU(3)_C$). The physical gauge bosons which mediates the electroweak

---

[1] The first two numbers correspond to the dimension of the representation in the basis $(SU(3)_C, SU(2)_L \otimes U(1)_Y)$; a representation of dimension n is written as $\underline{n}$; the third number is the value of the hypercharge.

force are W^p, γ and Z^0. While $W^{\pm}$ correspond physically to the generators $W^{1,2}$ of $SU(2)_L$, the Z^0 and γ boson are a superposition of the W^3_μ and B_μ generators:

$$\begin{aligned} A_\mu &= \cos(\theta_{\mathrm{W}})\mathrm{B}_\mu + \sin(\theta_{\mathrm{W}})\mathrm{W}_3^\mu \\ Z^0_\mu &= -\sin(\theta_{\mathrm{W}})\mathrm{B}_\mu + \cos(\theta_{\mathrm{W}})\mathrm{W}_3^\mu \end{aligned} \tag{2.2}$$

where θ_W is the so-called *Weinberg angle*.

Fermion sector: spin 1/2. A total number of 12 fermions are observed and described by the SM. They are divided in the two families of leptons and quarks. The six leptons are μ, τ, e and the three corresponding neutrinos ν_μ, ν_τ, ν_e. While μ, τ and e have charge $Q = -1$ and are massive, neutrinos are described neutral and massless in this simplified SM[2]. The 6 quarks are u, d, c, s, t, b. They are all massive and charged.

The left-handed leptons and quarks are organized as doublets under the $SU(2)_L \otimes U(1)_Y$ symmetry group. As the neutrino is considered massless, it does not have a right-handed counterpart. The right handed leptons are organized in singlets under $SU(2)_L \otimes U(1)_Y$. Also the right-handed quarks are singlets under $SU(2)_L \otimes U(1)_Y$. However, as quarks are all massive, a right-handed counterpart of all quarks exists.

The quantum numbers of the fermions under the SM gauge symmetry group $(SU(3)_C, SU(2)_L, U(1)_Y)$ are[3]:

$$\begin{array}{llllll} \textit{quarks} & & & & & \\ & \begin{pmatrix} U^i_\alpha \\ D^i_\alpha \end{pmatrix}_L = & \begin{pmatrix} u^i \\ d^i \end{pmatrix}_L, & \begin{pmatrix} c^i \\ s^i \end{pmatrix}_L, & \begin{pmatrix} t^i \\ b^i \end{pmatrix}_L & (\underline{3}, \underline{2}, 1/3) \\ & U^i_{\alpha,R} = & u^i_R, & c^i_R, & t^i_R & (\underline{3}^*, \underline{1}, 4/3) \\ & D^i_{\alpha,R} = & d^i_R, & s^i_R, & b^i_R & (\underline{3}^*, \underline{1}, -2/3) \\ \textit{leptons} & & & & & \\ & L_{\alpha,L} = & \begin{pmatrix} \nu_e \\ e \end{pmatrix}_L, & \begin{pmatrix} \nu_\mu \\ \mu \end{pmatrix}_L, & \begin{pmatrix} \nu_\tau \\ \tau \end{pmatrix}_L & (\underline{1}, \underline{2}, -1) \\ & R_{\alpha,R} = & e_R, & \mu_R, & \tau_R & (\underline{1}, \underline{1}, -2) \end{array} \tag{2.3}$$

The index α represents the three generations in which the fermions are divided. The existence of the generations is a specific feature of the nature and it is just described

---

[2] The introduction of the mass of the neutrinos is an unavoidable extension of the SM, due to the experimental evidences. It will not be treated in this thesis.

[3] See equations 2.1 for the notation used in this thesis

by the SM, but not really explained. The electroweak interaction is left-right asymmetric; left-handed fermions are doublets under the $SU(2)_L \otimes U(1)_Y$ gauge group while right-handed fermions are singlets, with different quantum numbers.

The index i indicates the colour quantum number of quarks in the $SU(3)_C$ group. The strong interaction bounds only quarks, while leptons are totally unaffected.

The gauge structure of the Standard Model was tested in a series of successfully experiments in the last decades. In this introduction just some significant examples about the electroweak force will be shown, mainly taken from the complete report in [6].

The precision measurement at the Z^0 pole was performed in the experiments ALEPH, DELPHI, L3, OPAL at LEP [60] and SLD at SLC [61]. The mass and total width of the Z^0 boson are today known as [19]:

$$\begin{aligned} m_Z &= 91.186 \pm 0.0021 \ \text{GeV} \\ \Gamma_Z &= 2.4952 \pm 0.0023 \ \text{GeV} \end{aligned} \tag{2.4}$$

The $W^\pm$ boson was initially discovered and measured in the pp-collider experiment UA2. Precise measurements were done also at the pp-collider Tevatron, in the CDF and D0 experiments. The extension of the LEP machine from the Z^0 pole up to 208 GeV centre of mass allowed to produce $W^\pm$ pairs also in the e^+e^- machine, with a consequent increase in precision. The best measurement of the $W^\pm$ boson mass and width is [19]:

$$\begin{aligned} m_W &= 80.398 \pm 0.0025 \ \text{GeV} \\ \Gamma_W &= 2.141 \pm 0.041 \ \text{GeV} \end{aligned} \tag{2.5}$$

The experimental precision of the measurement of the Standard Model allowed to test the theory up to radiative loop corrections. At the e^+e^- machine, the measured line-shape asymmetry of the Z^0 resonance spectrum matched the SM expectation, with the inclusion of the QED radiative corrections. A more striking example of the prevision power of the SM is the constraint on the mass of the top quark from electroweak precision measurements. In Fig. 2.1 the indirect measurement of m_t and m_W with the LEPI+SLD data is compared with the direct measurements at LEP and Tevatron. The LEP1+SLD data constrained $m_t = 174.1^{+9.7}_{-7.6}$ GeV and the CDF experiment confirmed the value $m_t = 170.9 \pm 1.8 \pm 0.6$ GeV [19].

A basic feature of the Standard Model is the generation structure in the leptonic and in the quark sector. In Fig. 2.2a the measurement of the hadron production cross-section at the Z^0 resonance measured at LEP is shown. The theoretical prediction with a total number of neutrino generations $N_\nu = 2, 3, 4$ is also shown. The decay width of the Z^0 boson into neutrinos was found compatible to a total number of families $N_\nu = 2.984 \pm 0.008$ as expected from the Standard Model [6, 63].

A precise determination of the Standard Model is offered by the quark sector. The mass eigenstates of quarks are not eigenstates of the $SU(2)_L \times U(1)_Y$ group. The weak

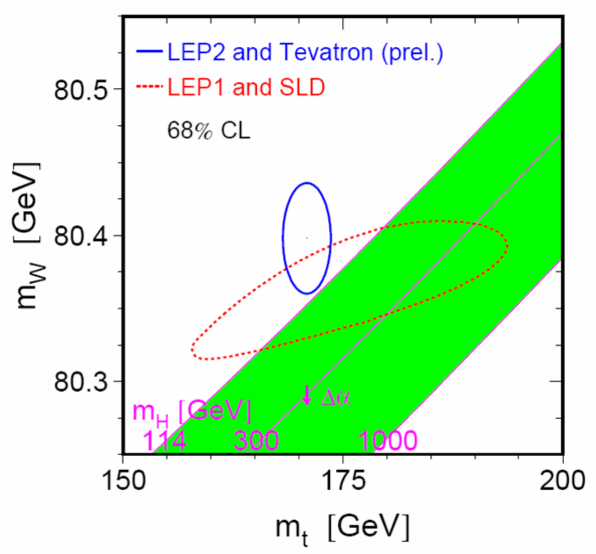

Figure 2.1: Mass of the top quark and of the $W^\pm$ boson. Comparison of the indirect estimation (LEPI+SLD data) and the direct measurement (Tevatron and LEP-II data). The 68% C.L. contours are plotted in both cases. The band describes the SM relationship between the Higgs Mass and the W boson mass. The arrow shows the variation of this relation if the electroweak coupling constant $\alpha(m_Z^2)$ is changed by one standard deviation. Figure taken from [62].

eigenstates and the mass eigenstates are related by the CKM matrix. In Fig. 2.2b the typical representation of this matrix in the form of the *unitarity triangle* is shown. The measurement of the elements of the CKM matrix confirms very precisely the Standard Model expectation. The validity of the CKM model allows also constraining the CP violation source of the Standard Model to the single not-vanishing phase of the CKM matrix [19].

To conclude, the experimental validation of the Standard Model allowed confirming this gauge theory as a good description of the nature at the actual energy scale of the universe. Many other experimental successes of the SM could be mentioned in this overview, in particular regarding the $SU(3)_C$ symmetry [64] and the QCD measurements [7, 8]. The SM was tested at a quantum level and is the basic pilaster of the present understanding of the interactions between fundamental particles.

2.3 The Problems of the Standard Model

2.3.1 The Unification of the Gauge Couplings

According to the *Grand Unification Hypothesis* the gauge symmetry increases with the energy up to the unification of the forces. The coupling of the electroweak and strong forces have to be identical at a Grand Unification energy scale M_{GUT} [59]. The running of the three coupling constants α_i is described by the Renormalization Group (RG)

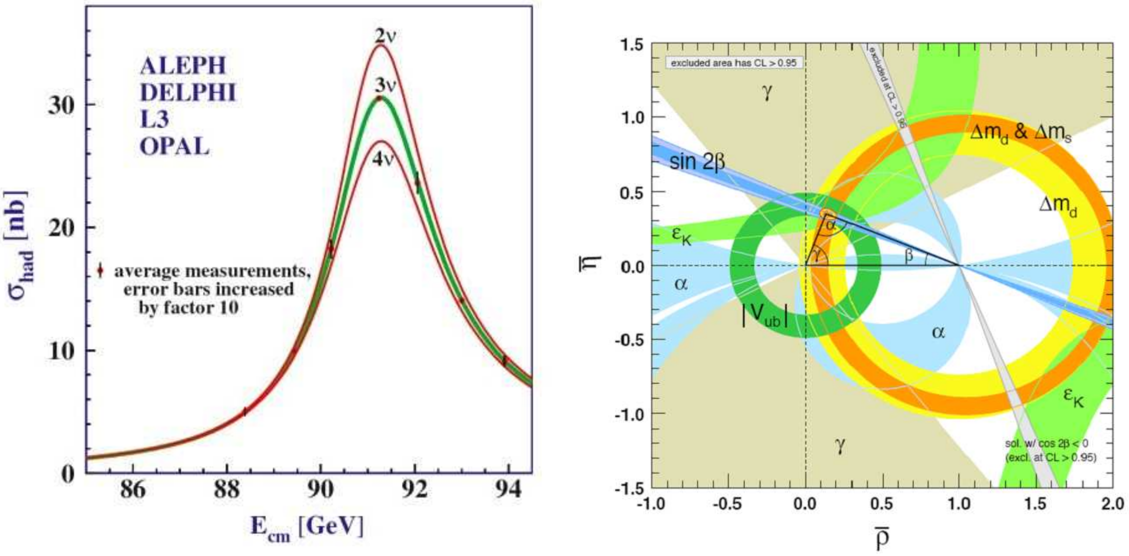

(a) (b)

Figure 2.2: Measurement of the properties of the generations of the fermions in the SM. In (a) the hadronic production at the Z^0 resonance observed at LEP is shown (full dots). The solid lines are the theoretical predictions with the assumption of a number of neutrino generations $N_\nu = 2, 3, 4$. The data are consistent with $N_\nu = 2.994 \pm 0.012$ [6]. In (b) the experimental constraints on the (ρ,η) plane describing the unitarity triangle are shown. The shaded areas have 95% C.L. and does not show any evidence of violation of the unitarity [19].

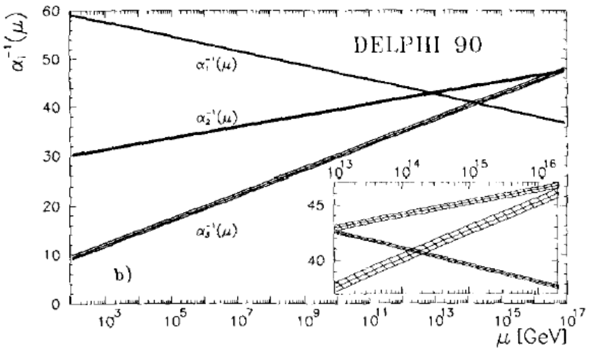

Figure 2.3: First order evolution of the coupling constants in the SM using $M(Z)$ and $\alpha(M(Z))$ from DELPHI data. The three coupling constants disagree with a single unification point by more than 7 standard deviations. Figure from [14].

equations [14]:

$$\frac{d\tilde{\alpha}_i}{dt} = b_i\tilde{\alpha}_i^2, \qquad \tilde{\alpha}_i = \frac{\alpha_i}{4\pi}, \qquad t = \log\left(\frac{Q^2}{\mu^2}\right) \tag{2.6}$$

where α_i are the three coupling constants of the electroweak and strong interactions and the coefficients b_i are expressed by the following relation [59]:

$$b_i = \begin{pmatrix} b_1 \\ b_2 \\ b_3 \end{pmatrix} = \begin{pmatrix} 0 \\ -22/3 \\ -11 \end{pmatrix} + N_{gen}\begin{pmatrix} 4/3 \\ 4/3 \\ 4/3 \end{pmatrix} + N_{Higgs}\begin{pmatrix} 1/10 \\ 1/6 \\ 0 \end{pmatrix} \tag{2.7}$$

In the SM there are 3 generations (N_{gen}) and 1 Higgs complex field (N_{Higgs}). Therefore the coefficients are $b_i = (41/10, -19/6, -7)$. In the modified minimal subtraction scheme ($\overline{MS}$), the world averaged values of the couplings at the Z^0 energy are obtained from a fit to the LEP and Tevatron data [19], that gives:

$$\alpha_1(M_Z) = 0.017 \qquad \alpha_2(M_Z) = 0.034 \qquad \alpha_3(M_Z) = 0.118 \tag{2.8}$$

The solution of the RG equation reads [59]:

$$\frac{1}{\tilde{\alpha}_i(Q^2)} = \frac{1}{\tilde{\alpha}_i(\mu^2)} - b_i\log\left(\frac{\mathrm{Q}^2}{\mu^2}\right) \tag{2.9}$$

In Fig. 2.3 the running of the coupling constants in the SM is shown according to equation 2.9. The possibility of the unification at a single point is excluded by more than 7 standard deviations. The Standard Model however naively suggests that the grand Unification Scale is at a $M_{GUT} \sim 10^{15-16}$ GeV.

The gravity stays completely outside this picture. A big problem of the Standard Model is that it does not allow even to couple the gravity with the other forces in nature.

2.3.2 The Higgs Boson: missing proof and the problem of hierarchy

The most challenging puzzle of the Standard Model is the mass pattern of the particles. If the gauge symmetry has been exact, the particles would not have had mass. The theoretical solution to this problem is the *spontaneous electroweak symmetry breaking*: $SU(2)_L \otimes U(1)_Y \otimes SU(3)_C \rightarrow U(1)_{em} \otimes SU(3)_C$. A new complex scalar field is introduced, the Higgs boson. It is a doublet under $SU(2)_L \otimes U(1)_Y$ with quantum numbers $T = 1/2$ and $Y = 2$:

$$H = \left(\begin{array}{c} H^+ \\ H^0 \end{array} \right) \tag{2.10}$$

According to the $SU(2)$ gauge invariance, the Higgs field can be written as:

$$\Phi = \frac{\lambda}{\sqrt{2}} e^{i\alpha(x)\hat{T}} \begin{pmatrix} H^+ \\ H^0 \end{pmatrix} \Rightarrow e^{\left(\frac{i}{\lambda}\Theta(x) \cdot \mathbf{T}\right)} \begin{pmatrix} 0 \\ H^0 \end{pmatrix} \Rightarrow (\lambda + \chi(x)) \begin{pmatrix} 0 \\ 1 \end{pmatrix} \tag{2.11}$$

This new complex field is described with a potential:

$$U(|\Phi|^2) = -\mu^2|\Phi|^2 + h|\Phi|^4 \tag{2.12}$$

The breaking mechanism enters in the vicinity of the vacuum state Φ_0, defined at the minimum of the potential $U(|\Phi|^2)$:

$$\Phi_0 \equiv \langle 0|\Phi|0\rangle = \frac{\lambda}{2} \begin{pmatrix} 0 \\ 1 \end{pmatrix} \Rightarrow \frac{\mu}{\sqrt{2h}} \begin{pmatrix} 0 \\ 1 \end{pmatrix} \tag{2.13}$$

The vacuum expectation value (v.e.v.) of the Higgs fields reads:

$$\text{v.e.v.} \equiv |\langle 0|\Phi|0\rangle| = \frac{\mu}{\sqrt{2\text{h}}} \tag{2.14}$$

The consequence of the Higgs potential is hence that the vacuum expectation value is invariant under the $SU(2) \otimes U(1)$ gauge group, while the vacuum state is not — being defined up to a complex phase. The symmetry is hence spontaneously broken by the vacuum state.

The particles get massive interacting with the Higgs field. The coupling of the gauge bosons with the Higgs field is described by :

$$\begin{gathered} \left|\left(i\partial_\mu + g\hat{T} \cdot W_\mu + \tfrac{g^{'}}{2} B_\mu \hat{Y}\right) \Phi\right|^2 = \\ \tfrac{1}{2}\left(\partial_\mu^2 \chi(x) + g^2\lambda^2 W_1^\mu W_\mu^1 + g^2\lambda^2 W_2^\mu W_\mu^2 + \tfrac{g^2\lambda^2}{\cos^2(\theta)} Z^\mu Z_\mu\right) \end{gathered} \tag{2.15}$$

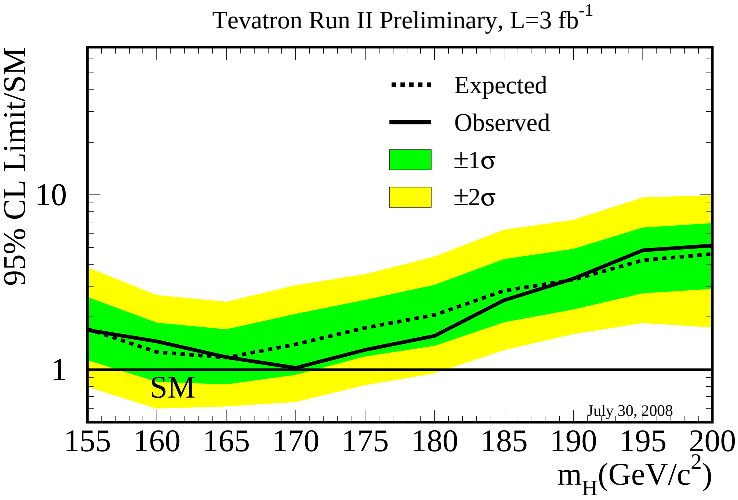

Figure 2.4: Upper bound on the SM Higgs boson cross section obtained by combining CDF and D0 search results, as a function of the mass of the Higgs boson. The limits are shown as a multiple of the SM cross section. The solid curve shows the observed upper bound, the dashed black curve shows the median expected upper bound assuming no signal is present, and the bands show the 68% and 95% probability bands around the expected upper bound [65].

The terms quadratic in the gauge fields define the mass of the bosons: The quadratic term of the boson fields allows the masses of the bosons to be:

$$M_W = g\lambda \qquad M_Z = \frac{g\lambda}{\cos(\theta_\mathrm{W})} = \frac{M_W}{\cos(\theta_\mathrm{W})} \qquad M_\gamma = 0 \tag{2.16}$$

A nice consequence of the theory is that the choice of the quantum numbers of the Higgs bosons allows the photon to be naturally massless.

The interaction terms of the fermions with the Higgs field read:

$$\mathcal{L}_l = -\sqrt{2} f_l \left(\overline{R}_l \phi^* L_l + \overline{L}_l \phi^* R_l \right) = -f_l \left(\lambda + \chi \right) \overline{\psi}_l \psi_l \tag{2.17}$$

from which the mass of the fermions is $m_l = f_l \lambda$.

A strong theoretical argument about the expected mass of the Higgs Boson is the requirement of a unitary S-matrix of the electroweak force [18, 66]. The unitarity is a consequence of the fundamental conservation of the probabilities at the quantum level. The scattering cross section is usually expressed in term of the partial-wave expansion a_J. The constraint coming from unitarity reads:

$$Im(a_J) \geq |a_J|^2 = Re(a_J)^2 + Im(a_J)^2 \tag{2.18}$$

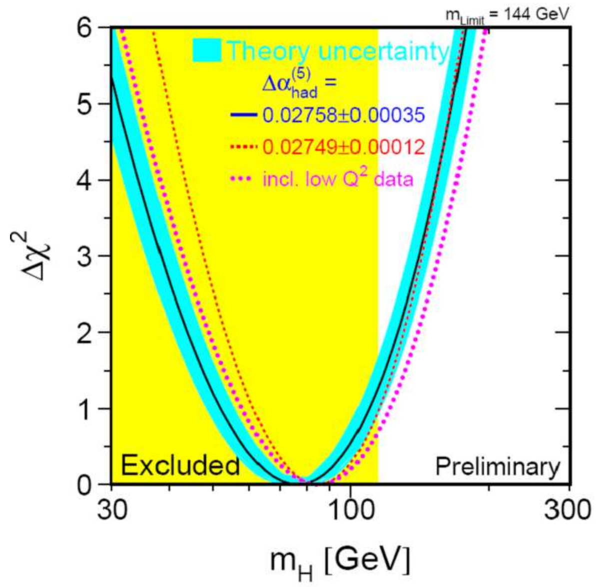

Figure 2.5: Result of the SM fit using all the LEP data and the determination of the W and top quark masses form pp-colliders. The vertical band shows the 95% exclusion limit on m_H from the direct searches [62].

for which it is obtained:

$$Im(a_J) \geq |a_J|^2 = \left(Re(a_J)^2 + Im(a_J)^2\right) \Rightarrow |Re(a_J)| \leq \frac{1}{2} \tag{2.19}$$

In case of the $W_L^+ W_L^- \rightarrow Z_L Z_L$ scattering, the $J = 0$ tree level amplitude is $a_0(s) = G_F\sqrt{(}2)s/(16/\pi)$. The unitarity relation requires than new physics to appear at a scale $\Lambda_U = \sqrt{8\pi/(G_F\sqrt{(}2))} \sim 1.2$ TeV. If the Higgs doublet is included, $a_0(s)$ can be expressed as:

$$a_0(s) = \frac{G_F\sqrt{2}s}{16\pi} - \frac{G_F\sqrt{2}s}{16\pi}\frac{s}{s-m_h^2} + O\left(\frac{M_W^2}{s}\right) \overset{s>>m_h^2}{\rightarrow} -m_h^2\frac{G_F\sqrt{2}}{16\pi} \tag{2.20}$$

from which the constraint on the Higgs mass can be calculated. It is shown [67] that the most stringent constraint on the Higgs mass from these considerations is 780 GeV. The absence of a Higgs boson in this energy range would compromise the high energy behaviour of the scattering of the gauge bosons, which would start undergoing new gauge interactions or strong interactions.

A weak side of the theory of electroweak symmetry breaking is the so-called *hierarchy problem* [15, 43]. It has two aspects. The first one is the existence of the hierarchy. In order to obtain the observed spontaneous symmetry breaking pattern, the Higgs Boson mass is required at the Electroweak scale ($m_H \sim 10^2$ GeV), very far from the Higgs Boson mass required for the symmetry breaking at the GUT scale ($m_\Sigma \sim 10^{16}$ GeV). The ratio between the two scales is $m_H/m_\Sigma \sim 10^{-14}$. There is no natural way of getting this extremely small number within the SM. The second aspect is that also if the mechanism generating the hierarchy was known, the stabilization of the hierarchy at loop level would not be possible. In Fig. 2.9a the one-loop correction diagram to the Higgs Boson mass is shown. It usually gives a contribution:

$$\delta m^2 = \lambda \int^{\Lambda} \frac{d^4k}{(2\pi)^4} \frac{1}{k^2} \sim \frac{\lambda}{16\pi^2} \int^{\Lambda} dk^2 \tag{2.21}$$

The one-loop level mass squared of the particle is hence expressed as:

$$m^2 = m_0^2 + \alpha\lambda \frac{\Lambda^2}{16\pi^2} \tag{2.22}$$

where α is a positive or negative number of order 1 and m_0 is the bare mass of the scalar field without any underlying physics. In the Standard Model the Higgs mass receives the following one-loop corrections:

$$\delta m_h^2 = \frac{3\Lambda^2}{8\pi^2 v^2} \left[\left(4m_t^2 - 2M_W^2 - M_Z^2 - m_h^2 \right) + O\left(\log \frac{\Lambda}{\mu} \right) \right] \tag{2.23}$$

The assertion that the quadratic contribution vanishes translates into the relation between the masses (Veltman condition [68]):

$$4m_t^2 = 2M_W^2 + M_Z^2 + m_h^2 \tag{2.24}$$

This relation is not ensured at higher-loop orders. The mechanism which stabilizes these corrections is not included in the Standard Model.

Up to now there is no experimental evidence of such scalar complex field. In Fig. 2.4 the probability of the Higgs Boson discovery in the CDF experiment is shown. The Higgs Boson masse 170 GeV is excluded at 95% C.L. [20]. In Fig. 2.5 the χ^2 of the fit of the Standard Model is shown using the full set of LEP data [69, 70] and the measurement of the W and top mass from pp colliders. The current best fit of all the data is $m_{H^0} = 91^{+45}_{-32}$ GeV at 95% C.L.[4]. The leak of an experimental proof of the Higgs Boson is by far the biggest problem of the SM.

2.3.3 Dark Matter

The measurement of the rotation of spiral galaxies provided the clearest evidence for the presence of the dark matter in the Universe. In Fig. 2.6a the orbital speed of the planets is shown as a function of the distance from the sun. The rotational speed of the planets follows precisely the expectation of the Newton mechanics:

$$\frac{mv^2}{r} = G\frac{mM}{r^2} \Rightarrow v = \sqrt{\frac{GM}{r}} \tag{2.25}$$

In Fig. 2.6b the same measurement for the stars in the galaxies is shown as a function of the distance from the centre of the galaxy. At a distance of 4 kpc the velocity reaches

---

[4] These values are obtained using a top quark mass of 172.7 ± 2.9 GeV.

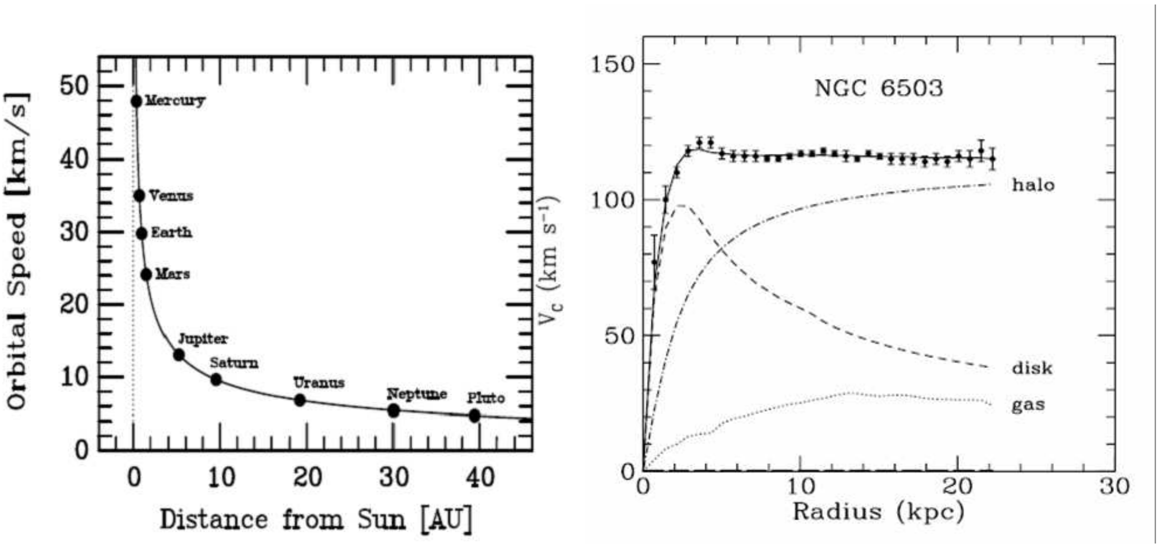

(a) (b)

Figure 2.6: Evidence of Dark Matter in the Universe. In (a) the speed of the planets around the sun is shown as a function of their distance. The speed follows the expected Newton's law. In (b) the same measurement is shown for the rotation of luminous objects in galaxies. At a distance of 4 kpc the velocity reaches a plateau, in disagreement with the Newton's law. Figures from [71]

a plateau, with an evident discrepancy from the Newton law. This behaviour can be explained with the presence of Dark Matter which participates to the gravitational interaction of the stars. Spiral galaxies consist of a central bulge and a very thin disk and are surrounded by an approximately spherical halo of Dark Matter.

A more precise quantification of the Dark Matter content of the universe is recently made with the detection and analysis of the Cosmic Microwave Background (CMB) Anisotropies [72]. The CMB is composed of photons with a typical black body distribution at a temperature $T = 2.725°$ K. Recent observations showed that the angular distribution of this spectrum is featured by small anisotropies. In Fig. 2.7 the temperature power spectrum of the CMB measured in the most recent experiments is shown. The interpretation of this spectrum is based on the actual cosmological model. At the time of generation of the CMB the early universe was composed of baryons (protons, neutrons, and helium nuclei), electrons, photons, neutrinos and dark matter. While neutrinos and Dark matter interact only gravitationally, since the weak interaction cross sections are too small at this energy scale, photons and baryons have a reach interplay. They interact electromagnetically via Compton scattering of the radiation from the electrons. The typical interaction energies are low energetic enough to be approximated with the Thompson scattering. All the other interactions have a small cross section and can be neglected. At a temperature of about 0.5 eV the electrons recombine with the protons and helium nuclei, forming neutral atoms. At this point the elastic photon scattering is reduced and photons begin to propagate freely in the universe. The Microwave Background is an image of the *surface of the last scattering.*

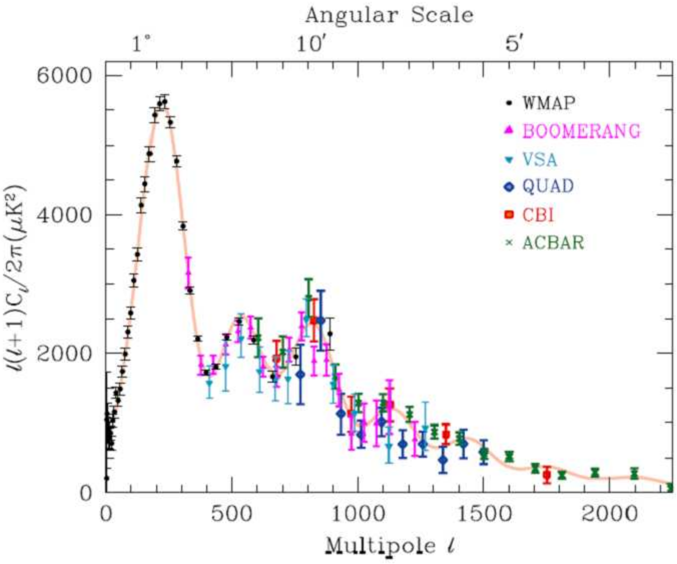

Figure 2.7: Band-power estimates from the WMAP, BOOMERANG, VSA, QUAD, CBI, and ACBAR experiments. Some of the low-l and high-l band-powers which have large error bars have been omitted. The acoustic peaks can be recognized and measured with precision. Figure from [19].

The interplay between gravitational forces and radiation pressure set up acoustic fluctuations inside the baryon-photon fluid, which reflects into the temperature anisotropy observed today [11–13]. The baryonic and dark matter content of the early universe influenced the gravitational forces and hence the quality of the oscillations and can be included in the models. The fit of the power spectrum according to the cosmological model provides the following experimental indirect determination of the dark matter content in the Universe:

$$\Omega_m h^2 = 0.132 \pm 0.004 \qquad \Omega_b h^2 = 0.0219 \pm 0.0007 \tag{2.26}$$

where Ω_m is the relative matter density, Ω_b is the relative baryonic matter density. The baryonic matter is only a small fraction ($\sim 16\%$) of the total matter, while 84% of the total matter in the universe is at the moment unknown.

The Dark Matter is expected to be cold and not relativistic. It has to couple very weakly with the electromagnetic field and it must be stable at cosmological time scale. Moreover it must have the right relic density. The only candidate within the Standard Model would be the neutrino, which was ruled out at 95% C.L. ($\Omega_\nu < 0.0076$ [19]). The SM does not provide any other possible candidate to the Dark Matter, leaving the problem completely open.

2.4 Supersymmetry

The Supersymmetry (SUSY) is a symmetry between fermions and bosons. A supersymmetric operator $\mathcal{Q}$ is defined according to the prescription:

$$\mathcal{Q}|boson\rangle = |fermion\rangle \qquad \mathcal{Q}|fermion\rangle = |boson\rangle \tag{2.27}$$

In section 2.2 it was pointed out that the SM describes fermions and bosons in two separate sectors. The first are the basic constituents of the matter, the second mediate the interaction. Thus SUSY introduces a completely new perspective of the description of the physics of fermions and bosons.

2.4.1 An example: the SUSY harmonic oscillator

Before showing the phenomenological consequences of SUSY in particle physics, it is useful to introduce the main concepts of SUSY with a Quantum Mechanics example. The following discussion is freely quoted from [73] and [74]. Let's consider a harmonic oscillator system in non-relativistic Quantum mechanics. The lagrangian and Hamiltonian description of the system is searched in case of a fermionic field (ψ) and bosonic field (ϕ). A Supersymmetric system with mixed fermions and bosons will be finally build. This example aims at:

- underlining the difference between fermions and bosons in QM,
- showing the construction of a natural SUSY $\mathcal{Q}$ operator in QM.

In QM the difference between a fermionic (ψ) and a bosonic (ϕ) field is expressed by their commutation rules[5]:

$$\begin{aligned} &\left[\phi(x,t), \phi^{+}(x^{'},t)\right] = \delta^{3}(x-x^{'}) \\ &\left[\phi(x,t), \phi(x^{'},t)\right] = 0 \end{aligned} \tag{2.28}$$

and

$$\begin{aligned} &\left\{\psi(x,t), \psi^{+}(x^{'},t)\right\} = \delta^{3}(x-x^{'}) \\ &\left\{\psi(x,t), \psi(x^{'},t)\right\} = 0 \end{aligned} \tag{2.29}$$

In case of the bosonic field the Lagrangian of the harmonic oscillator can be written as:

$$\mathcal{L}_{B} = \frac{1}{2}\dot{\phi}^{2} - \frac{1}{2}\omega^{2}\phi^{2} \tag{2.30}$$

In order to calculate the Hamiltonian, first the canonical variables of the system have to be derived. They can be expressed using the creation and annihilation operators $\hat{a}$ and

---

[5] The notation $[A, B]$ indicates the commutation rule $[A, B] \equiv AB - BA$. The notation $\{A, B\}$ indicates the anti-commutation rule $\{A, B\} \equiv AB + BA$.

$\hat{a}^+$, which satisfy the commutation rules:

$$\left[\hat{a}, \hat{a}^+\right] = I \tag{2.31}$$

The canonical variables of a bosonic field hence read:

$$\begin{aligned} \phi &= \tfrac{1}{\sqrt{2\omega}} \textstyle\sum_i \left(\hat{a}_i e^{i\omega t} + \hat{a}_i^+ e^{-i\omega t}\right) \\ \Pi = \dot{\phi} &= \tfrac{\omega}{\sqrt{2}} \textstyle\sum_i \left(-\hat{a}_i e^{-i\omega t} + \hat{a}_i^+ e^{i\omega t}\right) \end{aligned} \tag{2.32}$$

from which the Hamiltonian is:

$$\begin{aligned} \mathcal{H}_B = \dot{\phi}\Pi - \mathcal{L} &= \omega\left(\hat{a}\hat{a}^+ + \hat{a}^+\hat{a}\right) \\ &= \tfrac{\omega}{2}\left(\hat{a}\hat{a}^+ + \tfrac{1}{2}\right) \end{aligned} \tag{2.33}$$

The Lagrangian of the harmonic oscillator in case of a fermionic field is:

$$\mathcal{L}_F = \frac{1}{2}\left(\dot{\psi}\psi^* - \dot{\psi}^*\psi\right) - \frac{1}{2}\omega^2\left(\psi\psi^* - \psi^*\psi\right) \tag{2.34}$$

The canonical variables can be expressed using the fermionic annihilation and creation operators $\hat{b}$ and $\hat{b}^+$ which follows the anti-commutation rule:

$$\left\{\hat{b}, \hat{b}^+\right\} = I \tag{2.35}$$

The canonical variables of the fermionic system are hence:

$$\psi = \hat{b}e^{i\omega t} \qquad \psi^* = i\hat{b}^+ e^{-i\omega t} \tag{2.36}$$

from which the Hamiltonian is defined:

$$\begin{aligned} \mathcal{H}_F = \dot{\psi}\psi^* + \dot{\psi}^*\psi - \mathcal{L} &= \omega\left(\hat{b}^+\hat{b} - \hat{b}\hat{b}^+\right) \\ &= \tfrac{\omega}{2}\left(\hat{b}^+\hat{b} - \tfrac{1}{2}\right) \end{aligned} \tag{2.37}$$

The features of the two Hamiltonians are:

1. A product term of the creation-annihilation operators ($\hat{a}\hat{a}^+$ and $\hat{b}\hat{b}^+$).

2. A constant term $+1/2$ for the bosons and $-1/2$ for the fermions.

The first can be interpreted as the *number of particles operator* of the system N_B for bosons and N_F for fermions:

$$\hat{N}_B = \hat{a}^+\hat{a} \qquad \hat{N}_F = \hat{b}^+\hat{b} \tag{2.38}$$

In the fermionic case the consequence is self-explanatory. From the commutation rules of $\hat{b}$ and $\hat{b}^+$ it follows:

$$\begin{aligned} \hat{N}_F^2 &= \hat{b}^+\hat{b}\hat{b}^+\hat{b} \\ &= \hat{b}^+(1-\hat{b}^+\hat{b})\hat{b} \\ &= \hat{b}^+\hat{b} = \hat{N}_F \end{aligned} \tag{2.39}$$

The consequence of this relationship is that the eigenvalues of N_F are either 0 or 1 on an eigenstate of the Hamiltonian. In other words in a quantum system two fermions can not stay in the same quantum state, i.e. the Pauli principle. Such limitation does not apply to the bosons.

The second feature of the Hamiltonian is a direct consequence of the commutation rules. The presence of a constant energy level in the vacuum state is the limitation of the theory and it is a basic problem in the extension to an infinite number of harmonic oscillators, i.e. in Quantum Field Theory.

The supersymmetry can be now introduced. A Supersymmetric harmonic oscillator is featured by both bosonic and fermionic fields in the same quantum system. The lagrangian can be defined as the sum of $\mathcal{L}_B$ and $\mathcal{L}_S$:

$$\mathcal{L}_S = \frac{1}{2}\dot{\phi}^2 - \frac{1}{2}\omega^2\phi^2 + \frac{1}{2}\left(\dot{\psi}\psi^* - \dot{\psi}^*\psi\right) - \frac{1}{2}\omega^2\left(\psi\psi^* - \psi^*\psi\right) \tag{2.40}$$

The Hamiltonian of this system is:

$$\mathcal{H}_S = \frac{\omega}{2}\left(\hat{b}^+\hat{b} + \hat{a}^+\hat{a}\right) \tag{2.41}$$

The nice feature of this Hamiltonian is that the constant term observed in H_B and H_F separately cancels out.

Moreover, the Lagrangian is invariant — up to a total derivative — under the transformation of the fields:

$$\begin{aligned} \delta\phi &= \epsilon\psi + \epsilon^*\psi^* \\ \delta\psi^* &= \left(-i\dot{\phi} - \omega\phi\right)\epsilon^* \\ \delta\psi &= \left(+i\dot{\phi} - \omega\phi\right)\epsilon \end{aligned} \tag{2.42}$$

This transformation maps fermionic fields into bosonic ones and vice-versa. It is a supersymmetric transformation. A supersymmetric quantum operator can be defined:

$$\begin{gathered}\delta\phi = \left[\left(\epsilon^* \overline{\mathcal{Q}} + \epsilon\mathcal{Q}\right), \phi\right] \\ \delta\psi^* = \left[\epsilon^* \overline{\mathcal{Q}}, \psi\right] \\ \delta\psi = \left[\epsilon\mathcal{Q}, \psi^*\right]\end{gathered} \tag{2.43}$$

from which $\mathcal{Q}$ reads:

$$\mathcal{Q} = \left(i\dot{\phi} - \omega\phi\right)\psi = -\sqrt{2\omega}\hat{a}^+\hat{b} \tag{2.44}$$

This supersymmetric operator commutes with the Hamiltonian and the following relation holds:

$$\dot{\mathcal{Q}} = i\left[Q, H\right] = 0 \tag{2.45}$$

This relation implies that there is a conserved *supercharge* $\mathcal{Q}$. Moreover, the Hamiltonian can be re-defined using the operator $\mathcal{Q}$:

$$\mathcal{H}_S = \frac{1}{2}\left[\mathcal{Q}, \overline{\mathcal{Q}}\right] \tag{2.46}$$

The energy eigenstates of the Hamiltonian are hence positively defined.

To conclude, this example showed that the introduction of supersymmetry in the easy quantum harmonic oscillator system causes new interesting features:

1. The null point energy cancels out between bosonic and fermionic contributions
2. A supercharge operator $\mathcal{Q}$ can be defined which maps bosonic fields into fermionic ones and vice versa
3. The supercharge is conserved, being a symmetry of the system.
4. The eigenstates of the energy are positively defined

The supersymmetry seems to be an interesting option for the extension of the symmetry group of the traditional Quantum Mechanics

2.4.2 Phenomenology of the Minimal Supersymmetric Standard Model

The super-multiplets in SUSY

A complete systematic description of the treatment of the Supersymmetry as a relativistic Quantum Field Theory can be found in the famous book by J. Wess [48]. In this section only the phenomenological consequences of the theory are shown, quoting one of the introductory lectures held by J. Wess in Hamburg in Winter 2006 and the introduction to SUSY by M. Peskin [75]. The considered SUSY model has only one

SUSY generator $\mathcal{Q}$ ($N = 1$ SUSY). Starting from the definition of the algebra of the operator $\mathcal{Q}$ the possible supermultiplets in an unbroken supersymmetry are analysed, in the framework of the Minimal Supersymmetric extension of the SM.

The key-point of SUSY is the introduction of a specific *graded algebra* for the symmetry generator $\mathcal{Q}$:

$$\begin{gathered} \{\mathcal{Q}_\alpha, Q_\alpha\} = 2\sigma^\mu_{\alpha\dot{\alpha}} P_\mu \\ \{\mathcal{Q}_\alpha, \mathcal{Q}_\alpha\} = \{\overline{\mathcal{Q}}_\alpha, \overline{\mathcal{Q}}_\alpha\} = 0 \\ [P^\mu, \mathcal{Q}_\alpha] = [\mathcal{Q}_\alpha, P^\mu] = 0 \end{gathered} \tag{2.47}$$

The definition of the particle multiplets in supersymmetry follows from the commutation rules of the operator $\mathcal{Q}$. It can be observed that also the following relations hold:

$$[\mathcal{Q}, \mathcal{H}] = 0 \qquad \left[\mathcal{Q}, -P^2_\mu\right] = 0 \tag{2.48}$$

The full set of commutation rules of $\mathcal{Q}$ suggests hence a degeneracy of the eigenstates of SUSY. In order words SUSY particle states are grouped in super-multiplets.

The first property of the particles in the same multiplets is that they have the same mass. In fact $\mathcal{Q}$ commutes with P_μ and with $-P^2_\mu$, which is the mass operator. Moreover, as Q_μ commutes with the full Hamiltonian, the particles in the same multiplets are featured by the same quantum numbers under the $SU(2)_L \otimes U(1)_Y$ gauge symmetry group.

A second fundamental property of a supermultiplet is that the number of fermionic n_F and bosonic n_b degrees of freedom is identical. Let's define for this purpose the operator $(-1)^{2s}$, where s is the spin of the particle. This operator commutes with any bosonic operator and anti-commute with any fermionic operator. For example the following conditions hold:

$$\begin{gathered} (-1)^{2s}\mathcal{Q}|boson\rangle = (-1)^{2s}|fermion\rangle = -|fermion\rangle \\ \mathcal{Q}(-1)^{2s}|boson\rangle = (+1)\mathcal{Q}|boson\rangle = |fermion\rangle \end{gathered} \tag{2.49}$$

Let's take the trace of the operator $(-1)^{2s}\{\mathcal{Q},\mathcal{Q}\}$:

$$\begin{aligned}
Tr\left((-1)^{2s}\{\mathcal{Q},\mathcal{Q}\}\right) &= \textstyle\sum_i \langle i|(-1)^{2s}\left\{\mathcal{Q},\overline{\mathcal{Q}}\right\}|i\rangle \\
&= \textstyle\sum_i \langle i|(-1)^{2s}\mathcal{Q}\overline{\mathcal{Q}}|i\rangle + \sum_i \langle i|(-1)^{2s}\mathcal{Q}\overline{\mathcal{Q}}|i\rangle \\
&= \textstyle\sum_i \langle i|(-1)^{2s}\mathcal{Q}\overline{\mathcal{Q}}|i\rangle + \sum_{i,j} \langle i|(-1)^{2s}\mathcal{Q}|j\rangle\langle j|\overline{\mathcal{Q}}|i\rangle \qquad (2.50) \\
&= \textstyle\sum_i \langle i|(-1)^{2s}\mathcal{Q}\overline{\mathcal{Q}}|i\rangle + \sum_i \langle i|\overline{\mathcal{Q}}(-1)^{2s}\mathcal{Q}|i\rangle \\
&= \textstyle\sum_i \langle i|(-1)^{2s}\mathcal{Q}\overline{\mathcal{Q}}|i\rangle - \sum_i \langle i|(-1)^{2s}\mathcal{Q}\overline{\mathcal{Q}}|i\rangle = 0
\end{aligned}$$

From the commutation rules of $\mathcal{Q}$ it follows:

$$0 = \sum_i \langle i|(-1)^{2s}P^\mu|i\rangle = p^\mu \sum_i \langle i|(-1)^{2s}|i\rangle = n_f - n_b \qquad (2.51)$$

This relationship demonstrates that the number of fermionic degrees of freedom is equal to the number of bosonic degrees of freedom.

The possible supermultiplets which satisfy these requirements, in an unbroken supersymmetry, are:

Chiral supermultiplet. It is composed by a 1/2 Weyl spinor ($n_F = 2$) and a complex scalar field ($n_B = 2$).

Gauge supermultiplet. It is composed by a spin-1 massless gauge boson ($n_B = 2$) and a spin 1/2 spinor ($n_f = 2$).

Supergravity multiplet It is composed by a spin-2 graviton (2 helicity states[6], $n_B = 2$) and a spin 3/2 gravitino ($n_f = 2$).

The field content of MSSM

A first phenomenological application of the theory is the attempt of expanding the Standard Model. Each SM field can be expanded as a part of a SUSY multiplet. This Minimal Extension of the Standard Model is called MSSM. The full set of the fields required in MSSM is shown in table 2.1.The fermion doublets of the SM are included in a chiral supermultiplet, with its super-partner spin-0 s-fermion field. For example, in case of the electron generation, the SM L_e doublet is completed with a SUSY $\tilde{L}_e$ doublet composed of the *selectron* and the *sneutrino*:

$$L_e = \begin{pmatrix} \nu_e \\ e \end{pmatrix}_L \Rightarrow \tilde{L}_e = \begin{pmatrix} \tilde{\nu}_e \\ \tilde{e} \end{pmatrix}_L \qquad (2.52)$$

---

[6] In the unbroken supersymmetry the graviton is massless and it is described only with two helicity states.

This is done for all the fermionic doublets and singlets, both for leptons and for quarks. The SUSY in principle does not explain the origin of the 3 fermionic generations in nature and there is no fundamental difference in the inclusion of each generation in a dedicated super-multiplet.

The gauge sector of the SM is extended in a spin-1 gauge super-multiplet. Each spin-1 gauge boson has a spin 1/2 *gaugino* super-partner. The superparticles of this sector are the 8 gluinos ($\tilde{g}$), 3 winos ($\tilde{w}$) and 1 bino ($\tilde{b}$).

The Supersymmetry extends the Higgs Boson sector. In order to give mass to up-type and down-type quarks two scalar fields are needed:

$$\begin{pmatrix} H_u^+ \\ H_u^0 \end{pmatrix} \qquad \begin{pmatrix} H_d^+ \\ H_d^0 \end{pmatrix} \tag{2.53}$$

Each scalar Higgs field is included in a chiral supermultiplet. Their superpartners are the neutral spin-1/2 *higgsinos* ($\tilde{h}_u$ and $\tilde{h}_d$)

In summary, the Minimal extension of the Standard Model consists of a doubling of the Standard Model fields, technically obtained by including the SM particles in the corresponding supermultiplets.

2.4.3 Supersymmetry Breaking

If the Supersymmetry was realized in nature, the mass of the SUSY particles would have been equal to the mass of the SM particles and they would have been discovered since long time. A mechanism of breaking of Supersymmetry has to be postulated. There are two different options. One is to condensate the ignorance about the SUSY breaking mechanism in a *ad hoc* parameterization. It is shown that the most generic broken SUSY Lagrangian has 105 masses, phases and mixing angles that can not be rotated away by redefining the phases and flavour basis for the quarks and lepton supermultiplets and that have no counterpart in the SM [76].

The second approach to the SUSY breaking problem is to model the mechanism which breaks the symmetry. The most common scenario for producing low-energy supersymmetry breaking is called *hidden sector* [77–79]. According to this scenario two sectors exist. The usual matter belongs to a *visible* sector, while the second sector is *hidden* and contains the fields which break supersymmetry. The interaction between the two sectors is possible by the exchange of some fields called *messengers*.

The four most studied mechanisms of SUSY breaking are:

- Gravity mediation (SUGRA) [80–84]
- Gauge mediation [85, 86]
- Anomaly mediation [87, 88]
- Gaugino mediation [89, 90]

The analysis presented in this thesis, in Chapter 4, refers to the SUGRA breaking mechanism. In this case the two sectors interact with each other via gravity. The mass

Superfield	Bosons	Fermions	$SU(3)_C$	$SU(2)_L$	$U(1)_Y$
Gauge					
$\mathbf{G}^a$	gluon g^a	gluino $\widetilde{g}^a$	8	1	0
$\mathbf{V}^k$	Weak W^k (W$^\pm$,Z)	wino,zino $\widetilde{w}^k(\widetilde{w}^\pm,\widetilde{z})$	1	3	0
$\mathbf{V}'$	Hypercharge B (γ)	bino $\widetilde{b}$ ($\widetilde{(\gamma)}$)	1	1	0
Matter					
$\mathbf{L}_e$	$\widetilde{L}_e = (\widetilde{\nu}_e, \widetilde{e})$	$L_i = (e, \nu_e)_L$	1	2	-1
$\mathbf{L}_\mu$	$\widetilde{L}_\mu = (\widetilde{\nu}_\mu, \widetilde{\mu})$	$L_\mu = (\mu, \nu_\mu)_L$	1	2	-1
$\mathbf{L}_\tau$	$\widetilde{L}_\tau = (\widetilde{\nu}_\tau, \widetilde{\tau})$	$L_i = (\tau, \nu_\tau)_L$	1	2	-1
$\mathbf{R}_e$	$\widetilde{R}_e = (\widetilde{e})$	$R_r = (e)_R$	1	1	2
$\mathbf{R}_\mu$	$\widetilde{R}_\mu = (\widetilde{\mu})$	$R_\mu = (\mu)_R$	1	1	2
$\mathbf{R}_\tau$	$\widetilde{R}_\tau = (\widetilde{\tau})$	$R_\tau = (\tau)_R$	1	1	2
$\mathbf{Q}_1$	$\widetilde{Q}_1 = (\widetilde{u}, \widetilde{d})$	$L_i = (u, d)_L$	3	2	1/3
$\mathbf{Q}_2$	$\widetilde{Q}_2 = (\widetilde{c}, \widetilde{s})$	$L_\mu = (c, s)_L$	3	2	1/3
$\mathbf{Q}_3$	$\widetilde{Q}_3 = (\widetilde{t}, \widetilde{b})$	$L_i = (t, b)_L$	3	2	1/3
$\mathbf{U}_1$	$\widetilde{U}_1 = (\widetilde{u})$	$R_1 = (u)_R$	3^*	1	-4/3
$\mathbf{U}_2$	$\widetilde{U}_2 = (\widetilde{c})$	$R_2 = (c)_R$	3^*	1	-4/3
$\mathbf{U}_3$	$\widetilde{U}_3 = (\widetilde{t})$	$R_3 = (t)_R$	3^*	1	-4/3
$\mathbf{D}_1$	$\widetilde{D}_1 = (\widetilde{d})$	$D_1 = (d)_R$	3^*	1	2/3
$\mathbf{D}_2$	$\widetilde{D}_2 = (\widetilde{s})$	$D_2 = (s)_R$	3^*	1	2/3
$\mathbf{D}_3$	$\widetilde{D}_3 = (\widetilde{b})$	$D_3 = (b)_R$	3^*	1	2/3
Higgs					
$\mathbf{H}_u$	H_u	$\widetilde{h}_u$	1	2	-1
$\mathbf{H}_d$	H_d	$\widetilde{h}_d$	1	2	1

Table 2.1: The field component of the minimal supersymmetric extension of Standard Model

scale of the hidden sector can be estimated as:

$$M_{SUSY} \sim \frac{M_{Hidden}^2}{M_{Plank}} \tag{2.54}$$

which is of the order of 10^{11} GeV for a typical SUSY breaking scale of 1 TeV. The lagrangian terms at the GUT scale depends only on four free parameters and a sign:

- tanβ, the ratio of the Higgs v.e.v. of the H_u and H_d doublets,
- $M_{1/2}$, the mass scale of the gauginos of $SU(3)_C$, $SU(2)_L$ and $U(1)_Y$,
- M_0, the mass scale of the sfermions and higgsinos,
- A_0, the common trilinear coupling between H and $f\overline{f}$,
- sign(μ), the sign of the Higgsino mixing parameter.

The specific mSUGRA SUSY scenario investigated in the analysis proposed in this thesis is the $SPS1a^{'}$ [91]. It is defined with the set of parameters

$$\begin{aligned} M_{1/2} &= 250GeV & sign(\mu) &= +1 \\ M_0 &= 70GeV & tan(\beta) &= 10 \\ A_0 &= -300GeV \end{aligned} \tag{2.55}$$

In the $SPS1a^{'}$ scenario the supersymmetric lagrangian is constructed with terms satisfying lepton flavour conservation and CP conservation. The SUGRA parameters are hence real. Moreover the R-parity conservation holds. The R quantum number is defined as:

$$R = (-1)^{3(B-L)+s} \tag{2.56}$$

and it is 1 for SM particles and -1 for SUSY particles. This implies that SUSY particles are produced in pairs. The lightest SUSY particle can not decay into SM particles and it is stable. The mass spectrum of this specific SUSY point is shown in table 2.2. A complete set of studies is at the moment available for the future collider experiments in this SUSY scenario, in order to have a coherent view of the potential of the discovery of the SUSY at future colliders [92]. The $SPS1a^{'}$ set is compatible with all high energy mass bounds and with the low energy precision data, as well as with the observed CDM data calculated as $\mathcal{B}(b \to s\gamma) = 3.0 \cdot 10^{-4}$ [93], $\Delta[g-2]_\mu/2 = 34 \cdot 10^{-10}$ [94], $\Delta\rho_{SUSY} = 2.1 \cdot 10^{-4}$ [94] and $\Omega_{CDM}h^2 = 0.10$ [93].

The other SUSY breaking models offer a different explanation of the interaction between the visible and hidden sector, but the phenomenological result is very similar. Only the mass spectrum of the particles changes significantly. An interesting scenario is the GMSB where the gravitino is the lightest SUSY particle and it is often investigated. In this thesis, if not specified, the reference scenario will be always the mSUGRA.

Particle	Mass [GeV]	Particle	Mass [GeV]
h^0	116.0	$\widetilde{\mu}_L$	189.9
H^0	425.0	$\widetilde{\mu}_R$	125.3
A^0	424.9	$\widetilde{\tau}_1$	107.9
H^+	432.7	$\widetilde{\tau}_2$	194.9
χ_1^0	97.7	$\tilde{\nu}_\mu$	172.5
χ_2^0	183.9	$\tilde{\nu}_\tau$	170.5
χ_3^0	400.5	$\widetilde{u}_L$	564.7
χ_4^0	413.9	$\widetilde{u}_R$	547.2
χ_1^+	183.7	$\widetilde{d}_L$	570.1
χ_2^+	415.4	$\widetilde{d}_R$	546.9
$\widetilde{e}_L$	189.9	$\widetilde{t}_1$	366.5
$\widetilde{e}_R$	125.3	$\widetilde{t}_2$	585.5
$\tilde{\nu}_e$	172.5	$\widetilde{b}_1$	506.3
$\tilde{g}$	607.1	$\widetilde{b}_2$	545.7

Table 2.2: Mass spectrum of the $SPS1a'$ SUSY scenario [91].

2.4.4 Supersymmetry as possible solution to the SM problems

The extension of the SM to a larger symmetry group has important effects to the problems specified before.

A first theoretical evidence is that SUSY restores the unification of the coupling constants of the three forces. In Fig. 2.8 it is shown the running of the coupling constants. In SUSY the coefficients of the Normalization Group Equations are
$b_i = (33/5, 1, -3)$ [59]. The break point M_{SUSY} and the unification point M_{GUT} are found [14]:

$$\begin{aligned} M_{SUSY} &= 10^{3.4\,\pm\,0.9\,\pm\,0.4} \quad \text{GeV}, \\ M_{GUT} &= 10^{15.8\,\pm\,0.3\,\pm\,0.1} \quad \text{GeV}, \\ \alpha_{GUT}^{-1} &= 26.3 \pm 1.9 \pm 1.0 \end{aligned} \tag{2.57}$$

The unification of the three coupling constants at a single point is not trivial. The introduction of new fields affects in fact all the three couplings at the same time and gives rise to strong correlations. Supersymmetry offers a nice combination of all the effects naturally providing the unification.

A second important success of SUSY is that it solves the hierarchy problem. The quadratic divergences of SM particles are cancelled out by the contributions of their

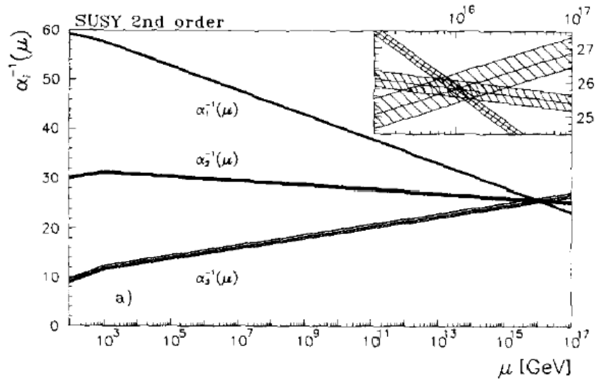

Figure 2.8: Second order evolution of the coupling constants in MSSM. The coupling constants meet at a single point. Figure from [14].

super-partners. In Fig. 2.9a and Fig. 2.9b it is shown how the contribution of the heavy scalar Higgs boson to the light scalar higgs mass is cancelled out by the contribution of its fermionic superpartner. Moreover in Fig. 2.9c and 2.9d it is shown that the gauge boson contribution (spin-1), cancelled out by its super-partner gaugino. However, a perfect cancellation yields until the symmetry is unbroken and the particle have the same mass. This consideration sets a requirement for the breaking of SUSY. It has to satisfy the condition that the theory stays *softly* broken until a scale M_{SUSY} in order to preserve the mass of the Higgs Boson. A more quantitative approach reads:

$$\delta M_h^2 \sim g^2 M_{SUSY}^2 \sim M_h^2 \tag{2.58}$$

The correction of the Higgs boson mass has to be of the same order of magnitude of the Higgs Boson mass itself. This condition yields $M_{SUSY} \sim 1$ TeV, in perfect agreement with the GUT expectation. The breaking mechanism of SUSY described in last section offers somewhat a justification of the existence of two mass scales, M_{GUT} and M_{SUSY}, solving also the very essence of the hierarchy problem.

A third important feature is that the conservation of $R - parity$ makes the lightest SUSY particle (LSP) stable. The LSP is hence the best candidate for a massive cold Dark Matter. In most of the SUSY models the LSP is the χ_1^0, which will be treated with accuracy in the next section.

A fourth property of SUSY is that the gravity is included in the theory. The consequence of the algebra of the $\mathcal{Q}$ operator is that general relativity is obtained making SUSY a local symmetry. Moreover, gravity is also connected to the SUSY breaking in the mSUGRA symmetry breaking model.

Although the theory of Supersymmetry is very elegant and powerful, its main limitation is that there is no experimental evidence of Supersymmetry.

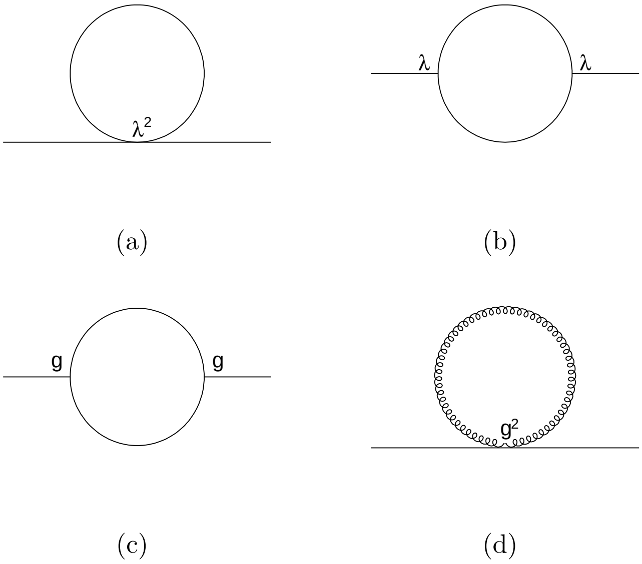

(a) (b)

(c) (d)

Figure 2.9: Cancellation of the correction terms of the mass of the Higgs. The contribution of the scalar higgs boson (a) is cancelled out from its fermionic superpartner (b). The contribution of the gauge boson (spin-1) (c) is cancelled out by its supersymmetric partner, the spin 1/2 gaugino (d).

2.5 The neutralino sector in MSSM

The four neutralinos are the mass eigenstates of the ($\tilde{b}$,$\tilde{w}^3$,$\tilde{h}_{up}$,$\tilde{h}_{down}$) system. These four gauginos have in fact the same quantum numbers under $U(1)_Y \otimes SU(2)_L$ and can in principle mix after super-symmetry breaking.

The Lagrangian terms which contribute to the mass of the four particles is [67, 74]:

$$
\begin{aligned}
\mathcal{L}_\chi = \; & \underbrace{-\frac{g}{2}\lambda_3\left(v_1\tilde{h}_1 - v_2\tilde{h}_2\right) + \frac{g_Y}{2}\lambda_0\left(v_1\tilde{h}_1 - v_2\tilde{h}_2\right)}_{gauge-term} + \\
& \underbrace{+\mu\tilde{h}_1\tilde{h}_2}_{W-term} \qquad (2.59) \\
& \underbrace{-\frac{1}{2}M_2\lambda_3\lambda_3 - \frac{1}{2}M_2\lambda_0\lambda_0}_{soft-term} + h.c.
\end{aligned}
$$

In the basis ($\tilde{b}, \tilde{w}^0, \tilde{h}^0_u, \tilde{h}^0_d$) the mass term of the lagrangian can be expressed as:

$$\mathcal{L} = -\frac{1}{2}\left(\psi^0\right)^T \mathbf{M}_{\tilde{N}}\psi^0 + c.c. \qquad (2.60)$$

where

$$\mathbf{M}_{\tilde{N}} = \begin{pmatrix} M_1 & 0 & -g^{'}v_d/\sqrt{2} & g^{'}v_u/\sqrt{2} \\ 0 & M_2 & -gv_d/\sqrt{2} & gv_u/\sqrt{2} \\ -g^{'}v_d/\sqrt{2} & gv_d/\sqrt{2} & 0 & -\mu \\ -g^{'}v_u/\sqrt{2} & -gv_u/\sqrt{2} & -\mu & 0 \end{pmatrix} \tag{2.61}$$

This matrix can be rewritten using the Weinberg angle θ_W and the mixing angle of the two higgs fields β as:

$$\mathbf{M}_{\tilde{N}} = \begin{pmatrix} M_1 & 0 & -c_\beta s_W m_Z & s_\beta s_W m_Z \\ 0 & M_2 & c_\beta c_W m_Z & -s_\beta c_W m_Z \\ -c_\beta s_W m_Z & c_\beta c_W m_Z & 0 & -\mu \\ s_\beta s_W m_Z & -s_\beta c_W m_Z & -\mu & 0 \end{pmatrix} \tag{2.62}$$

The mass matrix is not diagonal. The mass eigenstates are obtained with a diagonalization of $M_{\tilde{N}}$ by a unitary matrix $\mathbf{N}$, to obtain the mass eigenstates:

$$\tilde{N}_i = \mathbf{N}_{ij}\psi_j^0 \tag{2.63}$$

The diagonalized neutralino mass matrix is:

$$\mathbf{N}^*\mathbf{M}_{\tilde{N}}\mathbf{N}^{-1} = \begin{pmatrix} m_{\tilde{N}_1} & 0 & 0 & 0 \\ 0 & m_{\tilde{N}_2} & 0 & 0 \\ 0 & 0 & m_{\tilde{N}_3} & 0 \\ 0 & 0 & 0 & m_{\tilde{N}_4} \end{pmatrix} \tag{2.64}$$

The four mass eigenstates of m_{N_i} are the χ_i^0 composing the neutralino sector. The mass eigenstates, and hence the diagonalized mass matrix, are determined experimentally. However, the not-diagonalized neutralino mass matrix $M_{\tilde{N}}$ depends directly on the SUSY parameters which are, in general complex; the experimental determination of the unitary diagonalization matrix $\mathbf{N}$ offers the possibility of an experimental constraint of the SUSY parameters. A complete analysis of the neutralino system in supersymmetric theories is reported in [26]. In this study it is shown that by a reparameterization of the fields, M_2 can be taken real and positive without loss of generality, and the two non-trivial phases, which are reparameterization-invariant are associated to M_1 and μ:

$$M_1 = |M_1|\, e^{i\Phi_1} \qquad \mu = |\mu|\, e^{i\Phi_\mu} \qquad (0 \leq \Phi_{1,\mu} \leq 2\pi) \tag{2.65}$$

According to this study, the analysis of the chargino system at tree level will allow to measure $tan(\beta), M_2, \mu, \Phi_\mu$ (see also [95]). The masses of the neutralinos are described by the equation:

$$(\mathcal{R}eM_1)^2 + (\mathcal{I}mM_1)^2 + u_i\mathcal{R}eM_1 + v_i\mathcal{I}mM_1 = w_i \qquad (i = 1 \ldots 4) \tag{2.66}$$

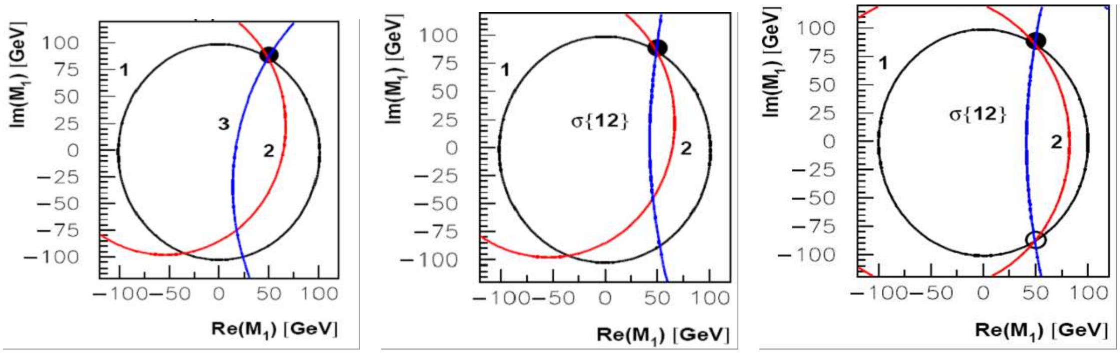

(a) (b) (c)

Figure 2.10: Analysis of the neutralino system in e^+e^- collision from [25]. In (a) it is shown the possible constrain of the parameter M_1 from the measurement of χ_1^0,χ_2^0 and χ_3 (indicated with the numbers 1,2,3). In case only χ_1^0 and χ_2^0 can be produced, the measurement of their mass and of their production cross section $\sigma(12) \equiv \sigma(\chi_1^0\chi_2^0)$ is sufficient for a constrain of M_1 (b) up to a two-fold degeneration in case of a real M_1 (c).

The masses of the neutralino describe hence circles in the $\mathcal{R}eM_1$,$\mathcal{I}mM_1$ space. In Fig. 2.10 it is shown how the value of M_1 can be constrained with a two-fold ambiguity at tree level measuring $m_{\chi_1^0}$ and $m_{\chi_2^0}$. The ambiguity can be solved with the adjunctive measurement of the $\chi_1^0\chi_2^0$ production cross section, in case of a non-zero Φ_μ.

The presence of finite phases in the neutralino mass matrix is also an interesting source of CP-violation and was studied in detail in [96, 97]. Moreover, the $\chi_2^0 \to \tilde{l}l$ decay is a sensitive probe of lepton flavour violation [28] at future experiments.

The actual constraints of the masses of the χ_i^0 come from the results of the LEP [98–102] and of the Tevatron experiments. Extensive searches of di-lepton events with missing energy were performed at LEP. In Fig. 2.11a the region is shown of the ($m_{\chi_1^0}$,$m_{\tilde{\mu}_R}$) plane excluded at LEP in the direct smuon searches ($e^+e^- \to \tilde{\mu}_R\tilde{\mu}_R$). Moreover, the combination of charginos, sleptons and Higgs boson searches provided the dependence of the lower limit of $m_{\chi_1^0}$ on $\tan(\beta)$ (Fig. 2.11). The lower limit of the mass of the $m_{\chi_1^0}$ is nowadays quoted as 78 GeV [19]. The direct search of χ_2^0 at LEP consisted of the interpretation of the di-lepton plus missing energy events from the process $e^+e^- \to \chi_1^0\chi_2^0$. At Tevatron the search of clear tri-lepton plus missing energy events from $\overline{p}p \to \chi^{\pm}\chi_2^0$ was performed. In both cases no evidence of events above the expected SM background was found. The current lower limit of the mass of the $m_{\chi_2^0}$ is 62.4 GeV. In the same searches at LEP the lower limits of $m_{\chi_3^0}$ and $m_{\chi_4^0}$ were found respectively as 99.9 GeV and 116 GeV. The meaning of these limits is only purely qualitative. They depend strongly on the set of SUSY parameters used to formulate the statistical hypothesis for the interpretation of the experimental data. It can be concluded that there is an experimental indication that the mass scale of the lightest SUSY particles can be expected above about 100 GeV.

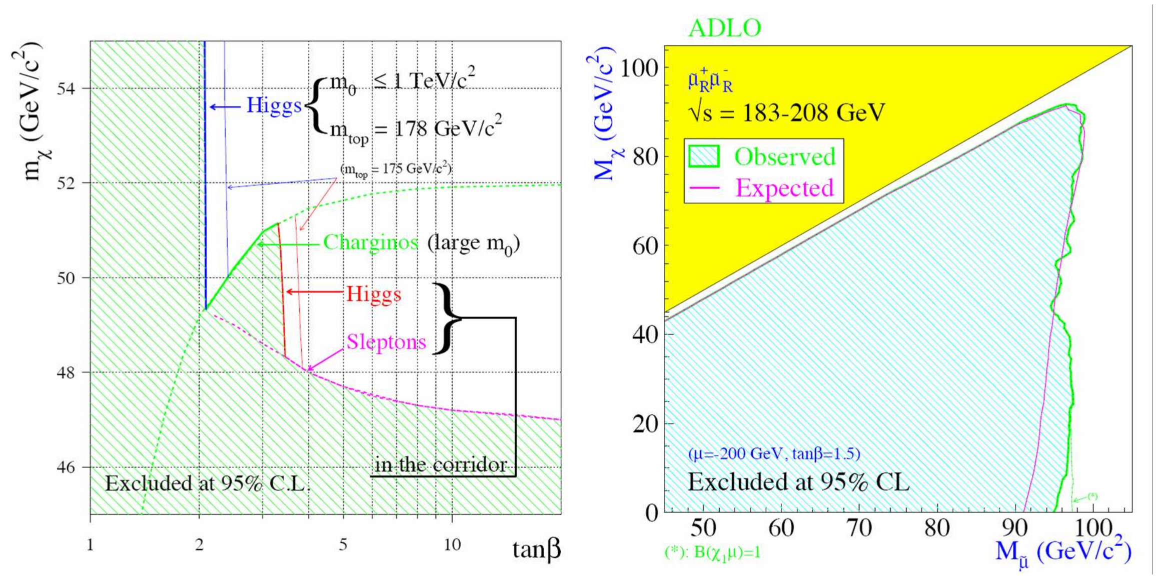

(a) (b)

Figure 2.11: Limits from the searches of χ_1^0. In (a) the region of the ($m_{\chi_1^0}$,$m_{\tilde{\mu}_R}$) plane excluded by the searches for smuons at LEP is shown. In (b) the lower mass limit for the lightest neutralino is shown as a function of tan β, from searches at LEP for charginos, sleptons, and neutral Higgs bosons. Figures from [19]

Conclusion

The Supersymmetry is an interesting option for the description of the physics beyond the Standard Model. The proposed symmetry between fermions and bosons cancels out the loop corrections to the mass of the Higgs Boson, offering a solution to the hierarchy problem. Moreover, the three coupling constants of the $SU(3)_C \otimes SU(2)_L \otimes U(1)_Y$ merge in a single point at a scale $M_{GUT} = 10^{15.8 \pm 0.3 \pm 0.1}$ GeV in the Minimal Supersymmetric Standard Model framework. A nice feature of SUSY is that it includes also gravity.

The neutralino system contains lots of information about the investigated SUSY scenario. In the mSUGRA models the χ_1^0 is the lightest SUSY particle. As it is neutral, stable and massive, it is a good candidate for the Dark Matter. Moreover it was shown that the measurement of the χ_1^0 mass, the χ_2^0 mass and the $e^+e^- \to \chi_1^0\chi_2^0$ production cross section would allow constraining the mSUGRA parameters at a tree level. In CP violating scenario, CP-odd observables can be build in the neutralino system in order to investigate these properties. The χ_2^0 is also sensitive to lepton flavour violation processes, when allowed by the SUSY scenario.

However, there was no experimental evidence of SUSY in the collider experiments up to now. The definition of the discovery potential of the neutralino system in the future planned experiments is hence an important topic of study and it will be exploited in the next chapters of this thesis.

Chapter 3

The International Linear Collider. Experiment and Detectors

"I have the right tool, I remember the words
so said the good fairy of the white cloud,
and she touched the ladybird with her shining wand,
Babbitabbu! The two bridesmaid were terrified."
— ibidem

Introduction

In the last chapter it was shown that many extensions of the SM expect new physics to appear at an energy scale of less than 1 TeV. At the present the most powerful running accelerator is TEVATRON, a $p\overline{p}$ machine with a centre of mass of 1.96 TeV [19]. As it is a hadron collider, the centre of mass of the real qq or gg interaction is much lower and it turns out to be not enough to reveal with high sensitivity the new physics effects. However Higgs Boson and SUSY searches are currently being performed by CDF and D0 experiments [20]. In spring 2009 the LHC will start data taking. It is a 14 TeV pp collider and it is believed to have high sensitivity for the discovery of the Higgs Boson and of the new physics beyond the SM [21, 22].

After the discovery a precision measurement will be needed. Proton machines are not suitable for this, due to the large undetermination of the collision of quarks and gluons. A lepton machine would offer a cleaner environment. The International Linear Collider is a proposal of an e^+e^- accelerator with a centre of mass energy of 500 GeV extendible up to 1 TeV. The physics potential of such machine and the R&D of the best detector for ILC are currently being intensively investigated with an international effort.

This chapter proposes a description of the International Linear Collider proposal. First the accelerator is shown, with particular stress on its technological challenges and on its possible performances. Then the physics program of ILC is analysed. The physics potential of ILC is one of the most important steering parameter for the optimization of the detector, in this design phase of the experiment. The particle flow approach is believed to be a good analysis tool for the reconstruction of jet in the multi-jet dense environment expected at ILC. After the description of this method, the 3 traditional detector concepts (LDC,GLD,SiD) based on the particle flow are shown, with particular emphasis on the requirement of this reconstruction method on the technology and design of the full detector. In order to underline the rich offer of the R&D program for ILC, also a not-particle-flow concept is briefly described. The last part of the chapter treats with more detail the LDC detector concept which is the basic framework of the physics analysis and of the R&D program studied in this thesis.

3.1 The Accelerator

3.1.1 The e^+e^- machine

The International Linear Collider is a 200-500 GeV centre of mass high luminosity linear electron-positron collider, based on 1.3 GHz superconducting radio-frequency (SCRF) accelerating cavities. The layout of the ILC is shown in Fig. 3.1. The basic parts of the accelerator are:

- A polarized electron source based on a photocathode DC gun
- An undulator-based positron source, driven by the 150 GeV main electron beam
- 5 GeV electron and positron damping rings (DR) with a circumference of 6.7 Km, housed in a common tunnel at the centre of the ILC complex
- Beam transport from the damping rings to the main linac, followed by a two-stage bunch compressor system prior to injection into the main line
- Two 11 km long main linacs, utilizing 1.3 GHz SCRF cavities, operating at an average gradient of 31.5 MV/m, with a pulse length of 1.6 ms.
- A 4.5 km long beam delivery system, which brings the two beams into collision with a 14 mrad crossing angle.

Mainly cost reasons brought to the proposal of a single interaction point. It can be eventually shared between two detectors which can be pushed in and pulled out of the experimental area.

The superconducting RF cavity is by far the most expensive and the most technological advanced part of the accelerator. A single cavity (Fig. 3.2) is 1 m long and must be operated at a temperature of 2° K in order to reach its full performance. Since 1992 an intensive R&D has aimed at increasing the gradient by a factor of 5, from the LEP-like [103] 5 MV/m up to 25 MV/m. Nowadays the goal of 35 MV/m was reached, with isolated cases of single cavities with an accelerating field of 50 MV/m [104, 105]. The ultra-clean and defect-free inner surface is the key-point for a high gradient performance and much effort is done in order to improve the polishing techniques in dedicated experimental facilities. It can be said that at the moment the technological proof of principle of the possibility of the acceleration of electrons up to this high momentum is established. However the scaling to a mass production is still under discussion — requiring about 17000 cavities for the full accelerator.

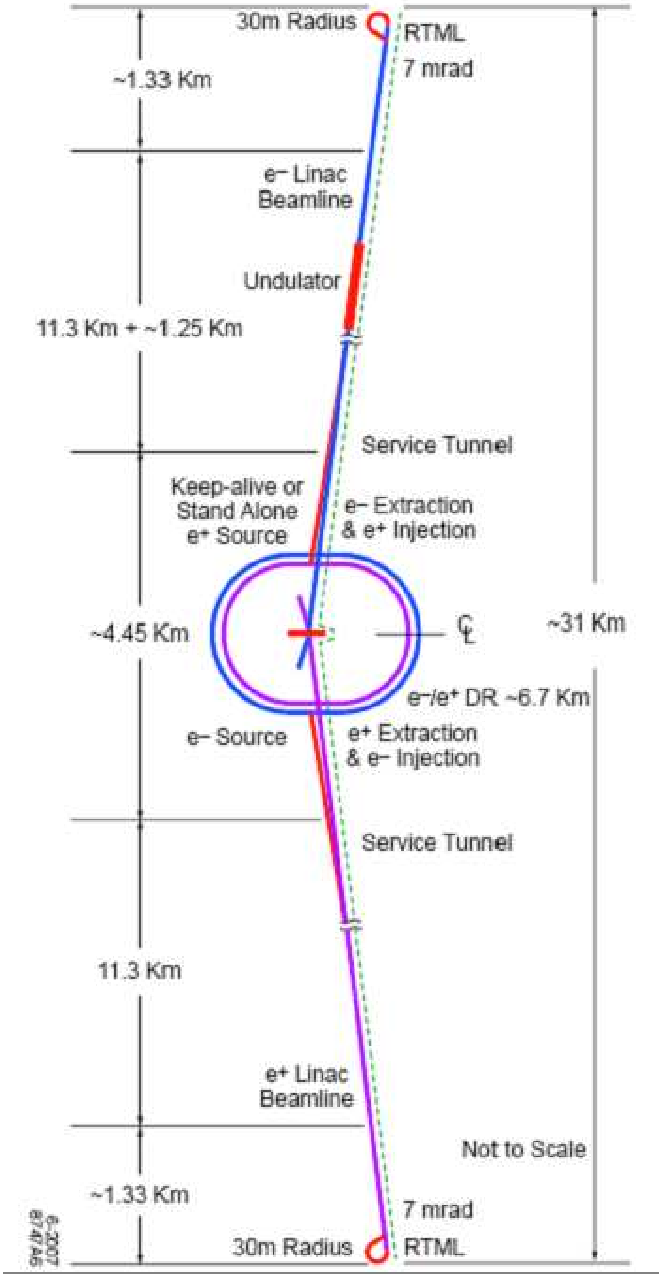

Figure 3.1: Schematic layout of the ILC complex for a centre of mass of 500 GeV [2]

3.1.2 Beam Parameters

The accelerator is designed to provide a continuous centre of mass energy range between 200 GeV and 500 GeV, with a possible extension up to 1 TeV. The energy of the centre of mass is foreseen to be stable within a precision $\leq 0.1\%$. The peak luminosity goal of the machine is about 2×10^{34} cm^{-2}s^{-1}, consistent with an availability of 75% in order to produce 500 fb^{-1} in the first four years of operation. The polarization of the beams will be a unique and important feature of the experiment [24]. The electron beam will

Figure 3.2: A TESLA nine-cell 1.3 GHz superconducting niobium cavity [2]

be provided with a 80% polarization at the interaction point, while the positron beam will reach 60% polarization. The current achieved polarization is only 30% and there is space in the beamline for a 60% polarization upgrade.

A considerable source of degradation of the centre of mass energy of the collider is the beamstrahlung. The colliding particles emit hard synchrotron radiation in the strong electromagnetic spacecharge field of the opposing bunch. The parameter which describes the quality of this effect is the fractional RMS energy loss to beamstrahlung δ_{BS}. The nominal spectrum of the beam energy at a 500 GeV e^+e^- linear colliders is shown in Fig. 3.3. This spectrum is used as reference in the simulation studies proposed in this thesis. The nominal value of δ_{BS} is 0.024, corresponding to a RMS of $0.024 \times 500 = 12$ GeV.

Also other combinations of the beam parameters are taken in consideration to achieve the proposed peak luminosity; the contribution of the beamstralung can differ significantly from the nominal one. The so-called *LowN* option proposes a reduction of the bunch length and of the bunch population; the consequent reduction of the luminosity is balanced with a more precise focusing of the beam at the interaction point. The lower number of particles per bunch reduces also δ_{BS} down to 1.7% (8.5 GeV). In the *LargeY* option the vertical and horizontal emittance of the beam are rescaled; the vertical emittance is increased and the horizontal emittance is reduced. The larger focusing in the horizontal direction of the beam causes an increase of the beamstrahlung, which is somewhat reduced increasing the bunch length; the resulting δ_{BS} is 0.027, not very different than the nominal one. The strongest effect on the beamstrahlung is observed in the *LowP* option. In this case the beam current is reduced of 30% and the luminosity is recovered with an increased focusing; the value of δ_{BS} is 0.055 (27.5 GeV), almost a factor 2 higher than in the other designs.

The design of the ILC provides also a possible option of $\gamma\gamma$ collisions and a high statistics running at the Z resonance (92 GeV) and at the W^+W^- threshold (161 GeV) — respectively the *giga-Z* and *mega-W* options. In this sense it will be a very powerful machine for the precision measurement of new physics beyond the Standard Model.

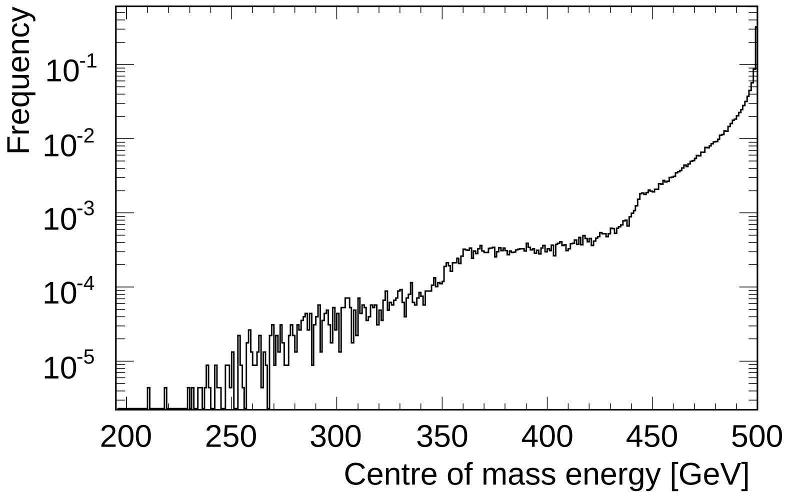

Figure 3.3: Spectrum of the centre of mass energy of a 500 GeV e^+e^- Linear Collider. The beamstrahlung effect is calculated with GUINEA-PIG [106]. This spectrum is used as reference in the analysis proposed in this thesis.

3.2 The physics program of the ILC

There was an intensive theoretical effort in order to define the physics potential of a e^+e^- collider in the Tev region [107, 108]. These studies range from the possibility of precise measurements of SM processes up to the precise investigation of the brand new physics scenario.

In the last chapter it was shown that the Standard Model was intensively measured and tested in many collider experiments of the last two decades. However there is space for improvements. At the present the top quark mass is known with an absolute error of about 2 GeV. In Fig. 3.4 the precision is shown which can be reached at the ILC in the measurement of the top mass with a scan of the $t\bar{t}$ excitation curve. This study is performed with a top quark mass of 174.5 GeV, including initial state radiation and beamstrahlung, and demonstrates that the top mass can be measured with an absolute error of 100 MeV. Other improvements will come from the *giga-Z* and *mega-W* options, which will allow to measure in dedicated runs the properties of the Z and W bosons. The ILC will also supplement the analysis performed at beauty factories by studying with high accuracy the CKM matrix elements directly in W decays and in CP violating B meson decays.

However, the central topic of the physics program of the ILC will be the Higgs Boson. In the last chapter it was shown that this scalar field is the largest ambiguity of the Standard Model, as it is postulated but never experimentally seen. If the LHC experiment will detect it, then the ILC will provide a precise characterization. A first point to be addressed will be to verify that the Higgs boson follow the expectations from the SM. ILC can measure the mass, the lifetime, the production cross sections, the branching ratios to quarks of different flavours, to leptons and to bosons, the self

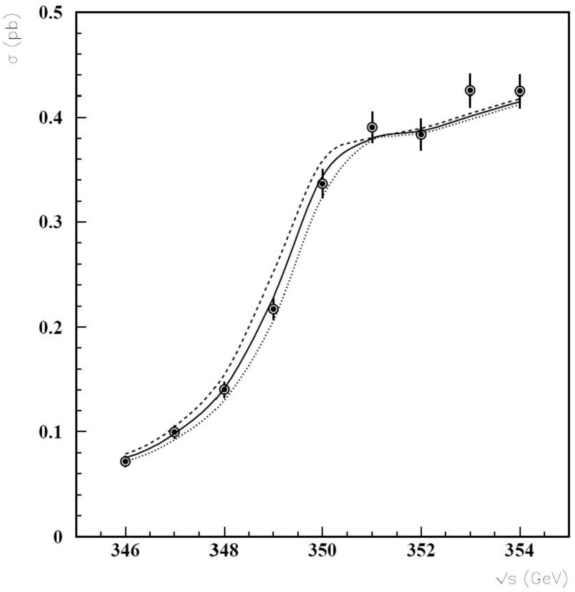

Figure 3.4: Excitation curve of $t\bar{t}$ quarks including initial-state radiation and beamstrahlung [109]. The errors of the data points correspond to an integrated luminosity of 100 fb^{-1}. The dotted curves indicate a shift of the top mass by ± 100 MeV. Figure from [23].

coupling with unprecedented precision. Moreover, the Yukawa coupling of the top quark with the Higgs boson can be studied in the $t\bar{t}H$ production, provided a centre of mass energy higher than 500 GeV. If the Higgs does not have a Standard Model profile, then the physics program has to be redefined in order to constrain the model at a quantum level. The lack of concordance between the precision measurement of θ_W at the $giga-Z$ option and the Higgs Boson properties would underline the theoretical problems of the SM.

Supersymmetry has also an important role in the physics program of the ILC. In the theoretical overview of the last chapter it was stressed that SUSY is at the moment one of the most favourite theories which would naturally extend the Standard Model. An intensive amount of studies were done in order to investigate the impact of a Linear Collider in the testing of this theory [3, 92]. If SUSY is broken at the TeV scale, many particles will be light enough to be directly produced in the continuum at 500 GeV and even in the better conditions offered by the 1 TeV extension of ILC. The SUSY events will be characterized by the typical and clean signature of large missing energy, associated to the LSP which leaves the detector without being observed. The masses of the sparticles in the reachable energy range of the ILC are usually measured with a precision of $0.05\% - 1\%$. The ILC offers also the possibility of a threshold scan, for the individual production and measurement of the s-particles.

Last but not least, the investigation of alternative new physics is being also considered in the design of the experiments. Among the large amount of possible models, two physics cases are discussed with more emphasis. It was shown that the unification of gravity with the other forces in nature would occur at a much lower energy scale than thought before if the existence of extra-dimensions is postulated. Such extra-dimensions are curled-up, perhaps even at semi-macroscopic length scales. This could generate new effective spin-2 forces and in the linear collider phenomenology could provide spectacular missing energy signatures. A second case is offered by the unitarity bound described in section 2.3.2. If the Higgs boson does not exist, the vector boson scattering will become strong at high energies. The studies for a 800 GeV linear collider showed that ILC will have a good sensitivity required to explore the onset of these strong interactions in a range up to the limit of about 3 TeV, analysing the e^+e^- annihilation into two W bosons.

3.3 The Challenges of a Detector for the International Linear Collider

The various ILC physics program requires a detector capable to deal with highly energetic and complex multi-jet final states. The experiment will be self-triggering, running continuously in order to collect the largest possible amount of information.

The requirements on the detector for the ILC, supported by some selected physics examples, can be summarized in the following main points [23]:

Momentum Resolution. The momentum resolution precision $\delta p/p$ is requested to be about 5×10^{-5} (a factor of ten better than what achieved at LEP). It is particularly relevant for the study of the $e^+e^- \to ZH$ process. The mass of the higgs boson can be measured with precision from the recoil mass of the Z, identified and measured through the decay $Z \to \mu\mu$. Also the measurement of the mass of the χ_1^0, χ_2^0 and of the $\tilde{\mu}_{L,R}$ profits of the precise measurement of the muon momentum, in the di-muon + missing energy final state, as it will be shown in chapter 4.

Impact parameter resolution. It is needed for a good b and c quark tagging. The investigation of the electroweak symmetry breaking requires a detailed study of the decay properties of the Higgs boson. It is hence important to distinguish between a light Higgs boson decaying into $b\bar{b}$,$c\bar{c}$ and gg pairs. Moreover, the measurement of the Higgs self-coupling mechanism $e^+e^- \to H^0H^0Z^0$ is a key-process at ILC. It has a complicated multi-jet final state and the quark tagging would allow a significant reduction of the background. An extended Higgs sector will manifest more likely with the production and decay of heavy Higgs particles, like in processes $e^+e^- \to H^+H^- \to t\bar{b}t\bar{b}$ or $e^+e^- \to A^0H^0 \to \bar{b}b\bar{b}b$. Finally, in some SUSY scenarios, the scalar $\tilde{t}$ can be identified in the complex final state $\tilde{t} \to b\chi_1^+ \to bW^+\chi_1^0$ and the b- and c-tagging are very important. The required resolution is:

$$\sigma_{d_0}^2 < (5.0 \quad \mu\mathrm{m})^2 + \left(\frac{5.0 \quad \mu\mathrm{m}}{\mathrm{p(GeV/c)sin}^{3/2}\theta}\right)^2 \tag{3.1}$$

Jet Energy resolution Many interesting physics channel will be characterized by multi-jet final states. The important case of the $e^+e^- \to H^0H^0Z^0$ was shown previously. Moreover, in the SUSY scenario which allow the decays $\chi_2 \to Z^0\chi_1^0$ and $\chi^\pm \to W^+\chi_1^0$, the identification of the Z^0 and $W^\pm$ bosons is essential in order to

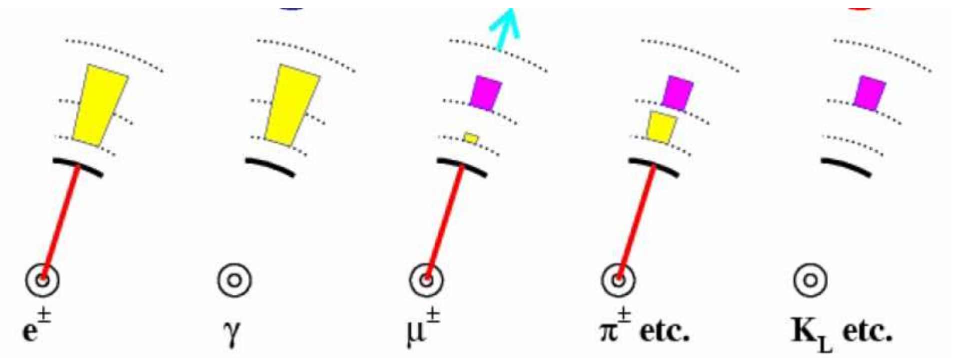

Figure 3.5: Schematics of the particle flow approach at ILC. The full four momentum of visible particles is reconstructed. The momentum of electrons is measured in the tracker and the identification is performed with the electromagnetic calorimeter. The energy measurement and identification of the photon is performed with the electromagnetic calorimeter. The muon momentum is measured in the tracker and the identification is performed with the muon chamber. The momentum of the charged pions is measured in the tracker and the identification is performed in the hadronic calorimeter. Finally neutral hadrons are measured and identified in the hadronic calorimeter. Figure from [32].

distinguish the two SUSY particles. The performance goal of ILC is to reconstruct the mass of the vector bosons with a precision equivalent to their natural decay width ($\sigma_m/m = 2.7\% \sim \Gamma_W/m_W \sim \Gamma_Z/m_Z$). This observation leads to the requirement of a di-jet mass resolution of roughly $\sigma_m/m = \alpha/\sqrt{E_{jj}}$, where α is the energy resolution coefficient and E_{jj} is the di-jet energy. At the energy scale of the typical di-jet energy (150-350 GeV) the energy resolution goal is hence $\sigma_E/E \sim 0.3/\sqrt{E_{jj}}$. This is more than a factor of 2 better than what achieved at LEP.

Hermiticity The specific signature of physics beyond the Standard Model is a consistent missing energy. The e^+e^- pairs produced through Babbha scattering and Initial State Radiation high energetic photons can fake the missing energy signature. For this purpose, the goal of the detector design is to reach a good coverage down to a 5 mrad polar angle around the beam pipe.

High granularity The high energy of the centre of mass will cause a very high track density in the multi-jet final state. In order to achieve the good jet energy resolution, the ILC detector would require high spatial resolution power between jets and particles inside the jets.

3.4 The Particle Flow approach

The particle flow [30–32] (PFA) is the method proposed for the improvement of the jet energy resolution of the ILC detector. Instead of performing a pure calorimetric measurement, as in traditional environments, the reconstruction of the four vector of all the observable particles is proposed. The reconstructed jet energy is the sum of the energy of the individual particles. The momenta of the charged particles are measured in the tracker, while the energy of the neutral particles is measured in the calorimeters. The electromagnetic calorimeter is used for the measurement of the energy of photons and for the identification of photons and electrons. The hadronic calorimeter is used for the measurement of the energy of neutral hadrons and for the identification of hadrons. The muon chambers are used for the identification of muons.

A precise measurement of the jet composition was performed at LEP [110, 111]. On average, after the decay of short lived particles, 62% of the energy of jets is carried by charged particles, 27% by photons, 10% by long lived neutral hadrons $(n, K^0_{L,S})$, and around 1.5% by neutrinos. In case of a perfect association between the energy detected and the primary particles, the jet energy resolution can be explicated as:

$$\frac{\sigma(E)}{E} = \frac{\sigma_{had}(E)}{E} \oplus \frac{\sigma_{em}(E)}{E} \oplus \frac{\sigma_{charged}(E)}{E} \tag{3.2}$$

where σ_{had} and σ_{em} refer respectively to the neutral hadrons and to the photons measured in the hadronic and in the electromagnetic calorimeters. Assuming a typical performance of the energy resolution of the calorimeters $(\sigma_{em}(E)/E \sim 0.15/\sqrt{E}$, $\sigma_{had}(E)/E \sim 0.55/\sqrt{E})$ and the typical jet energy composition, the ideal achieved jet energy resolution is hence $\frac{\sigma(E)}{E} = \frac{0.19}{\sqrt{E(GeV)}}$.

The main limitation of the particle flow is that it is not possible to associate perfectly all energy deposits with the correct particles. The association of all the clusters corresponding to the shower generated from a charged hadron in the hadronic calorimeter is a very difficult task. If one cluster is identified as isolated particle, its energy is effectively double-counted. This systematic error introduces the so-called *confusion term* $\sigma_{conf}(E)$.

Simulation studies suggest [33] that the PFA can reach a jet energy resolution of 24% at 45 GeV, with an increasing degradation of the performance with increasing energy of the jets, up to 54% at 250 GeV. The performance of the particle flow is intimately connected with the sub-detector characteristics and this reconstruction algorithm is used to drive the design of the detector for ILC [1].

3.5 Detector design for ILC

An intensive discussion in the scientific community is currently going on about the best detector to achieve the goals proposed by the International Linear Collider. The strong interplay between physics requirements and technological innovation makes the design of a detector for ILC a challenging experience. Three detector design based on the Particle Flow are proposed [3], the LDC, the GLD and the SiD. Besides, one more traditional concept, the so-called 4^{th} concept, is also considered as an option.

The strong requirements of the ILC physics introduce a common baseline between the concepts. All the concepts are characterized by pixellated vertex detectors, in order to provide high precision vertex reconstruction and have sophisticated tracking systems which have been optimized for high track reconstruction efficiency and excellent momentum resolution. All the concepts are based on very powerful magnetic coil, relying on the successful experience of the CMS solenoid [112]. Last but not least, in all the concepts a compact detector is embedded inside the coil.

The detector optimized for the particle flow have in addiction an excellent separation power of the components of the jets. The most important features in this respect are:

- A large detector, for the spatial separation of the particles.
- A large magnetic field, for a good identification of charged versus neutral particles.
- Highly granular calorimetry, in order to increase the resolution power of the showering particles.

The quoted figure of merit of the PFA is BR^2/σ, where B is the magnetic field, R is the outer radius of the detector and σ is the granularity of the calorimeters. The detector designs for ILC differs in the choice of these parameters in order to optimize their PFA performance.

It is outside the scope of this thesis to describe all the detector concepts, which can be found in detail in [1]. The studies presented in this thesis are done in the framework of the LDC concept. Therefore only the most relevant points of the SiD and GLD concepts will be described and the full LDC system will be then shown in detail.

3.5.1 The SiD detector concept

The SiD concept [113] is mostly based on the silicon technology. It uses silicon tracking and silicon-tungsten electromagnetic calorimeter, pixel vertex detector, highly granular hadronic calorimeter and a muon system. The main feature of silicon detectors is the extreme high read-out spread, which allows recording background only for a single bunch crossing with a consequent improvement of event cleanness. Moreover the silicon technology reached a excellent level of radiation hardness. Therefore silicon vertex detector, tracker, calorimeters can absorb a consistent amount of background radiation without any sizable damage. A strict requirement of the particle flow is the placement of the detectors inside the magnetic coil. The highly granularity is a must of the calorimeters. The pixelated silicon-tungsten electromagnetic calorimeter is designed to be as small in radius as possible, in order to reduce the total coast of the detector. The hadronic calorimeter is thought as a gaseous digital calorimeter. The silicon tracker would achieve a high performance together with a total magnetic field of 5 T. The high magnetic field would confine the e^+e^- pairs to a minimal radius, allowing a reduction of the beam pipe size with a consequent improvement of the vertexing performance.

3.5.2 The GLD detector concept

The basic design of GLD [114] is shown in Fig. 3.7. It incorporates a calorimeter with fine segmentation and large inner radius to optimize it for particle flow. Charged tracks are measured in a large gaseous tracker, a Time Projection Chamber (TPC), with excellent momentum resolution. The TPC reconstructs tracks with high efficiency, even those from decaying particles, ks and hit clusters in the calorimeter. The solenoid magnet is located outside the calorimeter, so as not to degrade energy resolution. Because the detector volume is huge, a moderate magnetic field of 3 Tesla has been chosen.

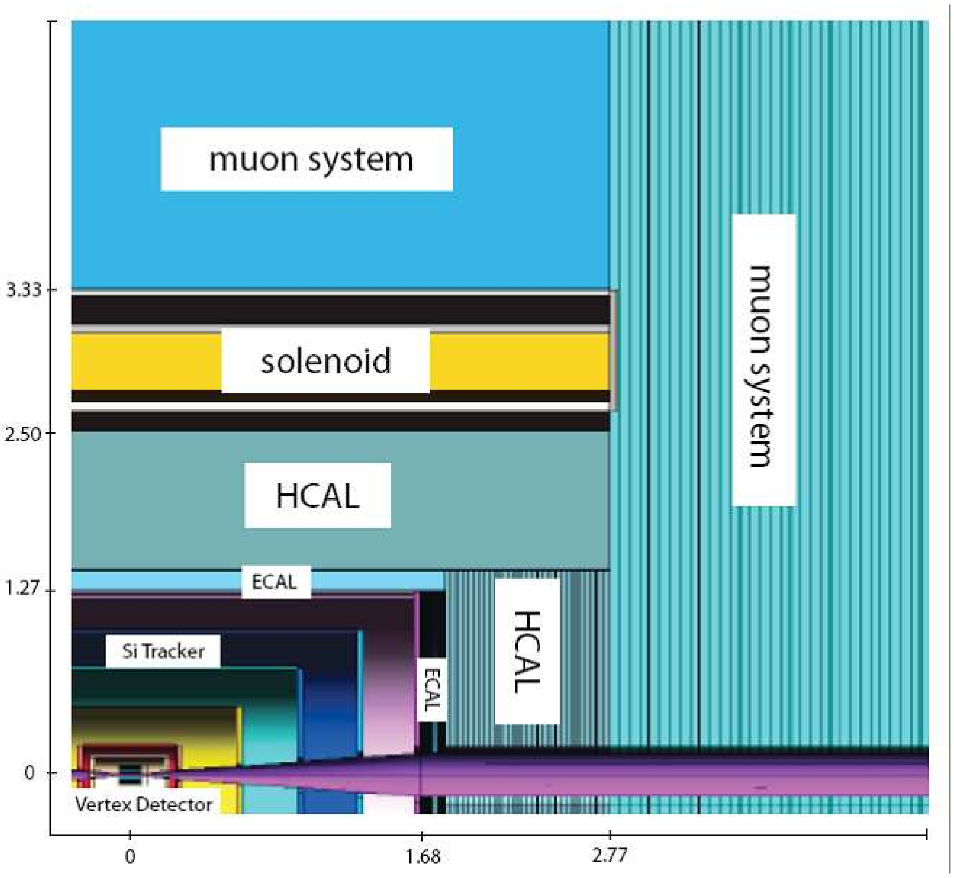

Figure 3.6: Schematic of a quadrant of the SiD detector. The scale is shown in metres. Figure from [1].

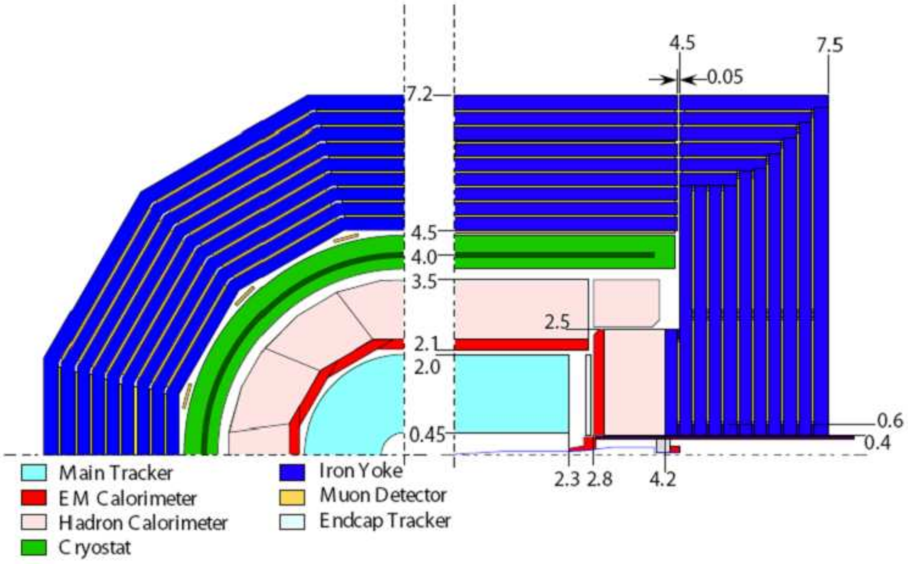

Figure 3.7: Schematic of a quadrant of the GLD detector. The left figure shows the rz view and the right figure shows the $r\phi$ view. The scale is shown in metres. Figure courtesy from [1].

The GLD detector is composed by the following sub-detectors [1]:

- Silicon vertex detector
- Silicon inner and end-cap trackers
- A Time Projection Chamber as large gaseous detector
- A highly segmented tungster-scintillator electromagnetic calorimeter
- A highly segmented iron-scintillator hadronic calorimeter, with a radial thickness of bout 6 λ.
- Forward electromagnetic calorimeters which extend solid angle coverage down to small angles
- A muon detector interleaved with the iron plates of the return yoke

This design is characterized by a large radius, compensated with a relatively small magnetic field, according to the Particle flow figure of merit. The technologies proposed for each sub-detector are very similar to the LDC design.

3.5.3 The 4^{th} concept

In opposition to the detector optimized for the Particle Flow, the 4^{th} concept [115] introduces the idea of using a high resolution hadron calorimeter. It utilizes an innovative implementation of compensating dual read-out calorimetry, which balances the response to hadrons and electrons and so is insensitive to fluctuations in the fraction of electromagnetic energy in showers. The layout is shown in Fig. 3.8. The calorimetric system is composed of a electromagnetic and hadronic calorimeter. The former is based on

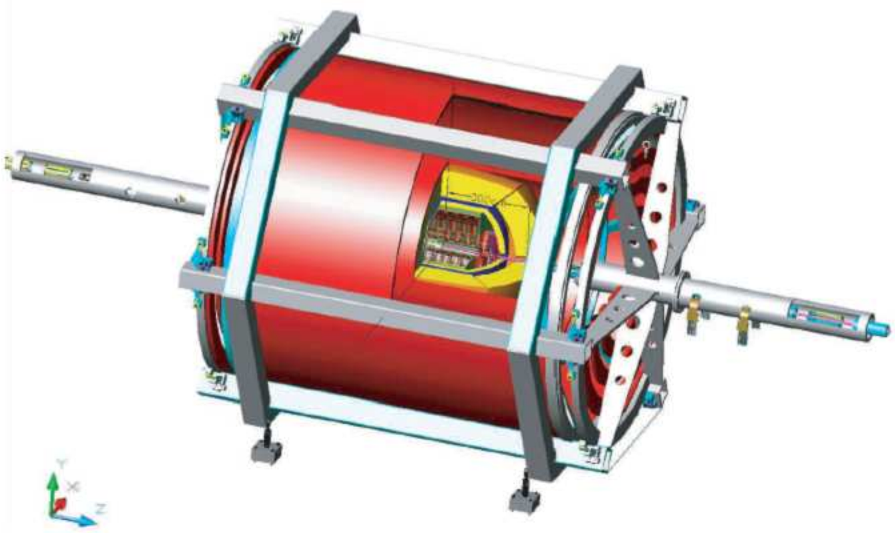

Figure 3.8: Design of the 4^{th} concept detector. Figure courtesy from [3].

a crystal calorimeter, with readout of both Cerenkov and scintillation light to provide compensation. The latter is composed of towers of dual-readout fibre sampling calorimeters. The towers have good transverse segmentation, no longitudinal segmentation, a depth of 10 λ, and are read out with photo detectors at their outer radius.

The tracking system is very similar to the other concepts. The central tracking is performed with a Time Projection Chamber, the vertexing and b-c tagging with a silicon vertex detector.

The magnetic field system is also innovative, in comparison with the other detector models. The 3.5 T field is created with a large solenoid and the detector is encapsulated in it. In addiction a second larger outer solenoid of lower intensity and with magnetic field opposite to the first is used to create a return field. Moreover, in the space between the two solenoids precision drift tubes can measure the momentum of muons with high accuracy. This is a big difference with the other concepts, which use the muon system only for muon identification, leaving the momentum measurement of muons to the tracking system.

3.6 The LDC concept

The LDC detector design [116] is shown in Fig. 3.9. It is optimized as a particle flow detector, with a reliable and highly redundant tracking system. The layout consists on a large tracking volume, highly granular calorimeters inside a large volume magnetic field up to 4 T.

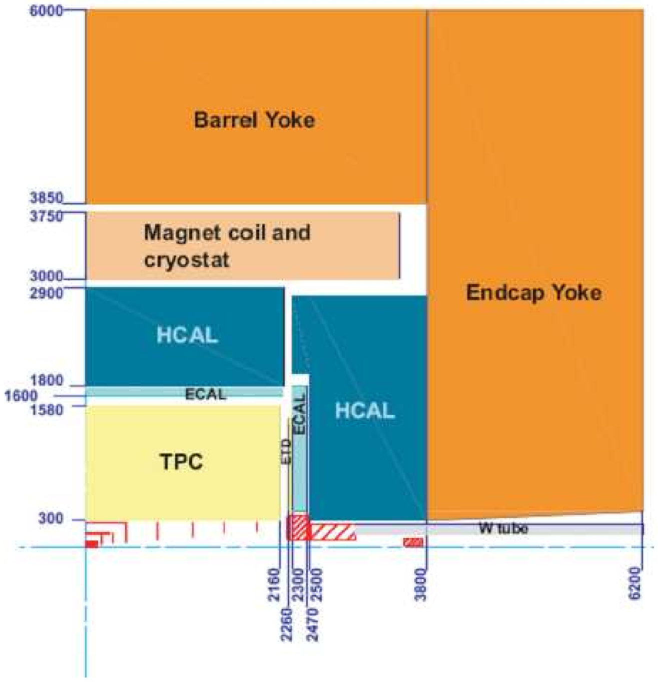

Figure 3.9: Schematic of a quadrant of the LDC detector. The scale is shown in metres. Figure courtesy from [3].

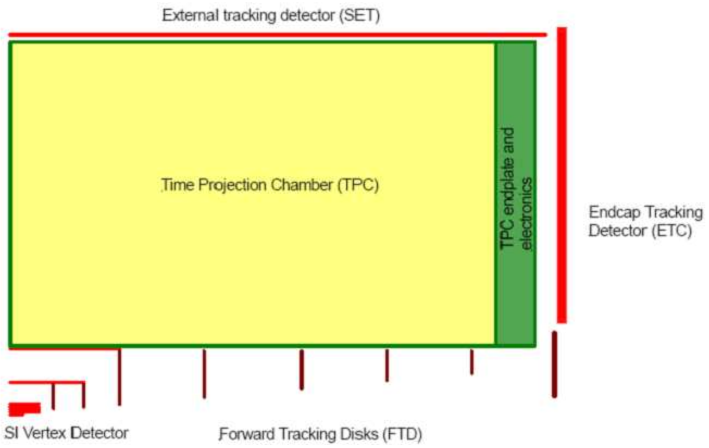

Figure 3.10: Schematic of the LDC tracking system [116].

3.6.1 Tracking system

The tracking system (Fig. 3.10) is composed of several sub-detectors, whose interplay contributes to the final momentum resolution goal of ILC.

A high precision pixel vertex detector (VTD). It is dedicated to the accurate measurement of the impact parameter of charged tracks, vertex identification and b-c-tagging. Moreover it provides independent track segments to the main tracker, improving the pattern recognition. It consists of 5 concentric layers, very close to the interaction point. The radius of the innermost layer is just 16 mm. The main challenge of this detector is the low material budget, in order to reduce its impact on the performance of the further detectors. Moreover this sub-detector needs an excellent single-point resolution. As the VTD is positioned near the beam pipe, a major constrain is the radiation hardness. Silicon pixel sensors (i.e. CCD, DEP-FET) are chosen as technological solution for this application.

Silicon Inner Tracking (SIT). It is positioned between the vertex detector and the TPC. This detector has many applications. First, the momentum resolution at large momenta improves considerably with a very precise space point directly before the TPC. Second it measures the momentum of these low energy particles which do not reach the TPC and are abundantly produced in jets. Third, it improves the vertex reconstruction of many K^0 and Lambda particles decaying between the vertex detector and the TPC. Two layers of silicon strip detectors are used.

Forward Tracking Detector (FTD). It is essential for the tracking in the forward region, where the VTD and the TPC have no coverage. It is composed of 7 disks on either side. In addition it is under study the extension of the forward tracking by installing silicon disks in front of the luminosity calorimeter. Silicon technology is the preferred option also for this application. Low material budget and high radiation hardness are the challenge of this detectors. The most advanced pixel device technology available is the hybrid bump bonded pixels developed for the BTeV experiment at the TEVATRON [117]. At present the first three FTD disks are pixel devices using the bump bonding technology and the other four are double sided silicon strip detectors.

Central tracker (TPC). A large Time Projection Chamber is dedicated to measure the tracks of charged particles with a large number of true 3D space points, up to 200 3D space points per track. A TPC is a gaseous particle detector. The TPC has to provide a momentum resolution $\delta p/p$ of 10^{-4} and a solid angle coverage $cos(\theta) < 0.98$, with a very low material budget ($< 0.03X_0$ to outer field cage in r and $< 0.3X_0$ for readout endcap in z). The slow read-out of the TPC resolves in the integration over background and signal events from 160 ILC bunch crossings at 500 GeV for the nominal accelerator configuration. This is being compensated by designing for the finest possible granularity: the sensitive volume will consist of several (10^9) 3D-electronic read-out voxels (two orders of magnitude better than at LEP). The technological solutions under test and development is the hole type gas multiplication systems, currently produced by GEM [118] and Micromega [119].

Endcap Tracking Detector (ETD) It is one layer of tracking between the endcap TPC and the endcap ECAL. It improves the tracking performance of the TPC in the endcap region. Multiple technologies are being considered for the ETD, including straw tubes, long silicon strip detectors, and GEM-based tracking chambers. The useful resolution of the ETD is determined by the thickness of the TPC endplate in terms of radiation length. In addition the ETD should be as thin as possible to keep the distance of the TPC endplate to the calorimeter small in order to preserve the particle flow performance.

Silicon External Tracking (SET). It will be installed very close to the central e.m. calorimeter, outside the TPC. It will provide an extra-point for the tracking in this critical region. It is made of Silicon microstrip detectors of 60 cm length as a basic unit. It is a double sided Silicon layer, able to provide a high precision tracking point for the connection between TPC and ECAL.

The momentum resolution is by far the most relevant parameter for the analysis of the neutralino system proposed in this thesis. In dedicated studies [1, 116] the momentum resolution of the tracking system is found to be $10^{-4} - 10^{-5}$ can for particle momentum down to about 10 GeV/c in the LDC detector.

3.6.2 Calorimetric system

The calorimetric system is the essential detector for the Particle Flow analysis. It is divided in two dedicated sub-detectors, the electromagnetic and hadronic calorimeter.

Electromagnetic Calorimeter. It is positioned between the SET and the HCAL. The task of this detector is to identify and measure electrons and photons with maximal spatial resolution. The general requirement about compactness (small Moliere radius) has led to a sandwich calorimeter with a tungsten radiator (the possibility of lead is also studied) and silicon for the sensitive medium. To reach an adequate energy resolution (which impacts also position and angular resolution) with an acceptable polar angle dependence the following sampling is under consideration: In depth 12 radiation lengths are filled with 20 layers of 0.6 X_0 thick tungsten absorbers (2.1 mm) and another 11 radiation lengths are made out of 9 layers of tungsten 1.2 X_0 thick. The calorimeter starts with an active layer. The technological option for the active layers is silicon pads, with a single pixel dimension of 1×1 cm^2. The expected energy resolution of this device is in the range $14 - 17\%/\sqrt(E)$ [1].

Hadronic Calorimeter (HCAL). The hadronic calorimeter is placed between the HCAL and the magnetic coil. Stainless steel or brass are proposed as absorber material. They are featured, in fact, by $X_0/\lambda_I << 1$ and allow a good containment and localization of the electromagnetic component of the hadronic showers[1]. Moreover, their low magnetic permeability ($\mu < 1.01$) minimize the energy stored inside the magnetic coil and hence the total energy required for the generation of the constant

---

[1] The description of hadronic and electromagnetic showers in the matter is proposed in chapter 5 and section 6.1.

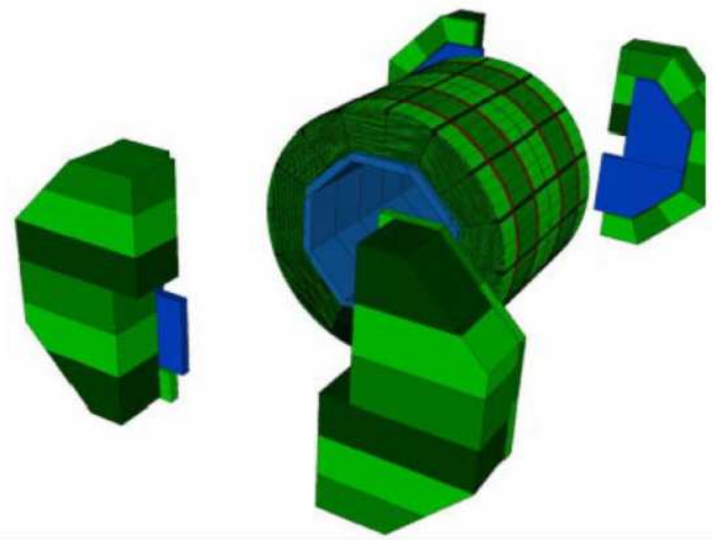

Figure 3.11: The design of the calorimeter system for the International Linear Collider. The HCAL is arranged in 2 cylindrical half barrel parts and two endcaps. The barrel HCAL fills the magnetic field volume between the ECAL and the cryostat. The endcaps close the barrel on either side in order to fully cover the solid angle [120].

magnetic field. The HCAL is arranged in 2 cylindrical half barrel parts and two endcaps. The barrel HCAL fills the magnetic field volume between the ECAL and the cryostat. Each HCAL half barrel is subdivided into 16 modules. Two HCAL modules together form an octant, and support the ECAL modules in this Φ range. In addition the space between the rear of the HCAL endcap and the endcap of the iron return yoke is filled with iron to guarantee the high quality of the magnetic field. The endcaps close the barrel on either side in order to fully cover the solid angle. The gap between the barrel and the endcap is needed for support and for cables from the inner detectors. The total material in the available space has to be maximized, in order to minimize the probability of punch through. Also if the muon system will act as tail catcher, in fact, the 1.6 λ of the coil between the HCAL and the muon system severely limits the energy resolution of the device. Two technological options are under consideration for the active layers. The first proposal is a digital calorimeter, using GEMs (Gas Electron Multipliers) [118], Micromegas [119] or RPCs. The chamber anode is segmented in small pads of about 1 cm^2 size, matching the granularity needed for the PFA application. The second proposal is a highly granular hadronic calorimeter, composed of $3 \times 3 \times 0.5$ cm^3 scintillator tiles, readout with a SiPM [34, 35, 121]. The second option is extensively discussed in chapter 5 and the analysis of the test beam data of a prototype of this scintillator/steel hadronic calorimeter is presented in Chapter 6.

Beam Calorimeter (BeamCal) This detector is adjacent to the beam-pipe and covers a polar angle down to about 5 mrad. Its main task is the measurement of the energy distribution of the beamstrahlung photons, helping in the beam tuning. Moreover, it should identify highly energetic electrons coming from the $e^+e^- \rightarrow$

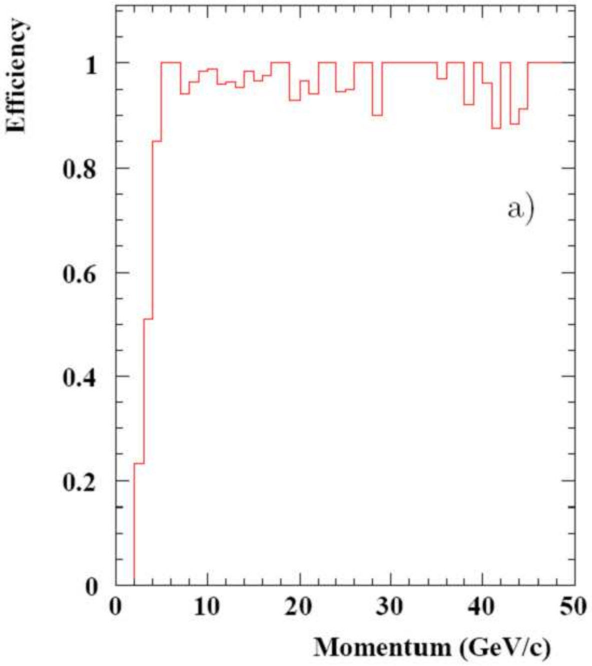

Figure 3.12: Muon identification efficiency versus momentum for isolated muons. Figure from [120].

$e^+e^-(\gamma\gamma)$ events which can improve the power of reduction of this background at ILC. The BeamCal is a sampling calorimeter consisting of tungsten as absorber disks alternating with pad-structured solid state sensor planes.

Luminosity Calorimeter (LHCAL). It is the luminometer of the detector and covers larger polar angle outside the reach of beamstrahlung pairs. The main task of this detector is to measure the luminosity by counting babbha events with an accuracy better than 10^{-3}. It consists of a silicon/tungsten detector.

3.6.3 Muon system

The role of the muon system at ILC is only the identification of muons, both isolated and within jets. The clean environment of the ILC offers the possibility of a direct measurement of the muon momentum directly in the tracker. Consequently the design of a muon system for ILC is a less complicated task than at Hadron Colliders, where also triggering and momentum measurement performances are required. A muon is usually identified as a track in the calorimeters; qualitatively the signature gets better, the more material the muon has gone through; so, barring range effect, identification tends to improve with energy. The most difficult task of the detectors is to identify muons within the dense multi-jet final state expected at the International Linear Collider.

The problem of the instrumentation of the iron yoke for muon identification consists of the requirement of a large area (thousands square meters) covered with detectors whose performances would not be extremely demanding. The most important requests for the

Parameter	**LDC**	**LDC$'$**	**GLD**
TPC			
Inner radius [m]	0.30	0.30	0.45
Outer radius[m]	1.58	1.80	2.00
Maximal z [m]	2.16	2.36	2.50
ECAL			
Barrel Inner radius [m]	1.60	1.82	2.10
Endcap inner z [m]	2.30	2.45	2.80
HCAL			
Barrel inner radius [m]	1.8	2.02	2.3
Endcap inner z [m]	2.6	2.67	2.9
Endcap outer radius [m]	2.66	3.05	4.2
B Field [T]	3	3.5	4

Table 3.1: Main parameters of the LDC, GLD and of the intermediate LDC' detector design studied in this thesis.

active detector are that they would be efficient in detecting minimum ionizing particles with minimal dead zones, and that they would have a spatial resolution per track crossing of the order of a centimetre. Both gas detector and extruded scintillator strips can fulfil such requests and both devices have been proposed as muon filter detectors. Gas detectors tend to be less expensive and offer more flexibility as for what segmentation is concerned.

For the LDC design, the total thickness needed to close the magnetic flux is about 150 cm so that 15 layers of detector could be accommodated in the end caps, 16 in the barrel as one layer could be placed immediately after the superconducting coil. In order to retain as much as possible of the calorimetric capability of the subsystem, the muon system in the LDC design consists of 10 cm segmentation for the first 10 layers and one last plane of detector at the very end of the flux return iron.

The muon identification efficiency of the muon system is an important parameter for the analysis presented in this thesis. In Fig. 3.12 the muon identification for isolated muons in the LDC detector is shown. A identification efficiency of about 100% is achieved down to muons with $4-5$ GeV/c momentum.

3.7 The ILD detector optimization framework of this thesis

This thesis was developed in the framework of the LDC detector concept. The status of the project developed rapidly between 2007 and 2008. In January 2008 it was suggested to merge the LDC concept with the GLD. The two concepts differ only in total size and strength of the magnetic field, while the basic features are essentially in common. The new detector concept is called ILD.

The technical parameters of the ILD detector were established only late October 2008. The simulation studies presented in this thesis refer to a rescaled version of the LDC concept, the so-called LDC$'$. This was the first attempt of a modification of the LDC concept in order to reach a compromised middle geometrical point with the GLD. The main parameters of LDC, LDC$'$ and GLD are shown in Table 3.1. There is nowadays a strong international effort in order to optimize the detector according to its physics performance. The aim of these studies is to show that the proposed detector satisfies the standard requirements which were described in section 3.3. Also the analysis shown in this thesis is included in this most general framework of a detector optimization with physics simulations.

Conclusion

The International Linear Collider is an interesting and powerful option for a precise measurement of the features of the Standard Model and the exact investigation of the new physics beyond the SM. The supersymmetry is a central topic of the physics program of ILC. In case SUSY is broken at the TeV scale, the masses of many sparticles will be in the energy range of the ILC and can be measured with an accuracy of less than 1%.

There is an intensive international effort which aims at defining the best detector for ILC. The precision measurement of physics at this high energy scale, characterized by multi-jet dense final states, requires an excellent tracking system and a new generation imaging calorimeter system, able to resolve the single contributions of jets. Moreover the detector has to cover as much solid angle as possible, in order to constrain the missing energy, important signature of new physics.

The study of the neutralino system reported in chapter 4 is inserted in the more general analysis of the performance of the LDC$'$ detector concept, towards the unification between the LDC and ILD concepts. Furthermore, the analysis of the experimental data presented in chapter 6 focuses on the highly granular hadronic calorimeter which was developed in the R&D program of LDC/ILD detector, whose main features were outlined in this chapter.

Chapter 4

Study of the χ_1^0 and χ_2^0 in the di-muon channel

"How beautiful was the princess who appeared from the ladybird,
Camomilla was her name,
the bridesmaid looking at her with wander,
the good fairy leaving with her white cloud. "
— ibidem

Introduction

In chapter 3 it was shown that one of the key-features of the International Linear Collider is the possibility of precise measurements of the physic phenomena beyond the Standard Model at the electroweak scale. The clean environment offered by this lepton machine and the exact knowledge of the initial state of the interaction reduce the systematic uncertainties of the measurement.

The study presented in this chapter focuses on the precision measurement of the neutralino sector at the Linear Collider using the di-muon channels. One of the cleanest final states at ILC consists of muons. As shown in Chapter 3, the muon detection efficiency is very high and their momentum is measured with a relative accuracy $\delta p/p$ of about 10^{-5}.

The physics relevance of the neutralino sector in SUSY was discussed in Chapter 2. It was shown that while at loop level the precision measurement of the neutralino sector allows improving the precise determination of the MSSM Lagrangian parameters, at a tree level the neutralino mixing matrix is related to the SUSY fundamental parameters [25, 26]. Moreover, it was evidenced that the χ_i^0 sector has a relevant role in CP and lepton flavour violating scenarios [27, 28].

The precise measurement of the parameters of SUSY is one of the priorities of the ILC physics program. The ATLAS [21] and CMS [22] experiments at LHC will have a high potential of establishing the experimental evidence of SUSY [122]. The International

Linear Collider will allow constraining with more precision the observations at LHC and measuring with accuracy the basic properties of the SUSY particles [23]. Although the determination of the mass spectrum of SUSY will be accessible at the future Colliders, the measurement of the parameters of the SUSY Lagrangian is more challenging. According to the actual theoretical understanding, the SUSY Lagrangian contains more than 100 new parameters which are related to each other through the Supersymmetry Breaking mechanism (SSB) [75, 123]. The precise measurement of the Lagrangian parameters implies hence a deep insight into the unknown SSB process. In this respect the interplay between LHC and ILC will be crucial. Several studies were performed in order to test the possibility of this measurement at ILC and LHC. Under the assumption of no CP violation, no Lepton Flavour violation and of the universality of first and second generation coupling, it is shown that the number of free parameters of the Lagrangian is reduced to 19. In this case it was also shown that the SUSY observables at LHC and ILC over constrain the system and allow fitting the SUSY scenario [29]. The information of the neutralino system, namely the mass and the cross sections of the neutralino pair production ($\sigma_{\chi_i^0\chi_j^0}$), are used as input variables to determine the SUSY Lagrangian parameters in a general fitting approach [124]. It is hence of crucial importance to measure with precision as more observables as possible for a precise constraining of the SUSY parameter space. This would allow to choose a specific realization of theory against other ones.

The neutralino sector is extensively studied in the physics case of ILC and LHC [23, 92]. At LHC the kinematics of the two body decays in the chain $\tilde{q}_L \rightarrow q\chi_2^0 \rightarrow ql_2^{\pm}\tilde{l}_R^{\mp} \rightarrow ql_2^{\pm}l_1^{\mp}$ allows to express the masses of the χ_1^0, χ_2^0, $\tilde{q}_L$ and $\tilde{l}_R$ as a full solved system [22]. The masses of the particles are determined with a precision of $4-5\%$. The $\tilde{e}^+_{L,R}\tilde{e}^-_{L,R}$ and $\tilde{\mu}^+_{L,R}\tilde{\mu}^-_{L,R}$ pair production are the most sensitive channels to the χ_1^0 mass measurement at ILC. The combination of all the channels would allow a precision of few parts per mille. The continuum production of neutralino χ_2^0 has been studied in the reaction $e^+e^- \rightarrow \chi_1^0\chi_2^0$ followed by the dominant decay mode $\chi_2^0 \rightarrow \tilde{\tau}\tau\chi_1^0$ [125]. The shape of the $m_{\tau\tau}$ invariant mass distribution is sensitive to the χ_2^0 mass within $\delta_m \sim 2$ GeV. The threshold scan of $e^+_R e^-_L \rightarrow \chi_2^0\chi_2^0 \rightarrow 4\tau + 2\chi_1^0$ is more promising, due to the very low background. Assuming a total luminosity of 100 fb^{-1} a precision of 1.2 GeV can be achieved [92].

In this chapter it is proposed the precision measurement of the mass of the χ_1^0 and of the χ_2^0 in the di-muon channel with a full detector simulation at ILC. As the kinematic plays an essential role in the analysis of the SUSY decay chains, the first part of the chapter describes extensively the used kinematic variables. The analysis is divided in two parts. The first one reports the study of the $e^+e^- \rightarrow \tilde{\mu}_L\tilde{\mu}_L \rightarrow \chi_1^0\mu\chi_1^0\mu$, which is used to perform the estimation of the mass of the χ_1^0. As a complementary result, also the mass of the $\tilde{\mu}_L$ and the cross section times branching ratio squared of the $\tilde{\mu}_L\tilde{\mu}_L$ pair production with the decay $\tilde{\mu}_L \rightarrow \mu\chi_1^0$ are obtained. The second part describes the measurement of the χ_2^0 mass in the $\chi_1^0\chi_2^0$ pair production, analysing the decay chain $\chi_2 \rightarrow \tilde{\mu}_R\mu \rightarrow \mu\mu\chi_1^0$. The measurement of the cross section of the this process is also proposed.

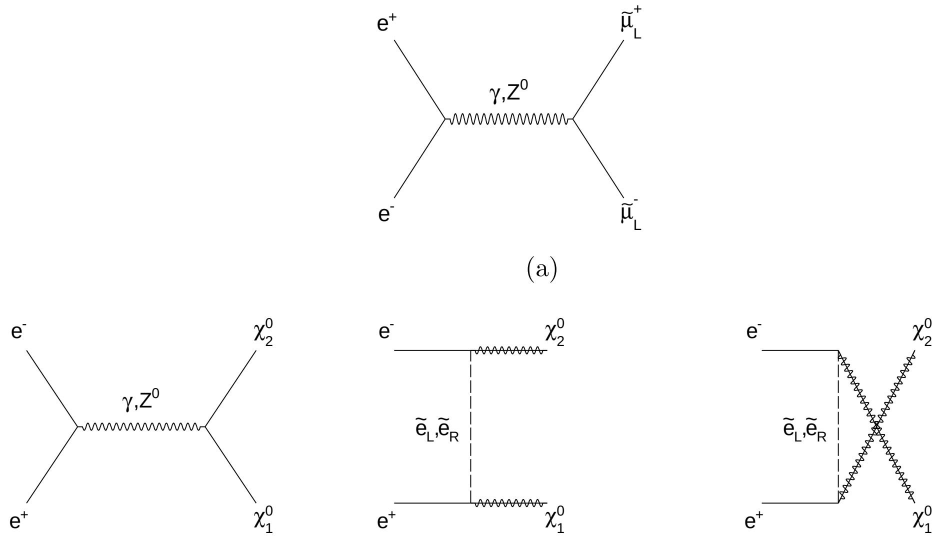

(a)

(b) (c) (d)

Figure 4.1: Feynman diagrams of the signal processes. The $\tilde{\mu}_L$ pairs are produced only through the s-channel (a). The process $e^+e^- \rightarrow \chi_1^0\chi_2^0$ is mediated by a Z^0 bosons (b) or by a $\tilde{e}_{L,R}$ (c,d).

4.1 The Signal Processes

The properties of the χ_1^0 and of the χ_2^0 are studied with the usual kinematic edges techniques [75, 126, 127], which are described extensively in the next sections.

In this study two channels are proposed for the precision measurement of the properties of the χ_1^0 and of the χ_2^0. The χ_1^0 can be measured in the process $e^+e^- \rightarrow \tilde{\mu}_L^+\tilde{\mu}_L^-$. The $\tilde{\mu}_L$ pairs are produced in the s-channel, through a Z^0 boson or a γ (Fig. 4.1a). The main decay of the $\tilde{\mu}_L$ is $\tilde{\mu}_L \rightarrow \mu\chi_1^0$, with a branching ratio of 92.5%. The two less frequent decays of the $\tilde{\mu}_L$ are $\tilde{\mu}_L \rightarrow \mu\chi_2^0$ (2.5%) and $\tilde{\mu}_L \rightarrow \mu\chi_1^-\nu_\mu$ (4.8%). The precision measurement of the mass of the χ_1^0 is performed in the $\tilde{\mu}_L \rightarrow \mu\chi_1^0$ channel.

The analysis of the χ_2^0 is performed in the $e^-e^+ \rightarrow \chi_1^0\chi_2^0$ process. At Linear Colliders the neutralino pairs can be produced both in the s-channel (Fig. 4.1b) and in the t-channel (Fig. 4.1c-d). The χ_2^0 decays predominantly in the channel $\chi_2^0 \rightarrow \tau\tilde{\tau}$ (branching batio 57%). The decay $\chi_2^0 \rightarrow \tilde{e}_R e$ and $\chi_2^0 \rightarrow \tilde{\mu}_R\mu$ has a branching ratio of 2.5%. The remaining 48% of the width of the χ_2^0 consists of neutral decays into $\tilde{\nu}\nu$ pairs. In this study the measurement of the χ_2^0 mass in the $\mu\tilde{\mu}_R$ decay channel is proposed. Although the branching ratio is very small in comparison with the other decay processes, the precision of the identification and measurement of the muons in the final state would allow an identification of the events at the kinematic limit of the di-muon invariant mass distribution.

The two processes are described by a similar kinematic. This justifies their treatment with the same analysis tools. The signal-like event are featured by two muons with a consistent missing energy transferred to the χ_1^0, which escapes the detector being the LSP in the considered $SPS1a'$ scenario.

4.2 Simulation Tools

The generation of the SUSY $SPS1a^{'}$ spectrum is performed using SPHENO [128]. This program calculates the supersymmetric particle spectrum within a high scale theory, such as minimal supergravity, gauge mediated supersymmetry breaking, anomaly mediated supersymmetry breaking or string effective field theories [1]. The program solves the renormalization group equations numerically to two-loop order. The obtained masses and mixing matrices are used to calculate decay widths and branching ratios of Supersymmetric particles as well as of Higgs bosons, $b \to s\gamma$, $\Delta\rho$ and $(g-2)_\mu$. The program includes also the polarization of the beams for the calculation of the cross section production of SUSY particles. The mass spectrum of the $SPS1a^{'}$ point was shown in table 2.2 in chapter 2.

The calculation of the final branching ratios and the generation of the events are performed with WHIZARD [129–131]. The beamstrahlung spectrum calculated with GUINEA PIG [106] and the Initial (ISR) and Final Radiation (FSR) are included in the event generation.

The full detector simulation is performed in GEANT4 [132]. The geometry of the detector is designed within MOKKA [133]. This program is an interface between the detector parameters stored in a database and GEANT4. In this study the detector model *LDCPrime02-Scint* is used[2]. The reconstruction of the events and the analysis is performed in the MARLIN [134] framework. The packages MARLINReco [135] and PANDORAPFA [30–33] are used respectively for the Tracking and the Particle Flow in the LDC detectors.

4.3 Expected Statistics at ILC

4.3.1 Signal processes

The total expected statistics depends on the polarization of the beam. In table 4.1 and 4.2 it is shown the dependence of the cross section of the signal processes on realistic combinations of the polarization of the beams at ILC. The t-channel production of the $\chi_1^0\chi_2^0$ pair makes the process sensitive to the polarization of the beams. The polarization of the electron beam introduces a dominant contribution to the total cross section. A left handed electron beam is preferred. Moreover, the combination with a right handed positron beam enhances significantly the cross section.

The $\tilde{\mu}_L$ are produced in diagonal pairs via s-channel Z boson and photon exchange. As the intermediate particle is a vector, the cross section of the process in case of RR and LL beam polarization is suppressed. The cross section of the $\tilde{\mu}_L$ pair production in

---

[1] A description of the SUSY breaking mechanisms is given in section 2.4.3.

[2] The description of the LDC$^{'}$ detector model can be found in sections 3.6 and 3.7

Process	**Cross section at the polarization (e^-,e^+) [fb]**		
	(-0.8,0.6)	(-0.8,-0.6)	(-0.8,0)
$e^+e^- \to \chi_1^0\chi_2^0 \to \chi_1^0\mu\tilde{\mu}_R \to \chi_1^0\chi_1^0\mu\mu$	4.2	1.1	2.4
$e^+e^- \to \tilde{\mu}_L\tilde{\mu}_L \to \chi_1^0\chi_1^0\mu\mu$	54	18	43

Table 4.1: Impact of the polarization to the cross section times branching ratio squared of the $\tilde{\mu}_L$ pair production ($\tilde{\mu}_L \to \mu\chi_1^0$) and to the cross section times branching ratio of the $\chi_1^0\chi_2^0$ production ($\chi_2 \to \tilde{\mu}_R\mu \to \mu\mu\chi_1^0$). Combinations of possible polarization states at ILC, for a right-handed polarized electron beam. Beamstrahlung, initial and final state radiation are included in the calculation of the cross sections. More combinations of polarization are reported in table 4.2.

Process	**Cross section at the polarization (e^-,e^+) [fb]**			
	(0,0)	(+0.8,0.6)	(+0.8,-0.6)	(+0.8,0)
$e^+e^- \to \chi_1^0\chi_2^0 \to \chi_1^0\mu\tilde{\mu}_R \to \chi_1^0\chi_1^0\mu\mu$	1.59	0.55	0.4	0.48
$e^+e^- \to \tilde{\mu}_L\tilde{\mu}_L \to \chi_1^0\chi_1^0\mu\mu$	27	10	15	13

Table 4.2: Impact of the polarization to the cross section times branching ratio squared of the $\tilde{\mu}_L$ pair production ($\tilde{\mu}_L \to \mu\chi_1^0$) and to the cross section times branching ratio of the $\chi_1^0\chi_2^0$ production ($\chi_2 \to \tilde{\mu}_R\mu \to \mu\mu\chi_1^0$). Beamstrahlung, initial and final state radiation are included in the calculation of the cross sections. Combinations of possible polarization states at ILC, for a left-handed polarized electron beam.

case of RL and LR beams is expressed by [136]:

$$\begin{aligned} \sigma\left[e_R^+e_L^- \to \tilde{\mu}_L^+\tilde{\mu}_L^-\right] &= \tfrac{2\pi\alpha^2}{3s}\beta^3\left[1+g_Lg_L\tfrac{s}{s-M_Z^2}\right]^2 \\ \sigma\left[e_L^+e_R^- \to \tilde{\mu}_L^+\tilde{\mu}_L^-\right] &= \tfrac{2\pi\alpha^2}{3s}\beta^3\left[1+g_Lg_R\tfrac{s}{s-M_Z^2}\right]^2 \end{aligned} \tag{4.1}$$

where g_L and g_R are the left-chiral and right-chiral Z boson couplings. Also in case of the $\tilde{\mu}_L$ pair production the LR polarization configuration is preferred to the RL one.

In the following study the polarization of the beams is chosen as (-0.8,0.6). The cross section of the process $e^+e^- \to \chi_1^0\chi_2^0 \to \chi_1^0\mu\tilde{\mu}_R \to \chi_1^0\chi_1^0\mu\mu$ is 4.2 fb. Consequently in the first four years of operation about 2000 signal events are expected for the measurement of the mass of the χ_2^0. At the same beam polarization the cross section of the process $e^+e^- \to \tilde{\mu}_R\tilde{\mu}_R \to \chi_1^0\chi_1^0\mu\mu$ is 54.32 fb, resulting in about 27000 events for the measurement of the χ_1^0 in the first 4 years of operation of ILC.

4.3.2 SUSY Background

There is a significant number of SUSY processes in $SPS1a^{'}$ which is featured by two muons and high missing energy in the final state. The most serious SUSY background is the production of $\widetilde{\mu}_R\widetilde{\mu}_R$. The $\widetilde{\mu}_R$ undergoes only the decay $\widetilde{\mu}_R \to \mu\chi_1^0$ with a branching ratio of 100%. The total cross section times branching ratio squared is 39 fb. It is one order of magnitude above the $\chi_1^0\chi_2^0 \to \tilde{\mu}_R\mu\chi_1$ process (4.2 fb) and of the same order of magnitude of the $\tilde{\mu}_L$ pair production (54.32 fb).

In the SPS1a$^{'}$ point there is a large variety of lower order contributions to the background, featured by two muons, two χ_1^0 and a pair of $\nu_{e,\mu,\tau}$ in the final state. These processes involve also the production of τ's which decay according to $\tau \to \mu\nu_\mu\nu_\tau$. They sum up to a total cross section of about 10 fb.

The $\widetilde{\tau}_{1,2}^{\pm}\widetilde{\tau}_{1,2}^{\mp}$ pair production is a consistent source of this background, mainly through the $\widetilde{\tau}_{1,2}^{\pm} \to \tau\chi_1^0$ decay .

The $\widetilde{\mu}_L$ pair production contributes to this SUSY background through the less frequent decay chains $\widetilde{\mu}_L\widetilde{\mu}_L \to \chi_1^0\mu\nu_{\mu,e}\widetilde{\nu}_{\mu,e}$, $\widetilde{\mu}_L\widetilde{\mu}_L \to \chi_1^0\mu\chi_2^0\mu$ and $\widetilde{\mu}_L\widetilde{\mu}_L \to \chi_1^0\mu\chi_1^{\pm}\nu_\mu$.

The $\chi_2^0\chi_2^0$ pair production is a background source only when one χ_2^0 decays in $\widetilde{\nu}_{e,\mu}\nu_{e,\mu}$ and the other χ_2^0 decays in $\widetilde{\mu}_R\mu$ or $\widetilde{\tau}_1\tau$. Moreover, the $\chi_1^0\chi_2^0$ pair production is also a source of background when the χ_2^0 decays in $\tau\widetilde{\tau}_1$.

The $\chi_1^{\pm}\chi_1^{\mp}$ pair production constitutes also a background source, mainly in the decay chains $\chi_1^{\pm}\chi_1^{\mp} \to \mu^{\pm}\widetilde{\nu}_\mu\mu^{\mp}\widetilde{\nu}_\mu$ and $\chi_1^{\pm}\chi_1^{\mp} \to \tau^{\pm}\widetilde{\nu}_\tau\tau^{\mp}\widetilde{\nu}_\tau$.

A total number of about 37000 background events are expected in the first 4 years of operation at ILC. The full SUSY background considered in this analysis is reported in table 4.3.

4.3.3 SM Background

There are also several Standard Model processes which contribute to the background. These processes are featured by the production of two μ or τ and $\nu_e, \nu_\mu, \nu_{tau}$. The τ decays through $\tau^{\pm} \to \mu^{\pm}\nu_\mu$. The W^+W^- pair production contributes through the semileptonic decays $W^{\pm} \to \mu^{\pm}\nu_\mu$ and $W^{\pm} \to \tau^{\pm}\nu_\tau$.

An irreducible background consists of the production of ZZ $\gamma\gamma$ and γZ, where one particle decays into a $\mu\mu$ or $\tau\tau$ pair and the other undergoes an invisible decay into $\nu_{e,\mu.\tau}, \nu_{e,\mu,\tau}$ pairs.

The WW fusion diagram, into Z or γ is also an irreducible background. A pair of ν_e is produced together with a γ or Z, which can decay into $\mu\mu$ or $\tau\tau$ pairs.

A characteristic source of SM background at this high beam energy is the radiative return to the Z peak in the $e^+e^- \to \mu^{\pm}\mu^{\mp}$ and $e^+e^- \to \tau^{\pm}\tau^{\mp}$ processes. In this Initial State Radiation process, a photon is radiated from the incident electron or positron, or from both. The photon is high energetic and propagates along the beam pipe, escaping from the detector without any further interaction, faking the missing energy signature.

The creation of $\mu\mu$ and $\tau\tau$ pairs from the $e^+e^- \to e^+e^-\gamma\gamma$ background in the beam interaction influences only the low transversal momentum region. The cross section of this process is 229312 fb, resulting in about 110 million events in 4 years of operation at

Final State	Processes	Cross section [fb]
$\mu\mu\chi_1^0\chi_1^0$	$\tilde{\mu_R}\tilde{\mu}_R$	39.77
$\mu\mu\nu_e\nu_e\chi_1^0\chi_1^0$	$\tilde{\mu_L}\tilde{\mu}_L \rightarrow \chi_1^0\chi_2^0$ $\chi_2^0\chi_2^0 \rightarrow \mu^\pm\tilde{\mu}^\mp\nu_e\tilde{\nu}_{e,L}$	1.6
$\mu\mu\nu_\mu\nu_\mu\chi_1 0\chi_1^0$	$\tilde{\mu_L}\tilde{\mu}_L \rightarrow \chi_1^0\mu\nu_\mu\tilde{\mu}_\mu$ $\chi_2^0\chi_2^0 \rightarrow \mu^\pm\tilde{\mu}_R^\mp\nu_\mu\tilde{\nu}_\mu$ $\tilde{\mu}_L\tilde{\mu}_L \rightarrow \chi_1^0\mu^\pm\chi_1^\mp\nu_\mu$ $\chi_1^\pm\chi_1^\mp \rightarrow \mu\tilde{\nu}_\mu\mu\tilde{\nu}_\mu$	9.29
$\mu\mu\nu_\tau\nu_\tau\chi_1^0\chi_1^0$	$\tilde{\mu_L}\bar{\tilde{\mu}}_L \rightarrow \chi_1^0\chi_2^0$ $\chi_2^0\chi_2^0 \rightarrow \mu\tilde{\mu}\nu_\tau\nu_\tau$	1.6
$\mu^\pm\mu^\mp\nu_\mu\nu_\tau\nu_\mu\nu_\tau\chi_1^0\chi_1^0$	$\tilde{\tau}_1\tilde{\tau}_1$ $\tilde{\tau}_1\tilde{\tau}_1$	6.1
$\mu^\pm\mu^\mp\nu_\mu\nu_\tau\nu_\mu\nu_\tau\nu_\mu\nu_\mu\chi_1^0\chi_1^0$	$\tilde{\tau}_1\tilde{\tau}_2 \rightarrow \chi_1^0\tau\chi_2^0\tau$ $\tilde{\tau}_2\tilde{\tau}_2 \rightarrow \chi_1^0\tau\chi_2^0\tau$ $\chi_2^0\chi_2^0 \rightarrow \tau\tilde{\tau}\nu_\mu\tilde{\nu}_\mu$	0.6
$\mu^\pm\mu^\mp\nu_\mu\nu_\tau\nu_\mu\nu_\tau\nu_\tau\nu_\tau\chi_1^0\chi_1^0$	$\tilde{\tau}_2\tilde{\tau}_2 \rightarrow \chi_1^0\tau\chi_2^0\tau$ $\tau_2\tau_2 \rightarrow \chi_1^0\tau\chi_1^\pm\nu_\tau$ $\tau_2\tau_2 \rightarrow \chi_1^0\tau\chi_1^\pm\nu_\tau$ $\tau_1\tau_2 \rightarrow \tau\chi_1^0\tau\chi_2^0$ $\tilde{\tau}_1\tilde{\tau}_2 \rightarrow \tau\chi_1^0\chi_1^\pm\nu_\tau$ $\chi_2^0\chi_2^0 \rightarrow \tau\tilde{\tau}\nu_\tau\tilde{\nu}_\tau$ $\chi_1^+\chi_1^- \rightarrow \tau\tilde{\nu}_\tau\tau\tilde{\nu}_\tau$ $\chi_1^+\chi_1^- \rightarrow \tau\tilde{\nu}_\tau\tilde{\tau}\nu_\tau$	7.4
$\mu^\pm\mu^\mp\nu_\mu\nu_\tau\nu_\mu\nu_\tau\nu_e\nu_e\chi_1^0\chi_1^0$	$\tilde{\tau}_2\tilde{\tau}_2 \rightarrow \chi_1^0\chi_1^0\tau\tau$ $\tilde{\tau}_1\tilde{\tau}_2 \rightarrow \tau\chi_1^0\tau\chi_2^0$ $\chi_2^0\chi_2^0 \rightarrow \tau\tilde{\tau}\nu_e\tilde{\nu}_e$	0.7
$\mu^\pm\mu^\mp\nu_\mu\nu_\tau\nu_\mu\nu_\tau\nu_\mu\nu_\tau\chi_1^0\chi_1^0$	$\chi_1^\pm\chi_1^\mp \rightarrow \mu\tilde{\nu}_\mu\tau\tilde{\nu}_\tau$	3.3
	$\chi_1^\pm\chi_1^\mp \rightarrow \mu\tilde{\nu}_\mu\nu_\tau\tilde{\tau}$	3.4
	$\tilde{\mu_L}\tilde{\mu}_L \rightarrow \chi_1^0\mu\chi_1^\pm\nu_\mu$	0.35

Table 4.3: Table of the SUSY background. The background processes are classified according to the final state. The signature of the signal is made of two muons and missing energy associated to a pair of χ_1^0 which leave undetected. The SUSY background is composed of all the processes which have μs or τs, χ_1^0s and $\nu_{e,\mu.\tau}$s in the final state. the $\widetilde{\mu}_R$ pair production. After 4 years of operation the ILC will provide a total luminosity of 500 fb^{-1}. The expected number of SUSY background events is 37000.

.

500 fb^{-1}. It was shown that one of the scopes of the BeamCal [3] is to tag this background detecting the two highly energetic electrons which moves undeflected at very low polar angles in the forward region. It was possible to simulate about 100000 $\gamma\gamma$ events, only a very small fraction of the real expected number. Nevertheless, after the cuts proposed in the following discussion none of the simulated $\gamma\gamma$ events was selected. This background source concentrates in the low energy region, below 30 GeV, while the di-muon signals are higher energetic. This channel is not considered hence a significant background source for this analysis.

The Standard Model contribution to the background is summarized in table 4.4. The total number of expected Standard Model background events after 4 years of operation of the Linear Collider is 1100000 [4].

4.4 Pre-selection of Di-muon Events

The first step of the analysis is the pre-selection of hard di-muons events with two isolated muon tracks and photons. The photons are allowed as the result either of the Initial State Radiation or of the Final State Radiation processes.

The muons are identified as charged *mip-like* particles which leaves a clear track in the TPC and in the calorimeters and deposits energy in the Muon System. As the muon system is positioned outside the magnetic coil, the muon is the only particle which can traverse the full detector and the magnetic coil depositing energy only through ionization.

The hits in the muon chambers are grouped in tracks. All the hits with a separation of 2.8° in θ and 3.4° in ϕ are associated to the same track. A track in the muon chamber is identified as possible muon if it has more than 7 aligned hits. The direction of each track segment in the muon system is calculated in the (θ, ϕ) plane. Two isolated tracks have to be found.

The muon candidate event presents 2 isolated tracks in the tracker connected to two isolated *mip-like* clusters in the calorimeters. A cluster with total energy e_c and total number of hits n_c is defined *mip-like* if $0.5 < e_c/n_c < 1.5$. More isolated photon clusters can be also found in the ECAL. The particle flow algorithm PANDORAPFA identify particles with this topology as *punch-thru* π, and identify with high efficiency the photon clusters. Tracks and clusters are defined *isolated* if no other clusters or tracks are found within a cone of 1°.

Therefore a particle is identified as muon if the cluster found in the hadronic calorimeter matches with a track found in the muon system, within a angular distance of 11° in θ and ϕ. This angular acceptance is optimized to the deflection of muons with momentum higher than 20 GeV/c. It is observed that for lower momentum a more precise extrapolation of the muon track from the hadronic calorimeter to the muon chamber would be needed, but it is outside the scope of this analysis.

---

[3] The BeamCal is a small calorimeter positioned in the very forward region. For more information ref. to chapter 3.

[4] This number does not include the $e^+e^- \rightarrow e^+e^-\gamma\gamma$ background, for the reasons explained in the text.

Final State	**Processes**	$\boldsymbol{\sigma \times BR}$ **[fb]**
$e^+e^- \longrightarrow \mu\mu$	Z γ	1890
$\mu\mu\nu_\mu\nu_\mu$	W^+W^- ZZ	288
$\mu\mu\nu_e\nu_e$	ZZ WW fusion $\gamma\gamma$ γZ	54.43
$\mu\mu\nu_\mu\nu_\tau\nu_\mu\nu_\tau$	Z γ	57.2
$\mu\mu\nu_\mu\nu_\tau\nu_\mu\nu_\tau\nu_e\nu_e$	ZZ WW fusion $\gamma\gamma$ γZ	2.1
$\mu\mu\nu_\mu\nu_\tau\nu_\mu\nu_\tau\nu_\tau\nu_\tau$	W^+W^- ZZ	8.9
$\mu\mu\nu_\tau\nu_\tau\nu_\mu\nu_\mu\nu_\mu\nu_\mu$	ZZ $\gamma\gamma$	0.23
$\mu\mu\nu_\tau\nu_\tau$	ZZ $\gamma\gamma$	7.6

Table 4.4: The contribution of the Standard Model to the background. The main SM background source is the production of $\mu\mu$ pairs affected by radiative return to the Z peak. An irreducible background process is the production of ZZ and $\gamma\gamma$ pairs, where one of the two particles undergoes a di-muon or di-τ decay and the other an invisible decay into a pair of $\nu_{e,\mu,\tau}$s. In this table the $\gamma\gamma \rightarrow \mu\mu$ background is excluded, as it interests a energy range much lower than the signal. The total number of SM background events in the first four years of operation of ILC is 1100000.

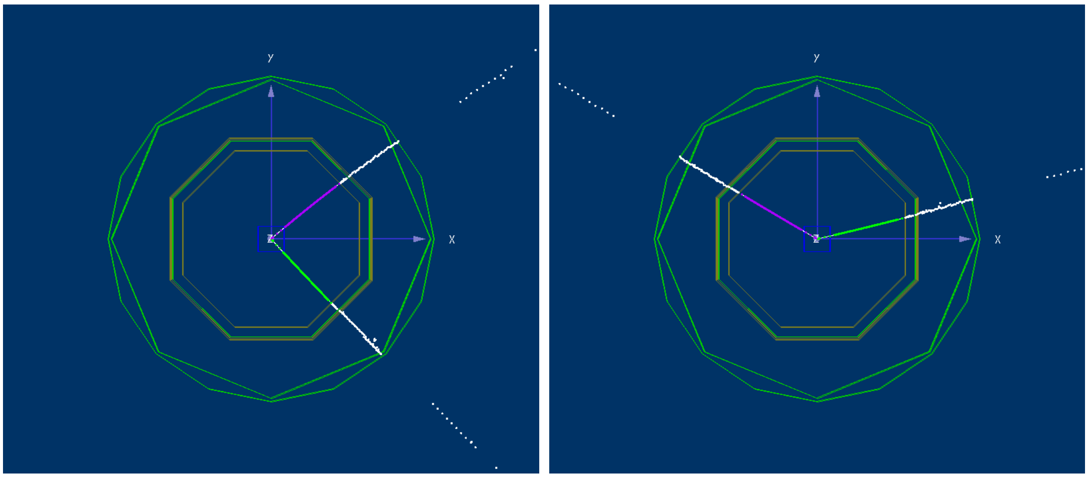

Figure 4.2: Event display of two di-muon candidates after the pre-selection. In (a) the final state of the $\chi_1^0\chi_2^0$ pair production with the $\chi_2^0 \to \mu\tilde{\mu}_R$ decay is shown. In (b) the final state of the $\tilde{\mu}_L\tilde{\mu}_L$ pair production with the decay $\tilde{\mu}_L \to \mu\tilde{\mu}_R$ is shown. In both cases the final state consists of two muons and sizable missing p_t and missing energy.

The total event selection efficiency is 95% for the two signal processes studied in this analysis. The rejected events are featured by muons produced at very low θ. These events are not detected in the TPC and presents only energy deposit in the calorimeters and in the muon system — being hence identified as not charged particles. The typical topology of the events which passes the pre-selection is shown in Fig. 4.2.

4.5 Kinematic Variables used in the Analysis

4.5.1 Energy of the two Muons

The 4-momentum of the two muons in the laboratory frame ($E_{\mu,1,2}$,$\vec{p}_{\mu,1,2}$) is the only direct observable which can be measured. All the other kinematic quantities are calculated from them. The momentum of the muons in the final state is measured in the tracking system with an expected relative precision $\delta p/p = 10^{-5}$. The distribution of $E = \sqrt{|\vec{p}_{\mu,1,2}|^2 - m_\mu^2}$ is shown in Fig. 4.3 for the two signal processes considered in this analysis, the SUSY background and the SM background.

$e^+e^- \to \tilde{\mu}_L\tilde{\mu}_L \to \chi_1^0\chi_1^0\mu\mu$

The $\tilde{\mu}_L$ pair production is a symmetric process. In the laboratory frame, which is also the centre of mass frame of the full system, the two $\tilde{\mu}_L$ share the energy of the centre of mass ($E_s = 500$ GeV). Hence they are produced with the same energy $E_{\tilde{\mu}_{L,1,2}} = E_s/2 =$ 250 GeV.

The following decay $\tilde{\mu}_L \to \mu\chi_1^0$ can be conveniently analysed in the reference frame ($\circ$) of the $\tilde{\mu}_L$. In this frame the μ and the χ_1^0 are monochromatic, according to the

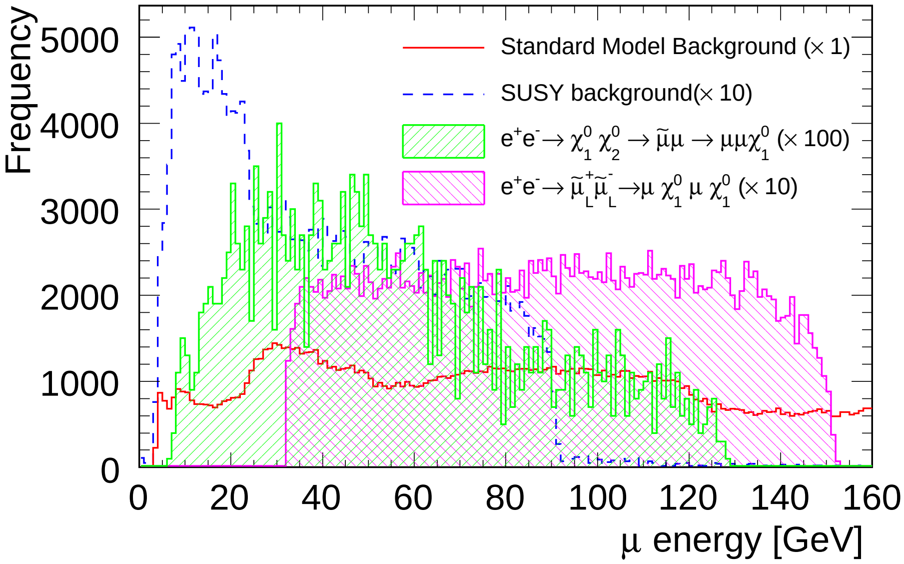

Figure 4.3: Energy of the muons in the final state for the background (SM and SUSY) and the signal processes. The distributions are weighted with the factors shown in the legend.

properties of the two body decay kinematics. The energy of the particles in the final state is:

$$E_\mu^\circ = \frac{m^2_{\tilde{\mu}_L} - m^2_{\chi_1^0}}{2 \cdot m_{\tilde{\mu}_L}} \qquad E_{\chi_1^0}^\circ = \frac{m^2_{\tilde{\mu}_L} + m^2_{\chi_1^0}}{2 \cdot m_{\tilde{\mu}_L}} \tag{4.2}$$

In the laboratory frame, the energy of the μ and of the χ_1^0 can be calculated applying a Lorentz boost to the $\circ$ frame. The γ and $|\beta|$ of the boost are:

$$\gamma = \frac{E_{\tilde{\mu}_L}}{m_{\tilde{\mu}_L}} = \frac{E_s}{2 \cdot m_{\tilde{\mu}_L}} \qquad \beta = \sqrt{1 - \frac{1}{\gamma^2}} \tag{4.3}$$

The energy of the muons is distributed uniformly between a minimum and a maximum ($E_\mu^\pm$) defined as:

$$E_\mu^\pm = \gamma\,(1 \pm \beta)\,E_\mu^\circ = \frac{E_s}{2} \cdot \left(1 \pm \sqrt{1 - \frac{4m^2_{\tilde{\mu}}}{E_s^2}}\right) \cdot \frac{m^2_{\tilde{\mu}_L} - m^2_{\chi_1^0}}{2 \cdot m^2_{\tilde{\mu}_L}} \tag{4.4}$$

The extremes of the distribution are $E_{\mu}^{-} = 32.11$ GeV and $E_{\mu}^{+} = 151.68$ GeV in the SPS1a$^{'}$ scenario.

$e^+e^- \rightarrow \chi_1^0\chi_2^0 \rightarrow \chi_1^0\mu\tilde{\mu}_R \rightarrow \chi_1^0\chi_1^0\mu\mu$

The distribution of the momentum of the muons in the final state is the result of the decay chain of the χ_2^0. The decay chain $\chi_2 \rightarrow \widetilde{\mu}^{\pm}\mu^{\mp}$ can be analysed easily in the frame of the centre of mass of the χ_2^0. This frame will be indicated with an asterisk $(*)$ in the following discussion. The first step of the decay chain is the two body decay $\chi_2^0 \rightarrow \widetilde{\mu}^{\pm}\mu^{\mp}$. The energy distribution of the two particles is monochromatic, according to the kinematic of the two body decay:

$$\begin{aligned} E^{*}_{\mu,1} &= \frac{m^2_{\chi_2^0} - m^2_{\widetilde{\mu}}}{2 \cdot m_{\chi_2^0}} \\ E^{*}_{\widetilde{\mu}} &= \frac{m^2_{\chi_2^0} + m_{\widetilde{\mu}2}}{2 \cdot m_{\chi_2^0}} \end{aligned} \tag{4.5}$$

The successive decay $\widetilde{\mu}^{\pm} \rightarrow \mu^{\pm}\chi_1^0$ is a two body decay. The energy of the two particles has a monochromatic distribution in the centre of mass frame of the $\widetilde{\mu}$. In the frame $*$ it has a flat distribution. The maximum $(+)$ and minimum $(-)$ extremes of the distribution are described by the following equations:

$$\begin{aligned} E^{\pm *}_{\mu,2} &= \gamma^{*}\left(1 \pm \beta^{*}\right) \frac{m^2_{\widetilde{\mu}} - m^2_{\chi_1^0}}{2 \cdot m_{\widetilde{\mu}}} \\ E^{\pm *}_{\chi_1^0} &= \gamma^{*}\left(1 \pm \beta^{*}\right) \frac{m^2_{\widetilde{\mu}} + m^2_{\chi_1^0}}{2 \cdot m_{\widetilde{\mu}}} \end{aligned} \tag{4.6}$$

where γ^{*} and β^{*} describe the $\widetilde{\mu}$ in the $*$ frame:

$$\begin{aligned} \gamma^{*} &= \frac{E^{*}_{\widetilde{\mu}}}{m_{\widetilde{\mu}}} = \frac{m^2_{\chi_2^0} + m^2_{\widetilde{\mu}}}{2 \cdot m_{\chi_2^0} \cdot m_{\widetilde{\mu}}} \\ \beta^{*} &= \sqrt{1 - \frac{1}{\gamma^2}} = \frac{m^2_{\chi_2^0} - m^2_{\widetilde{\mu}}}{m^2_{\chi_2^0} + m^2_{\widetilde{\mu}}} \end{aligned} \tag{4.7}$$

According to the kinematics of the two body decay, the distribution of the momentum of the muon coming from the decay $\chi_2^0\widetilde{\mu}^{\mp}\mu^{\pm}$ is flat in the laboratory frame. The minimum (-) and maximum (+) value is expresses by the following equation:

$$E^{lab}_{\mu,1} = \gamma_{\chi_2^0}\left(1 \pm \beta_{\chi_2^0}\right) \cdot \frac{m^2_{\chi_2^0} - m^2_{\widetilde{\mu}}}{2 \cdot m_{\chi_2^0}} \tag{4.8}$$

where

$$\gamma_{\chi_2^0} = \frac{E_{\chi_2^0}}{m_{\chi_2^0}}$$
$$\beta_{\chi_2^0} = \sqrt{1 - \frac{1}{\gamma^2_{\chi_2^0}}} \qquad (4.9)$$

In Fig. 4.3 the flat distribution of the harder muon μ_1 is visible. It presents an upper kinematic edge at 128 GeV, as predicted in equation 4.8.

The muon generated in the $\widetilde{\mu}_R$ decay (μ_2) is softer. In the centre of mass frame the momentum follows a uniform distribution according to equation 4.6. In the laboratory frame the Lorentz boost of the decaying χ_2^0 is convoluted with the uniform distribution of the parent $\widetilde{\mu}_R$, resulting in a non flat distribution. The contribution of a non flat distribution of softer muons with energy ranging between about 10 GeV and 60 GeV is visible in Fig. 4.3.

SUSY background

In the $SPS1a^{'}$ SUSY scenario muons in the final state are the result of a two body decay of a supersymmetric particle into a lighter SUSY particle and a muon. The mass difference Δm between the parent and daughter SUSY particles in the decay chains affects the momentum distribution of the muon. At higher Δm more kinetic energy is available for the muon after the creation of the massive daughter SUSY particle.

The $\tilde{\mu_R}$ pair production background offers a significant example of this mechanism. The mass of the $\widetilde{\mu}_L$ is 189 GeV and the mass of the $\widetilde{\mu}_R$ is 125 GeV in the $SPS1a^{'}$ scenario. Consequently the muons produced in the decay $\widetilde{\mu}_R \rightarrow \mu\chi_1^0$ are softer than the muons produced in the decay $\widetilde{\mu}_L \rightarrow \mu\chi_1^0$. The upper kinematic edge of the μ_R background at about 90 GeV is visible in the distribution of the SUSY background in Fig. 4.3.

In the SUSY background channels featured by the production of $\nu_{\tau,\mu}$ the energy available for the SM particles is shared between muons and neutrinos, with the consequent production of soft muons compared to the signal processes.

SM background

The distribution of the momentum of the muons in the SM background is featured by peaks associated to the two body decay of the Z and γ. In the ZZ and $\gamma\gamma$ production at a centre of mass of 500 GeV, the two particles share 250 GeV on average, producing a pair of 125 GeV muons. The distribution of the muons from the $W^{\pm}W^{\mp}$ and W fusion background is continuous, with an upper value of 250 GeV.

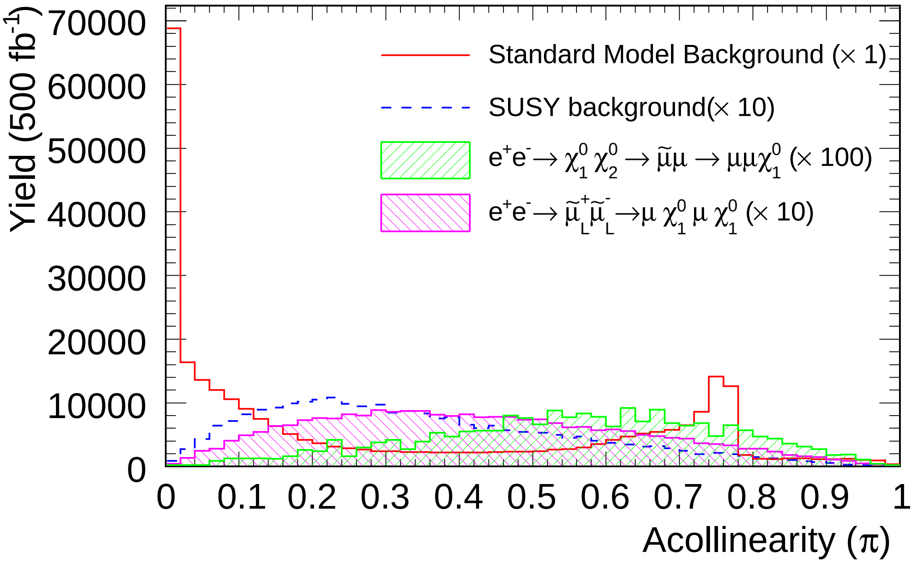

Figure 4.4: Acollinearity of the two muons in the final state for the background (SM+SUSY) and the signal processes. The distributions are weighted with the factors shown in the legend.

4.5.2 Acollinearity

The acollinearity θ_{acol} is defined as the supplement of the 3-d angle between the muons. It is calculated from the momentum of the two muons in the final state:

$$\theta_{acol} = 1 - acos\left(\frac{\vec{p}_{\mu,1} \cdot \vec{p}_{\mu,2}}{|\vec{p}_{\mu,1}|\,|\vec{p}_{\mu,2}|}\right) \tag{4.10}$$

The acollinearity of the signal and of the SM and SUSY background is shown in Fig. 4.4.

Signal processes

In first approximation the muons in the final state follow the direction of their parent particles in the decay chain. Acollinear muons are expected from the $\chi_2^0\chi_1^0$ pair production. This process is asymmetric as the χ_1^0 escapes undetected. On the contrary the $\tilde{\mu}_L$ pair production is a symmetric process. However the acollinearity angle depends on the mass difference between the parent and daughter particles in the decay chain. The mass of the $\tilde{\mu}_L$ and of the χ_1^0 is high in $SPS1a^{'}$ and these particles are produced almost at rest at a Linear Collider with 500 GeV centre of mass. This implies that the muons in the final state have no preferred direction. The smearing effect introduced by this mechanism is visible in Fig. 4.4 where the acollinearity distribution of the muon pairs produced in the $\chi_1\chi 2$ process is peaked around 1 but with a large tail towards low values and the distribution of the muon pairs produced in the $\tilde{\mu}_L\tilde{\mu}_L$ process is peaked around 0.3, extending also towards the high acollinearity region.

SUSY background

The SUSY background is influenced significantly by the Δm between parents and daughter particles in the SUSY decay chains. The muons coming from symmetric processes, as $\tilde{\mu}_R$ pair production, are mainly collinear, with a large tail towards high acollinearity. Moreover the acollinearity distribution of SUSY background channels with τs is smeared by the presence of $\nu_{\mu,\tau}$ in the final state.

SM background

The SM processes as $ZZ, Z(\gamma)$ production are mainly asymmetric when one Z or γ decays into two μ and the other into a pair of $\nu_{\mu,e,\tau}$. In this case a pair of acollinear muons is produced, but the acollinearity angle and the momentum of the two muons are fixed by the relativistic kinematics of the two body decay of the Z:

$$\theta_{acol}^{Z} = \pi - acos\left(\frac{2 \cdot E_{\mu,1} \cdot E_{\mu,2} - m_Z^2}{2 p_{\mu,1} \cdot p_{\mu,2}}\right) = 0.74\pi \qquad Z \rightarrow \mu\mu \tag{4.11}$$

The peaks at θ_{acol}^{Z} is visible is the distribution of the acollinearity of the SM background in Fig. 4.4.

The $W^{\pm}W^{\mp}$ pair production and the $Z^0 \rightarrow \mu\mu$ are mainly featured by collinear muons in the final state.

4.5.3 Acoplanarity and transverse momentum

The kinematics in the plane transverse to the beam axis is sensitive to the production of massive invisible particles in the final state. This is observed with the acoplanarity (θ_{acop}) and the total transverse momentum ($|\vec{p}_t|$).

The acoplanarity is defined as the supplement of the angle between the muons in the plane perpendicular to the beam. It is calculated from the momentum of the two muons in the final state:

$$\theta_{acop} = \pi - acos\left(\frac{(\vec{p}_{\mu,1} \cdot \vec{p}_{\mu,2})_{x,y}}{|\vec{p}_{\mu,1}|_{x,y}\, |\vec{p}_{\mu,2}|_{x,y}}\right) \tag{4.12}$$

The total transverse momentum is defined as the total momentum of the two muons in the final state in the (x,y) plane transversal to the (z) beam axis:

$$|\vec{p}_t| = \left|(p_{\mu,1} + p_{\mu,2})_{x,y}\right| \tag{4.13}$$

The distribution of θ_{acop} and of the p_t is shown in Fig 4.5 and Fig. 4.6.

Signal processes

The generation of a invisible χ_1^0 in the $\chi_1^0\chi_2^0$ signal process is the source of a significant p_t. The two muons in the final state are also acoplanar. As in the case of the acollinearity the muons from the $\tilde{\mu}_L$ pair production are expected to be highly coplanar. However,

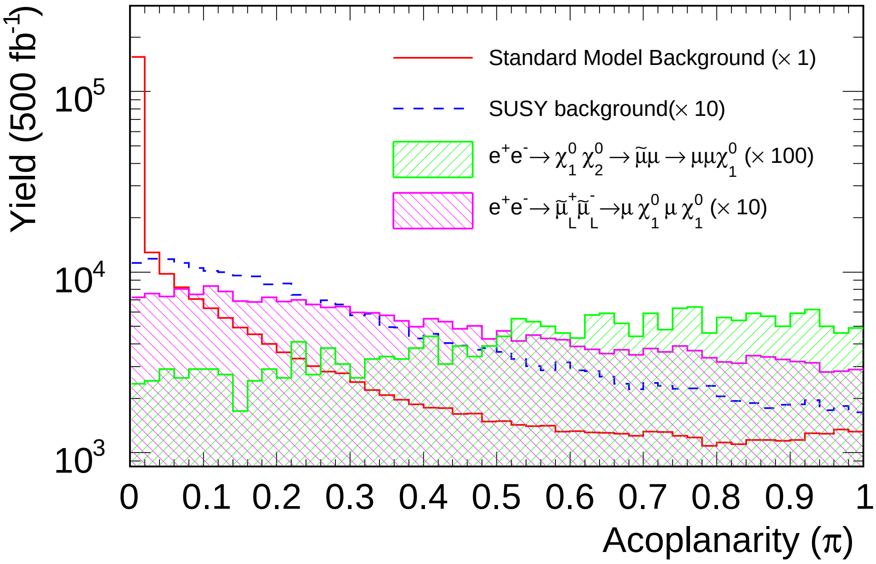

Figure 4.5: Acoplanarity of the muons in the final state for the signal processes and the background (SM+SUSY). The distributions are rescaled with the factors defined in the legend.

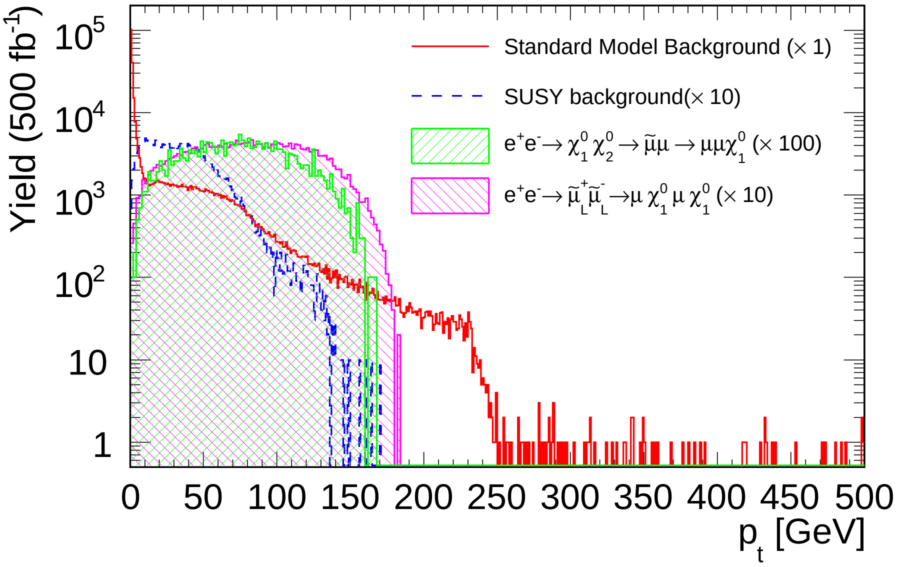

Figure 4.6: Total transverse momentum of the muons in the final state for the background (SM+SUSY) and for the signal processes. The distributions are rescaled with the factors defined in the legend.

the mass difference between parent and daughter particles in the decay chains affects the acoplanarity of the muons in the final state, as in case of the acollinearity.

This effect is evident in the two signal processes considered in this analysis. As the $\tilde{\mu}_L$ is heavy, the muons generated in the $\tilde{\mu}_L \to \mu\chi_1^0$ can be as acoplanar as the muons produced in the asymmetric $\chi_1^0\chi_2^0$ process. The acoplanarity distributions of the two signal processes are very similar, as it is shown in Fig. 4.5.

SUSY background

The SUSY background channels are all consistent with high transverse momentum, caused by the production of massive χ_1^0s. Moreover the acoplanarity distribution results always smeared, because of the relatively small Δm between parents and daughters SUSY particles in the decay chains.

SM background

The Standard Model background is mainly featured by a pair of coplanar muons with low p_t. This signature identifies the $\gamma \to \mu\mu$ and $Z^0 \to \mu\mu$ background, when no return to the Z peak occurs. It also describes the $W^\pm W^\pm$ production.

In case of the τ decays, both in the SUSY and in the SM background, the muons are always produced with $\nu_{\mu,\tau}$, resulting in low p_t.

4.5.4 The invariant mass of the di-muon system

The invariant observable which is often used to describe the decay chains is the invariant mass squared of the di-muon system $m_{\mu\mu}^2$ [137, 138]:

$$m_{\mu\mu}^2 = (E_{\mu,1} + E_{\mu,2})^2 - (\vec{p}_{\mu,1} + \vec{p}_{\mu,2})^2 \tag{4.14}$$

The distribution of the invariant mass of the di-muon system is shown in Fig. 4.7.

$e^+e^- \to \chi_1^0\chi_2^0 \to \chi_1^0\mu\tilde{\mu}_R \to \chi_1^0\chi_1^0\mu\mu$

The observable $m_{\mu\mu}^2$ is Lorentz-invariant. It can be calculated in the centre of mass frame and its value will be the same also in the experiment frame. From the equation 4.14 and neglecting the mass of the muon, it follows that:

$$\begin{aligned} m_{\mu\mu}^2 &= (E_{\mu,1} + E_{\mu,2})^2 - c\,(p_{\mu,1} + p_{\mu,2})^2 \\ &= E_{\mu,1} \cdot E_{\mu,2} - |p\mu, 1|\,|p\mu, 2|\,cos\,(\theta_{1,2}) \end{aligned} \tag{4.15}$$

The distribution of $m_{\mu,\mu}^2$ is featured by a maximum. In the centre of mass frame of the χ_2^0 the two muons are acollinear and μ_2 has the maximum possible energy ($E_{\mu,2}^{+;*}$ in equation 4.6). The maximum value of μ_2 is hence:

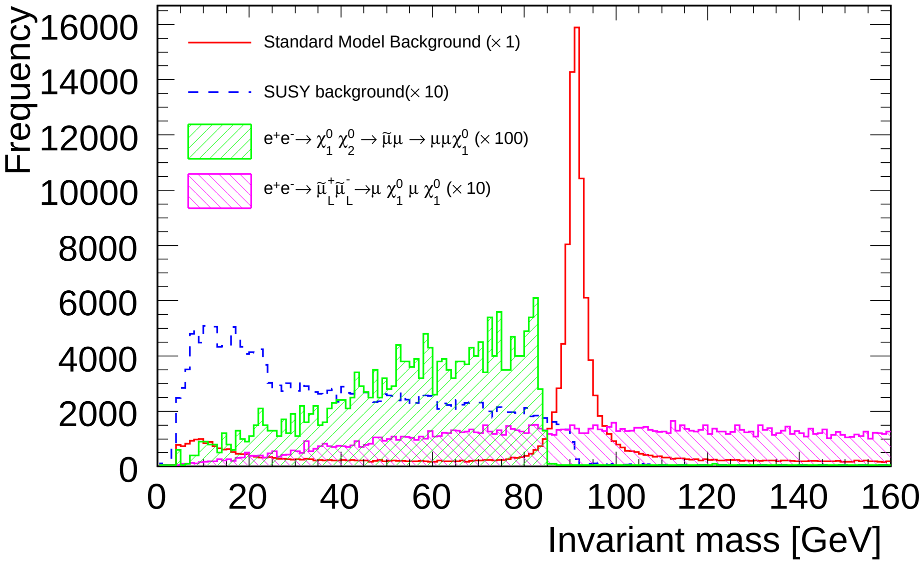

Figure 4.7: Invariant mass of the di-muon system in the final state for the background (SM+SUSY) and for the signal processes. The distributions are rescaled with the factors defined in the legend.

$$\begin{aligned} m_{\mu\mu}^2(max) &= E_{\mu,1}^{*} E_{\mu,2}^{+*} + p_{\mu,1}^{*} p_{\mu,2}^{*} \\ &= 4 \cdot E_{\mu,1}^{*} E_{\mu,2}^{+*} \\ &= m_{\chi_2^0}^2 \left(1 - \frac{m_{\tilde{\mu}}^2}{m_{\chi_2^0}^2}\right) \cdot \left(1 - \frac{m_{\tilde{\chi}_1^0}^2}{m_{\tilde{\mu}}^2}\right) \end{aligned} \tag{4.16}$$

The kinematic maximum of the distribution of the invariant mass of the di-muon system generated from the χ_2^0 decay is 83.9 GeV in the SPS1a$'$ point.

SUSY background

The SUSY background extends widely from the low $m_{\mu\mu}$ regions of the spectrum up to the very high regions. The background channels which involve the production of a χ_2^0 and missing energy are also featured by a maximum in the same range than the $\chi_1^0\chi_2^0$ process.

SM background

The standard model background is mainly featured by three well defined peaks. First the invariant mass of di-muons coming from γ peaks at 0. $Z\gamma$, $\gamma\gamma$ background have this property. Second the invariant mass of di-muons from Z^0 peaks at the Z pole (98 GeV). γZ^0, $Z^0 Z^0$, radiative return to the Z^0 events are in this class. Moreover, the $e^+e^- \rightarrow \mu\mu$ process generates muons with the full centre of mass energy (500 GeV).

W^+W^- pair production, W fusion and processes with τs and νs in the final state are featured by a continuous distribution of the invariant mass.

4.5.5 the $\vec{\beta}$ of the centre of mass of the di-muon system.

The $\vec{\beta}$ of the centre of mass frame of the di-muon system is expressed by the following equation:

$$\vec{\beta^\circ} = \frac{(\vec{p}_{\mu,1} + \vec{p}_{\mu,2})}{E_{\mu,1} + E_{\mu,2}} \tag{4.17}$$

It describes the Lorentz transformation from the laboratory frame to the centre of mass of the di-muon system. The module and polar direction of $\vec{\beta}$ ($|\vec{\beta}|$ and θ_β) are introduced in this analysis as kinematic observables. The first is used for the description of the $\chi_0^1\chi_2^2$ and the second is mainly used to characterize and reject the Standard Model background.

Signal processes

The module of $\vec{\beta}$ is used to describe the kinematic of the $\chi_0^1\chi_2^2$ process near the maximum of the invariant mass distribution. As it was shown in equation 4.16 the two muons are collinear at the edge of the invariant mass distribution. However the creation of a massive intermediate $\tilde{\mu}_R$ in the decay chain causes a slight asymmetry between the momentum of the two muons in the centre of mass system of the χ_2^0. The centre of mass frame of the di-muon system is the nearest frame to this configuration, although the two muons have the same momentum. The kinematic description of the centre of mass system of the di-muon system depends on the considered SUSY scenario. In the LHC Point 3 ($m_0 = 200$ GeV, $m_{1/2} = 100$ GeV and $tan\beta = 2$) the χ_2^0 undergoes more likely a three body decay via a virtual Z^0 decaying off-shell. In this case the system of the centre of mass of the di-muons corresponds to the centre of mass of the χ_2^0. This kinematic property is used in the χ_2^0 analysis at LHC for the complete reconstruction of the kinematics of the events [122, 139].

However, the speed of the centre of mass of the di-muon system is a good discriminator between the $\chi_1^0\chi_2^0$ signal process and the $\tilde{\mu_L}\tilde{\mu_L}$ pair production. In Fig. 4.8 it can be observed that $|\vec{\beta}|$ is always higher than 0.5 in the first process, while the second process allows kinematically also lower values. The acollinearity and acoplanarity distributions showed that the final state of the $\tilde{\mu_L}\tilde{\mu_L}$ pair production and the $\chi_1^0\chi_2^0$ pair production are kinematically very similar. The $|\vec{\beta}|$ is hence a very powerful variable to enhance the kinematic discrimination between the two processes.

Backgrounds

The polar direction of $|\vec{\beta}|$ is the direction of the total momentum of the di-muons in the laboratory frame rescaled to the total visible energy. In the Standard Model background

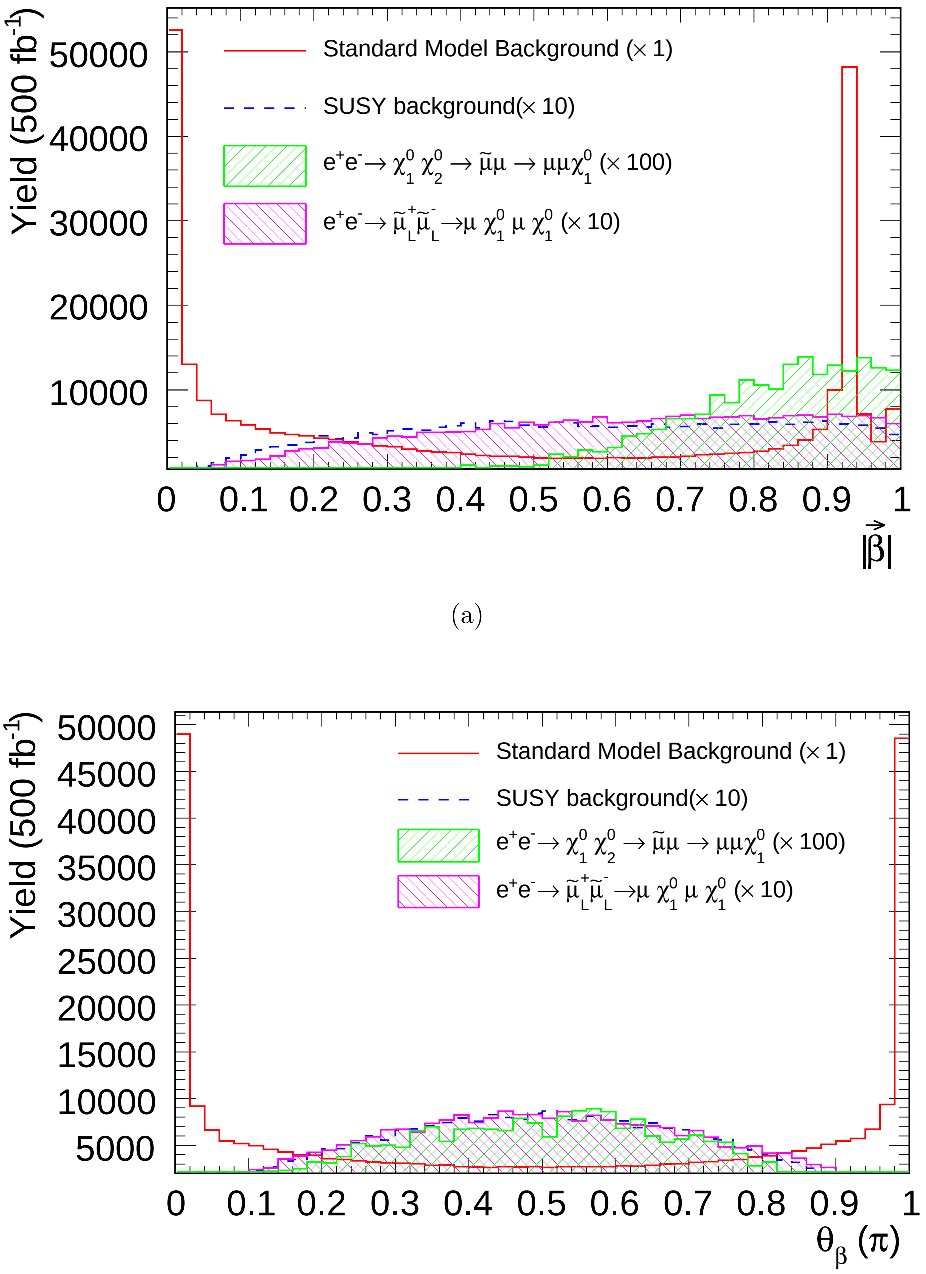

(a)

(b)

Figure 4.8: $\vec{\beta}$ of the Lorentz transformation to the centre of mass of the di-muon system. In (a) the distribution of $|\vec{\beta}|$ and in (b) the distribution of the polar angle of $\vec{\beta}$ are shown.

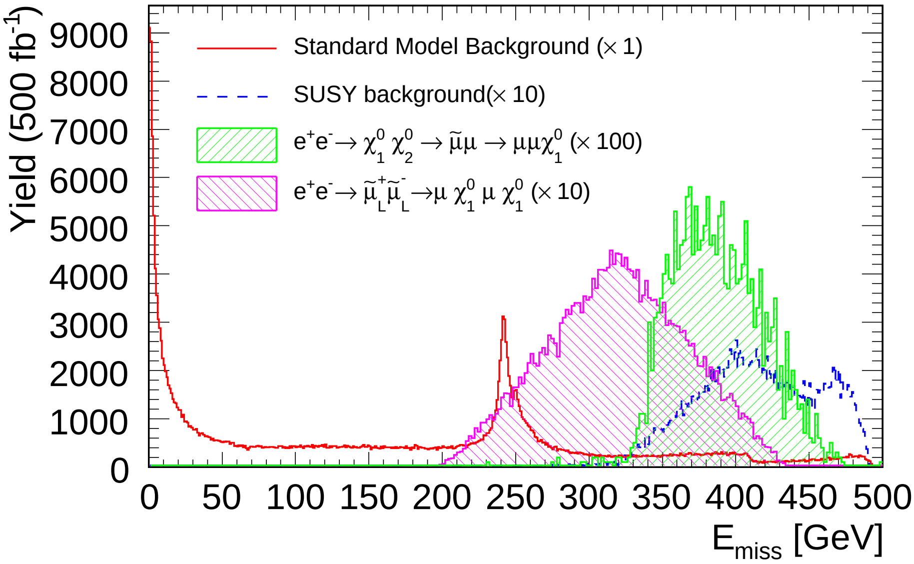

Figure 4.9: Total missing energy for the signal processes and the background (SM+SUSY). The distributions are rescaled according to the factors shown in the legend.

the di-muon system is mainly forward and backward-peaked while the SUSY processes are localized more in the barrel. All the processes with strong ISR and with radiative return to the Z are featured by a forward or backward peaked total momentum.

4.5.6 Total Missing Energy

The missing energy is the typical signature of the SUSY processes, due to the production of several χ_1^0 in the final state. The signal processes are featured of a high missing energy, due to the production of χ_1^0s.

Also the SUSY background is featured by high missing energy, associate to χ_1^0s and νs.

The only contribution to the missing energy in the SM background consists of the $\nu_{e,\mu,\tau}$. The missing energy associated to this process is in general lower than in the SUSY channels. However the missing energy signature is often faked by the radiative return to the Z peak. In this case an energetic photon is produced and propagates along the beam line escaping undetected. The typical energy transferred to this photon is of 200-250 GeV for a Linear Collider with a centre of mass energy of 500 GeV.

4.6 Methods and Results of the Analysis of the χ_1^0

4.6.1 Selection cuts

The combination of cuts used to select the $\tilde{\mu}_L$ pair candidates is optimized in order to not bias the position and the shape of the low and high edges of the energy distribution of the muons in the final state. As the physics at the kinematic limit depends strongly on the acollinearity and on the acoplanarity, the angular variables are not used for the selection. The applied cuts are:

1. $200 < E_{miss} < 430$ GeV. This cut selects the missing energy region of the signal (Fig. 4.9).
2. The events with $80 < m_{\mu,\mu} < 100$ GeV are rejected, in order to exclude the contribution of the di-muon generated from a Z^0 boson (Fig. 4.7).
3. $m_{\mu,\mu} > 30$ GeV, in order to reject the muon pairs originated from a γ.
4. $0.1\pi < \theta_\beta < 0.9\pi$ in order to reject the forward and backward-peaked SM background (Fig. 4.8b).

Just for illustration purpose, two cases are studied. In the first all the events are included, with the full beamstrahlung effect. It is the realistic reference case. In the second only the events with a total energy of the centre of mass ranging between 499 GeV and 500 GeV are considered, in order to study the effect of the beamstrahlung on the result.

In the realistic case the selected events for signal n_s and background n_b are $n_s = 16300$ and $n_b = 18000$. In the second case $n_s = 10900$ and $n_b = 10400$. The contribution of each background channel is shown in table 4.5.

4.6.2 The measurement of the mass of the χ_1^0

Methods

The measurement of the χ_1^0 consists of the identification and measurement of the upper and lower edge of the distribution of the energy of the muons in the final state. From the equations, it follows that:

$$\begin{aligned} m^2_{\tilde{\mu}_L} &= E_s^2 \frac{E_\mu^+ \cdot E_\mu^-}{\left(E_\mu^+ + E_\mu^-\right)^2} \\ m^2_{\chi_1^0} &= m^2_{\tilde{\mu}_L}\left(1 - \frac{2\left(E_\mu^+ + E_\mu^-\right)}{E_s}\right) \end{aligned} \tag{4.18}$$

The distribution of the energy of the μ^+ in the laboratory frame after the event selection is shown in Fig. 4.10. The lower E_μ^- and upper E_μ^+ edges of the distribution are visible. They are fitted with the function:

$$\begin{aligned} f(E|E^+, A, B, S) &= B + \frac{A}{1+e^{-\frac{E-E^+}{S}}} \\ f(E|E^-, A, B, S) &= B + \frac{A}{1+e^{\frac{E-E^+}{S}}} \end{aligned} \tag{4.19}$$

The parameters of the fit are:

Final State	**With Full Beamstrahlung**	**$499 < E_s < 500$**
$\mu\mu\chi_1^0\chi_1^0$	8250	5200
$\mu\mu\nu_e\nu_e\chi_1^0\chi_1^0$	40	20
$\mu\mu\nu_\mu\nu_\mu\chi_1 0\chi_1^0$	450	300
$\mu\mu\nu_\tau\nu_\tau\chi_1^0\chi_1^0$	450	300
$\mu^\pm\mu^\mp\nu_\mu\nu_\tau\nu_\mu\nu_\tau\chi_1^0\chi_1^0$	1200	800
$\mu^\pm\mu^\mp\nu_\mu\nu_\tau\nu_\mu\nu_\tau\nu_\mu\nu_\mu\chi_1^0\chi_1^0$	10	10
$\mu^\pm\mu^\mp\nu_\mu\nu_\tau\nu_\mu\nu_\tau\nu_\tau\nu_\tau\chi_1^0\chi_1^0$	20	10
$\mu^\pm\mu^\mp\nu_\mu\nu_\tau\nu_\mu\nu_\tau\nu_e\nu_e\chi_1^0\chi_1^0$	100	70
$\mu^\pm\mu^\mp\nu_\mu\nu_\tau\nu_\mu\nu_\tau\nu_\mu\nu_\tau\chi_1^0\chi_1^0$	20	10
$\mu\mu$	650	420
$\mu\mu\nu_\mu\nu_\mu$	10000	5200
$\mu\mu\nu_e\nu_e$	1550	900
$\mu\mu\nu_\mu\nu_\tau\nu_\mu\nu_\tau$	0	0
$\mu\mu\nu_\mu\nu_\tau\nu_\mu\nu_\tau\nu_e\nu_e$	90	50
$\mu\mu\nu_\mu\nu_\tau\nu_\mu\nu_\tau\nu_\tau\nu_\tau$	10	5
$\mu\mu\nu_\tau\nu_\tau\nu_\mu\nu_\mu\nu_\mu\nu_\mu$	700	400
$\mu\mu\nu_\tau\nu_\tau$	250	150

Table 4.5: Background selected events in the $\tilde{\mu}_L$ pair production process. The first column refers to the realistic simulation with the full beamstrahlung included. The second column refer to a sub-sample where only the events with the total centre of mass energy ranging between 499 GeV and 500 GeV are used, in order to show the effects of the Beamstrahlung.

.

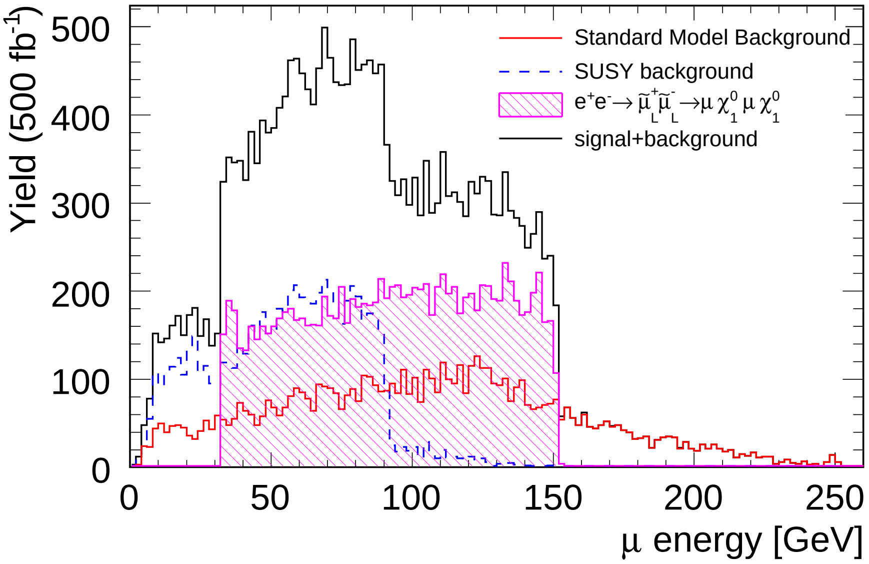

Figure 4.10: Distribution of the momentum of the μ^+ in the laboratory frame after the selection of the $\tilde{mu}_L\tilde{mu}_L$ pair candidates. The total observed signal and the backgrounds (SUSY and SM) are reported. The mass of the χ_1^0 is measured from the kinematic edges of the distribution of the momentum of the di-muons.

1. The constant background level ($B^\pm$)
2. The position of the kinematic edge $E^\pm$
3. The amplitude of the step function ($A^\pm$)
4. The slope of the step function ($S^\pm$)

The lower edge is fitted in the region (30 GeV, 45 GeV) and the upper edge in the region (145 GeV, 156 GeV). The underlying background can be approximated with a constant in these regions of the spectrum. The fit is shown in Fig. 4.11.

The statistical uncertainty of the edge position is assumed as the statistical uncertainty of the parameter $E^\pm$. Moreover, the systematic uncertainty of the parameterization of the smearing of the fitted edge is quoted as one half of the FWHM of the derivative of the fitted function in the edge region. The final uncertainty is hence the squared sum of the two statistics and systematic uncertainties contributions.

The beamstrahlung and the initial and final state radiation are responsible of a deterioration of the edge profile of the momentum distribution. The kinematic edge extracted with the fit is hence affected by a small bias. The systematic error is estimated changing the mass of the $\tilde{\mu}_L$. The positions of the kinematic edges of the energy distribution of the muons are measured and are compared with their expected value according to equation 4.4. The study of the systematic bias on the determination of the lower edge is performed setting the mass of the $\tilde{\mu}_L$ to 189.86 GeV (nominal), 190.86 GeV, 191.86 GeV and 192.86 GeV; the study of the systematic bias on the determination of the higher kinematic edge is performed setting the mass of the $\tilde{\mu}_L$ to 169.86 GeV

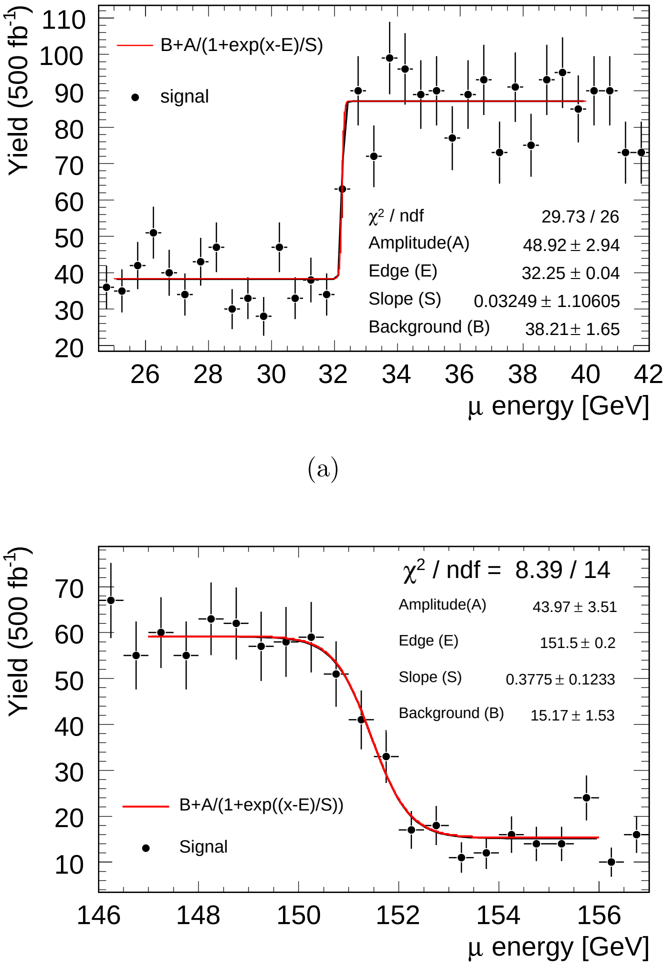

(a)

(b)

Figure 4.11: Fit to the lower and upper kinematic edge of the di-muon distribution. The fitting function and the parameters are expressed in equation 4.19

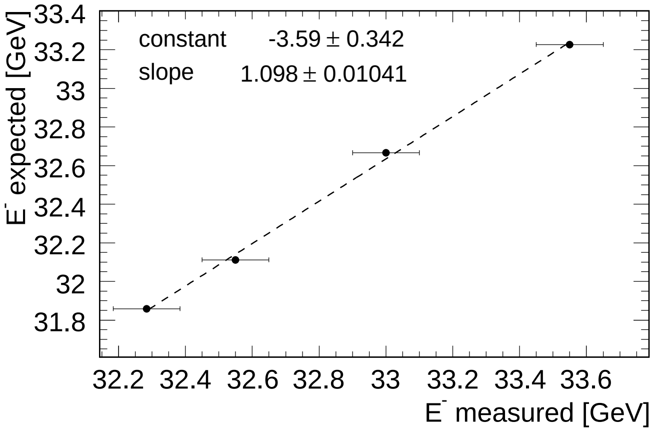

(a)

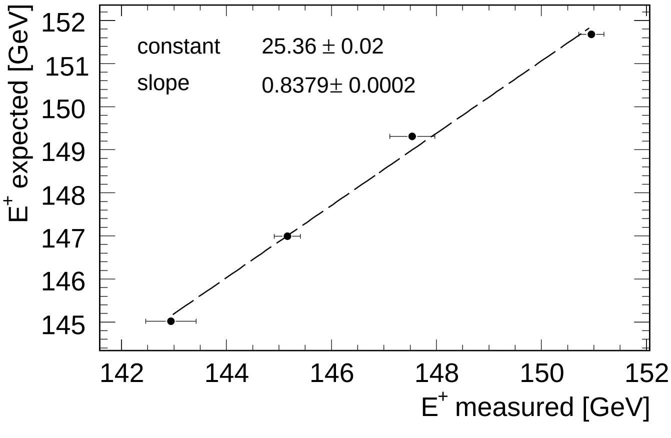

(b)

Figure 4.12: Linear correlation between the fitted and expected kinematic edge position for E^- (a) and E^+ (b). A linear transformation can be applied for the determination of the exact edges reducing the bias of the calculation.

Parameter	**Fitted value**
$\boldsymbol{A^+}$	70.32 ± 6
$\boldsymbol{E^+}$	150.95 ± 0.24
$\boldsymbol{S^+}$	0.67 ± 0.19
$\boldsymbol{B^+}$	33.45 ± 2.10
$\boldsymbol{A^-}$	71.07 ± 4.12
$\boldsymbol{E^-}$	32.55 ± 0.14
$\boldsymbol{S^-}$	0.22 ± 0.01
$\boldsymbol{B^-}$	69.27 ± 2.28
$m_{\chi_1^0}$ (Th. 97.71 GeV)	97.55 ± 1.07 GeV
$m_{\tilde{\mu}_L}$ (Th. 189.86 GeV)	189.87 ± 0.39 GeV

Table 4.6: Results of the fit of the distribution of the di-muon energy spectra. The calibration of the fit method is applied for the determination of the mass of the χ_1^0 and of the $\tilde{\mu}_L$

(nominal), 173.86 GeV, 179.86 GeV and 189.86 GeV. The correlation between fitted and expected position of the edges is reported in Fig 4.12 for E^- (a) and E^+ (b). A linear transformation to the result of the fit needs to be applied in order to correct the systematic bias introduced by this method. The calibrated position of the upper edge E_c^+ is defined as:

$$E_c^+ = (0.8379 \pm 0.0002) \cdot E^+(\text{GeV}) + (25.36 \pm 0.02) \quad \text{GeV} \tag{4.20}$$

and the calibrated position of the lower edge E_c^- is defined as:

$$E_c^- = (1.098 \pm 0.010) \cdot E^-(\text{GeV}) - (3.59 \pm 0.34) \quad \text{GeV} \tag{4.21}$$

These transformations are applied to the results of the fit presented in the following discussion.

Results

The result of the fit is shown in table 4.6. The mass of the χ_1^0 is estimated as 97.55 ± 1.07 GeV and the mass of the $\tilde{\mu}_L$ as 189.87 ± 0.39 GeV. The values are in agreement with the nominal values used in the Monte Carlo.

The precision of the determination of the centre of mass energy (ΔE_s) and the precision of the measurement of the momentum of the two muons in the final state ($\Delta E^{\pm}$) are the main contribution to the uncertainty of the measurement of the mass of the χ_1^0 and of the $\tilde{\mu}_L$.

As already discussed in section 3.1.2 the beamstrahlung is by far the most significant contribution to the degradation of the centre of mass energy. The expected spectrum of the centre of mass energy for a e^+e^- Linear Collider designed for 500 GeV centre of mass energy was shown in Fig. 3.3.

The precision of the determination of the energy of the muons in the final state is affected by the precision of the measurement of the momentum in the tracker and by the photons radiated via Final State Radiation. The tracking system at ILC is able to measure the momentum of charged particle with a relative precision $\delta p/p \sim 10^{-5}$. Consequently the precision of the measurement of the photons in the 100 GeV range is about 0.1%. However, the emission of a real photon through the final state radiation mechanism affects more the muons with momentum higher than 100 GeV. Hence the lower kinematic edge of the energy distribution is less affected than the upper kinematic edge.

ΔE_s is by far the leading contribution to the uncertainty of the determination of the mass of the χ_1^0. It is expressed by the propagation of errors:

$$\begin{aligned}&\Delta m_{\chi_1^0}(\Delta E_s) = \\ &= \left(2 \cdot E_s \cdot \left(\tfrac{E_\mu^+ E_\mu^-}{(E^+ + E^-)^2}\right)\right) \cdot \left(1 - 2 \cdot \tfrac{(E^+ + E^-)}{E_s} + 2 \cdot E_s \cdot \left(\tfrac{E^+ E^-}{(E^+ + E^-)^2}\right)\right) \Delta E_s\end{aligned} \tag{4.22}$$

The variance ΔE_s is calculated directly from the spectrum in Fig. 3.3, considering the region with 99% of the total signal; the resulting ΔE_s is calculated as:

$$\Delta E_s \approx \frac{\delta_{BS}}{6} \tag{4.23}$$

where δ_{BS} is the average RMS beamsstrahlung energy loss defined in chapter 3. From equation 4.22 the expected relative statistical uncertainty depends on δ_{BS} as:

$$\Delta m_{\chi_1^0}/m_{\chi_1^0} \approx 0.078\delta_{BS} \tag{4.24}$$

The effect of the beamstrahlung to the precision of the determination of the mass of the χ_1^0 is shown in Fig. 4.13. The expected dependence in equation 4.22 is shown as a not-continuous line. The result of the analysis presented in this thesis, with the nominal beamstrahlung effect ($\Delta E_s \approx 2$ GeV), is shown as a black triangle; it agrees with the expectation. As illustration the same analysis is performed using the sub-sample with total energy of the centre of mass between 499 GeV and 500 GeV ($\Delta E_s \approx 1$ GeV, white triangle). The expected resolution in the *Low N*, *Low P*, *Large Y* options is also shown[5]. As expected, while the LowN and highY configurations provide a results very close to the nominal one, the large beamstrahlung in the lowP configuration deteriorates significantly the resolution of the measurement of the mass of the χ_1^0.

---

[5] The *Low N*, *Low P*, *Large Y* options are possible beam configurations which guarantee the goal peak luminosity of 2×10^{34} cm^{-2}cm^{-1}. They are presented in section 3.1.2.

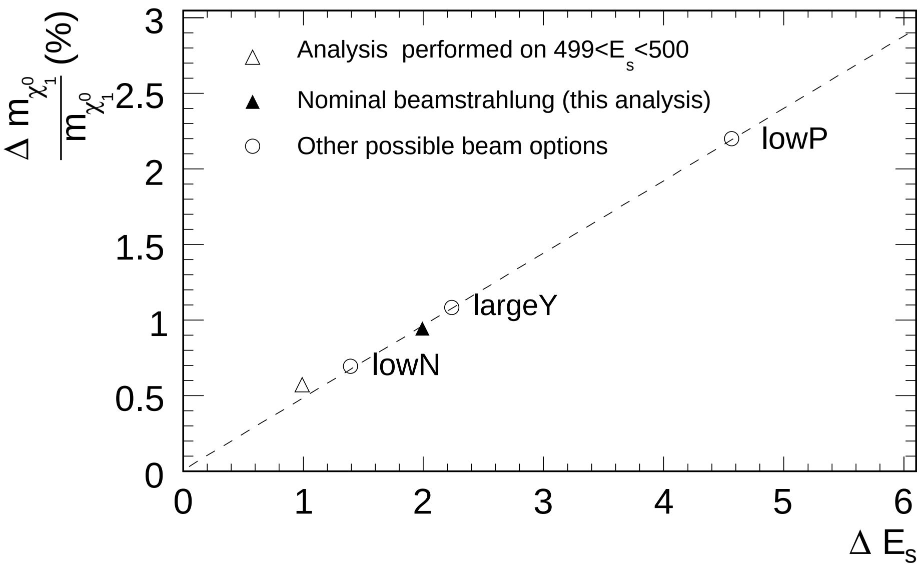

Figure 4.13: Effect of the beamstrahlung on the relative uncertainty of the measurement of the mass of the χ_1^0. The discontinuous line is the theoretical expectation calculated with the propagation of errors. The black triangle is the result of the full simulation, with the full bremstrahlung included. The white triangle is the result of the analysis of the events with the total energy of the centre of mass ranging between 499 GeV and 500 GeV. The empty dots correspond to the other possible beam options at ILC.

4.6.3 Estimation of $\sigma(e^+e^- \rightarrow \tilde{\mu}_L\tilde{\mu}_L) \times (BR(\tilde{\mu}_L \rightarrow \mu\chi_1^0))^2$

Method

After the determination of the kinematic edges of the distribution and after the measurement of the mass of the χ_1^0 and of the $\tilde{\mu}_L$ the analysis of the area underling the kinematic allowed region between E^+ and E^- is analysed.

The discrimination between the signal candidate ad the total SM and SUSY background is performed by considering the likelihood that an event is consistent with being either signal or background. A set of N parameters $(x_1 \dots x_N)$ which represent a good description of the event is found. The probability distribution of each parameter differs for the signal $(P_S(x_i))$ and the background $(P_B(x_i))$. The likelihood of an event being consistent with the signal (L_S) or the background (L_B) is defined as:

$$L_S = \prod_{i=1}^{N} P_S(x_i)$$
$$L_B = \prod_{i=1}^{N} P_B(x_i) \quad (4.25)$$

The discriminating quantity is the relative likelihood L_R:

$$L_R = \frac{L_S}{L_S + L_B} \tag{4.26}$$

The quantity L_R ranges from 0 to 1. Events with low L_R are background-like and events with high L_R are signal-like.

The x_i variables have to be a reasonable combination of the observables in the final state. The likelihood variables x_i used in this analysis are:

1. The total transverse momentum of each muon;
2. The acollinearity of the event;

The cross section times branching ratio squared at 68 % confidence level, σ_s is calculated using the extended maximum likelihood technique. The aim of this method is to form a likelihood variable $L(\sigma_s)$, based on the probability distribution of L_S and L_B. $L(\sigma_s)$ has to be sensitive to the presence in the data sample of signal events and background events. The signal is modelled with L_S and has to be consistent with the cross section σ_s. The background is modelled with L_B and has to be consistent with the known cross section σ_B.

The expected number of observed events ν is the sum of the expected number of background events (μ_B) and signal events:

$$\nu = \mu_B + \mathcal{L}\omega\sigma_s \tag{4.27}$$

where $\mathcal{L}$ is the luminosity of the experiment.

The signal hypothesis and the background hypothesis are described by the likelihood ratio function L_R. The distribution of the likelihood ratio function for the signal is expressed as $S(L_R)$ and the distribution of the likelihood ratio for the background is expressed as $B(L_R)$. Both $B(L_R)$ and $S(L_R)$ are normalized to 1.

In the hypothesis of the events being either signal like (S) or background like (B) in the expected proportion, the probability that a event is observed having L_R is:

$$P\left(L_{R;B,S}\right) = \mu_B \cdot B(L_R) + \mathcal{L}\omega\sigma_s \cdot B(L_S) \tag{4.28}$$

Moreover, the probability of having N observations when ν are expected follows a poissonian distribution:

$$P\left(N|\nu\right) = \frac{e^{-\nu}\nu^N}{N!} \tag{4.29}$$

The extended likelihood technique consists of the combination of the poissonian distribution of the number of observation and their likelihood ratio probability. The extended likelihood which describes N observations, when ν are expected is:

$$L(\sigma_s) = \frac{e^{-\nu}\nu^N}{N!} \prod_{i=1}^{N} \left(\mu_B \cdot B(L_R) + \mathcal{L}\omega\sigma_s \cdot B(L_S)\right) \tag{4.30}$$

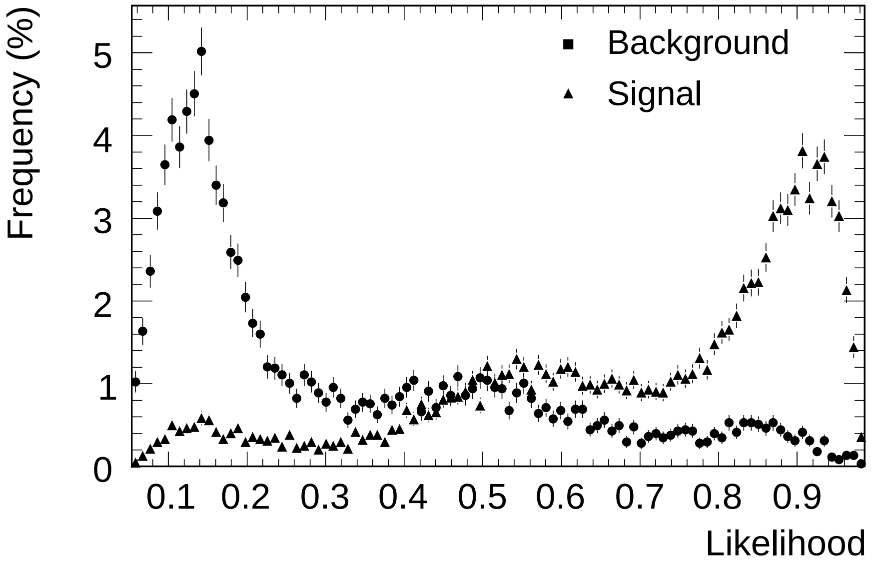

Figure 4.14: Likelihood distribution for the process $e^+e^- \rightarrow \tilde{\mu}_L\tilde{\mu}_L \rightarrow \mu\mu\chi_1^0\chi_1^0$ (triangles) and the full background (dots). The event selection described in section 4.6.1 is first applied. The likelihood function is then build using the total transverse momentum and the acollinearity of the muons in the final state.

The quantity which is always used is $log(L)$ which is:

$$\begin{aligned} log(L(\sigma_s)) = \; & -\nu + \sum_{i=1}^{N} log\left(\mu_B \cdot B(L_R) + \mathcal{L}\omega\sigma_s \cdot B(L_S)\right) \\ & = -\left(\mu_B + \mathcal{L}\omega\sigma_s\right) + \sum_{i=1}^{N} log\left(\mu_B \cdot B(L_R) + \mathcal{L}\omega\sigma_s \cdot B(L_S)\right) \end{aligned} \qquad (4.31)$$

The estimated $\overline{\sigma_s}$ is the value at which the extended likelihood function has a maximum. The 68% confidence belt around $\overline{\sigma_s}$ is calculated using a two tails hypothesis test. The extremes of the confidence belt $\sigma_{s,min}$ and $\sigma_{s,max}$ are defined from the probability distribution of the extended likelihood as:

$$\begin{aligned} 0.16 &= \int_{-\infty}^{\sigma_{s,min}} L(\sigma_s) d\sigma_s \\ 0.16 &= \int_{\sigma_{s,max}}^{+\infty} L(\sigma_s) d\sigma_s \end{aligned} \qquad (4.32)$$

In practice, the 68% belt is defined as that value at which the $Log(L(\sigma_s))$ function decrease of 0.5 from its maximum.

Results

The likelihood function for the signal and the background is shown in Fig. 4.14. The likelihood has a good separation power between signal and background. The dependence

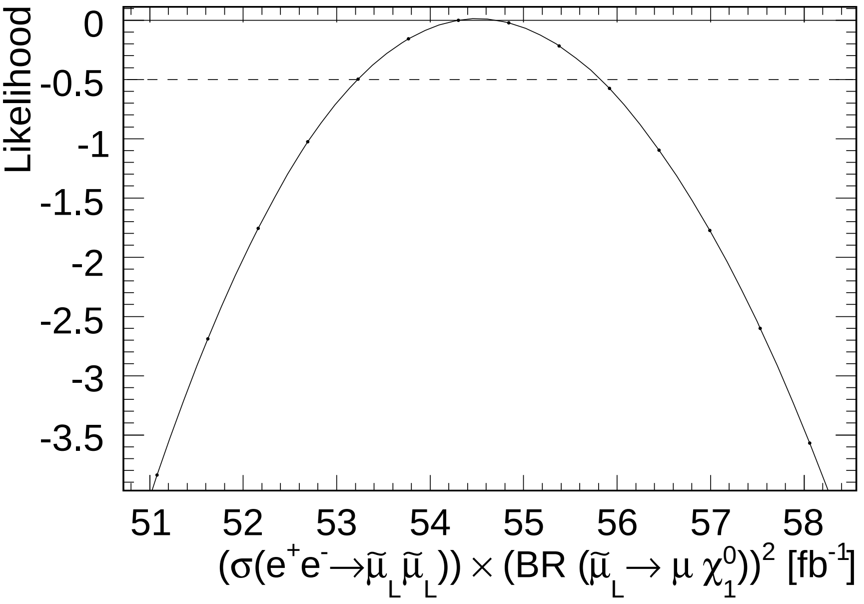

Figure 4.15: Dependence of the extended likelihood on the estimated cross section of the process $e^+e^- \rightarrow \tilde{\mu}_L\tilde{\mu}_L \rightarrow \mu\chi_1^0\mu\chi_1^0$. The 68% C.L. bound (discontinuous line) is defined by the values at which the likelihood is equal to -0.5.

of the extended likelihood on the estimated σ is shown in figure 4.15. The cross section of the process can be determined as 54.58 ± 1.35 fb, in agreement with the input of the Monte Carlo.

The sensitivity of the measurement is very high. The total number of signal and background events is respectively 16300 and 18000, leading to an evidence of the signal largely above 5σ.

4.7 Methods and Results of the Analysis of the χ_2^0

4.7.1 Event Selection

The event selection strategy of the

The following cuts are applied for the selection of the sample:

1. $0.2 < \theta_\beta < 0.8$. This cut rejects the forward and backward-peaked SM background
2. $|\beta| > 0.6$ (Fig. 4.8)
3. $355 < E_{miss} < 395$ GeV for the selection of the high missing energy range (Fig. 4.9)
4. $p_t > 40\ GeV/c$ for the selection of the high p_t range (Fig. 4.6)
5. $E_s > 40$ GeV. This cut rejects the di-muon events coming from a γ (SM) and rejects many SUSY background. In particular the background channels with τ in the final state are strongly suppressed.

Final State	**$40 < m_{\mu\mu} < 85$ GeV**
$\mu\mu\chi_1^0\chi_1^0$ from $\tilde{\mu}_L$	1500
$\mu\mu\chi_1^0\chi_1^0$ from $\tilde{\mu}_R$	400
$\mu\mu\nu_e\nu_e\chi_1^0\chi_1^0$	20
$\mu\mu\nu_\mu\nu_\mu\chi_1 0\chi_1^0$	200
$\mu\mu\nu_\tau\nu_\tau\chi_1^0\chi_1^0$	250
$\mu\mu\nu_\mu\nu_\mu$	280
$\mu\mu\nu_e\nu_e$	230

Table 4.7: Background of the analysis of the $\chi_2^0 \rightarrow \tilde{\mu}_R\mu$ after the selection cuts. In the left column the full spectrum is considered. In the right column it is used only the region of the invariant mass spectrum where the signal is present, before the kinematic upper limit of the distribution.

.

Although no cut is applied to the high kinematic edge of the $m_{\mu\mu}$ distribution, the total number of signal and background events is calculated in the significant range 40 GeV–85 GeV where the signal is expected. The total number of signal events n_s is 720, with a total number of background events n_b of 2950. The relevance of each background channel is reported in table 4.7. The channels which are not included in table 4.7 are suppressed by the cuts. The invariant mass spectrum of the di-muons after selection is shown in Fig. 4.16.

4.7.2 The Measurement of the Mass of the χ_2^0

Methods

The equation 4.16 relates the mass of the χ_2^0 with an invariant observable. In fact $m_{\chi_2^0}$ can be expressed as :

$$m_{\chi_2^0}\left(m_{\mu\mu}^2\right) = \sqrt{\frac{m_{\mu\mu}^2\,(max) + m_{\tilde{\mu}_R}^2 \cdot \left(1 - \frac{m_{\chi_1^0}^2}{m_{\tilde{\mu}_R}^2}\right)}{\left(1 - \frac{m_{\chi_1^0}^2}{m_{\tilde{\mu}_R}^2}\right)}} \tag{4.33}$$

The measurement of the χ_2^0 mass consists of the identification and measurement of the kinematical edge of the di-muon invariant mass. The masses of the $\widetilde{\mu}_R$ and of the χ_1^0 are supposed to be known from independent measurements [91]. The mass of the χ_2^0 is hence calculated using equation 4.33.

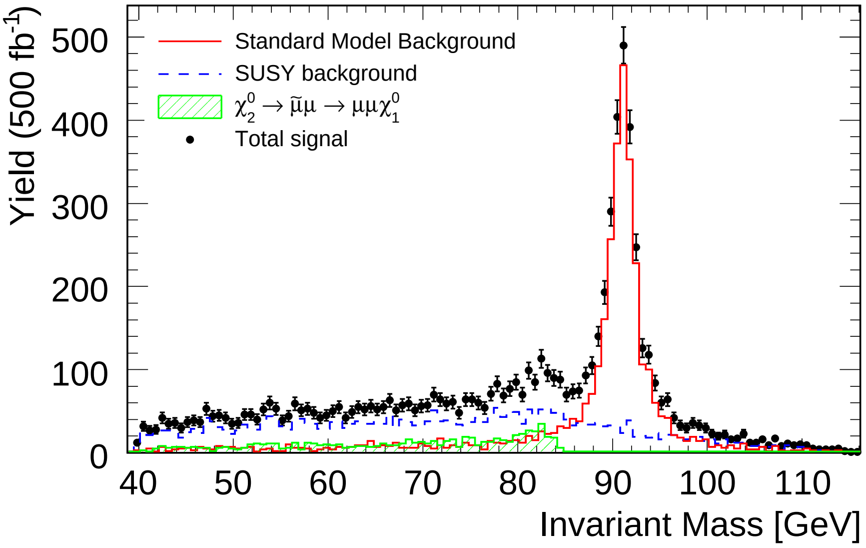

Figure 4.16: Invariant mass of the di-muon system after the event selection for the identification of $\chi_2^0\tilde{\mu}_R\mu$ candidates. The signal is expected to populate the invariant mass region below 83.9 GeV (see section 4.5.4). The kinematic edge corresponding to the χ_2^0 is visible in top of the Z^0 peak left tail.

The edge of the $m_{\mu\mu}$ invariant mass is fit with the function:

$$f(E) = \underbrace{B + e^{(BE+BS\cdot E)}}_{background} + \begin{cases} A\cdot e^{\frac{(E-E^+)^2}{W^2}} & E \geq E+ \\ \frac{A}{e^{T\cdot E+}}e^{T\cdot E} & E < E+ \end{cases} \tag{4.34}$$

The fit parameters are:

- Three parameters for the gaussian describing the right side of the kinematic edge of the signal (A,E^+ and W)
- One parameter for the exponential modelling the left tail of the signal distribution (T)
- Three parameters for the background. A constant level (B) and the constant and slope of an exponential (BE and BS).

The fit applied to the data is shown in Fig. 4.17.

The position of the edge is the value of the $m_{\mu\mu}$ corresponding to the half amplitude A of the gaussian defining the kinematic edge. The systematic uncertainty of the parameterization of the position of the edge is determined by the variance W of the gaussian.

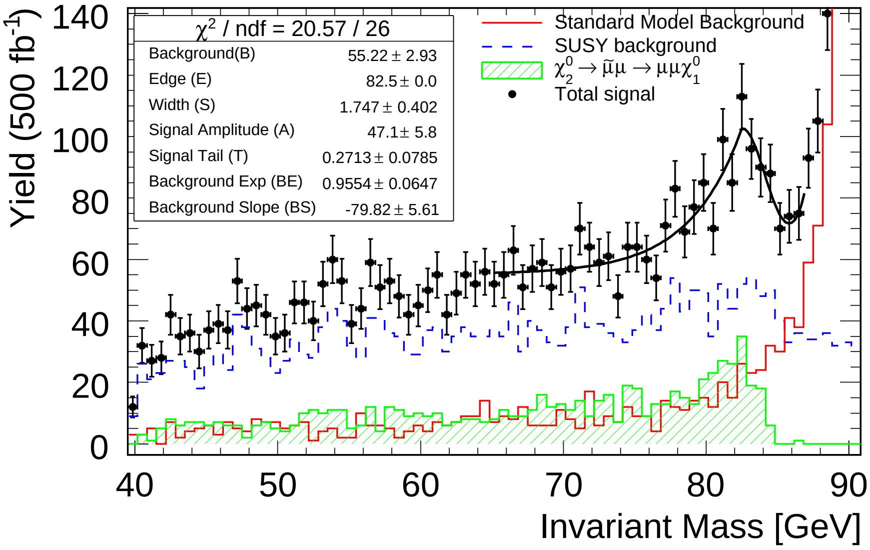

Figure 4.17: Fitted $m_{\mu\mu}$ spectrum. The kinematic edge corresponding to the $\chi_2^0 \rightarrow \tilde{\mu}_R\mu$ can be extracted form the fit on top of the left tail of the Z^0 peak.

Results

The input parameters for the determination of the mass of the χ_2^0 are the mass of the $\tilde{\mu}_R$ and the mass of the χ_1^0. It was shown [92] that the potential result of the measurement of the mass $\tilde{\mu}_R$ at the ILC is 125.3 ± 0.2 GeV. The χ_1 mass determined in the previous sections (97.55 ± 1.07 GeV) is used.

The kinematic edge in the $\sigma_{\mu\mu}$ distribution is estimated by the fit at 83.9 ± 0.9 GeV. The mass of the χ_2^0 is calculated with the formula 4.33. With a luminosity of 500 fb^{-1} the measured mass of the χ_2^0 is 183.50 ± 1.38 GeV. The nominal value of the mass of the χ_2^0 is 183.89 GeV.

The main contribution to the uncertainty on the mass measurement is the determination of the position of the edge (0.6%) and of the mass of the χ_1^0 (0.5%). As in case of the measurement of the χ_1^0 the final state radiation is the most significant effect to the shape of the kinematic edge. The excellent tracking performance allows resolving the edge position also in this not favoured case with low statistics.

4.7.3 Estimation of $\sigma(e^+e^- \rightarrow \chi_1^0\chi_2^0) \times B.R.(\chi_2^0 \rightarrow \mu\tilde{\mu}_R) \times B.R.(\tilde{\mu}_R \rightarrow \mu\chi_1^0)$

The background events which pass the selection present a very similar kinematic configuration to the signal events. The extended likelihood method is hence not effective in order to calculate the $\sigma \times BR$ of the process. As the number of events is large enough, a classical approach to the estimation of the confidence intervals is chosen.

It is assumed that the total number of expected signal (n_s) and background (n_b) events are distributed according to a Poisson distribution. The lower limit n_s^{low} and the upper limit n_s^{up} of the signal events at the 95% confidence level, given n_{obs} observed events are defined as [140]:

$$\begin{aligned} 0.025 &= \sum_{i=n_{obs}}^{+\infty} \frac{\left(n_s^{up}+n_b\right)^i}{i!} e^{-\left(n_s^{up}+n_b\right)} \\ 0.025 &= \sum_{i=0}^{n_{obs}} \frac{\left(n_s^{low}+n_b\right)^i}{i!} e^{-\left(n_{low}^{up}+n_b\right)} \end{aligned} \tag{4.35}$$

The 95% CL bound is the interval defined as $\left(\frac{n_s^{low}}{\mathcal{L}\epsilon}, \frac{n_s^{high}}{\mathcal{L}\epsilon}\right)$, where $\mathcal{L}$ is the luminosity of the experiment (500 fb^{-1}) and ϵ is the selection efficiency of the signal, estimated in the Monte Carlo ($\epsilon = 32\%$ with the applied cuts).

The estimated 95% confidence bound of the branching ratio of the process $e^+e^- \rightarrow \chi_1^0\chi_2^0 \rightarrow \chi_1^0\tilde{\mu}_R\mu$ is (3.75,5.57) fb, with a luminosity of 500 fb^{-1}.

4.7.4 Sensitivity of the discovery of the χ_2^0

The sensitivity of the measurement to the discovery of the χ_1^0 in the $\tilde{\mu}_L$ pair production at the discovery probability $\alpha(\Delta_{dis})$ is defined as [141–144]:

$$s = \frac{n_s}{\sqrt{(n_b)}} - k\left(\alpha(\Delta_{dis})\right)\sqrt{\left(1+\frac{n_s}{n_b}\right)} \tag{4.36}$$

This definition is the extension of the traditional $n_s/\sqrt{(n_b)}$ in case of a probability less than 50%. The interval (-$\alpha(\Delta_{dis})$,+$\alpha(\Delta_{dis})$) defines the region outside which the area of the gaussian distribution with parameters (μ,σ) is less than Δ_{dis}. It defines hence the probability level of the observation of the signal at a certain significance s. The discovery level of an observation is fixed at $s = 5\sigma$. In Fig. 4.18 the increase of the 5σ discovery probability in the first 4 years of operation is shown. The number of signal events will be compatible with a 5 σ observation of the χ_2^0 with a probability of 95% just after 2 years of operation.

The binned *CLb* method [145] was also used in order to calculate the sensitivity of the measurement and the same results were obtained.

Conclusion

The leitmotifs of this analysis are the physics discovery potential of the neutralino system at the international linear collider and the estimation of the impact of the experimental conditions — detector design and beam properties — on this measurement.

In the SPS1a$'$ mSUGRA SUSY scenario only the χ_1^0 and the χ_2^0 are light enough to be produced in pairs at a 500 GeV linear collider. The analysis of the neutralino system is hence restricted to the two lightest χ_i^0:

Measurement of the mass of the χ_2^0. The most important and original evidence of this study is that it is possible to individuate a clear signal from the χ_2^0 also in

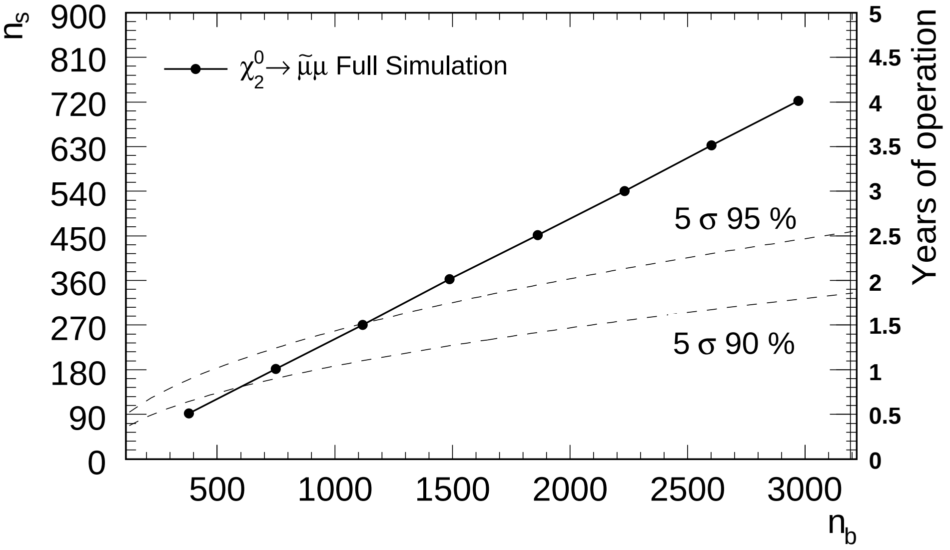

Figure 4.18: Discovery probability of the χ_2 at ILC. The thick line shows the expected number of signal (n_s) and the respective background (n_b) events at ILC in the corresponding operation time. The ILC would discover an excess of events in the χ_2^0 region just after 2 years of operation at 5 σ with a probability of 95%.

the continuum at a 500 GeV centre of mass energy. The traditionally referenced method for such measurement at ILC is in fact the scan at the $\chi_2^0\chi_2^0$ pair production threshold. In this analysis it is shown that the mass of the χ_2^0 (183.89 GeV) can be measured in the continuum with a relative statistical uncertainty of 0.75%, which is comparable with the quoted value obtained with a threshold scan.

Measurement of the mass of the χ_1^0. The kinematic edges of the energy distribution of the muons in the process $e^+e^- \to \tilde{\mu}_L\tilde{\mu}_L \to \mu\mu\chi_1^0\chi_1^0$ are individuated and fitted. The mass of the χ_1^0 (97.7 GeV) is reconstructed from the position of the edges and can be measured with a relative statistical uncertainty of 1.09% in this channel. This is not the ultimate precision reachable at ILC. Independent studies show that the mass of the χ_1^0 can be measured in the $\tilde{e}_{R,L}$ and $\tilde{\mu}_R$ pair production, using the same kinematic edges approach of this analysis. The combination of all the measurements would reduce significantly the uncertainty.

Estimation of $\sigma(e^+e^- \to \chi_1^0\chi_2^0) \times B.R.(\chi_2^0 \to \mu\tilde{\mu}_R) \times B.R.(\tilde{\mu}_R \to \mu\chi_1^0)$. The main feature of this process is that the expected signal is very small. However, due to its specific kinematics feature, it is possible to find a combination of efficient cutting variables in order to enhance the significance of the signal above the background. It is shown that the number of events would be compatible with the signal process hypothesis at 5σ with a probability of 95% after 2.5 years of operation. The cross section of this process (4.2 fb) can be restricted to the 95% C.L. bound (3.75,5.57) fb after 4 years of operation, with the expected total luminosity of 500 fb^{-1}.

An additional physics result of the analysis is the measurement of the properties of the $\tilde{\mu}_L$ sector:

Measurement of the $\tilde{\mu}_L$ mass. The kinematic edge analysis of the $e^+e^- \rightarrow \tilde{\mu}_L\tilde{\mu}_L \rightarrow \mu\mu\chi_1^0\chi_1^0$ process allows to measure also the mass of the $\tilde{\mu}_L$ (189.86 GeV) with a relative statistical uncertainty of 0.21%.

Estimation of $\sigma(e^+e^- \rightarrow \tilde{\mu}_L\tilde{\mu}_L) \times (BR(\tilde{\mu}_L \rightarrow \mu\chi_1^0))^2$. The $\tilde{\mu}_L$ pair production is not limited by the statistics. The total number of events is largely above the 5σ evidence. Using an extended likelihood approach the cross section of this process (54.32 fb) can be estimated with a relative statistical uncertainty of 2.47%.

From the point of view of the LDC/ILD detector optimization with physics simulations, the analysis of the processes with di-muon and missing energy final state touches some of the key-features presented in section 3.3:

Tracking performance. The measurement of the momentum and energy of isolated muons is the most important feature. The tracking system shows an excellent performance. In the $e^+e^- \rightarrow \tilde{\mu}_L\tilde{\mu}_L$ process, the detector does not introduce any significant smearing to the kinematic edges of the energy distribution of the muons. The precision tracking is even more important in the analysis of the $\chi_1^0\chi_2^0$ pair production. In this case it allows to isolate the small features of the invariant mass spectrum, with a consequent precise measurement of the mass of the χ_2^0.

Hermiticity. A missing energy of more than about 300 GeV is the main signature of the studied process. However, due to the relatively large mass difference between parent and daughter particles involved the decay chain, the missing momentum points mainly in the barrel. The very forward region does not affect significantly the missing energy signature.

Muon identification. Muons can be identified with a m.i.p. like track in the tracker and in the calorimeters, with a corresponding track in the muon chamber. It was shown that the detector has 95% muon detection efficiency in the muon momentum range of the signal processes. The identification of muons fails in the very forward region, because of lack of coverage in the proposed detector model.

The beam conditions play an important role in the determination of the quality of the physics results presented in this study:

Polarization. The cross section of the signal processes has a strong dependence on the polarization of the beam. In section 3.1 it was shown that while the polarization of the electron beam up to 80% is a consolidated feature of ILC, the polarization of the e^+ beam is still under investigation. This study put in evidence that the polarization of the positron beam is fundamental in order to double the cross section of the $\chi_1^0\chi_2^0$ pair production and observe with precision the kinematic edge corresponding to the χ_2^0. This means that the polarization of both beams is crucial in order to observe in the continuum small features generated by new physics mechanisms.

Beamstrahlung. An irreducible source of degeneration of the energy spectrum is the beamstrahlung. It was shown that it affects the shape of the kinematic edges of the energy distribution of the muons in the analysis of the $\tilde{\mu}_L$ pair production with a consequent degradation of the resolution of the measurement of the χ_1^0 mass. The beam options under investigation for the International Linear Collider were studied; while the *lowN* and the *highY* options would provide a relative statistical uncertainty not very different than the nominal option, the *lowP* option is expected to cause a worsening of the resolution of the mass up to a factor 2.

To conclude, it has to be remembered that the Linear Collider foresees the 1 TeV centre of mass extension. In this case also the χ_3^0 and the χ_4^0 can be accessed, providing a complete measurement of the neutralino system.

Chapter 5

The CALICE prototype of a highly granular hadronic calorimeter

"It was nothing more than a toad,
a voluble croacking toad.
He looked at Camomilla deeply in the eyes:
kiss me and I will become a Prince."
— ibidem

Introduction

The simulation study presented in the first part of this thesis focused on the exploitation of the physics potential of the International Linear Collider (ILC). In this second part of the thesis the analysis is presented of experimental data collected during the test-beam of a prototype of a highly granular hadronic calorimeter (AHCAL) for the ILD/LDC detector concept, developed by the CALICE collaboration. The detector R&D is a very important part of the research program of the ILC project and it evolves in parallel with the physics study.

The outline of the hadron calorimeter in the LDC concept was described in chapter 3. It was emphasized that the Particle Flow technique sets the most stringent requirement to the detector design. A high spatial resolution is an essential prerequisite in order to separate the single particles within the dense multi-jet environment expected at ILC.

The CALICE AHCAL is a scintillator/steel sandwich calorimeter with a fine longitudinal segmentation and a high lateral granularity. It is specifically designed to accomplish the requirements of the particle flow. The prototype has about 8000 sensitive cells in a total volume of about 1 m^3. The equipment of such detector is a big technological challenge. Each cell is read out separately by a Silicon Photomultiplier [34, 35, 121]. This new silicon photo-detector is characterized by a small size (about 1 mm^2), high gain (up to 10^6) and good quantum efficiency in the green spectral region. It is hence the ideal candidate for such compact and highly granular calorimeter.

The scope of this chapter is to describe the CALICE AHCAL prototype. The main stream of the following discussion is the interplay between the AHCAL design and the complex physics features of the hadronic interaction which the Particle Flow has to contrast. First the development of hadronic showers in the hadronic calorimeter is analysed. Then the impact is investigated of the event-by-event fluctuations on the particle flow and the consequent requirements to the hadronic calorimetry are treated. The AHCAL prototype is described, showing the main aims of the test beam conducted by the CALICE collaboration. Finally the recent developments in the technology of the Silicon Photomultiplier are shown, with emphasis on the blue sensitive Micro Pixel Photon Counter and its possible applications to Hadron Calorimetry.

5.1 The hadronic shower

The hadronic calorimeter measures the energy of hadrons through their total absorption [146, 147]. An ideal calorimeter is a block of dense material in which the particle is absorbed. This is the so-called *homogeneous calorimeter.* However, in order to allow a good measurement of the energy deposited by a hadron, most of the hadronic calorimeters are *sampling* devices. The absorber is interleaved with a sensitive layer in a regular alternating structure. Hadrons undergo strong interactions with the absorber and a corresponding signal is created in the sensitive material. The *visible* energy is defined as the pure calorimeter signal, while the *total deposited* energy is the energy released by the particle in the two sections of the detector. The energy measurement in the hadronic calorimeter consists hence of the reconstruction of the total energy from the information of the visible energy.

Hadrons deposit energy in the matter generating a typical cascade of secondary particles, the *hadronic shower.* This process consists of the succession of single hadron interactions, with the consequent generation of secondary particles. This topic is treated in three steps. First the physics of a single hadronic interaction is investigated. Second the resulting hadronic cascade is analysed using a simplified model. Third the results of the model are extended to a realistic classification and quantification of the energy content of a hadronic shower. Only **average** quantities are considered. The fundamental problem of the event-by-event **fluctuations** of the components of the hadronic shower is treated in the next section.

5.1.1 The physics of the interaction of hadrons with the matter

The nuclear scattering of hadrons (h) with the nuclei (N) of the absorber is the basic mechanism of generation of the signal in a hadronic calorimeter. The hadronic interaction can be described with the traditional methods of nuclear physics [148]:

$$h + N \to X + Y \to x_1 \dots x_n y_1 \dots y_n \tag{5.1}$$

where the intermediate products X and Y can be stable particles (n,p,π) or real resonances and the final products (x_i and y_i) are stable particles (n,p,π), nuclear remnants or nuclei. Nuclear interactions are very different from each other. They range from elastic to inelastic scattering, with increasing complexity of the possible final state.

The inelastic scattering is the mechanism responsible of the multiplication in the hadronic shower. Pions are the lightest hadrons and are more likely produced in the final state. The reaction which opens the inelastic nuclear scattering process is [1] $\pi p \rightarrow \pi\pi p$. Assuming the target proton at rest and the relativistic conservation of the 4-momentum, the threshold energy of this reaction is $E_{th} = 280$ MeV. This is considered the general threshold energy for the inelastic nuclear scattering. The inelastic scattering processes are classified in nuclear spallation and nuclear fission.

In the process of spallation a fast intranuclear cascade is followed by a slower evaporation step, which may also involve nuclear fission for heavy elements. The incoming particle makes quasifree collisions with the nucleons and triggers an intra-nuclear cascade of fast nucleons; pions and other hadrons are created in this stage and can be energetic enough to escape from the nuclear Coulomb potential wall. Other hadrons get caught and distribute their kinetic energy in the nucleus. The deexcitation of the resulting nucleus originates more neutrons and γ rays in the MeV energy range. It is observed that the main contribution to the signal of the calorimeter is due to the ionization of the spallation protons and pions emitted by the nucleus [149].

The process of nuclear fission consists of the splitting of the atomic nucleus in smaller nuclei. It is mainly due to the spallation processes and to the nuclear interaction of slow (few MeV) neutrons. Nuclear relict, α particles and mainly photons and evaporation neutrons constitute the final state and contribute to the signal of the hadronic calorimeter.

Nuclear elastic scattering (i.e. $n + p \rightarrow n + p$) is related to slow hadrons and to the *slowing down* of fast neutrons. In this process the energy of the incoming particle is mainly released to the recoil nuclear target or to low energetic recoil protons.

The scaling quantity which describes the hadronic interactions is the *nuclear interaction length* λ_{int}. It is defined as the average distance that a high energy hadron has to travel inside a medium before a nuclear interaction occurs. It depends on the density and Z of the material. In hadronic calorimeters with high Z absorbers λ_{int} is about 10 cm — i.e. Uranium, Gold. The nuclear interaction length is less than twice as long in iron and copper.

To conclude, the final state of a single hadronic interaction is very heterogeneous. Charged hadrons ($\pi^{\pm}, p, \ldots$) and neutral particles ($\pi^0, \gamma, n, \rho \ldots$) are abundantly produced. The reach variety of the products of the hadronic interaction constitutes the main difficulty of the treatment of the calorimetric measurement.

5.1.2 An example: a simple model of hadronic shower

The analysis of the development of hadronic showers in the detector is a complicated task. In general it has to be considered the full spectrum of secondary particles produced in the single hadronic interaction. Each secondary particle has to be tracked until it undergoes

---

[1] Due to the isospin symmetry, π^+,π^- and π^0 can be produced with equal probability in the final state. In the following discussion they will be indicated with π, assuming the total charge conservation.

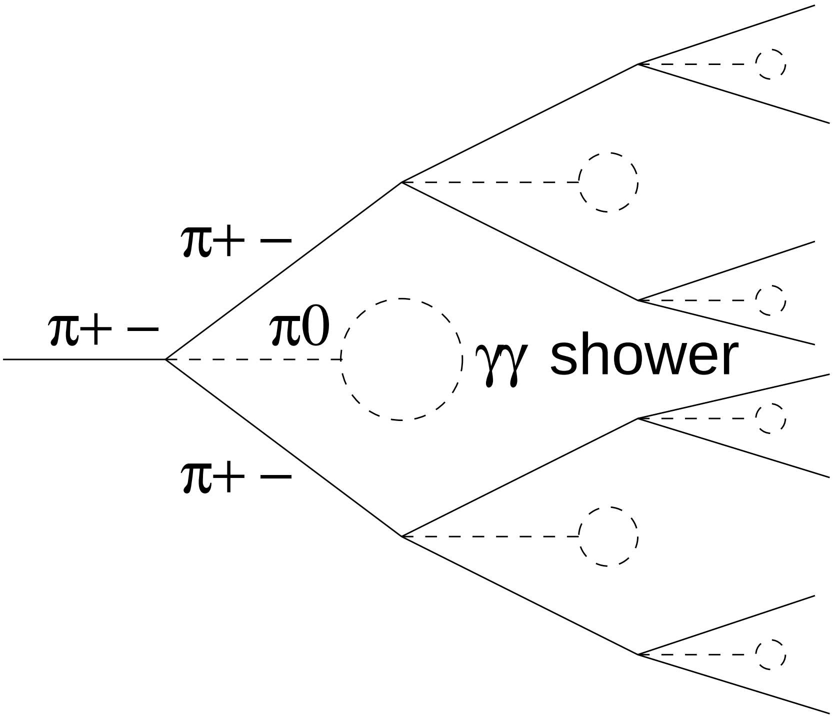

Figure 5.1: Schematic of a hadronic cascade. In this model only 3 pions (π^+,π^-,π^0) are produced at each hadronic inelastic interaction. Charged pions are indicated with the continuous line, neutral pions with the dotted line.

a further elastic or inelastic scattering. Simulation programs provide this information. However a qualitative and valid description can be done with a simplified model. The following example is freely quoted from [150]. Let's suppose that only secondary pions are produced. This hypothesis is not meaningless, being pions the lightest hadrons.

The first question to be addressed is the description of the mechanism of the development of a hadronic shower in the matter. In Fig. 5.1 the schematic of the propagation of a hadronic shower in this example is shown. It is supposed that only 3 pions ($\pi^+\pi^-\pi^0$) are produced in a hadronic inelastic interaction. Neutral and charged pions contribute differently to the development of the hadronic shower. The neutral pions decay into photons ($\pi^0 \rightarrow \gamma\gamma$). The photons are absorbed in the detector within a typical spatial scale of 1 radiation length[2] (X_0). Neutral pions are hence responsible of the irreversible conversion of the energy of the primary hadron into the calorimeter signal. Charged pions travel a mean free path λ_{int} depositing some energy via ionization. If they are energetic enough, they can undergo a further inelastic scattering and create a new generation of secondary particles. Hence charged pions are responsible of the propagation of the hadronic cascade. If a high Z materials is chosen, the radiation length is much shorter than the interaction length. Hence the deposit of the neutral pions is localized, while the charged pions travel further in the detector volume.

---

[2] The radiation length X_0 is defined as the distance over which a high energy electron or positron looses on average 68% of its total energy through Bremsstrahlung. The physics of the electromagnetic showers and the definition of the interaction length can be found in chapter 6.

Generation i	ϵ_i [GeV]	$\langle N_i^{\pm}\rangle$	$\langle N_i^0\rangle$	E_i^0 [GeV]
0	250	1	0	0
1	28	6	3	84
2	3.1	36	18	56
3	0.35	216	108	38
	Total			178 GeV

Table 5.1: Average energy deposited by neutral pions in a hadronic shower under the simplified hypothesis that only 9 pions are produced at each inelastic hadronic interaction. For each generation i of secondary particles the average energy per particle ϵ_i and the average number of charged ($\langle N_i^{\pm}\rangle$) and neutral ($\langle N_i^0\rangle$) pions are given.

A second question to be addressed is the definition of the quenching mechanism of the shower. According to the model used in this example, the average fraction of neutral pions f_0 is $\pi^0/(\pi^- + \pi^+ + \pi^0) = 1/3$. At each multiplication step $\langle N\rangle$ new pions are produced. The average total number of charged $\langle N_i^{\pm}\rangle$ and neutral $\langle N_i^0\rangle$ pions produced in the hadronic shower after i multiplication steps is:

$$\begin{aligned}
&\langle N_i^{\pm}\rangle \sim \left[\langle N\rangle\,(1-f_0)\right]^i \\
&\langle N_i^0\rangle \sim \langle N\rangle f_0\left[N\,(1-f_0)\right]^{i-1} \sim \langle N\rangle f_0 \langle N_{i-1}^{\pm}\rangle \qquad (5.2)\\
&\langle N_i\rangle = \langle N_i^0\rangle + \langle N_i^{\pm}\rangle \sim \langle N\rangle^i
\end{aligned}$$

Given a primary hadron with energy E, the energy associated to each particle at every step is $\epsilon_i = E/\langle N\rangle^i$. The shower propagates until charged pions with total energy higher than the threshold energy E_{th} are produced. This results in an average maximum number of generations n_g^{max} defined by the equation:

$$\frac{E}{\langle N\rangle^{n_g^{max}}} = E_{th} \qquad (5.3)$$

The multiplication mechanism stops after n_g^{max} generations, on average. The soft pions produced under threshold propagate in the medium and loose all their energy through ionization.

Finally it can be performed a qualitative calculation of the contributions of the neutral and charged sector to the energy components of the shower. In table 5.1 the average number of charged and neutral pions produced by a 250 GeV pion according to the simplified model is shown. The average number of secondary particles produced at each generation is $\langle N\rangle = 9$, as in [150]. According to eq. 5.3 the average number of generations in the hadronic cascade is $n_g^{max} = \log(250/0.28)/\log(9) \sim 3$. In average, the total energy deposited by the neutral sector is 178 GeV.

To conclude, the particles which contribute to the total deposited energy of a hadronic shower can be classified in two sectors. The *electromagnetic* sector is composed of the neutral pions, which deposit energy decaying into photons. The *hadronic* sector is composed of charged pions, which deposit energy through ionization before being stopped through an inelastic collision. The two sectors have a different physical function. The former is responsible of the local and irreversible conversion of the energy of the primary hadron into the calorimeter signal. The latter contributes mainly to the spatial propagation of the hadronic shower. On average most of the energy of the primary hadron is deposited in the detector through the electromagnetic sector.

5.1.3 Systematic classification of the energy sectors of the hadronic shower

The results of the previous example can be extended to a most complicated and complete scenario. In this sections the full range of possible final states in the inelastic hadronic interactions involved in a hadronic shower is considered. The final scope is to provide a classification of the process of energy deposition involved in the development of hadronic showers [151, 152].

It was observed previously that charged hadrons $(\pi^{\pm}, p, \ldots)$ and neutral particles $(\pi^0, \gamma, n, \rho \ldots)$ are produced. The charged hadrons release some energy through ionization and eventually undergo further hadronic interactions. Fast neutrons generate recoil protons in the *slowing down process*. Slow neutrons undergo nuclear reactions. The π_0 and η decay in two γ and deposit energy through the electromagnetic interaction of the γ.

In spite of the larger complexity of final states, the classification of the visible energy into a electromagnetic and hadronic sector can be extended from the simplified example to a general hadronic shower. The *electromagnetic* sector is composed of π^0 and η. Also the photons coming from the neutron evaporation and from the deexcitation of the nuclei contribute to a fraction of the total deposited energy. The *visible hadronic* sector consists of all the charged hadrons. They loose energy through ionization, travelling on average one interaction length, before they undergo a further hadronic interaction.

For a complete energy balance, the binding energy of the nucleus involved in the inelastic scattering has to be taken into account. The intermediate state of the nuclear fission and spallation is described by an excited nucleus. It is formed from the original target nucleus, adding some nucleons from the intranuclear shower process. As the binding energy per nucleon is about 8 MeV, some sizable energy of the incident hadron is required to bind more nucleons and to form the excited state. The binding energy is released in the deexcitation process through MeV photons and neutrons. The hadronic calorimeter is not sensitive to the full products of the deexcitation and some energy gets lost. This contribution is included in the energy balance through the *invisible hadronic energy* sector.

Absorber	**U**	**Pb**	**Fe**
(Ionization due to the spallation protons)	38	43	57
Excitation γ's (%)	2	3	3
Neutrons $<$ 20 MeV (%)	15	12	8
Invisible energy (binding energy target recoil)	45	42	32

Table 5.2: Average energy deposits in 5 GeV protons showers [149]. The average energy losses are normalized to the hadronic sector. The electromagnetic sector is not considered. The ionization is the main mechanism of energy deposition of the charged hadrons in the hadronic shower. A consistent fraction of the total energy is absorbed by the nuclei in the nuclear interactions involved in the hadronic shower. The fluctuations of the binding energy and of the hadronic energy sector are usually very large and represent the intrinsic physical limitation of the resolution of the hadronic calorimeters.

Finally, neutrinos from $\pi^\pm$, $K^\pm$ andρ decay escape from the detector without leaving any signal. Also neutrons can propagate freely and finally escape undetected. This contribution to the total energy balance is expressed in the *escaped hadronic energy* sector[3].

A quantitative calculation of the average different contributions of the showers was done for the ATLAS LAr calorimeter using Geant4 [153]. In that study it was shown that on average 70% of the visible energy deposited by a 100 GeV proton in the hadronic calorimeter is purely electromagnetic. It was found that the average visible energy is 76 GeV, out of which the average electromagnetic energy is 54 GeV and the average visible hadronic energy is 22 GeV. The average invisible binding energy was calculated as 20 GeV and only 2 GeV escaped from the toy detector used in the simulation. A detailed calculation of the composition of the hadronic sector was done in [149] for a 5 GeV proton in different materials. The results are shown in table 5.2. In iron 57% of the hadronic energy is deposited with the ionization process and only a small fraction of the signal is generated by neutrons and photons. The invisible energy was found also a significant part of the hadronic shower. This result is somewhat in agreement with the specific calculation performed by the ATLAS collaboration.

In conclusion the energy balance of the hadronic shower is composed of four sectors: electromagnetic, visible hadronic, invisible hadronic and lost hadronic. The signal of the hadronic calorimeter is generated by the electromagnetic and visible hadronic sector. On average, the electromagnetic component is larger than the hadronic one. Moreover, the hadronic visible energy consists mainly of the ionization deposit of charged hadrons. In this section the fluctuations associated to each sector were neglected. Their consequence is treated in the next section.

---

[3] The fact that neutrinos are included in this sector could seem improper. However they are generated in the decay of hadrons and they transport a part of the initial hadronic energy. Only in this respect they are part of the *escaped hadronic energy*.

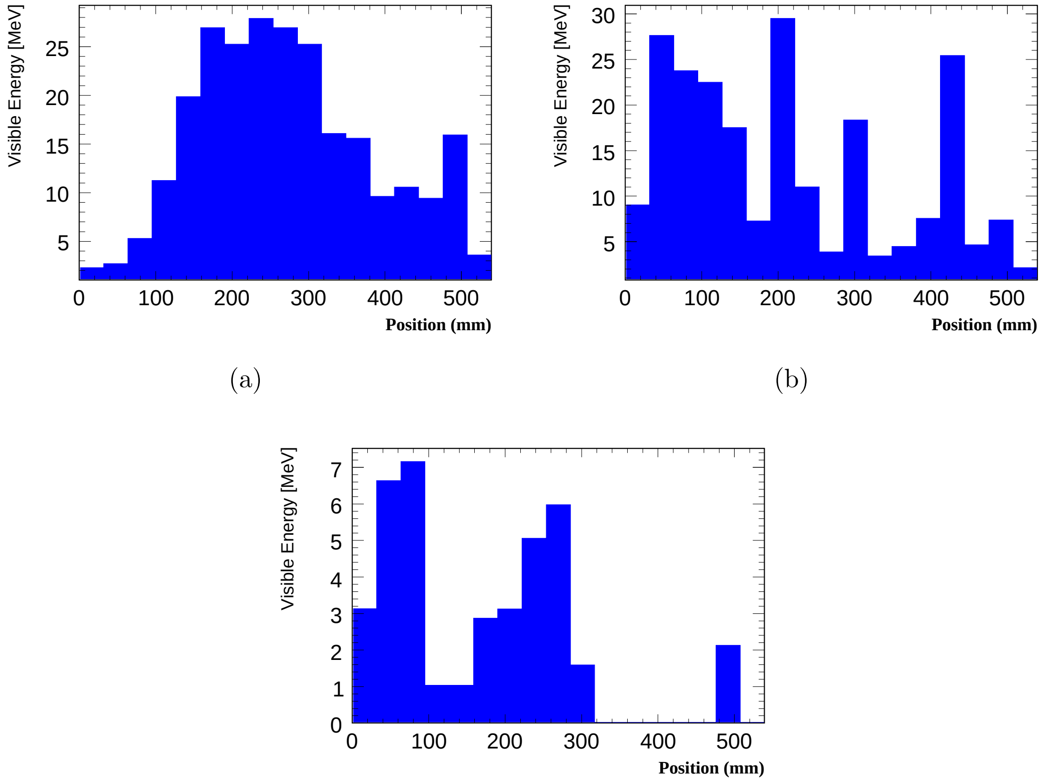

(a)

(b)

(c)

Figure 5.2: Longitudinal energy profile of three individual 12 GeV pions incident on the CALICE AHCAL prototype. The prototype is composed of 17 modules. Each module is divided into a 2 cm thick steel absorber plates alternating with a 0.5 cm thick scintillator sensitive layer.

5.2 Fluctuations in hadronic showers

The main problem which affects the measurement of hadronic showers is the large event-by-event fluctuation [147]. A first immediate effect of this feature is the topological difference of the single event respect to each other. As an example, the energy profiles of three single 12 GeV pions interacting with the CALICE AHCAL are shown. The data are collected in a dedicated test beam experiment whose details will be given in the next sections. The shape and the development of the hadronic showers differ significantly in the three cases. In similar experiments it was shown that the longitudinal profiles of the single hadron can be interpreted as a sum of electromagnetic clusters of fitted energy, characterized by a fixed shape [150]. Effectively the main source of fluctuation is the number of neutral pions produced at each inelastic interaction. Consequently the energy sharing of the electromagnetic and hadronic sectors is fluctuating significantly.

A second effect of this mechanism is an intrinsic worsening of the energy resolution of the hadronic calorimeter. It is caused by the different response of a hadronic calorimeter to electrons and to hadrons. The response of the hadronic calorimeter to electrons e is defined as the average visible signal of a electron. It is usually rescaled to the response of a minimum ionizing particle (mip) and it is expressed as e/mip ratio[4]. Similarly the average visible signal of hadrons is indicated as h ad it is rescaled to the mip response (h/mip). The fraction e/h is an important parameter for the characterization of the hadronic calorimeter. According to the classification of the energy components of a hadronic shower exposed in the previous section, it can be expressed as [149]:

$$\frac{e}{h} = \frac{e/mip}{f_{ion} \cdot ion/mip + f_n \cdot n/mip + f_\gamma \cdot \gamma/mip} \tag{5.4}$$

where e,h,n and γ are the signal of the hadronic calorimeter to electrons, hadrons, neutrons and photons. The quantities f_i are the average fractions of neutrons, ionizing particles and photons in the hadronic shower. In general $e/h < 1$, because of the sizable contribution of the missing energy in the hadronic interactions.

The combined effect of this feature with the fluctuation of the electromagnetic energy sector f_0 of the shower contribute to degrade the energy resolution of a hadronic calorimeter. The total energy resulting from the interaction of a hadron with initial energy E_{IN} can be expressed as:

$$E \sim [e f_0 + h\,(1 - f_0)]\, E_{IN} \tag{5.5}$$

from which the energy resolution can be written as:

$$\left(\frac{dE}{E}\right)_{df_0} \sim |e - h|\, df_0 \sim |e/h - 1|\, df_0 \tag{5.6}$$

Therefore, it e/h is different than 1, a term proportional to the fluctuations of the electromagnetic component of the shower is added to the energy resolution, with a consequent deterioration of the calorimeter response.

The equalization of the e/mip and h/mip response would reduce this effect; this technique is called compensation. The compensation is achieved either reducing the response to electrons or increasing the response to hadrons. In calorimeters with highly fissionable absorbers, as Uranium, the energy lost in the hadronic interaction is balanced by the big amount of spallation neutrons and evaporation photons. This method proposed by Amaldi [147] is used in the ZEUS and D0 Uranium calorimeters. A new technique which became favoured in the last decade is the offline compensation. The DREAM collaboration [115] proposes to measure separately the electromagnetic and hadronic energy sectors and to rescale the two energies with appropriate coefficients. This dual read-out technique identifies the electromagnetic sector of the hadronic shower measuring the Cherenkov light produced by the relativistic electrons. The hadronic sector is mainly composed of not relativistic particles and contributes only to the normal scintillation light signal. This compensating calorimeter is proposed for the 4^{th} concept detector design for ILC, as shown in chapter 3.

---

[4] The concept of e/mip ratio is treated in section 6.1.3.

In conclusion large event-by-event fluctuations are observed in the development of hadronic showers in the matter. This feature introduces a limit on the possible energy resolution achievable with hadronic calorimeters. Furthermore, the methods which aim at a geometrical description of the hadronic showers on a event-by-event basis have to contrast these large fluctuations.

5.3 A Hadronic Calorimeter for the LDC/ILD detector concept

The ILD/LDC detector concept was presented in chapter 3. It is a compact detector to be operated in a very high magnetic field, up to 4 T. It is designed specifically for the Particle Flow approach. In section 3.3 the general features of a detector for the Linear Collider were outlined. In the this section the specific requirements that the hadronic calorimeter has to satisfy are analysed.

5.3.1 Requirements of the Particle Flow

In chapter 3 it was shown that the role of the hadron calorimeter in the Particle Flow approach is to identify the charged hadrons and measure the energy of the neutral hadrons. This task is quite complicated. First the momentum of the hadron is measured in the tracker. Second the hits in the hadronic calorimeter are grouped in clusters. Finally the identification is performed with a geometrical association of the clusters with the respective track. As already shown, any mistake in this matching increases the so-called *confusion term* and worsens the jet energy resolution. All the clusters which are not associated to any track are identified as neutral hadrons.

This operation is done on a event-by-event basis. The Particle Flow has to contrast hence the large fluctuations which feature the hadronic showers. In order to allow a good reconstruction of the event and to reduce the confusion term significantly the hadronic calorimeter has to fulfil the following requirements:

High transversal and longitudinal granularity. The imaging capability of the detector is the most important property. The 3D reconstruction of the event allows separating clusters belonging to the different particles and to different jets.

Dense absorber material. The number of λ_I has to be large enough to contain neutral hadron showers and to minimize the leakage. A compact and dense absorber minimizes the size of the HCAL making it suitable to be placed inside the magnetic coil. Moreover the hadronic showers are more compact with dense absorbers and are easier to be separated geometrically.

Technological compatibility for high magnetic fields. The absorber material has to have a very low magnetic permeability (Fe, Pb). The equipment and read-out of the hadronic calorimeter has to be insensitive to high magnetic fields.

The particle flow sets hence the most significant requirements to the technical structure of the hadronic calorimeter.

5.3.2 Additional requirements from non hadronic final states

The particle flow is related to the physics channels with hadronic final states. This does not cover the full physics program of the International Linear Collider. There are interesting *non hadronic* scenarios in the physics beyond the SM which influence also the design of the hadronic calorimeter. In the following discussion some significant examples from SUSY are shown.

In the simulation studies presented in the previous chapter it was underlined that the missing energy is a typical signature of Supersymmetry. The hadronic calorimeter participates to the hermiticity of the full detector, assuring a coverage down to low polar angles.

In the GMSB scenario [82], with low tanβ and a restricted number of mediators $N_M = 1$, the gravitino $\tilde{G}$ is the lightest SUSY Particle (LSP) and the χ_1^0 is the next to lightest SUSY particle (NLSP). The most favoured decay of the χ_1^0 is $\chi_1^0 \to \gamma\tilde{G}$. The reaction studied at ILC is $e^+e^- \to \chi_1^0\chi_1^0 \to \gamma\tilde{G}\gamma\tilde{G}$. The life time of the χ_1^0 can be long enough to have a late decay in the hadronic calorimeter. The final state is characterized by two photons in the calorimeter non-pointing to the interaction point. This translates to the requirement of a good angular resolution.

The search of $\tilde{\tau}$ in the mSUGRA SUSY scenario defined by the parameters ($M_{1/2} = 440\quad \mathrm{GeV}, \mathrm{M}_0 = 20\quad \mathrm{GeV}, \mathrm{A}_0 = 25\quad \mathrm{GeV}, \mathrm{sign}(\mu) = +1, \tan(\beta) = 15$) offers a second interesting example [154]. In this scenario the $\tilde{\tau}$ has a long lifetime. It is trapped inside the hadron calorimeter and undergoes a late decay $\tilde{\tau} \to \tau\tilde{G}$. The hadronic calorimeter will need an excellent time stamping and self-triggering capability in order to be sensitive to these events which are totally uncorrelated with the beam bunches.

In conclusion the design of a hadronic calorimeter for the LDC/ILD detector has to satisfy a large spectrum of prerequisites set by the reach ILC physics. The R&D programs have to deal with the most recent technologies which can be adapted to a compact highly granular detector in a large magnetic field.

5.4 The CALICE Prototype of a Analog Highly Granular Hadronic Calorimeter

In this section the design of a prototype of highly granular hadronic calorimeter for the ILD/LDC detector concept is presented. While the general proposed design within this concept has been already shown in chapter 3, the scope of the following discussion is to present the innovative technological solutions which are tested in the current *R&D* programs.

5.4.1 The CALICE collaboration

An intensive R&D program is currently being performed by the CALICE collaboration [155]. The collaboration is interested on the full calorimetric system optimized for the Particle Flow and is testing the possible technological options. The sub-detectors studied in this framework are the electromagnetic calorimeter, the hadronic calorimeter and the muon system.

Two options are being investigated for the electromagnetic calorimeter. The first is a silicon tungsten sandwich calorimeter [156]; the active layers are instrumented with a array of silicon junction, with a sensitive area of 1×1 mm^2. The second is a scintillator/tungsten sandwich calorimeter [1]; the sensitive layer is composed of scintillator strips perpendicular to each other. The effective segmentation is given by the strips width of 1×1 cm^2. Each strip is read-out with a new generation MPPC[5].

Two options are also considered for the hadronic calorimeter. The first is a digital HCAL. It uses gaseous signal amplification in GEMs [118], Micromegas [119] or RPCs. Thin and large area chambers are interspersed between steel absorber plates. The chamber anode is segmented in small pads of about 1 cm^2 size. The second is a analog HCAL (AHCAL) consisting of a scintillator/steel calorimeter read out with Silicon PhotoMultipliers.

One option for the Muon Tail Catcher is studied. It consists of a scintillator/steel sandwich detector. The sensitive layer is made of scintillator strips read-out by a Silicon PhotoMultiplier.

A prototype of each sub-detector was build and an intensive test beam program is currently going on. The AHCAL prototype is the detector studied in this thesis and it is described in the next section. The test-beam experiment reported in this thesis involves also the prototypes of the silicon/tungsten ECAL and of the TCMT. They are described separately in the next chapter.

The aim of the test beam experiment regarding the highly granular hadron calorimeter can be resumed in the following points:

Technological feasibility. It is the first time that the Silicon Photomultiplier technology is used in such a high granularity environment. The feasibility of this technology for hadronic calorimetry has to be demonstrated and established.

Calibration issues. The Test Beam experiment wants to demonstrate the possibility of the technical control of the response of the detector, in case of variation of the external conditions. The systematic introduced by variations of temperature, voltages are studied.

Physics performance. The characterization of the AHCAL in terms of energy resolution, e/mip, h/mip, e/h is an essential part of the physics program of CALICE. Moreover, the experiment aims at demonstrating that the high granularity allows reconstructing the intrinsic topology of showers in the detector. This is the basic feature of a calorimeter system for the Particle Flow.

Validation of Monte Carlo models for hadronic showers. Many simulation models are nowadays available for the description of hadronic showers and the studies of the particle flow performance depend on the chosen model. The high granularity of the AHCAL prototype allows to study with unprecedented precision the topolog-

---

[5] The MPPC is a new silicon photo-detector. Its characterization for hadronic calorimetry is presented in section 5.5.

ical development of hadronic showers, introducing many new observables for the determination of the more suitable Monte Carlo model.

Combination of sub-detectors. The interplay between electromagnetic and hadronic calorimeter with the tail catcher is investigated, in order to study the physics potential in the full calorimetric measurement.

The calorimeters are tested in e,π,p and μ beams in CERN and FERMILAB. The studies presented in this thesis refer to the test beam in CERN. The experimental conditions will be described in the next chapter.

5.4.2 The CALICE AHCAL prototype

The prototype consists of a sampling structure alternating 2 cm thick absorber steel plate with a 0.5 cm thick sensitive layer. It has a total surface of 90×90 cm^2 and consists of 38 layers, for a total length of 5 λ_0[6]. Each sensitive layer is a array of 216 scintillators (Fig. 5.3a). The 30×30 cm^2 core has a granularity of 3×3 cm^2 and the outer region is equipped with tiles of increasing size — 6×6 cm^2 and 12×12 cm^2. Each tile is read-out individually by a Silicon PhotoMultiplier. As the SiPM is green sensitive, the coupling between the scintillator and the photo-detector is performed via a green wavelength shifter fibre arc. The fibre is inserted in a groove carved directly in the tile. The groove is quart-circle shaped in the 3×3 cm^2 tile and full circle shaped in the other tiles (Fig. 5.3b). This geometry of the fibre is studied in order to optimize the scintillation light collection efficiency. A mirror is placed on one side of the tile in order to minimize the light losses along the fibre. The photo detector is installed directly on the tile and detects the fibre green light on the opposite end to the mirror. A 3M reflector foil is applied on the surface of the tiles. The sensitive layer is housed in a steel cassette, with 2 cm thick rear and front plates. The reflector foil is glued to a rigid FR4 plastic board inside the cassette. The biasing and read-out cables are also fixed to this plastic structure. The calibration of the photo-detectors with light is done with a LED/clear fibre system. The fibres are embedded with the sensitive cassette itself and a proper electronic board controls the LED system. The electronic read-out of the signals of the Silicon Photomultipliers is made by the ILC-SiPM chip, manufactured in LaL Orsay, hosted on the Hcal Base Board (HBAB) [157]. The chip houses 18 channels, each containing a variable-gain, charge-sensitive amplifier, a variable shaper, track and hold stage and a multiplexing unit. In addiction it has an 8-bit DAC, which gives the possibility to perform single channel voltage adjustment in the range between 0 and 5 V. The physical properties of the HCAL layer are reported in Table 5.3.

5.4.3 Equipment of the AHCAL: The Silicon Photomultiplier

The Silicon Photomultiplier is a solid state detector. It can be approximately described as a 2D array of small (hundreds of μm^2) Avalanche Photodiodes, each working in single photon detection (non proportional) Geiger mode. When a photon creates a

---

[6] 1 λ_0 corresponds to 22.84 cm and the total length of the prototype is 114.57 cm.

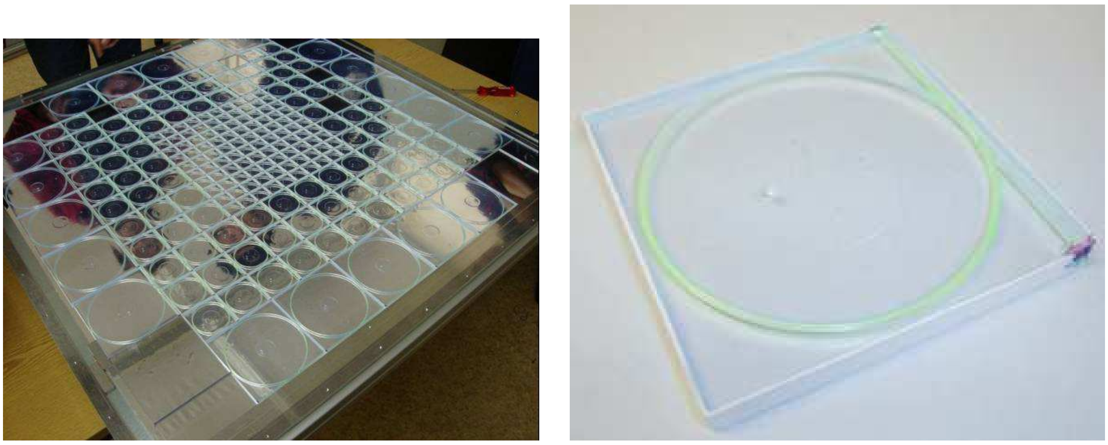

(a) (b)

Figure 5.3: The equipment of the CALICE AHCAL prototype. The HCAL is made of 38 layers, alternating 2 cm thick absorber and 0.5 cm thick scintillator. In (a) the sensitive layer is shown. It is segmented in 216 plastic scintillator cells, individually read-out by a Silicon Photomultiplier. In (b) the mechanical installation of the photo-detector in the scintillator tile is shown.

	ρ g/cm^3	λ_0 cm	X_0 cm	ρ_M cm	$\bar{E}_{mip}$ MeV	E^{mpv}_{mip} MeV
Absorber layer	7.83	16.86	1.8	1.78	22.78	21.40
Sensitive layer	1.032	68.5	42.4	10.32	1	0.859
AHCAL layer	5.95	22.84	2.62	2.47	23.78	22.26

Table 5.3: Main physical properties of a layer of the prototype of highly granular analog hadronic calorimeter. The extended calculations of the hadronic interaction length (λ_0), of the electromagnetic interaction length (X_0) and of the Moliere radius (ρ_M) can be found in [158]. The mean value and the most probable value of the energy deposited by a minimum ionizing particle in a layer of the hadronic calorimeter is calculated using the information of the DPG [19]; the extended calculation is reported in section 6.1.

photoelectron through the photoelectric effect in one of such APD microcell, a large breakdown current is produced: each cell functions like a binary system, meaning that the output signal is not proportional to the energy of the photon, but just registers that one event was detected. The summed output of all the microcells is then proportional to the number of fired cells and consequently to the flux of detected photons. The device is about 1 mm^2 in size with 1000/ mm^2 microcell density.

Each microcell is based on the well studied *reach through avalanche structure* [36]. A simplified layout is shown in Fig. 5.4. It consists of a $n^+ - p - \pi - p^+$ structure, where π is a slightly doped p-type layer. This combination of three p-type layers with different doping concentration next to the n^+, when bias is reverse, leads to a well defined shape

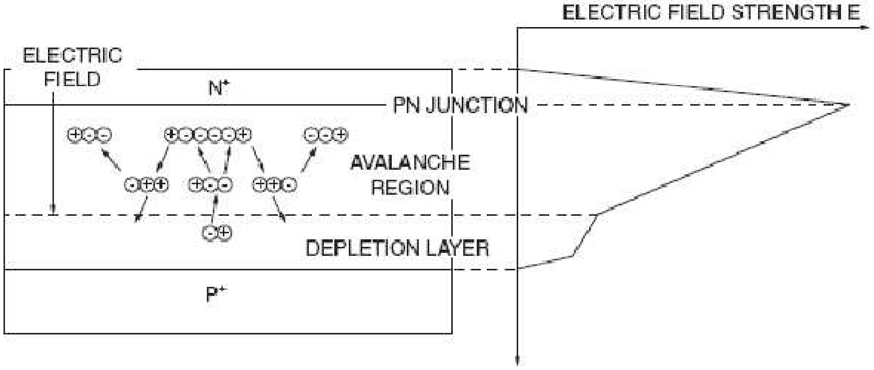

Figure 5.4: The fundamental design of a SiPM microcell is the so-called *reach-through-avalanche structure*. It consists of a $n^+ - p - \pi - p^+$ structure. The electric field is shown on the right side. It reaches a maximum value in the $n^+ - p$ junction.

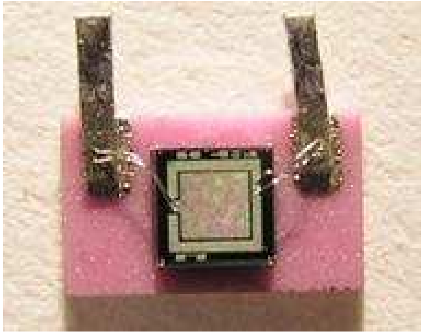

Figure 5.5: The Silicon Photomultiplier from PULSAR/MEPHI used in the CALICE prototype of highly granular hadronic calorimeter.

of the electric field and of the depletion region. As the n^+ layer is thick and more doped than the near p-layer, the depletion region extends more in the p-layers and widens to *reach through* the π layer. The field reaches its maximum in the $n^+ - p$ junction, then slightly decreases in the π layer and it vanishes at the end of the narrow depletion region in the p^+ layer. Hence the structure defines two different regions in the microcell: a low electric field (π layer) and a high electric field ($n^+ - p$ depletion region) zone. Photons mostly interact with the silicon in the π layer, creating electron-hole pairs. Under the influence of the electric field they drift respectively towards the n^+ and the p^+ region. Drifted electrons enter the high electric field region where they can acquire the necessary energy to create more electron-hole pairs through impact ionization, which will have the energy to create further ionization. A correct combination of doping profiles and electric field value can allow this junction going into breakdown. This process is potentially not limited in time once initiated by an electron in the depletion region, and a negative feedback to quench the avalanche is needed. A polysilicon resistance in series with the APD microcell is used to set a Geiger current limited mode.

The Silicon PhotoMultiplier used in the hadron calorimeter prototype (Fig. 5.5) is produced in PULSAR/MEPHI, in a *R&D* program dedicated to this project [159]. It has 1156 pixels on a total sensitive area of 1 mm^2 and it is typically operated at a bias voltage of 40 V. This photodetector was designed to have a high efficiency in the green spectral region.

The finite number of pixels causes a statistical saturation of the response of this photo-detector. This saturation behaviour was studied intensively as it affects the energy measurement of the hadronic calorimeter prototype [160]; furthermore systematic studies of the response of the SiPM to light pulses of different time width are shown in 5.5.

The dependence of the signal on the temperature and on the operation voltage was measured. It was found that SiPM signal amplitude variation is $4.5\%/\circ C$ and $7\%/0.1V$ for a SiPM gain of 10^6. The sensitivity to temperature and bias voltage decreases with increasing gain (and over voltage). The SiPM was tested also in magnetic field up to 4 T, for two orientations of the field line and the signal was found stable within the 1% accuracy of the measurement[161].

5.5 Study of the Micro Pixel Photon Counter for the read-out of the CALICE AHCAL

Intensive technological studies are currently ongoing in the design of the Silicon Photomultiplier. The main direction of research of the new generation of Geiger mode avalanche photodiodes is the improvement of the sensitivity to the blue spectral region. One of these new Geiger Mode avalanche photodiodes is the Multi Pixel Photon Counter [162], a Geiger Mode avalanche photodiode produced by Hamamatsu.

The MPPC shows a good optical sensitivity in the 420 nm spectral region. This feature of the MPPC opens the possibility a new R&D for the highly granular hadronic calorimeter, in order to prove the possibility of the direct coupling of the scintillator tiles with the photo-detector. The direct coupling would simplify noticeably the manufacturing of the hadronic calorimeter and would allow to extend the concept from a prototype to a large scale detector for the International Linear Collider.

The possibility of the direct coupling does not involve only the hadronic calorimeter design. The CALICE collaboration proposes also a scintillator/tungsten electromagnetic calorimeter equipped with MPPC, which is currently being tested.

This section reports a study the response to a minimum ionizing particle of a plastic organic scintillator read out by the most recent MPPC, with both 400 and 1600 pixels [163]. The m.i.p. signal is a benchmark for the high granularity hadron calorimeter design and has to be well separated from thermally induced noise. The direct readout option was compared with the established green wavelength shifting mediated design.

5.5.1 The Experimental Set-up

The study is based on 10 samples of MPPCs, 5 with 400 pixels and 5 with 1600 pixels. They are protected by a special plastic package. The suggested operation voltage is respectively 76 V and 78.1 V (estimated $\sim$2.5 V and $\sim$1.4 V above the breakdown

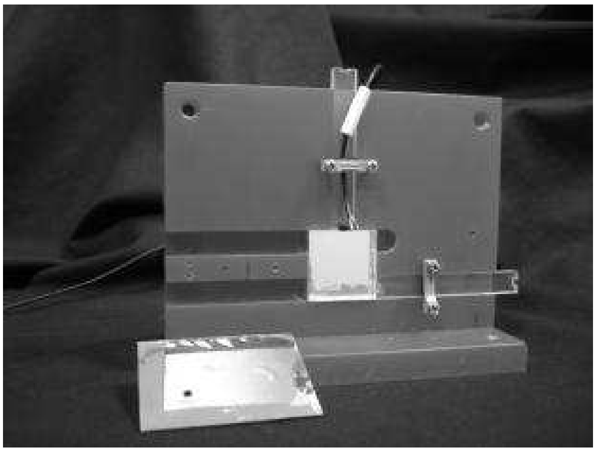

Figure 5.6: Setup for the study of the direct readout of a scintillator tile with an MPPC. The scintillator is installed in a specific housing. The MPPC is fixed at one end of a plastic holder which can be located in two different positions: the coupling is reproducible at a 3% level.

voltage), with a spread of 0.1 V. In this measurement two $3 \times 3 \times 0.5$ cm^3 plastic organic scintillator tiles (produced by *Uniplast* enterprise in Vladimir, Russia) are used. In one a 1 mm diameter green wavelength shifting fibre (Kuraray multicladding WLS fibre Y11(200)) is installed. The scintillators are wrapped in a Super-radiant VN2000 foil (3M).

A special setup is designed in order to guarantee the reproducibility of the measurement (Fig. 5.5.1). The scintillator is installed in a fixed housing, in the middle of a robust main structure. The MPPC is secured at one end of a plastic bar. Two grooves are carved in the main structure, one starting from the middle of the side of the tile, one from the centre and they host the MPPC holder. This allows the MPPC to be coupled to the scintillator in two positions. In the direct readout setup, a window of 3×3 mm^2 is open in the reflective coating, in front of the MPPC. Its holder is then completely guided in the casing and the MPPC plastic coverage is in contact with the scintillator; this improves the coupling between scintillator and photodetector. The distance between the sensitive region of the MPPC and the surface of the scintillator is $\sim$ 2 mm. In the green wavelength shifter mediated design, the scintillator equipped with fibre is installed in the dedicated housing and the green light is directly read out by the MPPC, held by the same bar. In both designs, no specific optical coupling is used. The response of the system to a β^- source (Ru^{106}) is investigated. A trigger plate, consisting of a $5 \times 5 \times 1$ cm^3 organic plastic scintillator, read out by a traditional photomultiplier tube, is installed behind the scintillator/MPPC system. The signal of the MPPC is amplified by the wide-band voltage amplifier Phillips Scientific 6954. The integration is performed by the QDC Lecroy 1182, in a gate of 80 ns, produced in coincidence with the trigger. The setup allows a reproduction of the measurement to within a systematic error of $\pm 3\%$.

5.5.2 The Results of the Measurement

A characterization of the devices is initially performed. The 1600 pixels MPPC show a typical gain of $(2.7 \pm 0.1) \cdot 10^5$. The dark rate at a threshold of 0.5 pixels[7] is (40 ± 1) kHz and the cross talk $(4.3 \pm 1)\%$. These values are measured at 2.5 V over the breakdown voltage. The 400 pixels MPPC exhibits a gain of $(7.7 \pm 0.1) \cdot 10^5$, a dark rate at a threshold of 0.5 pixels of (230 ± 3) kHz and cross talk of $(3.5 \pm 1)\%$, operated at 1.4 V over the breakdown voltage. The values are found to be in agreement with the data sheet performances of the photodetector.

The aim of the experiment is to extract the most probable value (MPV) of the number of photoelectrons produced in the MPPC when a minimum ionizing particle crosses the scintillator. The typical signal is shown in figure 5.7. Each peak corresponds to a certain number of pixels firing in the MPPC. The good separation of the peaks indicates a good uniformity of the device. The signal is fit with a multi-Gaussian function (Fig. 5.7.a). The extracted area of each peak is then plotted versus the number of photoelectrons (Fig. 5.7.b). The areas follow a Landau distribution, smeared by the Poisson photo-statistics. The maximum of this distribution is the searched MPV, which is estimated with a Gaussian fit around the peak. The results of these measurements for the green and blue light coupling for both 1600 pixels and 400 pixels MPPC are shown in figure 3, as a function of the voltage.

The efficiency of the 1600 pixels MPPC is found to be about half of that of the 400 pixels device, in agreement with the photo-detection efficiency declared in the producer data sheet. The MPV is in agreement within $\pm 3\%$, in both cases when the MPPC is either located centrally on the edge or near the corner. The two measurements agree within the systematic error quoted above.

5.5.3 Application to the Hadronic Calorimeter

In the calorimeter, mip signals are used as a reference for the calibration: the MPV of the signal sets the energy scale of each channel. An amplitude threshold[8] defines the discrimination between the noise and the physics signal. The normalized integral of the mip signal above the noise threshold is the mip detection efficiency. All signals, with amplitude above threshold, constitute a hit in the calorimeter. The procedure is shown in figure 5.9. The threshold is fixed considering the pedestal spectrum (Fig. 5.9.a) such that the noise rate above threshold is 3 kHz. This requirement corresponds to an occupancy of about 8 accidental hits, as observed in the present 8000 channel prototype with ~ 200 ns integration time. For the ILC detector, the occupancy of 10^{-4} during one beam crossing interval (~ 300 ns) translates into a sharper requirement of 300 Hz noise above threshold for a single photo-sensor.

The efficiency of the mip signal is then calculated using the determined threshold (5.9.b). For a given occupancy requirement, the dark noise of the sensor, the inter-pixel cross-talk and the most probable number of pixels corresponding to a mip determine the mip detection efficiency. The first defines the minimum allowed threshold, the latter de-

---

[7] This threshold is chosen in order to have the highest sensitivity to the dark pulses

[8] The total charge of the signal is considered as amplitude in this application.

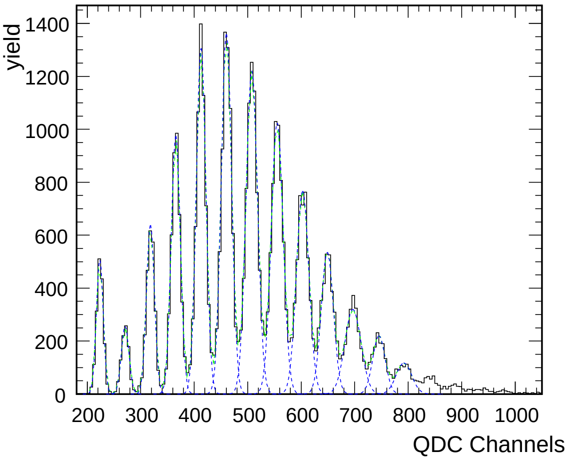

(a)

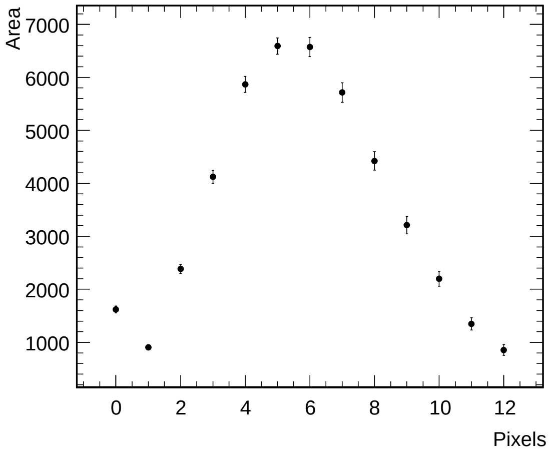

(b)

Figure 5.7: A plastic scintillator detects a mip: it is directly read out by a 1600 pixels MPPC, operated at 2 V over the breakdown voltage. To extract the MPV of the distribution the spectrum is fit with a multi-Gaussian function (a) and the areas of the Gaussians are plotted (b). The maximum of the area plot, estimated with a Gaussian fit, is the MPV.

termines position and Poisson width of the mip signal distribution and thus the integral above threshold. In the prototype of the hadron calorimeter, the MEPHI SiPMs provide 15 ± 2 photoelectrons at the MPV of the mip signal. The efficiency of the signal collection, as measured in the prototype[9], is 95%. The efficiency of the mip signal collection

---

[9] The measurement of the efficiency of the signal collection in the prototype is proposed in section 6.4.1.

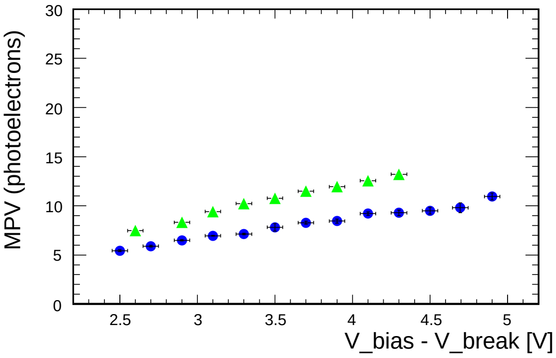

(a)

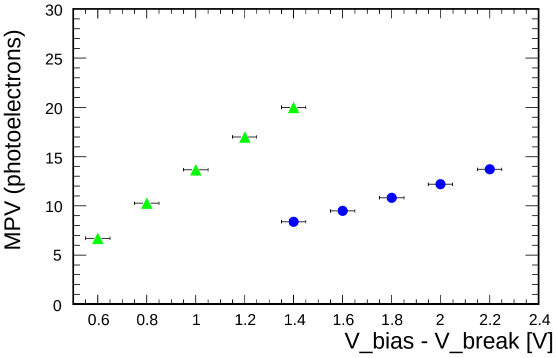

(b)

Figure 5.8: Most probable value of a mip spectrum detected by a 1600 pixels (a) and a 400 pixels (b) MPPC. The dots correspond to the direct coupling, while the triangles to the wavelength shifting mediated readout.

of MPPC, as a function of voltages, is shown in figure 5.10. The measurements with direct coupling and with wavelength shifting fibre mediated readout are presented for both 1600 and 400 pixels MPPC. The MPPC have a very low dark rate and cross talk, and the requested noise cut can be put at 1.5 - 2 pixels. The 1600 pixels device, in the direct coupling option, can be used at 2.5 - 3.5 V over the breakdown, providing 6 - 7 photoelectrons at the MPV, with a collection efficiency of $\sim$97 %. The performance of this solution is then comparable with the one used in the actual prototype, and allows even an improvement in the dynamic range. If the green wavelength shifting fibre is used, the MPPC are definitely competitive with the SiPMs in use in the present prototype: when operated at 3 - 3.5 V above the breakdown voltage, they provide a better signal efficiency (98%) and a larger dynamic range. The 400 pixels MPPC, in both direct and wavelength shifter mediated readout, shows a very high mip signal collection efficiency, but the reduced number of pixels imposes strict bounds on the dynamic range.

It has to be noted that in both MPPCs the dark rate drops rapidly as the threshold is raised, such that for the tighter requirements of the ILC a threshold of 2-4 pixels

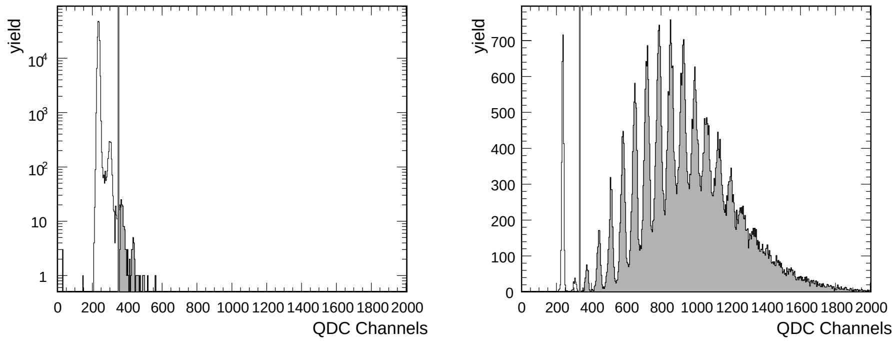

(a) (b)

Figure 5.9: Scintillator crystal read out by a 400 pixels MPPC. A threshold is defined considering the pedestal spectrum, so that the noise above it is 3 kHz (grey area in (a)). This threshold in amplitude defines the efficiency of the collection of the signal (b): in grey is the part of the signal above the cut, which is 98% of the total, after subtracting the pedestal contribution.

would be enough to keep the occupancy small. In this case it is possible to operate at a over voltage which preserves the mip efficiency above 95%. If thinner scintillator, e.g. 3 mm instead of 5 mm thickness with correspondingly smaller light yield, is to be used, a better coupling or a larger sensitive area of the photodetector have to be investigated. A possible solution could be the application of the new 3×3 mm^2 MPPC, but further systematic studies are needed.

Conclusion

The prototype of analog hadronic calorimeter developed by the CALICE collaboration seems to satisfy the main requirements of the Particle Flow. Its high granularity and longitudinal segmentation would allow a good topological reconstruction of the hadronic showers. This detailed geometrical information help the particle flow to contrast the large event-to-event fluctuations which feature the hadronic shower.

The hadronic shower in the calorimeter can be schematically described as a net of ionization tracks connecting electromagnetic dense energy deposits; additional hadronic deposits are randomly generated by the interaction of neutrons and neutral kaons in the detector. The ionization plays an important role in the geometrical reconstruction of the hadronic shower. Moreover the hadronic sector of the signal of the calorimeter consists of energy deposited through ionization.

Not only hadronic final states contribute to the definition of the design of the hadronic calorimeter. The search of exotic physics beyond the Standard Model requires good hermiticity, angular resolution and self triggering capabilities.

Finally, the design of such highly granular compact hadronic calorimeter is a technological challenge, as it has also to be operated in a strong magnetic field. The AHCAL

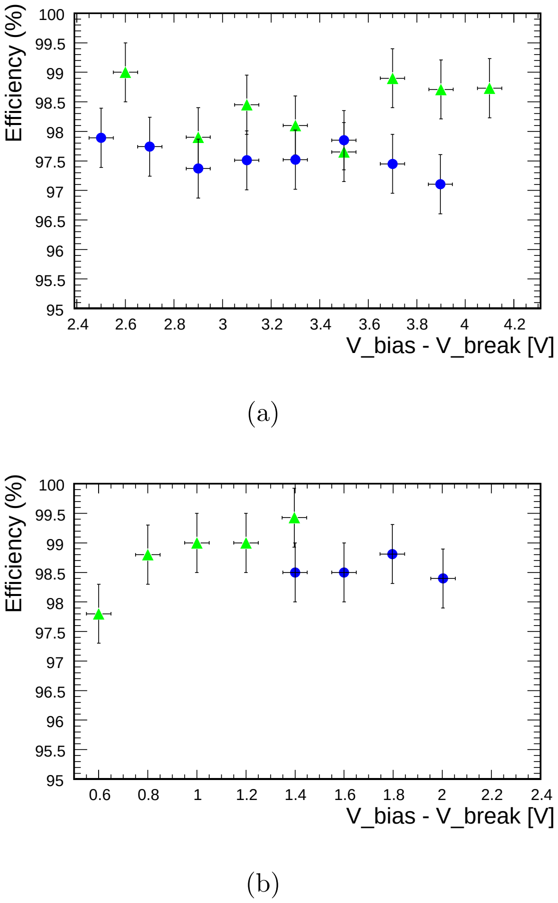

Figure 5.10: Signal collection efficiency for the 1600 pixels (a) and 400 pixels (b) MPPCs. The dots correspond to the direct coupling, while the triangles refer to the wavelength shifting mediated readout.

prototype uses for the first time the SiPM, an innovative silicon photodetector which is installed directly on the sensitive scintillator tile and allows the technical realization of a highly granular hadronic calorimeter.

The advances of the SiPM technology is also being investigated in the CALICE *R&D* program. The application of the blue sensitive MPPC to the direct read-out of plastic scintillator tiles can be considered for both the design of the scintillator/tungsten electromagnetic calorimeter and the design of the scintillator/steel hadron calorimeter.

The direct readout of a 3×3 cm^2 plastic organic scintillator by a Multi Pixel Photon Counter is possible, and can be an elegant solution for the future prototype of a hadron calorimeter. The MPPCs are suitable also for the green wavelength shifter fibre readout, chosen in the actual calorimeter prototype for the ILC, providing potentially even better performances than the ones in use at the moment, in term of dynamic range and mip signal collection efficiency. The 1600 pixels devices are preferred for this particular application, as the linearity of the signal would be extended to a wider range of light intensity. The uniformity of the light collection with respect to the particle impact position on the tile has still to be studied as well as the bounds on the dynamic range imposed by the physics observed at the linear collider.

A by-product of these studies is the application of MPPC to the Positron Emission Tomography. This topic is outside the main scope of this thesis and a more detailed investigation can be found in a dedicated publication [164].

Chapter 6

Analysis of Experimental Data

"So she kissed the toad
and it started to jump on her hand,
it became a nice prince,
Semola was his name."
— ibidem

Introduction

This chapter presents the analysis of the experimental data collected during the test beam of the prototype of highly granular hadronic calorimeter (AHCAL) developed by the CALICE collaboration. The scope of this analysis is the measurement of the response of the AHCAL to muons of energy ranging between 6 GeV and 120 GeV and incidence angle[1] between 0° and 28.3°. The AHCAL prototype was described in chapter 5. It is a hadronic calorimeter specifically developed for the particle flow. It was shown that its main task is the measurement of the energy deposited by neutral hadrons and the identification of charged hadrons. The study of the response to muons adds an important contribution to the understanding and validation of this detector; muons are very penetrating particles which deposit a small amount of their energy to matter through ionization.

The ionization is the basic mechanism of propagation of hadronic shower in matter. In chapter 5 the hadronic shower was described as a net of ionization tracks — the charged hadrons — connecting electromagnetic dense deposits; the average ionization component is about 40% of the total energy deposited by hadrons in the calorimeter. Moreover in the hadronic shower muons are generated from the decay of $\pi^{\pm}$ and $K^{\pm}$ mesons. The topological identification of the ionization tracks is the first step of the geometrical reconstruction of hadronic shower in the AHCAL, according to the Particle Flow technique. The measurement of the sensitivity of the AHCAL to the ionization is

---

[1] The angles refer to the perpendicular direction respect to the frontal surface of the AHCAL; hence an angle of 0° corresponds to perpendicular muons.

hence an important test of the validity of the AHCAL design for the Particle Flow. In this analysis the ionization energy level of muons is compared with the ionization energy deposited by charged pions. Moreover a measurement of the probability of the emission of muons from pion showers is proposed.

The most probable value of the ionization energy level of the muon signal is proposed as reference for the absolute calibration scale of the AHCAL. Any systematic uncertainty of the determination of the muon signal reflects to the quality of the analysis of the AHCAL response to hadrons. Moreover, the reconstruction of the response to muon at the electromagnetic scale allows to measure the e/mip ratio, which is an important parameter for the understanding of the energy resolution of the calorimeter, as shown in section 5.2.

Last but not least, the hadronic calorimeter plays an essential role in the identification of muons in the LDC/ILD detector concept. In the Monte Carlo studies presented in chapter 4, the imaging and tracking properties of the AHCAL are used to merge the track found in the tracker with the eventual deposits in the muon chamber. The muons are identified as *mip like* particles leaving a minimum ionization energy deposit in the three sub-detectors. The experimental verification of the possible identification of a muon track in the calorimeter is hence important.

The response of hadronic calorimeters to muons is treated in many studies. The analysis proposed in this chapter follows the classical methods used by the ATLAS [165], HELIOS [40], DREAM [166] and SPACAL [42, 167] collaborations. However, the unique high granularity of the AHCAL allows a more precise study of the muon interaction with the calorimeter. In this analysis the possibility is discussed for the identification and reconstruction of the δ-rays produced in the detector along the muon ionization track. Effectively the AHCAL is treated as an ionization chamber.

In this chapter first the theoretical basis of the muon interaction with matter is outlined. Then the experimental set-up and the collected experimental data are described. Finally the experimental results are discussed.

6.1 Muons in the HCAL prototype

The muon looses its kinetic energy in matter interacting with the atomic electrons. Its mass is 105.68 MeV, i.e. about 200 times more than the mass of electrons. Therefore a muon is a very penetrating particle. It deposits a minimum amount of its total energy. As an example, it was measured that the muons produced at LEP, at the Z^0 resonance, releases between 200 and 250 MeV in the BGO calorimeter of the L3 experiment [168, 169]. The muon is hence the natural best approximation to a minimum ionizing particle (mip) — i.e. a particle which looses only a little energy merely ionizing matter[2].

However the mip-like assumption on the mechanism of energy deposition of the muons is only an approximation. Large event-by-event fluctuations are caused by higher order electromagnetic interactions. The significance of these contributions increases with the energy of the primary muon. In Fig. 6.1 the GEANT4 simulation of a 120 GeV muon

---

[2] A more extended description of the concept of mip will be given in the next section

interacting with the CALICE AHCAL prototype is shown. In this particular case a cut in range of 5 μm is chosen. The typical pure ionization case is presented in Fig. 6.1a; the main ionization track (red) is surrounded by soft electrons (green). In Fig. 6.1b a muon event with higher order electromagnetic interactions is shown; compact electromagnetic showers are visible along the ionization track. The consequences of this effect are:

1. Sensitive difference between the energy deposited by a muon and by a pure ionizing particle
2. Enhanced energy dependence of the energy losses by muons

The order of magnitude and the relevance of these effects in calorimetric measurements can be quantified with accuracy.

A first quantity to be determined is the energy released by a muon in a single interaction with the atomic electrons. According to the conservation of the 4-momentum, the maximal kinetic energy transferred by a muon to an electron at rest in a single interaction is:

$$T_{max} = \frac{2m_e c^2 \beta^2 \gamma^2}{1 + 2\gamma m_e/M + (m_e/M)^2} \tag{6.1}$$

Even from this simple kinematic argument it emerges that a high energy muon can loose up to its total energy just in a single interaction.

A second quantity to be considered is the cross section of the mechanisms involved in the energy deposit of muons in matter. In general different approximations hold according to the ratio between the impact parameter of the primary particle and the atomic size [170]. If the distance of closest approach is larger compared with the dimension of the atom the pure *ionization* occurs. The atom reacts as a whole to the variable field set up by the passing particle. This case is described by the classical methods of quantum mechanics, neglecting the field radiation quanta. The forces related to the magnetic field decreases as the third power of the distance while the Coulomb force decreases as the square of the distance. Consequently its intrinsic magnetic moment and its spin are neglected and the muon is treated as point-like. If the distance of closest approach is of the order of the atomic dimensions the interaction is in the *knock-on* regime. The atomic electrons are ejected with considerable energy — the so-called δ-rays. Also in this case a classical quantum mechanics approach is sufficient to describe the process and the secondary electron is assumed to be free, if the acquired energy, after the collision, is much larger than the binding energy. The intrinsic magnetic moment and spin of the primary particles can not be neglected. They affect the energy distribution and the number of secondary particles. When the distance of closest approach becomes smaller than the atomic radius, deflections in the trajectory of the passing particle in the electric field of the nucleus becomes the most important effect. The resulting emission of photons is described with precision by quantum electrodynamics. These radiative effects are consistent at higher energies. They are characterized by small cross sections, hard spectra, large energy fluctuations and the associated generation of electromagnetic showers (bremsstrahlung and e^+e^- pair production [171, 172]) or hadronic showers (photo-nuclear interactions [173, 174]).

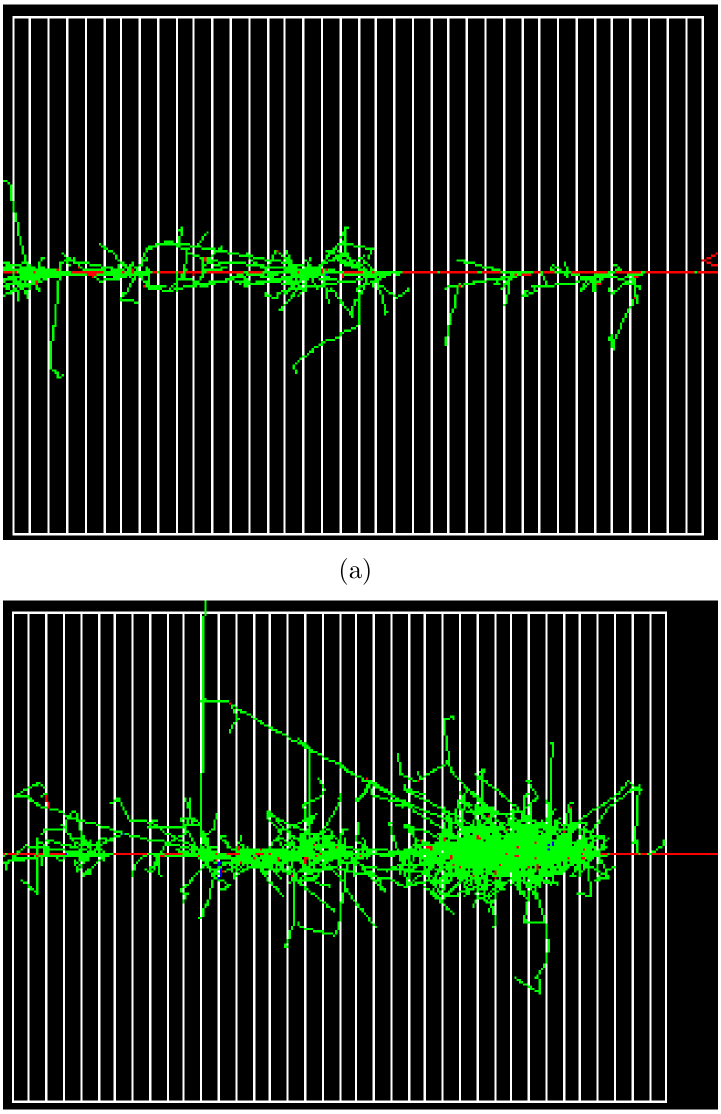

(a)

(b)

Figure 6.1: GEANT4 simulation of a 120 GeV muon detected by the AHCAL prototype. In (a) only few low energetic δ-rays are produced along the main ionization track. In (b) a large contribution of the higher order electromagnetic mechanisms of the interaction of the muons with matter are present. The muon is represented in red and the electrons in green.

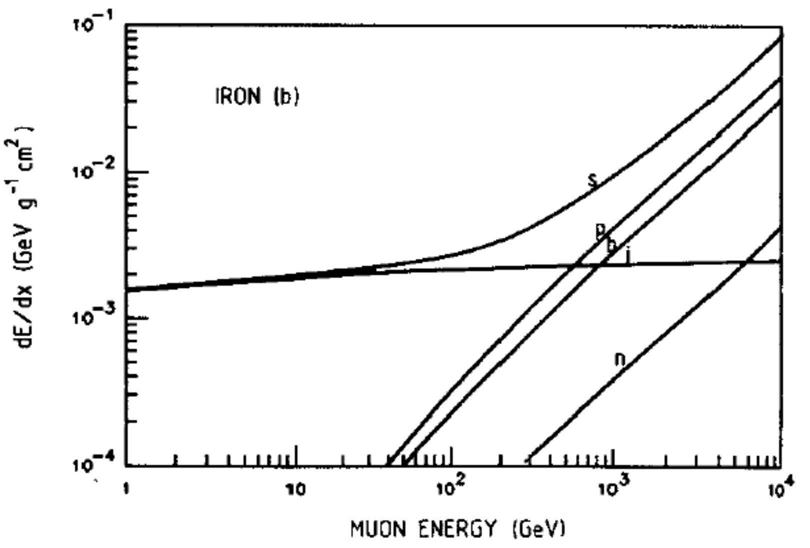

Figure 6.2: Energy loss by muons in iron. The different lines indicate singularly the pair production (p), the bremsstrahlung (b), the ionization — including δ-rays — (i) and the photo-nuclear interaction (n). The line marked with s is the total contribution. Figure from [175].

A complete calculation of the energy released by muons in different materials was done in [175] and the results for iron are shown in Fig. 6.2. At an energy below 100 GeV the ionization and the δ ray emission are the most important contribution to the muon energy loss. The radiative electromagnetic mechanisms start to be sizable above about 100 GeV. The bremsstrahlung and ionization cross sections becomes then equal at the critical energy of about 355 GeV. The photo-nuclear interaction is significant only in the TeV region, far from the energy range reached at the International Linear Collider and in the analysis proposed in this thesis; it will hence be neglected in the following discussion.

As a result of this calculation the energy loss of a muon in the CALICE AHCAL can be estimated. According to [175], in a absorber layer of the AHCAL[3] a 20 GeV muon looses on average $0.2091 \cdot 10^{-2}$ GeVcm^2/g $\times$ 7.87 g/cm^3 $\times$ 2 cm $\approx$ 32 MeV while a 120 GeV muon looses on average $0.2893 \cdot 10^{-2}$ GeVcm^2/g $\times$ 7.87 g/cm^3 $\times$ 2 cm $\approx$ 45 MeV. The energy dependence of the interaction of the muons with matter introduces a not negligible effect which has to be taken into account in the analysis of the response of the AHCAL to muons.

The energy losses of muons with momentum up to 10 TeV/c have been measured in cosmic-rays experiments, finding in general a good agreement between data and calculations. Muons at lower energies were measured in various accelerator experiments. In general a good agreement between data and theory was reported. Nevertheless, preliminary results of 300 GeV muon energy loss measurements in iron indicated about 7%

---

[3] As shown in chapter 5 an absorber layer of the AHCAL consists of 2 cm of steel and a sensitive layer of the AHCAL consists of 0.5 cm of scintillator. In this calculation the results in [175] for iron (density 7.87 g/cm^2) are used.

higher probability compared to Monte Carlo prediction. The ATLAS collaboration [21] dedicated many studies to the measurement of energy losses by muons in the hadronic calorimeter. Studies of 150 GeV [176] and 180 GeV [177] muons were performed in a test beam environment and confirmed the validity of the description of the energy loss by muons in matter as a combination of electromagnetic processes.

6.1.1 The mechanisms of the muon interaction with matter

According to the study in [175], muons release energy in matter through ionization, emission of high energy knock-on electrons, radiative e^+e^- pair production and bremsstrahlung, at energy lower than 200-300 GeV. In this section only the ionization and the production of δ-rays will be discussed in detail, as the analysis of the data refer explicitly to them.

Ionization

The ionization is by far the fundamental component of the energy loss of a muon in matter. The mean rate of energy loss in matter by ionization is given by the Bethe-Bloch equation [19][4]:

$$-\frac{dE}{dx} = Kz^2\frac{Z}{A}\frac{1}{\beta^2}\left[\frac{1}{2}\ln\frac{2\mathrm{m_e c^2}\beta^2\gamma^2\mathrm{T_{max}}}{\mathrm{I}^2} - \beta^2 - \frac{\delta(\beta\gamma)}{2}\right] \tag{6.2}$$

The range of validity of the Bethe-Bloch equation is determined by the pure ionization approximation, which neglects both magnetic properties and radiation effects of the primary particles. It describes i.e. the energy loss of pions in a material such as copper with 1% accuracy for energies between 6 MeV and 6 GeV.

The ionization depends explicitly on the mass and on the momentum of the primary particle. Fig. 6.3 shows the ionization curves for muons, pions and protons for different materials. The Bethe Block curve is featured by a minimum. The minimum of the ionization depends weakly on Z and on the mass M of the incoming particle. It drops from $\beta\gamma = 3.5$ to 3.0 as Z goes from 7 to 100 [19]. The released energy correspondent to the minimum ionization decreases for higher Z materials. It can be calculated [37] as 1.745 $\mathrm{MeVg^{-1}cm^2}$ for Carbon ($Z = 6$), 1.451 $\mathrm{MeVg^{-1}cm^2}$ for Iron ($Z = 26$) and 1.082 $\mathrm{MeVg^{-1}cm^2}$ for Uranium ($Z = 92$). An empirical dependence of the minimum ionization curve on Z is [19]:

$$\left(-\frac{dE}{dx}\right)_{min} = 2.35 - 1.47\cdot\ln(\mathrm{Z}) \tag{6.3}$$

The particles with energy corresponding to the minimum of the ionization are called *minimum ionizing particle* (m.i.p.).

After the minimum, the increase of the ionization is logarithmic up to a constant value — the *Fermi plateau.* As the particle energy increases the interplay between the

---

[4] In this formula the notation of the Particle Data Group [19] is used.

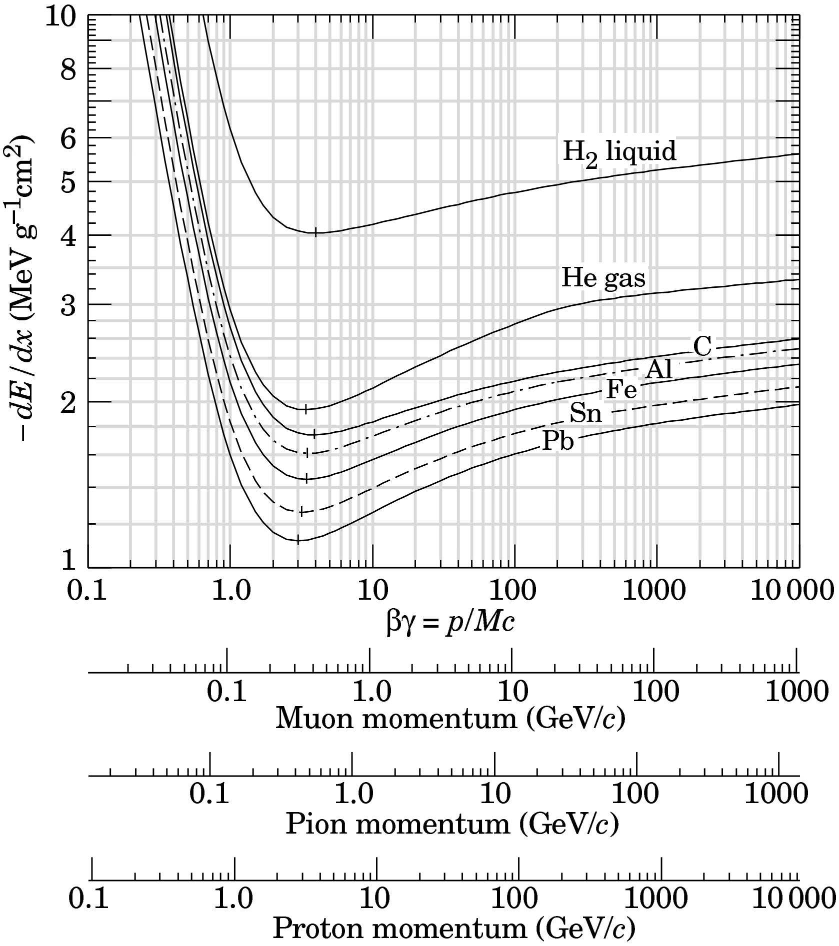

Figure 6.3: Mean energy loss rate in liquid, hydrogen gaseous helium, carbon, aluminium, iron, tin and lead. Radiative effects are not included. Figure from [19]

relativistic flattening of the electric field and the polarization of the medium introduces a further contribute to the logarithmic rise of the ionization losses. This so-called *density effect* is expressed by the term $\delta/2$ in the Bethe-Bloch equation.

As discussed previously, high energy muons have a mean energy loss rate close to the minimum and are always said to be minimum ionizing particles [19]. However, a mip is only a hypothetical particle. As a quantitative example the energy loss in the CALICE AHCAL prototype can be calculated from the information of the Data Particle Group. One absorber layer of the hadronic calorimeter is composed by 2 cm of steel, consisting of a mixture of 98.43% Iron, 1.4% Manganese and a negligible amount of Nichel Crome, Carbon, Phosfor and Sulfur[5]. The plastic support of the tiles is a 3 mm thick FR4 layer. The sensitive layer is a 0.5 cm thick plastic organic scintillator. An air gap of 3.5 mm is also present in the layout of a module of the hadronic calorimeter. The singular contributions of these parts are:

$$\begin{gathered}
E_{mip}^{abs} = 2\,[\mathrm{cm}]\,\times 2.88\,\left[\mathrm{MeVcm^2/g}\right]\,\times 7.83\,\left[\mathrm{g/cm^3}\right] = 22.55\ \mathrm{MeV} \\
E_{mip}^{FR3} = 0.1\,[\mathrm{cm}]\,\times 1.85\,[\mathrm{MeV/cm}] = 0.185\ \mathrm{MeV} \\
E_{mip}^{scint} = 0.5\,[\mathrm{cm}]\,\times 2.0\,[\mathrm{MeV/cm}] = 1\ \mathrm{MeV} \\
E_{mip}^{air} = 0.35\,[\mathrm{cm}]\,\times 0.00129\,[\mathrm{MeV/cm}] = 2.3\ \mathrm{keV}
\end{gathered} \tag{6.4}$$

The total average energy lost by a minimum ionizing particles in one module of the CALICE AHCAL is 23.78 MeV; 1 MeV is deposited in the scintillator and 22.78 MeV are deposited in the absorber. The sampling fraction of a mip in the CALICE AHAL is $E_{mip}^{scint}/\left(E_{mip}^{abs}+E_{mip}^{scint}\right) = 0.04205$. This is not the sampling fraction of a muon in the hadron calorimeter. The non-mip electromagnetic component of the muon energy loss causes a significant energy dependent difference between the sampling fraction of a muon and of a theoretical mip.

To conclude, the average energy deposited by a theoretical mip in the AHCAL is much lower than the expected average energy deposited by muons in the AHCAL; the non-mip component of the muon signal has to be taken into account for a precise study of the response of the AHCAL to muons.

Production of δ rays

The emission of δ-rays is one of the mechanisms responsible to the relativistic rise of the Bethe Bloch beyond the minimum. The energy spectrum of δ-rays with energy $T >> I$,

---

[5] The chemical composition of the absorber layer of the AHCAL used in this thesis refers to the S235 steel [133, 158]. However, the iron is the dominant contribution in the calculation of the energy losses by minimum ionizing particles, while the other component introduce a small effect at the sub-percent level.

with I the ionization energy of the material, is:

$$\frac{d^2N}{dTdx} = \frac{1}{2}Kz^2\frac{Z}{A}\frac{1}{\beta^2}\frac{F(T)}{T^2} \tag{6.5}$$

The function $F(T)$ includes the spin-dependence:

$$F(T) = \begin{array}{lll} 1-\beta^2\frac{T}{T_{max}} & \text{spin} & 0 \\ \\ 1-\beta^2\frac{T}{T_{max}} + \frac{1}{2m^2c^4}\left(\frac{T}{1+\gamma}\right)^2 & \text{spin} & \frac{1}{2} \\ \\ \left(1-\beta^2\frac{T}{T_{max}}\right)\left(1+\frac{1}{3}\frac{T}{T_c}\right) + \frac{1}{3m^2c^4}\left(\frac{T}{1+\gamma}\right)^2\left(1+\frac{1}{2}\frac{T}{T_c}\right) & \text{spin} & 1 \end{array} \tag{6.6}$$

where T_{max} is the maximum momentum transfer in a single interaction with the atomic electrons (eq. 6.1) and T_c is defined as:

$$T_c = \frac{m^2c^2}{m_e} \tag{6.7}$$

In Fig. 6.4 the differential energy spectrum is reported of the δ-rays produced by a 120 GeV particle, with the mass of a muon — 105 MeV. The three curves shown in the figure correspond to the spin-0, spin-1/2 and spin-1 hypothesis. The separation between the spin-0 and spin-1/2 hypothesis is significant only above about 50 GeV. According to eq. 6.6 it depends on the factor $2 \cdot mc^2 \cdot (1+\gamma)$ which introduces only a small contribution. The difference between the spin-1 and the spin-1/2 hypothesis is more evident. It is enhanced when the energy of the δ-ray is comparable with T_c or with the energy of the primary particle E. In the example of Fig. 6.4, $T_c = (105 \cdot 105)/0.511 \sim 20$ GeV. Hence, in order to observe a spin-dependent effect in the δ-ray production, the energy range above 20 GeV has to be investigated. This sets also a limit on the energy of the primary particle. As shown in equation 6.1, the energy of the primary particle has to be much larger than T_c. In this example only particles with energy above 20 GeV will show the spin-dependence. In the regime below the discussed limits, the spin-dependence is not significant.

The material property which mainly affects the emission of δ-rays is the density. It contributes linearly to the total number of knock-on electrons produced. The atomic number of the material enters the formula only through the term Z/A which is roughly constant. Hence it does not contribute significantly.

The measurements of the hard knock-on electrons are an established experimental technique used in the analysis of the cosmic rays detected with ionization chambers. Highly energetic knock on electrons in the range between 15 and 200 GeV are identified as bursts along the ionization tracks of cosmic muons. Their energy distribution was found in excellent agreement with the theoretical expectations [178–180].

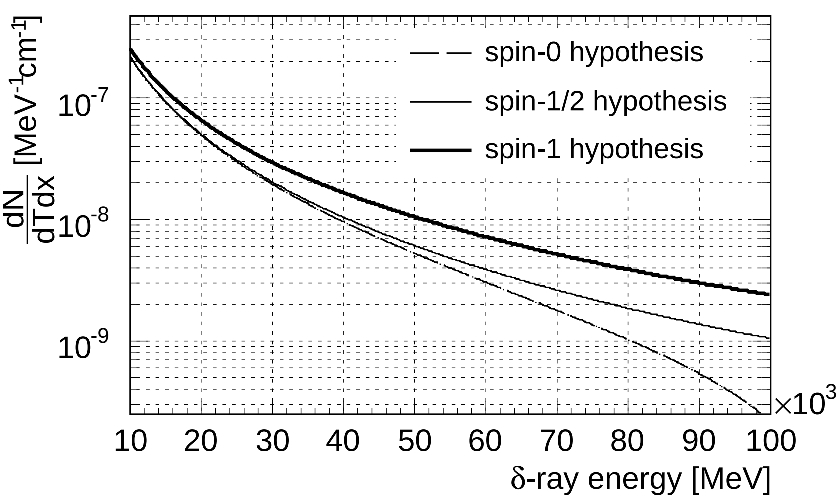

Figure 6.4: Differential energy spectrum of the δ-rays produced by a 120 GeV particle with the muon mass (105 MeV). The discontinuous line is the spin-0 expectation, the continuous thin line is the spin-1/2 expectation and the thick continuous line is the spin-1 expectation, according to equations 6.6.

6.1.2 The electromagnetic shower

The experimental signature of the higher order non-ionization energy losses of muons in matter is the presence of electromagnetic shower along the ionization track. The electromagnetic shower is the typical multiplication process initiated by a photon or an electron interacting with matter.

Interaction of Electrons with Matter

Electrons loose energy mainly through collision and bremsstrahlung. The small electron mass is the main source of differences from the behaviour of heavy charged particles. The probability of bremsstrahlung and ionization energy loss of electrons is shown in Fig. 6.5. The ionization is the most relevant process up to 10-20 MeV. More energetic electrons undergo bremsstrahlung with higher probability. A critical energy can be defined as the value ϵ_c (Fig. 6.6) at which the ionization loss per radiation length is equivalent to the energy of the primary electron. An approximation to the critical energy is given by:

$$\epsilon_c = \frac{610 \text{ MeV}}{Z + 1.24} \tag{6.8}$$

for materials in the solid and liquid phase, and

$$\epsilon_c = \frac{710 \text{ MeV}}{Z + 0.92} \tag{6.9}$$

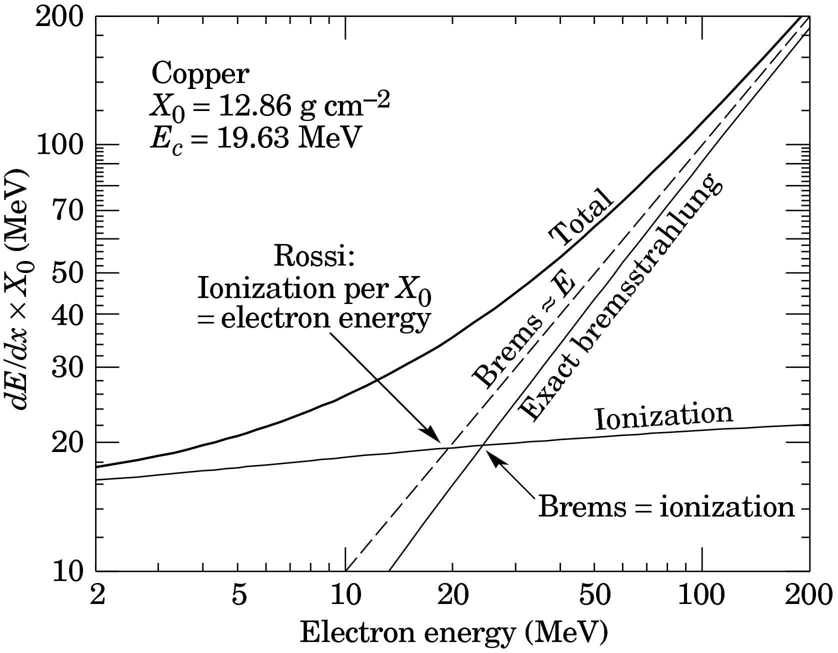

Figure 6.5: Ionization and bremsstrahlung of an electron in matter. The critical energy E_c s defined as the energy at which the ionization probability equals the bremsstrahlung probability. The different Rossi definition is also sown. Figure from [19].

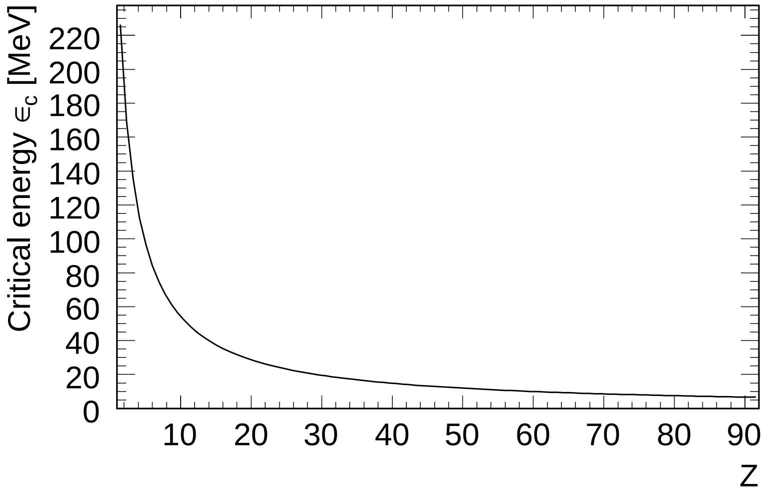

Figure 6.6: Dependence of the critical energy on the atomic number Z of the material. The critical energy does not exceed 250 MeV.

for gases. The emission of photon radiation is the dominant process when the energy of the electrons is higher than ϵ_c.

The scaling length parameter for the electromagnetic interaction of electrons in the hadronic calorimeter is the radiation length X_0. It is defined as the distance over which

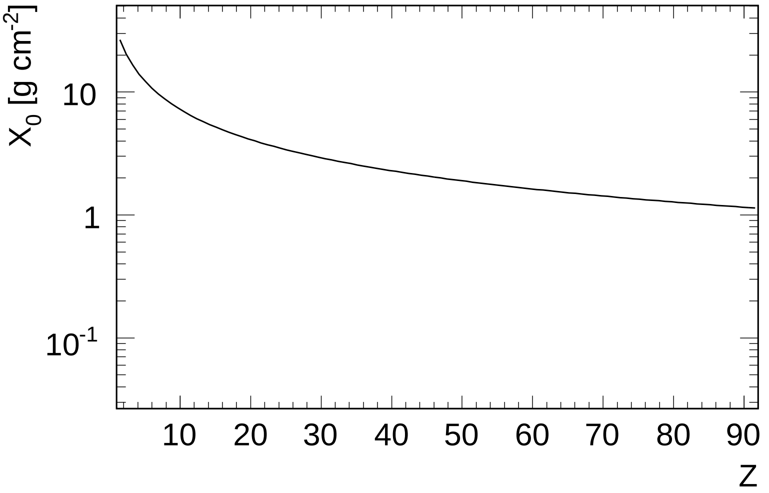

Figure 6.7: Dependence of the radiation length X_0 on the atomic number Z.

a high energy (>> 1 GeV) electron or positron loses on average 63.2% of its total energy to bremsstrahlung. It is calculated as [19]:

$$X_0 = \frac{716.4A}{Z\,(Z+1)\ln\left(287/\sqrt{\mathrm{Z}}\right)} \tag{6.10}$$

In the AHCAL prototype, the absorber material is mainly iron (Z=26). The critical energy is hence $\epsilon_c \approx 28MeV$. The X_0 is 1.8 cm in the absorber and 2.62 cm in the full absorber/scintillator layer.

Interaction of photons with matter

Photons release their energy to the electrons of the atomic shells through photoelectric effect, Compton scattering and e^+e^- pair production. The interaction of photons with matter is usually described with a scaling factor for length, the *attenuation coefficient* μ. It is the path which a photon can travel without undergoing any of the processes described above. The number of photons I which are transmitted after I_0 photons traverse a given thickness x is hence:

$$I = I_0 e^{-\mu x} \tag{6.11}$$

The attenuation coefficient of the three processes is shown in Fig. 6.8.

The photoelectric effect is dominant for energies lower than 500 MeV. The photon transmits its total energy to the atomic electron and it is absorbed in one single interaction. The total energy released to an electron with binding energy E_b by a photon with energy E_γ is $E_\gamma - E_b$. The cross section of the photoelectric effect is featured by discontinuities in the low energy region, corresponding to the binding energies of the

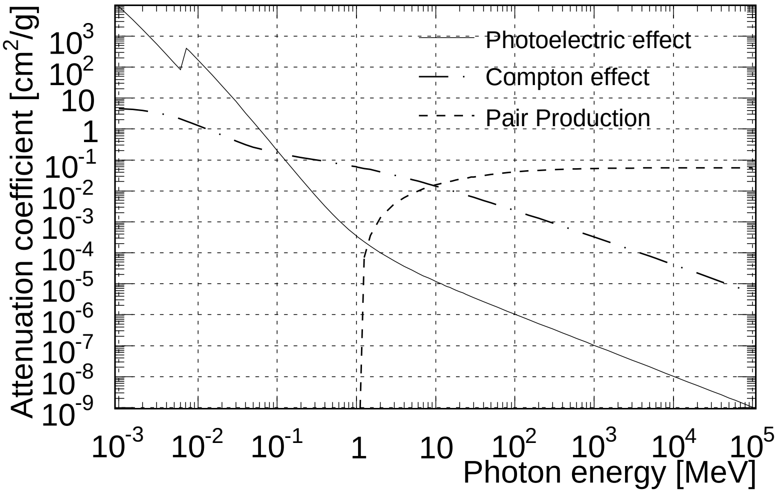

(a)

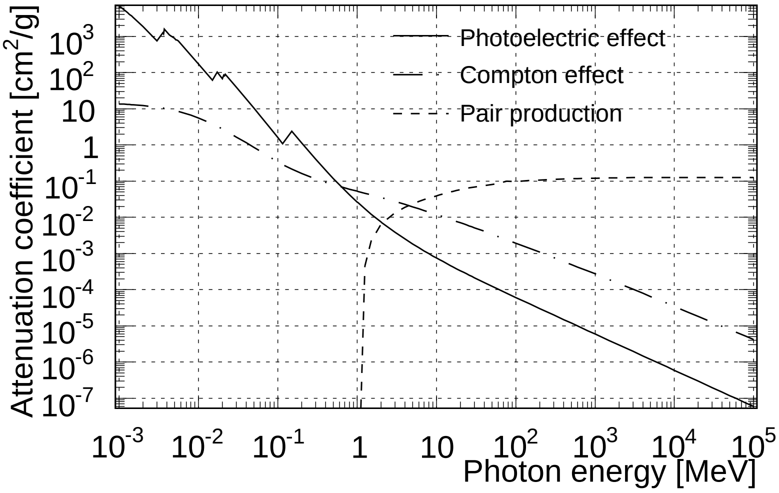

(b)

Figure 6.8: Contribution of photoelectric effect, Compton effect and pair production to the absorption coefficient in iron (a) and uranium (b).

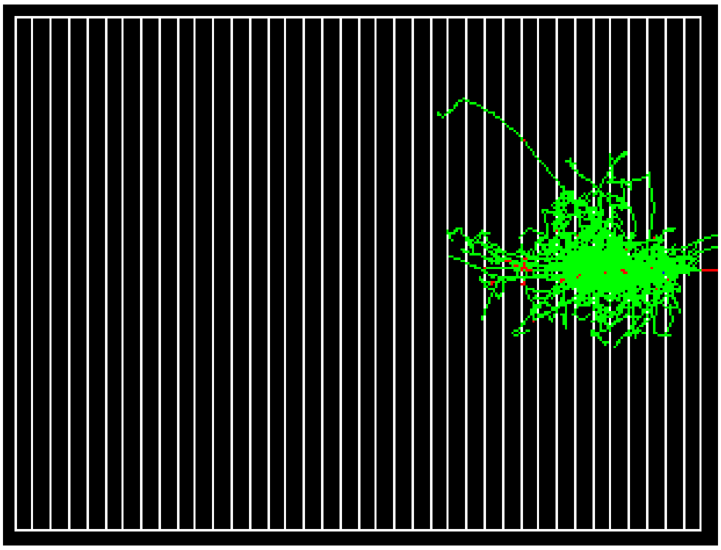

Figure 6.9: GEANT4 simulation of a 1 GeV electron interacting with the AHCAL prototype.

electrons in the various shells of the absorber atom. The probability of photoelectric effect is maximal when the photons have the same energy of the electrons in the shells, and then decreases abruptly. In Fig. 6.8(a) and 6.8(b) the peaks corresponding to the atomic shells are shown for iron and uranium. The dependence of the photoelectric effect probability on the material is empirically described by the following equation:

$$\tau \cong \frac{Z^n}{E_\gamma^{3.5}} \tag{6.12}$$

with n ranging between 4 and 5. The photoelectric effect is dominated by the atomic number of the material.

The Compton effect consists of a scattering of the incident photons in the electric field of the electrons of the atomic shells. The energy of the photon, after one interaction, is calculated with the conservation of the energy and momentum as:

$$E'_\gamma = \frac{E_\gamma}{1 + \frac{h\nu}{m_e c^2}\left(1 - cos\left(\theta\right)\right)} \tag{6.13}$$

where θ is the emission angle respect to the incident direction. The probability of Compton effect is dominant for photons with energy in the 1 MeV range. It depends on the number of electrons in the material and depends linearly on Z.

If the photon energy is above the sum of the masses of an electron and a positron (1.02 MeV) the production of an electron positron pair is possible. This mechanism is dominant for energies higher than 5-10 MeV.

Topology of an electromagnetic shower

The electromagnetic cascade is generated by the interplay of the radiation of Bremsstrahlung photons from electrons and of the production of e^+e^- pairs from photons. A primary electron can radiate many photons on its way through the detector. The majority of these photons are very soft, and loose their energy principally through Compton and photo-electric effect. But the most energetic undergo pair production. They generate electrons and positrons with energy higher than the critical energy (ϵ_c defined in eq. 6.6) which undergo further Bremsstrahlung. However, as the shower develops, the average energy of the shower particles decreases and at a defined depth — the *shower maximum* — no further multiplication occurs.

In Fig. 6.9 the longitudinal profile is shown of an electromagnetic shower generated by a 1 GeV electron in the AHCAL. The electrons produced in the shower are represented with the green segments. This is the typical electromagnetic component formed along the muon ionization track.

The transversal propagation of an electromagnetic shower is expressed in terms of X_0 (Eq. 6.10). The lateral size is parameterised in terms of the *Moliere radius* ρ_m. This quantity is defined as:

$$\rho_M = 21.2\frac{X_0}{\epsilon_c} \tag{6.14}$$

A cylinder with radius $2\rho_M$ contains 98% of the electromagnetic shower.

The Moliere radius is much less weakly dependent on Z than the radiation length. For example, copper (Z=29) and lead (Z=82) have a Moliere radius, respectively, of 15.2 mm and 16.0 mm, while the radiation length is 14.3 mm vs. 5.3 mm. The morphology of the shower is affected, hence, in the longitudinal more than in the lateral dimension. The Moliere radius of the CALICE AHCAL prototype is about 24.7 mm, as shown in table 5.3.

6.1.3 The e/mip ratio

The electromagnetic shower consists of a multiplication chain of electron and positrons. The corresponding signal in a sampling calorimeter is the sum of the ionization energy deposited in the active layers. The electron signal can be compared with the response to a sum of minimum ionizing particles whose combined energy deposit is equal to the primary electron. This comparison is quantified with the e/mip ratio.

The relation $e/mip = 1$ could be expected, being the electromagnetic shower an ensemble of minimum ionizing particles. On the contrary experimental measurements showed that it depends on the Z of the material[39–42]. The e/mip ratio can be as low as 0.6 in uranium sampling calorimeters. The low energetic electrons and positrons in the electromagnetic shower cause this difference between the response to electrons and to minimum ionizing particles. Monte Carlo simulations show that about 30% of the total energy of an incoming electron is deposited in the calorimeter by secondary particles with energy lower than 1 MeV [37]. These soft secondary particles are originated by bremsstrahlung photons.

The ratio $e/mip < 1$ is hence the consequence of the Z-dependent absorption of low energetic photons and electrons. On one side, the soft photons interact with matter mainly via photo-electric effect which depends on Z as Z^{4-5} (equation 6.12). On the other side, the range of soft electrons decreases significantly with Z. This effect plays an important role in the sampling calorimeters in which the Z of the absorber layer is much larger than the Z of the sensitive layer. In fact the soft photons generate soft ionizing electrons more likely in the absorber. These electrons are stopped in the absorber, without contributing to the signal in the sensitive layer. Only the few of them, which are produced just near the border between the absorber and the scintillator layer, eventually deposit energy also in the sensitive layer. Therefore the response to the soft electrons and photons produced in the electromagnetic shower is lower than the response to the pure ionization component.

The e/mip ratio is an important parameter for the characterization of the hadronic calorimeter. According to equation 5.4, it enters the e/h ratio, with a consequent effect to the energy resolution of the device.

6.2 Experimental set-up

6.2.1 The Detectors

The measurement is performed using the prototype of hadron calorimeter developed by the CALICE Collaboration described in section 5.4. In September 2006 the installation consisted of 30 layers. At that time only 23 sensitive modules were produced. The first 17 layers of the calorimeter were fully equipped, while the last 13 layers were equipped with the remaining 6 modules, one every other layer (Fig. 6.10). The SiPMs in the last 6 modules were particularly noisy. Therefore, the last 6 modules are not used in the analysis of the data presented in this paper. The full prototype was available in 2007 and the noisy modules were all repaired. The analysis of the 2007 AHCAL comprises all the modules. The analog hadron calorimeter (AHCAL) was tested in combination with the prototypes of the highly granular silicon-tungsten electromagnetic calorimeter (ECAL) and of the scintillator strip tail catcher (TCMT). The test beam set-up is shown in Fig. 6.11.

The ECAL has an 18×18 cm^2 lateral section. It is situated centrally, in front of the AHCAL, and covers only its high granular core. The ECAL prototype consists of 30 layers of tungsten, the first ten of thickness 1.4 mm, the next ten of 2.8 mm,and the last ten of 4.2 mm, comprising 24 radiation lengths in total at normal incidence. The development of the showers was sampled using 30 layers of silicon PIN diode pads interleaved between the tungsten plates. The silicon thickness was 525 mm, and each pad had dimensions 1×1 cm^2. The sensors were made on 4 inch wafers in units of 6×6 pads. In 2006 it was equipped with 30 sensitive layers of silicon pads, but each layer was missing one third of the readout channels, thus reducing the active area to 18×12 cm^2. The total number of instrumented readout channels was 6480 out of the 9720 foreseen. For the 2007 installation the bottom layers were also equipped, apart from the front-most 4 layers.

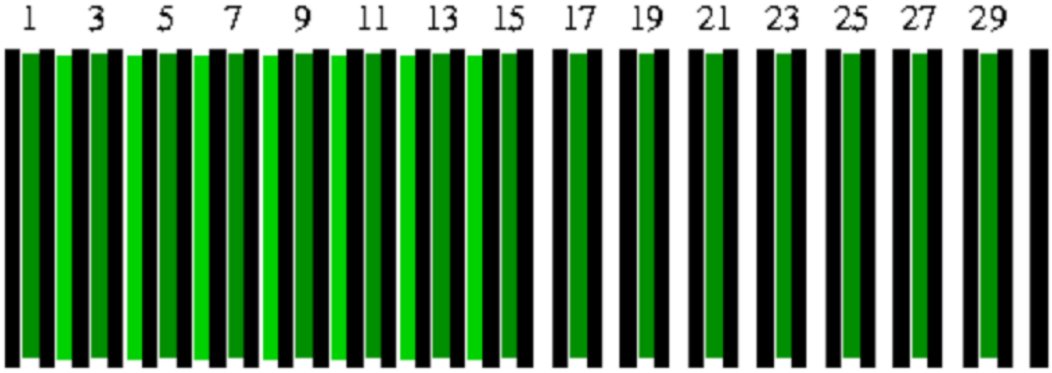

Figure 6.10: Equipment of the hadron calorimeter in the 2006 configuration. Only 23 sensitive modules (green) were installed. The absorber modules are indicated in black.

Figure 6.11: Set-up of the detectors in the CERN test beam. The AHCAL was tested in combination with a prototype of highly granular Silicon/Tungsten electromagnetic calorimeter (ECAL) and a strip-scintillator/steel Muon Tracker Tail Catcher (TCMT). Figure from [3].

The TCMT detects eventual leakages directly after the AHCAL. It measures 109×109 cm^2 perpendicular to the beam and 142 cm along. It consists of a *fine* and a *coarse* section. Each section has 8 layers of scintillating strips interspersed with steel absorbers. The absorber plates are 2 cm thick in the *fine* section and 10 cm in the *coarse*. The active layers of the TCMT are made of 5 cm wide, 0.5 cm thick plastic scintillators strips. The photons from the fibre are detected using SiPMs.

In the following sections the name *2006 set-up* (*2007 set-up*) will be used to refer to the detector configuration in 2006 (2007).

6.2.2 The Beam Line

The measurement presented in this thesis was performed at the H6 beam line of the CERN SPS facility in 2006-2007. A sketch of the Test Beam set-up is shown in Fig. 6.12. The beam line is equipped with a monitoring and trigger systems. A Cherenkov detector for e/π separation, 3 x/y pairs of Multi Wire Project Chambers (DC) with double read-out for tracking purposes are available but not used in this analysis. A veto counter allows separating the multi-particle events (Sc1) and several scintillator plates (Sc, Mc) can be used to form a trigger in different combinations.

The SPS proton beam has a momentum of 450 GeV/c. It is steered on a Beryllium target in order to generate a secondary beam, mainly composed of pions and neutral hadrons with a wide momentum spectrum. The momentum of the secondary beam is selected with a spectrometer system after the target and the maximal currents in the magnets limit the secondary beam momentum in the range between 30 GeV/c and 205 GeV/c. Electrons from the secondary beam usually loose lots of energy by synchrotron radiation and are not focused by the subsequent beam orbit. Therefore the secondary beam is a pure pion beam. A tertiary pion beam with energy as low as 5 GeV/c is obtained introducing a secondary polyethylene target in the beam line. Also a tertiary electron beam is available, introducing a secondary lead target. The π^0s produced in the interaction of the $\pi^\pm$ beam with the lead target initiate electromagnetic showers. The electrons and pions of the tertiary beam are focused with a series of magnets and spectrometers.

Two muon sources are available. First, muons are obtained as parasitic beam dumping the secondary beam with a series of collimators and beam dumps. Parasitic muons were collected at the secondary beam momentum of 120 GeV/c. Second, muons contaminate the secondary pion beam at any energy (E_π). They are the result of the decay $\pi \longrightarrow \mu\nu_\mu$. From the kinematics of a two body decay, the muon energy spectrum is flat, extending from $E_\pi \left(m_\mu/m_\pi\right)^2$ to E_π. The average muon energy is hence approximately $0.8 \cdot E_\pi$. Moreover, muons coming from early decays of pions, before the spectrometer momentum selection, are selected at the correct beam energy. The final distribution is hence more peaked at the beam energy. When in the following we speak about muons of E GeV, it is meant muons from the decay of an E GeV pion.

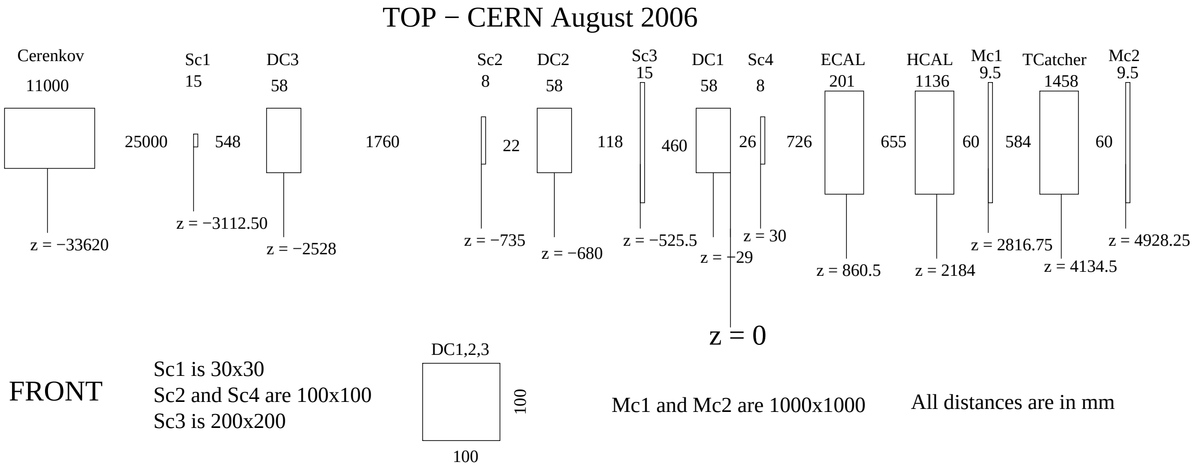

Figure 6.12: Test Beam set-up in 2006. The analog hadronic calorimeter (AHCAL) is tested in combination with the Electromagnetic Calorimeter (ECAL) and the Tail Catcher (TCMT). The beam line is equipped with a Cherenkov detector, 3 x/y pairs of Multi Wire Project Chambers (DC) and several scintillators (Sc, Mc) for the definition of the trigger. In particular the muon trigger for the identification of parasitic muons consists of two 1×1 m^2 scintillator plates (Mc1 and Mc2). The 2007 set-up is featured by the same components along the beam line. The Monte Carlo, developed in Geant4 for the test beam studies, includes all the elements shown in the figure.

6.2.3 Simulation of the Detectors and of the Beam Line

The test beam set-up is included in the geometry database of the modular simulation package for the International Linear Collider MOKKA [133] as described in Fig. 6.12. The Monte Carlo of the experiment is developed in GEANT4 [132] and the results are stored in LCIO format files [181] and are analysed in the MARLIN framework [134]. The equipment of the detectors is described in the Monte Carlo geometry for the 2006 set-up and the 2007 set-up.

The effects of the electronic read-out of the detector are included after the full simulation. The statistics of the detection efficiency in the scintillator and in the SiPM, the noise level and the saturation effect of each cell is convoluted with the result of the Monte Carlo. This procedure is called *digitization* [182].

6.2.4 The Calibration of the AHCAL

Three measurements are necessary for the calibration of the sensitive cells of the hadron calorimeter: the muon signal, the gain and the saturation response of the SiPM used to read out that specific cell. Moreover the temperature-dependent response of the SiPM requests also additional temperature correction of the amplitude of the measured signal. The calibration procedure of the AHCAL is described in [160, 182].

The most probable value of the muon signal (MIP) is used to set the absolute energy scale of the detector[6]. The amplitude of each calorimeter cell is expressed in multiples of the MIP. The position of the MIP defines the noise threshold of the cell; only these cells with energy deposited higher than 0.5 MIP are considered and define a physics hit in the detector.

The gain calibration, i.e. the signal of a single SiPM pixel, is extracted from a multi-Gaussian fit to the spectrum recorded from low-intensity LED light exposure. Such spectra are simultaneously obtained for all SiPM by fleshing low intensity LED light to each tile with the LED calibration system. For this measurement the VFE electronics is operated with the highest possible preamplifier gain (about 90 mV/pC). The shortest shaping time of the ASIC chip is selected (about 40 ns) to minimize integration of SiPM dark-rate and optimize single photo-electron peak separation. Though more favourable from the noise point of view, a 40 ns shaping time is not sufficient to provide the required trigger latency which in the test beam setup is typically of 150 ns (mainly driven by the DAQ logic and trigger distribution). A shaping time of about 200 ns is used when collecting physics data, in combination with a medium gain (about 8 mV/pC) to match the range of energy deposited in one tile to that of the 16-bit ADC. It is necessary hence to account for the different ASIC gains in these two modes of operation of the VFE electronics. For this purpose, an inter-calibration factor (I^{phys}_{calib}) is extracted for each channel as the ratio of SiPM response to medium-intensity LED light when operating the ASIC chip in the two modes (*phys* and *calib*).

The saturation effect of the photo-detector described in chapter 5 has to be taken into account. For correction of the non-linearity, beam data is converted to the pixel scale by the gain calibration, and mapped to the equivalent linear intensity.

Finally, the temperature correction is applied. The most probable value of the muon signal and the gain of the SiPM have a strong temperature dependence. The temperature is measured inside the AHCAL via five sensors in each module. In the 2007 set-up, 36 out of 38 modules have sensors arranged in a vertical line in the horizontal middle of the active area; the two modules left have one sensor in the geometrical centre and one sensor close to the four corners [183]. The calibration constants are scaled to match the data-taking condition of the analysed sample. It was measured that the average temperature slope for the amplitude of the most probable value A_{MIP} and for the gain G is:

$$\frac{1}{A_{MIP}}\frac{dA_{MIP}}{dT} = -3.7\frac{\%}{K} \quad \frac{1}{G}\frac{dG}{dT} = -1.7\frac{\%}{K} \tag{6.15}$$

After applying the correction chain the calorimeter response is expressed in multiples of the MIP energy. To convert this amplitude into energy in GeV the MC information is used. The most probable value of the energy deposited by a 120 GeV muon in one scintillator cell is 0.861 MeV; hence 1 MIP is set to 0.861 MeV. This transformation sets the absolute scale (in MeV) of the visible energy.

The energy scale for electrons is defined calibrating the visible energy (in MIP energy units) registered in the hadronic calorimeter detecting electrons, in dedicated electrons

---

[6] The extraction of the most probable value of the muon signal is treated in section 6.4.

runs. The visible energy in MIP, at the electromagnetic energy scale is related to the energy of the incoming beam by the following relation [182]:

$$\begin{aligned} E_{vis}\,[MIP] = (42.71 \pm 0.03_{stat} \pm 2.5_{syst})\,[\mathrm{MIP/GeV}]\ \times E_{tot}\,[\mathrm{GeV}] + \\ + (2.1 \pm 0.2_{stat} \pm 7.25_{syst}\,[\mathrm{MIP}]) \end{aligned} \tag{6.16}$$

The hadronic energy scale is studied in specific π runs. The systematic associated to this measurement is still under investigation and it will not be treated in this study [184, 185].

6.3 Experimental data

In this analysis the following samples are considered:

1. Monochromatic 120 GeV parasitic muon beam (about 1000000 events for the 2006 set-up and for the 2007 set-up). For the systematic study, a group of muon samples collected within 12 hours and a group of muon samples collected within 2 days are available for the 2007 set-up.
2. Muons contaminating pion runs in the 2006 set-up (about 20000 events for each of the following energies: 10 GeV, 15 GeV, 18 GeV, 20 GeV, 40 GeV, and 80 GeV)
3. 50 GeV muons impinging the detector at different angles contaminating the pion runs in the 2007 set-up (30000 events for each of the following configurations[7] : $0°$,$(10.0° \pm 0.1°)$,$(19.71° \pm 0.14°)$,$(28.3° \pm 0.1°)$)
4. Pion data, in the 2006 set-up (about 500000 events for each of the following energies: 10 GeV, 15 GeV, 18 GeV, 20 GeV, 40 GeV, and 80 GeV)
5. Pion data in the 2007 set-up (about 500000 events for each of the following energies 10 GeV, 15 GeV, 20 GeV, 25 GeV)

The samples contain only particles detected in the highly granular core of the HCAL.

Isolated muons have a very clean signature in the CALICE AHCAL. Because of the high granularity, they can be identified as isolated tracks in the detector. In Fig. 6.13 the typical muon track detected in the AHCAL prototype is shown. A simple clustering algorithm was developed in order to find muon tracks. The hits with a lateral displacement not larger than R_{tube} and belonging to any layer are grouped. The parameter R_{tube} is a multiple of a cell size (R_{cell}=3 cm in the highly granular core). The found groups have to satisfy two requirement in order to be considered isolated tracks:

Isolation. The number of hits grouped in a cluster with $R_{tube} = 2 \times R_{cell}$ is less than N_{hits}. The parameter N_{hits} depends on the number of expected noise hits in the volume of AHCAL where the cluster extends (N_{noise}), on the total number of layers used in the analysis (N_{lay}) and the margin of hits requested for the isolation (N^{is}_{hits}). N^{is}_{hits} is the maximum number of additional hits which can be found around the ionization track, because of higher order electromagnetic effects. N_{hits} is hence defined in the range ($N_{noise} < N_{hits} < (N_{lay} + N_{noise} + N^{is}_{hits})$).

---

[7] The angles refer to the direction perpendicular to the frontal surface of the AHCAL.

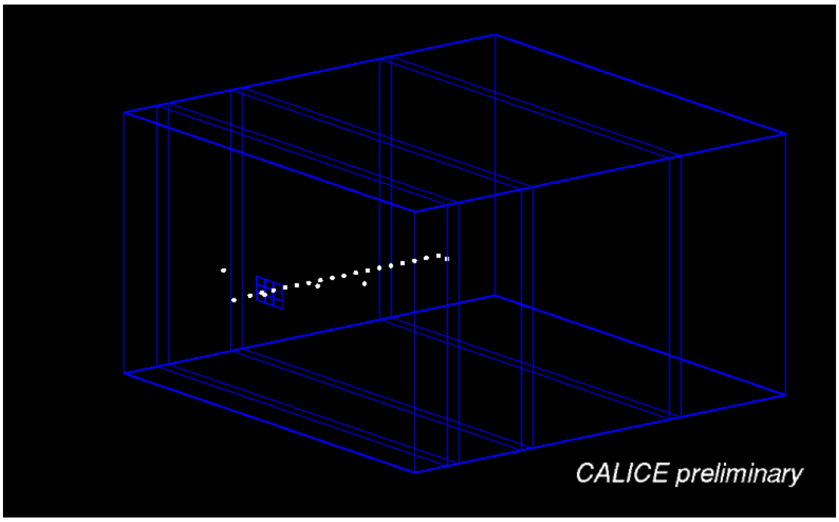

Figure 6.13: Signal from a 120 GeV muon collected in the test beam of the AHCAL prototype. The high granularity allows to identify a track. The isolated hits correspond to random noise in the detector.

Linear shape. The hits have to be displaced along a line in the detector. A least square 3-d linear fit is used to find the slope of the track.

In the following discussion a isolated muon track in the 2006 set-up is selected according to the requirement ($2 < N_{hits} < 30$), where $N_{noise} = 2$, $N_{lay} = 17$ and $N^{is}_{hits} = 11$. Moreover, a isolated muon track in the 2007 set-up is selected according to the requirement ($2 < N_{hits} < 60$), where $N_{noise} = 4$,$N_{lay} = 36$ and $N^{is}_{hits} = 20$.

The ECAL and TCMT are actively used for the event selection. Dedicated analysis tools are developed in order to handle the data of these two sub-detector. In this analysis the reconstruction of the data of the ECAL and TCMT proposed and implemented in [160, 186, 187] are used. These methods were specifically tested in the data analysis of the specific sub-detectors.

The sample of parasitic muons (1) is collected with the specific muon trigger formed with the coincidence of the scintillators Mc1 and Mc2 (Fig. 6.12). Therefore it has no contamination from other particles. Nevertheless the energy spread introduced by the material in front of the hadronic calorimeter can be significant. Muons can loose a significant amount of energy in the beam dumps and in the ECAL through δ-rays production, pair production and bremsstrahlung. In the first case the muon beam is contaminated by lower energy secondary particles, mainly electrons, which can eventually be detected in the ECAL. In the second case the electromagnetic activity is clearly visible in the ECAL. A clean muon event is hence identified as a isolated track found in the ECAL with a corresponding isolated track found in the HCAL. The measurement in the ECAL is used to reject the events in which a muon is detected with low energetic electrons or photons or events in which a muon deposits too much energy in the ECAL. Only the tracks which consist of perfectly aligned hits in the hadronic calorimeter are considered. Thus the angular acceptance is reduced to a cone with angle $\alpha \leq atan\,(1.5/50) = 3.8°$

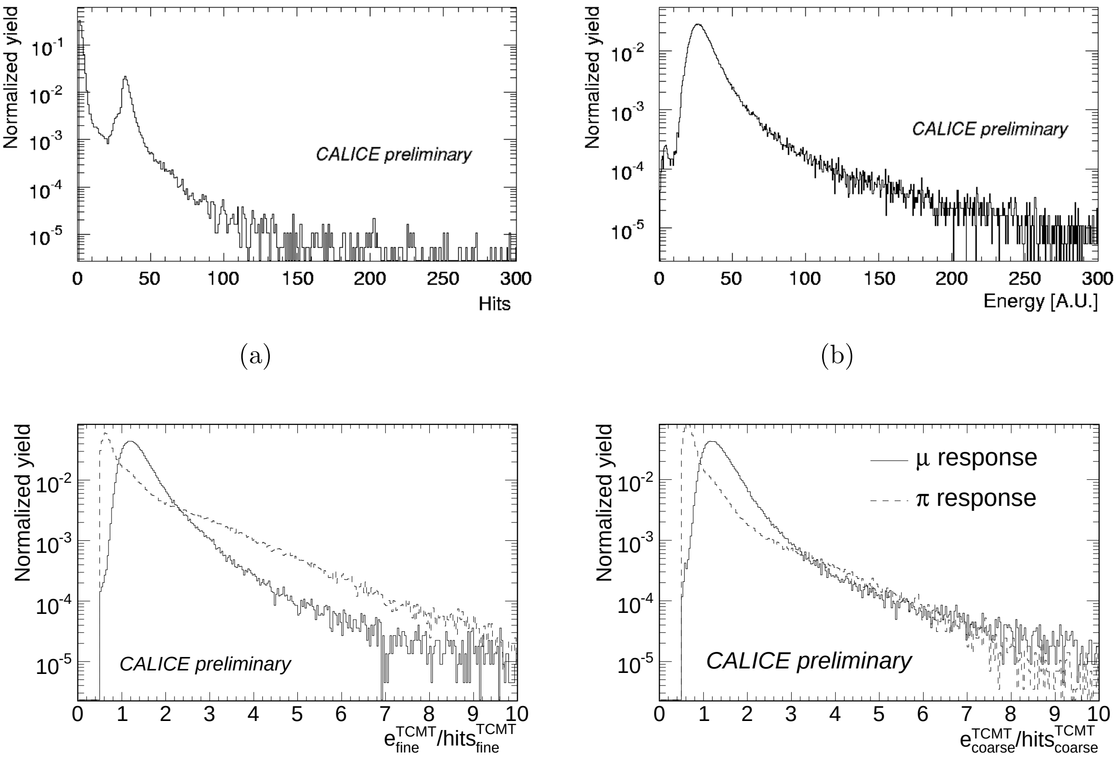

(a) (b)

(c) (d)

Figure 6.14: The most relevant observables used in the muon identification for the parasitic muon runs ((a) and (b)) and for the muons contaminating pion runs ((c) and (d)). In (a) the number of hits registered in the ECAL in a parasitic muon run is shown. The number of hits peaks at 32, corresponding to 30 active layers and 2 noise hits. The high concentration of hits at the noise level indicates muons which do not pass through the ECAL. In (b) the energy deposited in the TCMT through parasitic muons is shown. In (c) and (d) the ratio ($e/hits$) in the two sections of the TCMT is shown for parasitic muon runs and pion runs. A muon is identified with the requirement $1 < e/hits < 1.5$.

and the systematic contribution of the angular spread is minimized [8]. Moreover, not deflected muons are less biased by interactions in the material before the HCAL and the momentum acceptance of the muons is improved. To resume, the selection cuts applied in the sample of parasitic muons are:

1. One isolated perpendicular track in the ECAL
2. One isolated perpendicular track in the HCAL
3. The number of hits in the ECAL is about the total number of layers ($30 < N^{ECAL}_{hits} < 34$)

---

[8] In the calculation of the angle, 1.5 cm is half of the size of one tile and 50 cm is the length of the 17 layers of the analog hadronic calorimeter used in this analysis.

The selection of the muons contaminating the pion runs (2-3) is the same both in the 2006 and in the 2007 set-up. It is performed using the full information of the TCMT. A muon is identified as the only particle which leaves a mip-like signal in the *coarse* and *fine* sections of the TCMT. The probability that a pion punches through the full $7\lambda_0$ of HCAL and TCMT without interacting is about 0.09%. In addiction it is required a low electromagnetic activity before the HCAL. The selection cuts applied to the muons contaminating the pion runs are:

1. A cut on the total number of hits in the ECAL $30 < N_{hits}^{ECAL} < 34$
2. Mip like signature in the *fine section* of the TCMT: $1 < e_{TCMT1}/hits_{TCMT1} < 1.5$
3. Mip like signature in the *coarse section* of the TCMT: $1 < e_{TCMT2}/hits_{TCMT2} < 1.5$

Pions which interact after the 7^{th} layer of the hadronic calorimeter are extracted from the pion runs (4) in order to study the ionization energy deposited by pions in the AHCAL. The event is featured by one isolated track in the first 7 layers of the AHCAL and a hadronic shower in the rest of the AHCAL which leaks eventually in the TCMT. The selection cuts applied are:

1. The track in the first 7 layers has to be isolated: not more than 10 hits in the volume of 3×3 cells around the track.
2. The number of hits in the second part of the hadronic calorimeter is more than 100.

The 2007 pion data (5) are used for the search of muons produced in the pion showers. The specific cuts are shown in the dedicated section.

6.4 Data quality and systematic effects of the detector

The aim of this section is to quantify the effect of the operation of the detector on the quality of the data. This analysis has three key-points. First the systematic study of the smearing of the muon signal in a single cell is proposed. Second the systematic effects of the variation of the temperature in the typical time scale of the data taking is quantified. Third the global effect of the mentioned sources of degradation of the quality of the data on the measurement of the total visible energy is considered. The monochromatic 120 GeV muon samples are used in this analysis.

6.4.1 The signal of the muon in a single scintillator cell

The structure of a single tile of the AHCAL was described in chapter 5. The final signal of the AHCAL prototype in each cell is produced in three steps. First a charged particle in the shower excites the electrons of the plastic scintillator. Second the correspondingly emitted blue scintillation light is collected and shifted to the green spectrum by the wavelength shifter fibre. Third the green photons are detected by the SiPM positioned at one of the ends of the fibre. The produced electric signal is elaborated by the read-out electronics. The detection chain contributes to a sizable smearing of the original ionization signal in the cells. The poissonian fluctuation of the number of photo-electrons

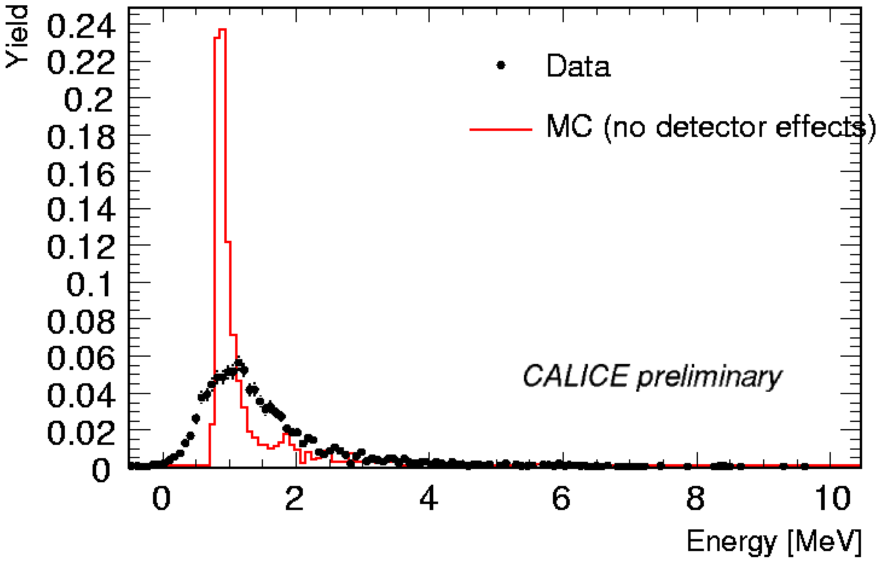

Figure 6.15: The visible signal of a 120 GeV muon in one cell of the hadronic calorimeter for data (points) and Monte Carlo without the effects of the noise of the detector (line).

($N_{p.e.}$) generated in the SiPM is the main source of the smearing of the signal. Its effect on the resolution of the visible energy depends on the $\sqrt{N_{p.e.}}$ and it is not negligible at the m.i.p. scale; the most probable value of the m.i.p. signal is 861 keV and corresponds to 15 ± 3 photo-electrons, with a consequent relative statistical fluctuation of $\sqrt{15}/15 = 25\%$. Moreover, the poissonian smearing does not affect the energy deposited in the single cell uniformly. According to a simulation of the energy response of the single AHCAL cell to muons, a Landau distribution with Most Probable Value at 861 keV and width 60 KeV approximates the energy deposited in the scintillator. The resolution is $60/861 \sim 5\%$. When a m.i.p. particle deposits less energy than 861 KeV (less than 15 photons detected on average), the poissonian fluctuations are in a range between $\sqrt{15}/15 = 25\%$ and $\sqrt{3}/3 = 45\%$, while they go down to about $\sqrt{45}/45 = 10\%$ in case of an energy deposition above 2-3 MeV (more than 30 photons detected in average).

In Fig. 6.15 the signal of a single calorimeter scintillator cell corresponding to a 120 GeV muon is compared with the pure Monte Carlo, excluding the detector read-out smearing. The discrepancy is sizable as expected from the above arguments. In Fig. 6.16 the signal of a single calorimeter scintillator cell corresponding to a 120 GeV muon is compared with the Monte Carlo including the systematic effects of the detector (digitized Monte Carlo). The agreement between data and simulation reflects a good understanding of the smearing and noise effects of the AHCAL [182].

The muon signal measured in the data can be fitted with a Landau distribution convoluted with a Gaussian distribution, which models the smearing of the detector read-out. The result of the χ^2 fit of the response of a single cell to a 120 GeV muon is shown in Fig. 6.17. The Most Probable Value (A_{MIP}) and the width of the smeared

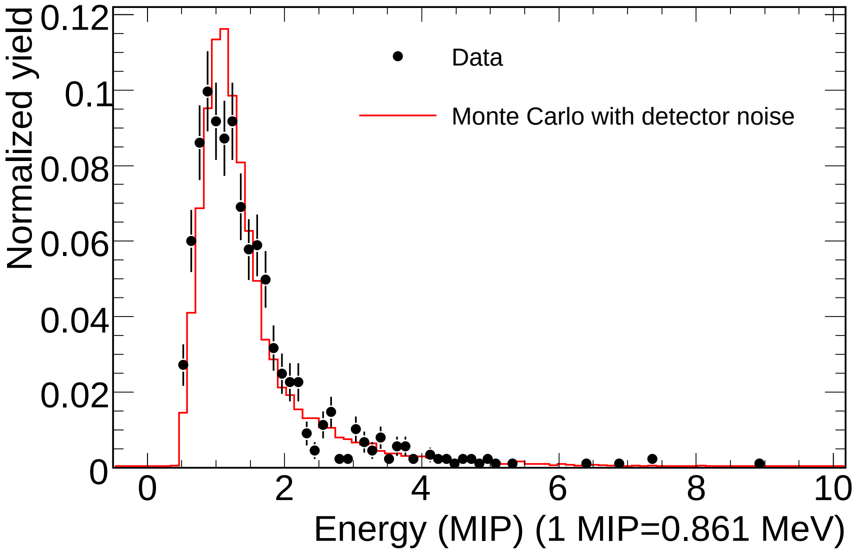

Figure 6.16: The visible signal of a 120 GeV muon in one cell of the hadronic calorimeter for data (points) and Monte Carlo including the smearing effects of the detector (line).

distribution can be extracted with a statistical error of $1 - 2\%$. This fit is used to set the energy scale of all the cells of the AHCAL.

The quality of the muon signal is described with the mip signal collection efficiency and the S/N ratio. The MIP collection efficiency (ϵ_{mip}) represents the amount of the muon signal above the 0.5 MIP noise significance threshold. It is defined as:

$$\epsilon_{mip} = \frac{\int_{0.5 \cdot MIP}^{+\infty} \mathcal{S}(E)dE}{\int_{-\infty}^{+\infty} \mathcal{S}(E)dE} \tag{6.17}$$

where $\mathcal{S}(E)$ is the energy distribution of the muon signal. The MIP collection efficiency is reported in Fig. 6.18 for the 2006 and 2007 set-up. The errors correspond to the spread (RMS) between all cells in one module. An average efficiency of 93% is obtained in 2007, whereas in 2006 the average mip detection efficiency if 96%. It was measured [160] that the number of photoelectrons corresponding to the mip peak (light yield, LY) in 2007 was lower than in 2006, affecting consequently the average quantity of the muon signal above the noise threshold.

The ratio S/N represents the separation between the most probable value of the muon signal and the pedestal. It is defined as:

$$S/N = \frac{A_{MIP}}{\sigma_{Ped}} \tag{6.18}$$

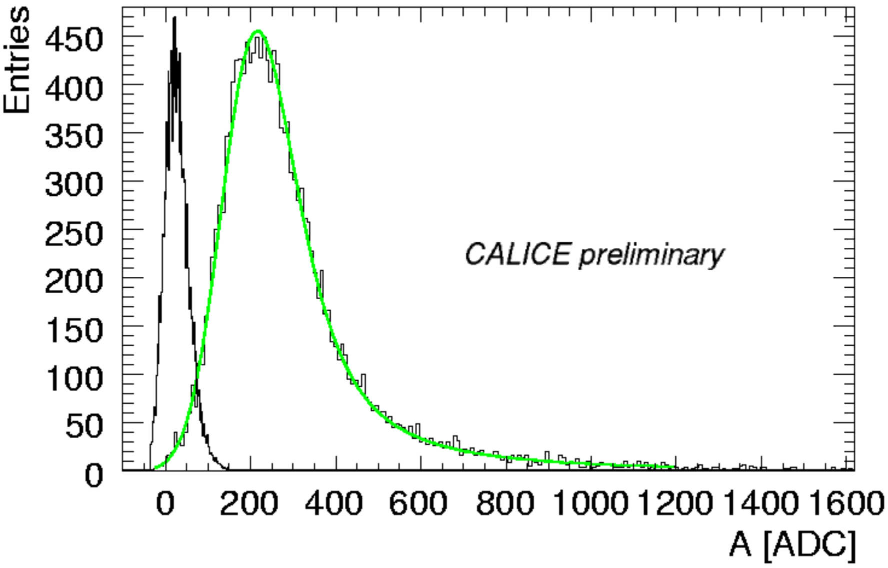

Figure 6.17: The signal corresponding to a 120 GeV muon registered in one cell of the hadronic calorimeter and a pedestal spectrum. The signal is fitted with a Landau distribution convoluted with gaussian (green line). The muon sample is selected in a dedicated parasitic muon run, with high purity. A noise spectrum is shown as a solid histogram. The hadronic calorimeter shows a good resolution power for m.i.p. signals.

where σ_{Ped} is the variance of the pedestal spectrum. Fig. 6.19 shows the average signal to noise ratio for the MIP signal in each module. A ratio of 9-10 is obtained in 2007 as an overall average in the calorimeter. In 2006 a ratio of 12 has been reached in the modules operated at higher LY.

6.4.2 Systematic effects associated to the temperature

The muon samples analysed in this study are collected within a maximum time window of two weeks. The short-term (long-term) systematic effects introduced by the variation of the temperature during the data taking is quantified comparing the average profiles of the muon response measured in a series of dedicated parasitic muon runs collected within 12 hours (2 days). The run temperature is measured with dedicated sensors on the LED board, as described in section 6.2.4. In this study the average temperature on the whole calorimeter measured in the sensors is considered.

In Fig. 6.20 the variation of the average profile of a 120 GeV muon in the hadronic calorimeter is reported. The energy deposited in the tower of tiles traversed by the muon is measured. In (a) the measurement is performed on data collected within 12 hours. In this time window an average temperature fluctuation of about 1° is measured; correspondingly an average fluctuation of the measured energy ranging between 2% and 5%. In (b) the result of the measurement of the average muon energy profile within

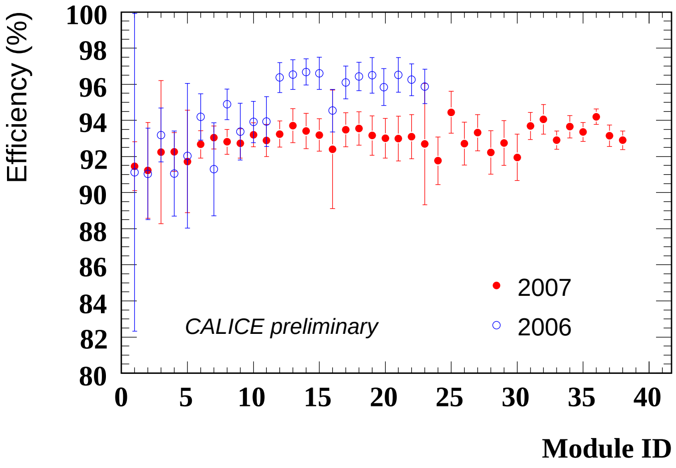

Figure 6.18: Average MIP detection efficiency in each AHCAL module for the 2006 and 2007 data taking periods. The MIP detection efficiency is defined as the integral of the muon signal in one cell above a noise threshold of 0.5, normalized on the total integral of the muon spectrum. The worsening of the mip signal collection efficiency in 2007 is due to a lower LY.

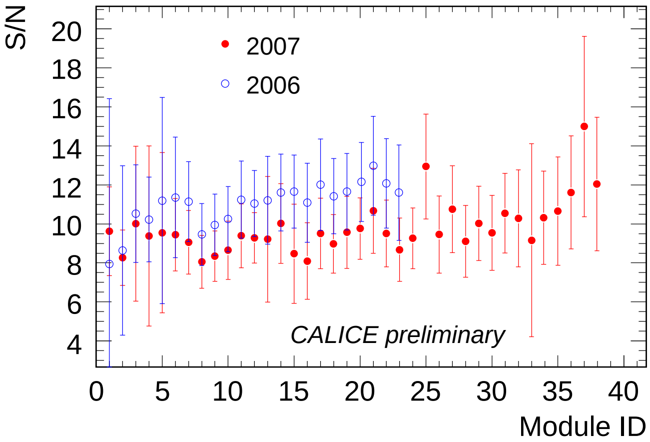

Figure 6.19: Average signal to noise ratio in each AHCAL module for the 2006 and 2007 data taking periods. The S/N ratio is defined as the Most Probable value of the MIP signal over the RMS of the noise spectrum. In the 2006 set-up the average S/N ratio is 11 and in the 2007 set-up it is about 9. As in case of ϵ_{mip}, the worsening of the detector performance in 2007 is due to a lower light yield than in the 2006 set-up. The error bars correspond to the spread (RMS) of the S/N between all cells in a module.

2 days is shown. In this time range an average temperature shift of 4° is measured; correspondingly the signal amplitude is affected by an average shift of 10%. Both the

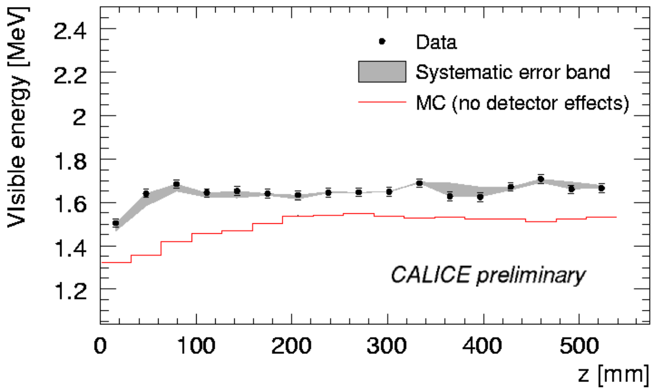

(a)

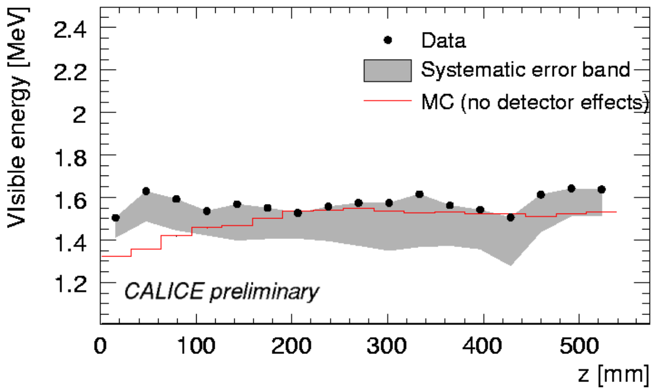

(b)

Figure 6.20: Systematic effect associated to the fluctuation of the temperature. The spread of the measurement of the average profile of a 120 GeV muon within 12 hours (a) and 2 days (b) is shown (grey band). A fluctuation of about 4%/° is observed, in agreement with the expected behaviour of the SiPM.

measurement agree with the expected average temperature slope of the amplitude of the muon signal in equation 6.15.

6.4.3 Systematic effects on the total visible energy

A last question to be addressed is whether the systematic effects mentioned above influence significantly also the total energy measured in the hadron calorimeter. In Fig. 6.21 the total visible energy is shown of a 120 GeV muon detected in data and Monte Carlo with and without systematic smearing effects. The energy deposited in the tower of tiles traversed by the muon is measured. The effects of the smearing of the muon signal in the single cell are statistically suppressed in the energy sum. The measurement in data is reproduced quite well in the Monte Carlo even without introducing the smearing of the

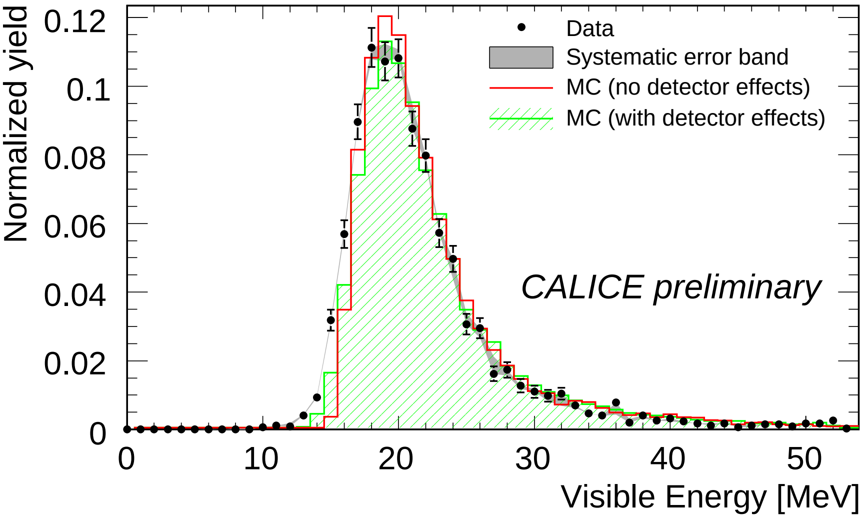

Figure 6.21: Total visible energy deposited by a 120 GeV muon in the AHCAL in a tube with a 3×3 cm^2 section — 1 tile. Comparison between data (filled dots), pure Monte Carlo (red line) and Monte Carlo including the read-out of the detector (filled area). The pure Monte Carlo, the digitized Monte Carlo and the data are found in agreement.

detector read-out. The absolute calibration of the visible energy of the AHCAL allows hence a precise measurement of the total visible energy of a muon.

6.5 Analysis of the response of the AHCAL to muons

6.5.1 Energy dependence of the muon response

The aim of this study is to measure the energy dependence of the average visible energy of muons in the AHCAL. The muon samples extracted from the pion runs in the 2006 set-up are analysed.

The definition of the average muon energy loss is ambiguous [42]. The visible energy spectrum for a 120 GeV muon in the AHCAL was shown in Fig. 6.21 in the previous section. A large tail towards the high energy is visible. Consequently the calculation of the average energy loss is biased by the considered energy range. In this analysis two methods are proposed for the determination of the average energy loss. The first consists of a truncated mean in the range between 15 MeV and 25 MeV. The second consists of the extraction of the Most Probable value of the energy distribution.

The systematic error introduced by the operation of the AHCAL is also considered. According to the results of the previous section, the smearing of the single cell signal caused by the AHCAL read-out does not affect significantly the measurement of the total deposited energy. However, the temperature fluctuations can cause a shift of the energy level and bias considerably the result. The muon samples used for the calibration are

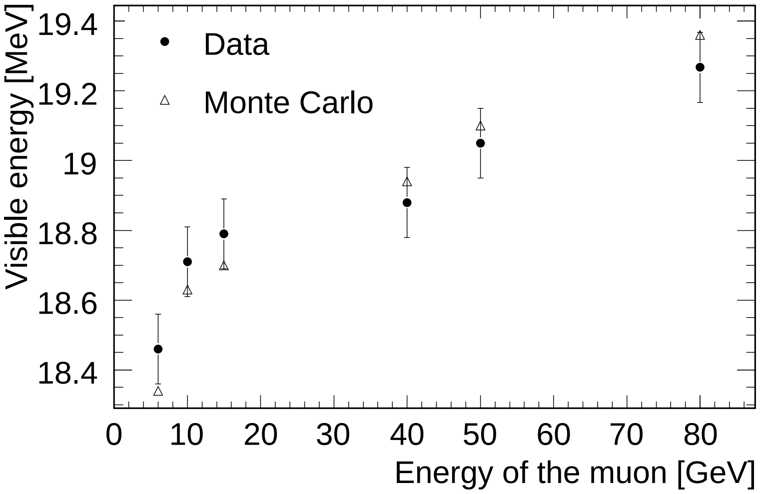

(a)

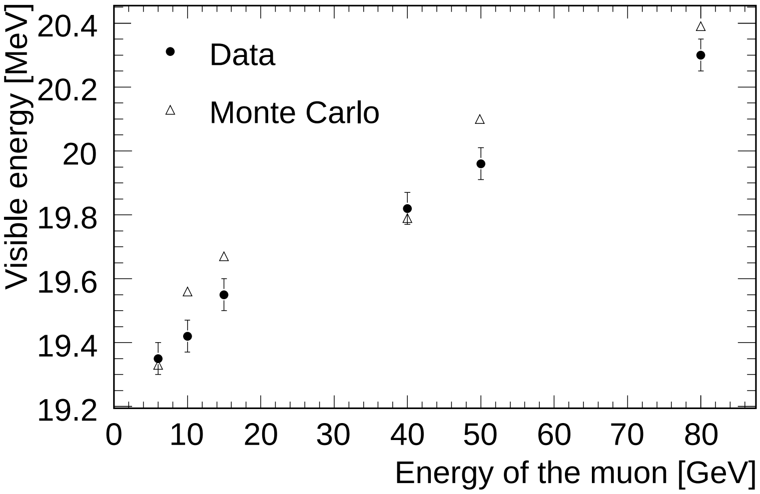

(b)

Figure 6.22: Energy dependence of the response of the hadronic calorimeter to muons. In (a) the dependence of the most probable value of the visible energy is shown. In (b) the dependence of the truncated mean in the range (15 GeV - 20 GeV) is shown. The data (dots) are in good agreement with the Monte Carlo expectation (triangles).

collected at a temperature of 22°. The muon samples at 40 GeV and 80 GeV used in this analysis are collected at an average temperature of 23° while all the other muon samples are collected at an average temperature of 28°. The average temperature correction shift according to the results of last section is applied.

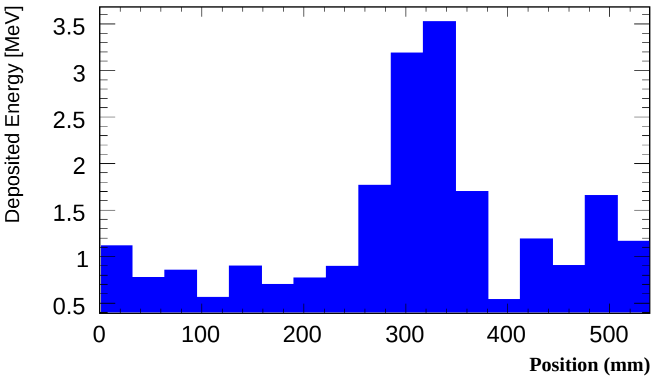

Figure 6.23: Longitudinal profile of a single muon traversing the CALICE hadronic calorimeter is shown. At a z position of about 300 mm from the beginning of the detector a clear electromagnetic shower is visible in top of the continuum ionization level. It corresponds to a δ-ray.

In Fig. 6.22 the results of the analysis are shown. The total visible energy deposited in the sensitive layer by muons of energy ranging between 6 GeV and 80 GeV is shown. The Monte Carlo describes well the data, within the systematic uncertainties of the measurement. The most probable value of the visible energy of a muon has a less steep dependence on the muon energy. The energy dependence of the truncated mean is more enhanced. The higher order electromagnetic interactions affect in fact the tail of the energy distribution, with a consequent shift of the mean value.

6.5.2 Recontruction of the δ-rays

The energy dependence of the muon signal measured in the previous section is a consequence of the higher order radiative electromagnetic interactions of the muon. As reported in section 6.1.2, the critical energy of electrons in the CALICE AHCAL is $E_c \approx 30$ MeV. Hence, the high granularity of the hadronic calorimeter allows to identify along the muon track the electromagnetic showers corresponding to these higher order effects.

In this section the identification and measurement of the δ-rays produced by a 120 GeV muon is proposed. This analysis has two main scopes:

1. Quantification of the effect of the emission hard knock-on electrons on the visible energy spectrum of the muon response.
2. Comparison between the energy spectrum of the emitted δ-rays with the theoretical expectation described in section 6.1.1.

The parasitic 120 GeV muon samples in the 2006 set-up are analysed.

A typical measured longitudinal profile of a single muon in the AHCAL is shown in Fig. 6.23. For each module only the visible energy of the hit tile is considered. At a z position of about 300 mm from the beginning of the AHCAL a clear electromagnetic

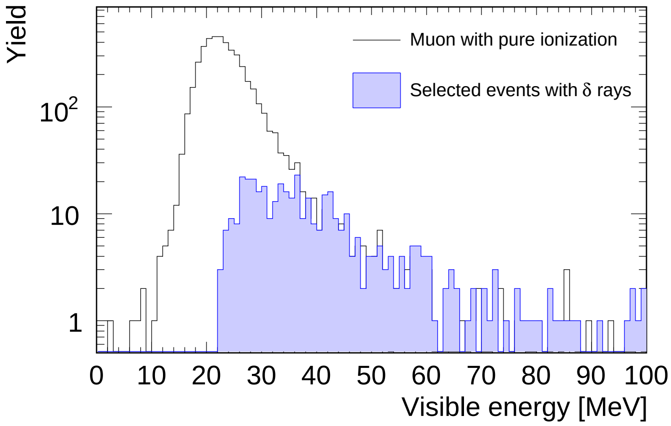

Figure 6.24: Distribution of the visible energy of the events identified as *high energy knock-on δ-rays*. The total energy of the events without δ rays is shown as the continuous line and the total energy of the events with δ-rays is shown as a filled histogram. The events with δ rays are featured by a higher visible energy in the hadronic calorimeter.

shower is visible in top of the continuum ionization level. The strategy of the analysis is hence to identify the δ-rays directly from the measurement of the energy profile.

Several cuts are developed in order to select a clean sample of δ rays. First electromagnetic shower patterns are identified along the visible energy profile, distinguishing them from noise and fluctuation artefacts. Second only isolated and compact showers which extends maximum along 3 layers are considered.

In order to identify real electromagnetic shower candidates, a continuous visible energy level of 740 keV per layer — evaluated in the Monte Carlo — is subtracted from the measured profile. The remaining contributions are random fluctuations and real showers. The shower maximum candidates and the shower region are then selected according to the following criteria:

1. The shower maximum candidate has a visible energy deposition consistently above noise ($E^{vis}_{max} > 2$ MeV).
2. The energy deposit of the layer before and after the shower maximum candidate is above noise ($E^{vis}_{max-1} > 1.5$ MeV,$E^{vis}_{max+1} > 1.5$ MeV)
3. The shower maximum candidate region satisfies the condition ($E^{vis}_{max-1} < E^{vis}_{max}$ and $E^{vis}_{max+1} > E^{vis}_{max}$)

The selection of the electromagnetic showers is performed fitting the shower candidates with a gaussian distribution. This function does not describe the typical profile of an electromagnetic shower. However it is a good approximation for such low energy showers; it is hence used to have an estimate of the width σ_δ, the position x_δ and the total visible energy (E^{vis}_δ) associated to each shower candidate. A final selection is applied:

1. The lower energy fluctuations are excluded imposing that $E^{vis}_\delta > 9$ MeV.
2. Failed fits and not regular profiles are excluded asking that $\sigma_\delta <$100 mm.

	a_δ	b_δ
Central interaction	12.27 ± 1.11 MeV	39.71 ± 0.03 MeV[1]
Interaction 1 cm from the border	24.61 ± 1.10 MeV	52.97 ± 0.04 MeV[1]

Table 6.1: Linear coefficient for the reconstruction of the energy deposited by a electron in the hadronic calorimeter interacting in the centre and near the border of a tile.

3. Overlapping δ rays and e^+e^- pairs produced along the track are excluded asking that the distance of the maximum of two showers on the same track is less than 100 mm.

The energy distribution of the selected events is reported in Fig. 6.24. The black continuous line is the energy distribution of the events without δ-rays, while the filled blue area corresponds to the energy distribution of the events with at least one identified δ-ray. The first class of events is described by the typical Landau distribution for the ionization energy losses. The second class of events is in the higher visible energy region; the visible energy of these events has a most probable value of about 30 MeV. The production of δ-rays contributes hence to increase the average energy loss by muons in the AHCAL.

The second step of the analysis consists of the reconstruction of the total energy of the identified δ-rays. This quantity is reconstructed with a linear transformation of the measured visible energy:

$$E^\delta_{tot} = a_\delta + b_\delta \times E^\delta_{vis} \tag{6.19}$$

The coefficients a_δ and b_δ are calculated with a GEANT 4 simulation of the response of the hadronic calorimeter to electrons in the energy range between 800 MeV and 5 GeV.

The hadronic calorimeter is not designed for so precise measurements and the potential sources of systematic errors are included in the evaluation of the errors of the data and in the precision of the theoretical expectation. The lateral profile of a electromagnetic shower generated by a δ ray extends in more than a single tile. As only the single tiles along the m.i.p. like track contribute to the energy profile, the uncertainty of the position of the interaction affects the evaluation of the total energy of the knock-on electron according to 6.19. The coefficients of the linear transformation are calculated for the two conditions of a muon interacting in the centre of the tile and at 1 cm far from the edge. The difference of the energy reconstructed using the two sets of coefficient is included in the total error of the measurement.

The requirements (2) and (3) of the electromagnetic shower selection decreases strongly the efficiency of detection of δ rays in the first two and last two layers. The total thickness of material affects linearly the prediction of the number of δ rays produced.

This uncertainty is taken into account in the theoretical prediction considering that the total number of layers used in the analysis is 13 ± 2. The uncertainty of the chemical composition of the absorber affects the estimation of the density and enters linearly in the theoretical prediction. A systematic uncertainty of 5% is associated with the density. The tolerance of the thickness of the absorber layers is neglected in the calculation.

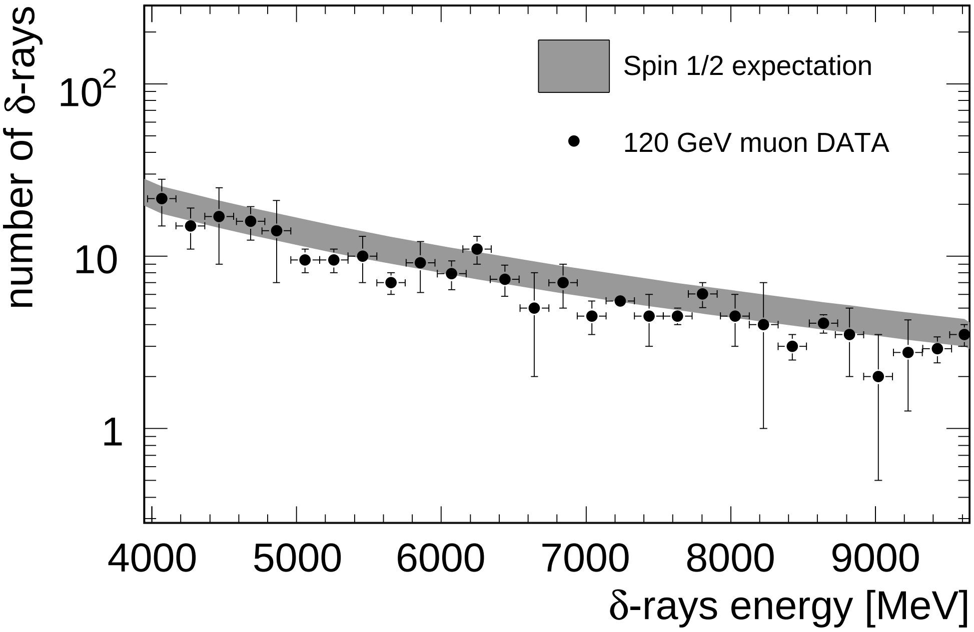

Figure 6.25: Energy distribution of the δ rays generated by a 120 GeV muons. The data (black dots) agree with the spin-1/2 theoretical expectation (gray band). The width of the theoretical expectation band takes into account the systematic uncertainty of the density and of the thickness of the AHCAL (see text).

The energy distribution of the selected knock-on electrons candidates and the theoretical expectation (eqs. 6.5 and 6.6) are shown in Fig. 6.25. The errors of the data points include the statistic and the systematic effects in the reconstruction of the total energy loss. The theoretical prediction is shown as a band which includes the statistic uncertainty and the systematic effects previously discussed. The energy distribution of the δ-rays identified and reconstructed along the muon ionization track in the AHCAL is well described by the theoretical expectation for the spin-1/2 particles. However, the energy range considered in this study is too low to appreciate the difference between spin-1/2 and spin-1 particles. As it was shown Fig. 6.4 the spin dependence is sizable only for the production of knock on electrons above about 50 GeV, which is above the sensitivity of this experiment.

6.5.3 Reconstruction of the total energy loss

A last question to be addressed is the possibility of the reconstruction of the total energy deposited by a muon in the hadronic calorimeter. This is not an essential point. At the International Linear Collider the measurement of the momentum of the muon is performed in the tracking system; the measurement of the visible energy is enough to establish the identification of a *muon-like* track and the muon identification is finally ensured by the muon chamber. However, as experienced in the ATLAS [21] collaboration,

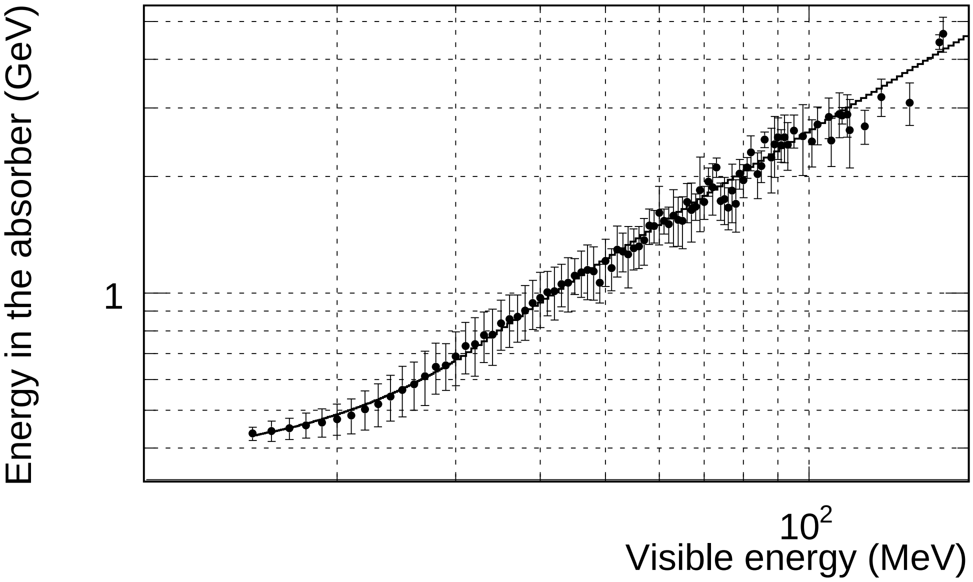

Figure 6.26: Correlation between the total energy deposited in the scintillator and in the absorber plates by a 120 GeV muon detected in the analog hadron calorimeter.

the measurement of the energy losses of muon in hadronic calorimeter is important for the precise measurement of the momentum in the muon chambers. In the present design of the LDC/ILD detector the muon chambers are not used for this purpose; yet it is interesting to investigate what performance can be achieved with a highly granular hadronic calorimeter. In this section the reconstruction of the total energy loss by a 120 GeV muon in the AHCAL is proposed. The parasitic muon samples in the 2006 set-up (1) are analysed.

The energy deposited in the absorber and in the sensitive material by a muon presents a well defined correlation. While the pure ionization component is affected by strong Landau-lie fluctuations, the energy deposited by higher order electromagnetic mechanisms via electromagnetic showers is sampled more regularly. This correlation calculated in Monte Carlo is shown in Fig. 6.26. The energy deposited in the absorber and in the scintillator is the sum of the energy deposited in the single hit tile in each AHCAL module; in other words, it is the energy associated only to the muon track and not the total energy sum of the hadronic calorimeter. It can be parameterized with the following function [188]:

$$\begin{aligned} E_{abs} &= (a + b \times E_{\mu})(E_{scint})^c + d \quad && E_{scint} < 30MeV \\ E_{abs} &= e + f \times E_{scint} && E_{scint} > 30MeV \end{aligned} \tag{6.20}$$

The results of a χ^2 fit of the Monte Carlo correlation with the parameterization function is shown in table 6.2. As shown in section 6.5.2, the effect of the electromagnetic showers starts to be sizable at a visible energy of about 30 MeV. For a visible energy value lower than 30 MeV the data are described by a parameterization similar to the one proposed by the ATLAS collaboration [165]. For a visible energy value higher than 30 MeV a linear correlation is observed, as expected from the electromagnetic shower behaviour. The slope of the linear correlation (f) can be compared with the expected slope from the development of a electromagnetic shower in the AHCAL. From equation 6.16 the ratio between energy in the absorber and in the scintillator is[9] $(1 - 0.861 \times 42.71 \times 10^{-3})/(42.71) = (2.25 \pm 0.23) \cdot 10^{-2}$, while the parameter f extracted from the fit is $(2.7 \pm 0.3) \cdot 10^{-2}$; the two quantities are in a reasonable agreement within the uncertainties of the measurement.

Parameter	**Value**
a	-2.3991 ± 0.0001
b	$(0.0199939 \pm 0.0000008)$ GeV^{-1}
c	2.33 ± 0.47
d	(0.369 ± 0.040) GeV
e	(-0.163 ± 0.062) GeV
f	0.027 ± 0.003

Table 6.2: Parameter of the function proposed to parameterize the correlation between total energy deposited by a muon in the analog hadron calorimeter.

A simplified reconstruction of the energy loss by muons consists of the application of the muon sampling fraction Sf_μ:

$$Sf_\mu = \frac{E_\mu^{vis}}{E_\mu^{vis} + E_\mu^{abs}} \tag{6.21}$$

It is evaluated from the Monte Carlo as 0.040 ± 0.001; the Landau fluctuations introduce a natural RMS of 12%. Sf_μ is comparable with the mip sampling fraction quoted in section 6.1 ($S_{mip} = 0.041$).

The result of the application of the parameterization method to the data is shown in Fig. 6.27. The true total energy distribution calculated in Monte Carlo is compared with the reconstructed total energy in data. In Fig. 6.27a the result is shown of the reconstruction of the total deposited energy with the parameterization method. The reconstructed energy distribution measured in data agrees with the Monte Carlo expectation. In Fig. 6.27b the result of the reconstruction of the total energy applying the sampling fraction method is shown. There is a large discrepancy between data and Monte Carlo expectation. The large fluctuations which affect the sampling fraction introduce a large smearing to the reconstructed energy distribution.

---

[9] The statistical error of the electromagnetic conversion factor is taken from equation 6.16 and the propagation of errors is applied.

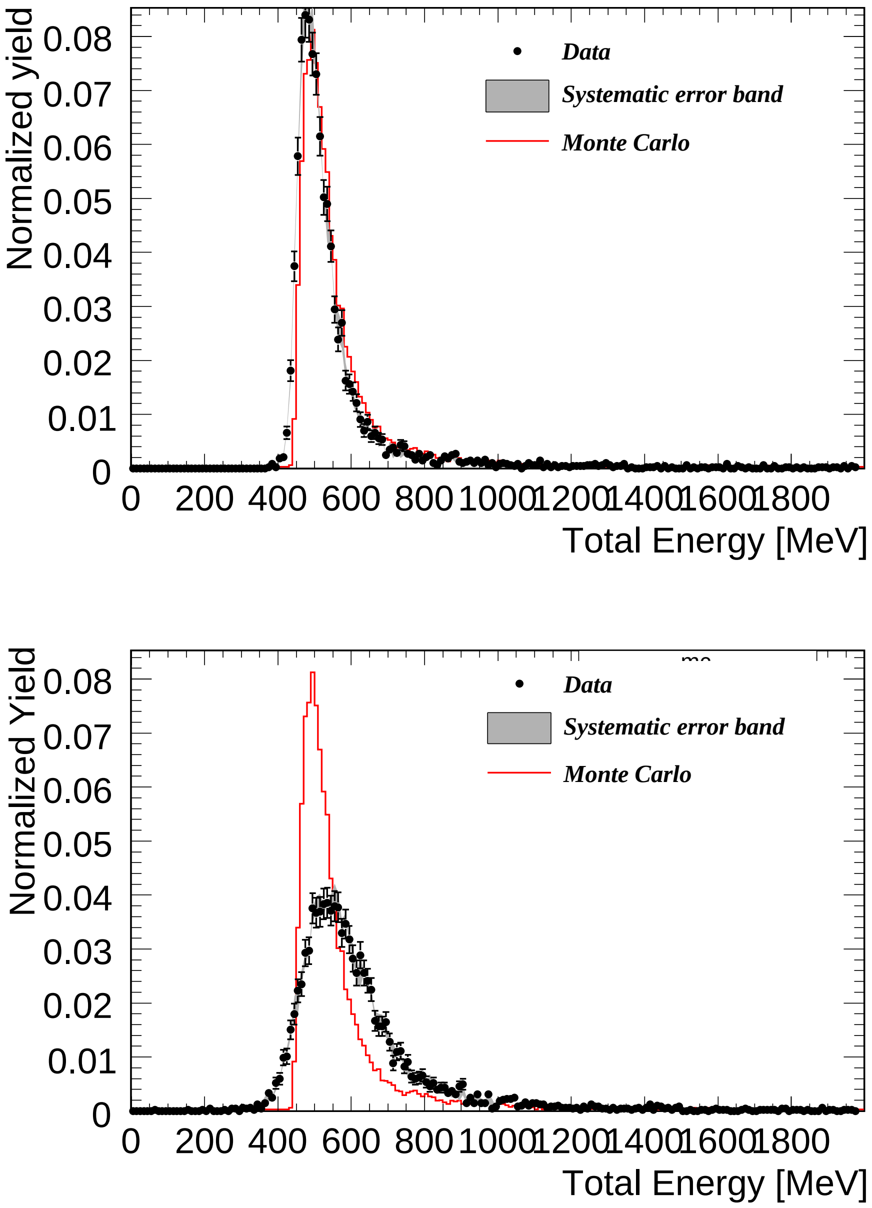

Figure 6.27: Reconstruction of the total energy lost by a 120 GeV muon in the calorimeter. In (a) the parameterization method is applied, resulting in a good agreement between data and Monte Carlo. In (b) the total energy is reconstructed just applying the sampling fraction, with a consequent smearing of the true distribution.

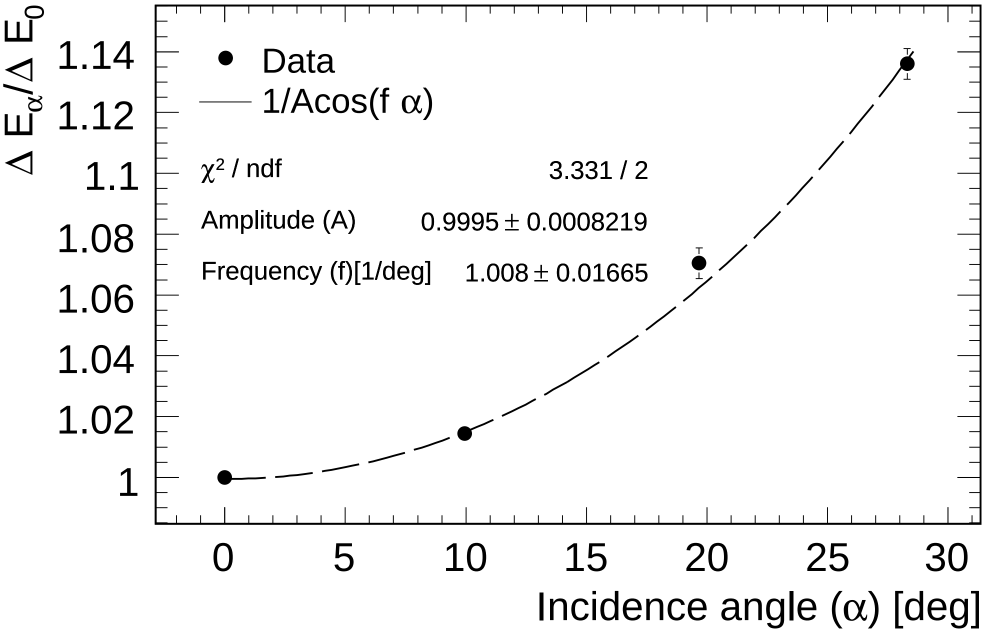

Figure 6.28: Dependence of the energy deposited by 50 GeV muons striking the detector at different angles (θ). The hadronic calorimeter is rotated in front of the beam. The expected dependence on $cos(\theta)$ is confirmed in data.

To conclude, the precise reconstruction of the muon energy losses requires a parameterization more sophisticated than the simple sampling fraction. In practice, the sampling fraction method is usually preferred for calibration purposes in the studies of the CALICE AHCAL; it has hence to be stressed that it reconstructs the muon energy scale introducing a bias. This study allows to quantify the difference between a muon and a minimum ionizing particle. The average energy deposited by a 120 GeV muon[10] is 512 MeV, much higher than the expected average total energy deposited by a minimum ionizing particle (404.25 MeV, as shown in section 6.1.1).

6.5.4 Angular dependence

The angular dependence of the hadronic calorimeter response is studied using the muons which contaminate pions runs in a dedicated angular scan (3). The calorimeter is exposed to the beam with an inclination of 0°,10°,20° and 28.3° respect to the direction perpendicular to the frontal surface of the AHCAL. A rotation of an angle α corresponds to a traversed thickness of:

$$\Delta x_\alpha = \Delta x_0/cos(\alpha) \tag{6.22}$$

---

[10] The average value quoted here is the truncated mean of the total energy distribution in the energy range between 400 MeV and 600 MeV

Energy GeV	$\overline{E_\mu^{vis}}$ MeV	$\overline{E_\mu^{tot}}$ MeV	$\overline{E_\mu^{vis,MC}}$ MeV
6	19.35 ± 0.05	514.44 ± 0.5	19.33 ± 0.01
10	19.42 ± 0.05	515.24 ± 0.4	19.56 ± 0.01
15	19.55 ± 0.05	517.04 ± 0.5	19.67 ± 0.01
40	19.82 ± 0.05	527.24 ± 0.4	19.79 ± 0.01
50	19.96 ± 0.05	529.04 ± 0.4	20.10 ± 0.01
80	20.30 ± 0.05	536.24 ± 0.5	20.39 ± 0.01

Table 6.3: Response of the hadronic calorimeter to muons used for the determination of the e/mip value. The average visible energy measured in data ($\overline{E_\mu^{vis}}$), the Monte Carlo expectation ($\overline{E_\mu^{vis,MC}}$) and the average energy reconstructed at the electromagnetic scale ($\overline{E_\mu^{tot}}$) are shown.

where Δx_0 is the total thickness traversed by a perpendicular muon. The energy deposited by a muon in the hadronic calorimeter is proportional to the total traversed thickness. The energy for a angle α normalized to the energy at a incident angle is therefore described by the following relation:

$$\frac{\Delta E_\alpha}{\Delta E_0} = \frac{1}{cos(\alpha)} \tag{6.23}$$

In Fig. 6.28 the angular dependence of the response to muons is plotted . The energy deposited in the hadronic calorimeter at a given incidence angle is rescaled to the energy deposited by a perpendicular muon. The experimental data are fitted with the function:

$$\frac{\Delta E_\alpha}{\Delta E_0} = \frac{1}{A \cdot cos(f\alpha)} \tag{6.24}$$

where A and f are left free parameter. The values of the parameters extracted with a χ^2 fit are $A = 0.9995 \pm 0.0008$ and $f = 1.00 \pm 0.01$, in excellent agreement with equation 6.23.

6.6 Measurement of the e/mip in the AHCAL

The concept of e/mip ratio was presented in section 6.1.3. It represents the difference between the signal of an electron and the signal of an ensemble of minimum ionizing particles. Its definition is:

$$\frac{e}{mip} = \frac{Sf_e}{Sf_{mip}} = \frac{\overline{E_e^{vis}}}{\overline{E_e^{tot}}} \frac{\overline{E_{mip}^{tot}}}{\overline{E_{mip}^{vis}}} \tag{6.25}$$

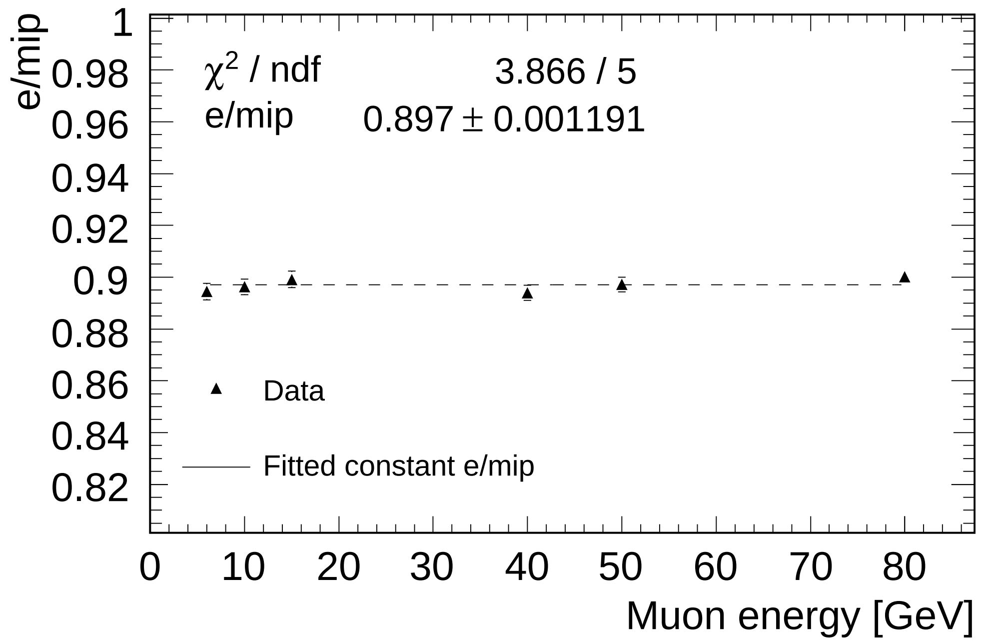

Figure 6.29: Value of e/mip extracted from the data. The total muon average energy deposited in the hadronic calorimeter is reconstructed at the electromagnetic energy scale and it is compared with the average energy released by a m.i.p. in the hadronic calorimeter. A correction for the non ionization energy losses by a muon is applied. The data are consistent with a constant $e/mip = 0.897 \pm 0.001_{stat} \pm 0.057_{syst}$.

where Sf_e is the electron sampling fraction and Sf_{mip} is the minimum ionizing particle sampling fraction, as defined in section 6.1.1. As the muon is the best natural approximation to a minimum ionizing particle, the comparison between the reconstructed muon response at the electromagnetic scale and the expected mip response provides a direct measurement of the e/mip ratio. The operational definition of this quantity hence reads:

$$\frac{e}{mip} = \frac{Sf_\mu}{Sf_{mip}} = \frac{\overline{E}_\mu^{vis}}{\overline{E}_\mu^{tot}} \frac{\overline{E}_{mip}^{tot}}{\overline{E}_{mip}^{vis}} = \frac{\overline{E}_{mip}^{tot}}{\overline{E}_\mu^{tot}} \cdot \frac{\overline{E}_\mu^{vis}}{\overline{E}_{mip}^{vis}} \tag{6.26}$$

It was shown in the previous section that a muon is not a perfect minimum ionizing particle. Higher order electromagnetic interactions provide a sizable contribution to the total visible energy. The analysis presented in section 6.5 shows that the CALICE AHCAL is sensitive to these effects. The difference between a muon and a mip is taken into account with the correction factor $\overline{E}_\mu^{vis}/\overline{E}_{mip}^{vis}$ in equation 6.26. The value of $\overline{E_\mu^{vis}}$, $\overline{E_\mu^{vis,MC}}$ and $\overline{E_\mu^{tot}}$ are reported in table 6.3.

The result of the estimation of the e/mip ratio is shown in Fig. 6.29. The extracted value does not depend on the energy. This is an important cross-check of the validity

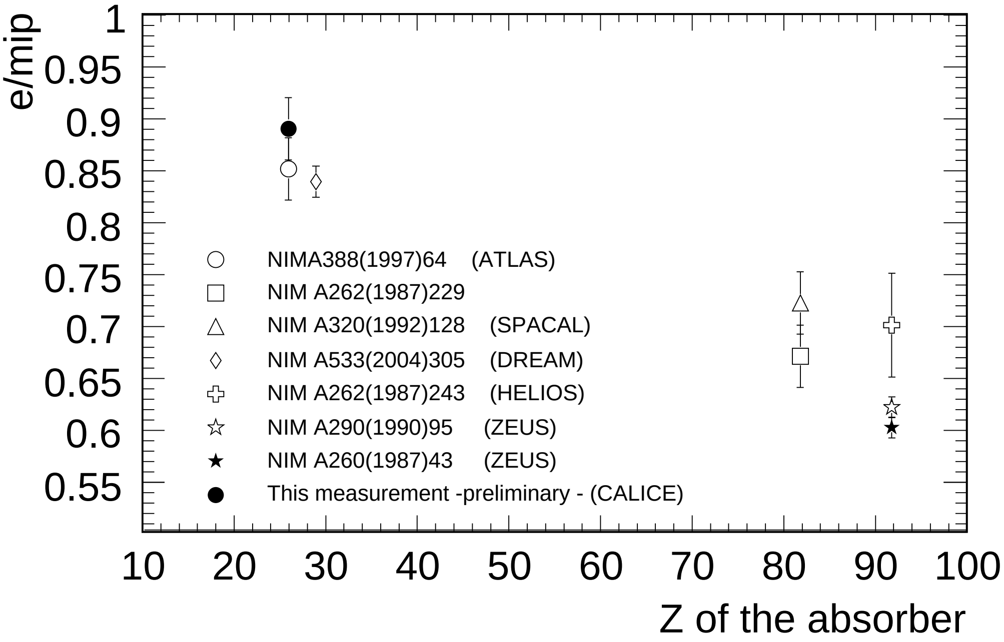

Figure 6.30: Dependence of the e/mip ratio on the atomic number of the absorber. The value of e/mip of the CALICE AHCAL measured in this analysis (filled point) is compared with the results of similar experiments with other hadronic calorimeters. The e/mip ratio reflects the difference between the atomic number of the absorber and of the scintillator because of the different sampling of the soft photons produced in the electromagnetic shower.

of the measurement. There are several systematic uncertainties related to this experiment. First the electromagnetic calibration of the detector is affected by a deviation of about 5% from the linear response in the high energy region contributing with a systematic uncertainty of 5% on the determination of the electromagnetic calibration constant [182]. Second, the determination of the mean energy deposited by a muon depends strongly on the energy range in which the calculation is performed; a systematic uncertainty of 1% is quoted changing the truncated mean energy range from (15,30) GeV to (12.5,32.5) GeV. The measurement of e/mip is consistent with a constant value of $(0.897 \pm 0.001_{stat} \pm 0.057_{syst})$.

In Fig. 6.30 the e/mip ratio measured in other hadronic calorimeters with the analysis of the response to muons is shown. The value of e/mip is observed to depend strongly on the Z of the absorber, as expected from the considerations discussed in section 6.1.3. In uranium calorimeters ($Z = 92$) e/mip is measured as low as 0.6. The result of this analysis is in a quite good agreement with the measurement performed with the similar ATLAS scintillator/steel calorimeter.

6.7 Analysis of the ionization component in π showers

The ionization plays a central role in the generation of a signal corresponding to a hadronic shower. As shown in chapter 5, the charged hadrons deposit energy in the hadronic calorimeter via ionization before undergoing further hadronic interactions. It was shown that in iron the amount of ionization energy deposited is about 60% — see table 5.2. However not only hadrons contribute to the ionization signal in the hadronic showers. Muons generated in the decay of charged pions and kaons leave a sizable signal in the hadron calorimeter and then escape from the detector. They represent a natural source of leakage of the hadron shower.

In this section the ionization signal of pions which undergo a late shower in the AHCAL prototype is shown. Moreover in the test beam data also a search of muons generated in the pion shower was performed and the results are reported.

6.7.1 Ionization measurements of π

The possibility of the μ/π separation using the ionization measurement in the hadronic calorimeter is investigated in the 2007 test beam set-up. Samples of pions at 6 10 GeV, 10 GeV, 15 GeV, 20 GeV, 40 GeV, 50 GeV and 80 GeV are used. The selected pions undergo a hadronic interaction after the 7^{th} layer of the hadronic calorimeter. Muons contaminating the same pion samples are also extracted at the different energies. A sub-sample of pion ionization tracks and a sub-sample of muon ionization tracks for each energy are hence available. The energy deposited by the pions in the first 7 layers (E_{π}^{mip}) is compared with the energy deposited by the muons in the first 7 layers (E_{μ}^{mip}). The ratio $E_{pi}^{mip}/E_{mu}^{mip}$ is found consistent with 1 at al the energies. The energy resolution of the hadronic calorimeter for the m.i.p. signal is 40% and the hadronic calorimeter does not have enough resolution power to separate muons and pions only through the ionization. The ionization tracks of the pions in the hadronic calorimeter can be identified using the same methods of the muon ionization tracks.

6.7.2 Muons emission from the pion showers

The analysis is performed with the pion showers data collected in the 2007 test beam set-up. The typical event is characterized by a clear signature: a hadronic shower, starting in the ECAL or in the HCAL, a m.i.p.-like track generated inside the hadronic shower and traversing the last layers of the HCAL and the two sections of the TCMT. The study was performed only with the 2007 set-up as the full sampling structure of the hadronic calorimeter was available. The first 30 modules are used for the identification of a hadronic shower. In the last 4 modules a isolated track has to be found. Such tracks can correspond both to muons and to low energy pions generated in the hadronic shower and leaving the AHCAL. The TCMT is used to discriminate between the two hypotheses. A muon-like signal is required in both the sections of the TCMT. Moreover, the number of hits in the two sections of the TCMT has to be comparable. In summary, the cuts applied for the identification of muons escaping from a pion shower are:

1. Hadronic shower in the AHCAL ($N_{hits}^{HCAL1} > 100$)

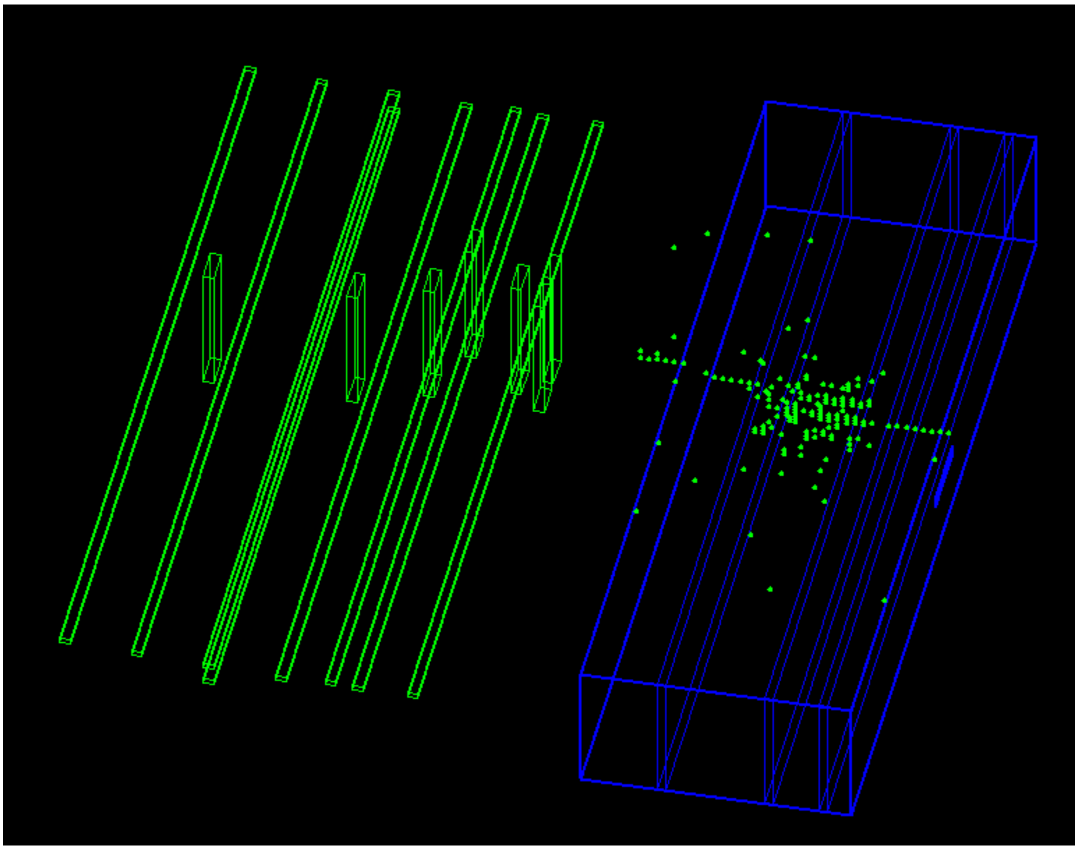

Figure 6.31: Muon generated in a 12 GeV pion shower identified in the data. The pion enters the HCAL (from the right in the picture)and undergoes a hadronic interaction. The hits in the HCAL are represented as dots. A minimum ionizing particle escapes from the shower and is visible as a track in the last part of the HCAL. It traverses also the full TCMT. The strips of the TCMT with a energy deposition above the noise level are shown. The strips identify a track in the TCMT, crossing the *fine* and *coarse* section of the TCMT. Only a muon can cross the whole TCMT without undergoing any other interaction.

2. One isolated track found in the last 4 layers of the HCAL; the hits found in a volume of 1 tile around the track candidate are less than 5 and more than 2.
3. Mip like signature in the *fine section* of the TCMT $1 < e_{TCMT1}/hits_{TCMT1} < 1.5$
4. Mip like signature in the *coarse section* of the TCMT $1 < e_{TCMT2}/hits_{TCMT2} < 1.5$
5. The event has to be *symmetric* in the TCMT $(0.8 < hits_{TCMT2}/hits_{TCMT1} < 1.2$)

A typical event identified as pion shower generating a muon is shown in Fig. 6.31.

The systematic uncertainty of this measurement depends on the geometrical acceptance and on the inefficiency of the muon identification; it is quoted as 10% with a variation of the cuts 2 and 5 which define the muon track candidate in the HCAL and in the TCMT.

The result of the search is summarized in Fig. 6.32. The probability that a muon is generated in the pion shower is found $P_\mu = (0.9 \pm 0.4_{stat} \pm 0.1_{syst}) \cdot 10^{-5} E_\pi$.

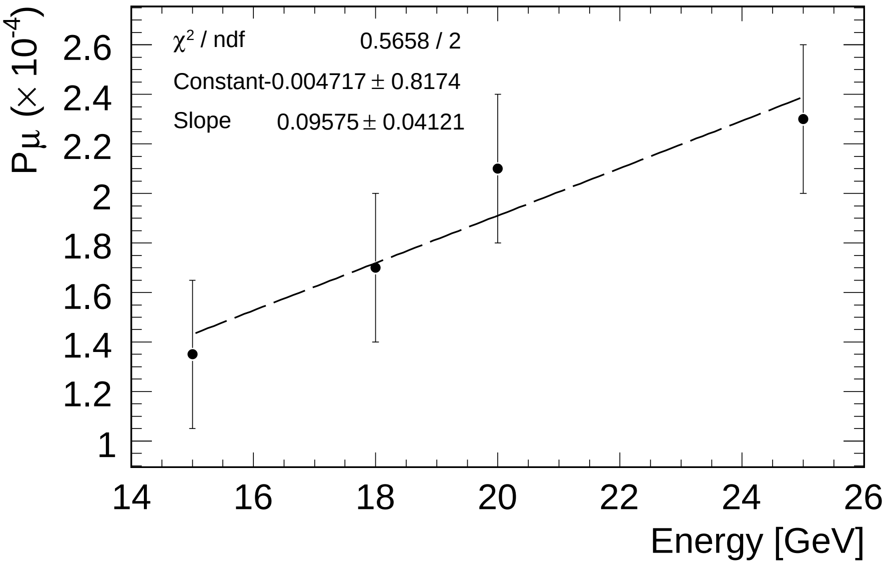

Figure 6.32: The probability that a muon is generated in the pion shower is plot as a function of the energy of the incident pion. The data are consistent with $P_\mu = (0.9 \pm 0.4_{stat} \pm 0.1_{syst}) \cdot 10^{-5} \cdot E_\mu$.

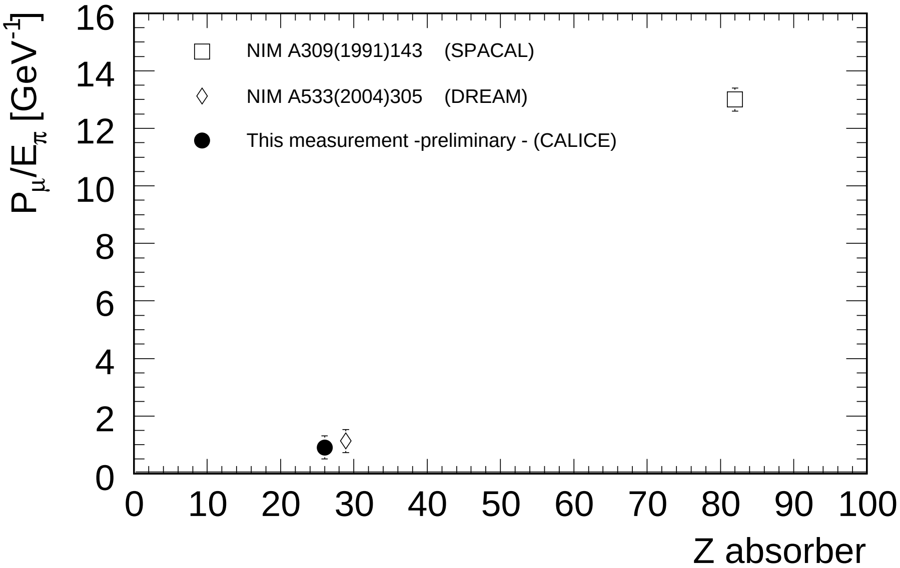

Figure 6.33: Probability of the generation of a muon in the pion shower measured in the DREAM [166], in the SPACAL [38] calorimeter and in this analysis.

Similar studies were performed with other hadronic calorimeters. In Fig. 6.33 the results of the SPACAL [38] and of the DREAM [166] calorimeter are shown. A dependence on the Z of the absorber is experimentally found. The measurement of this analysis (Z=26) is in good agreement with the results obtained by the DREAM collaboration in a copper calorimeter (Z=29). More detailed Monte Carlo studies and a reduction of the systematic errors of the measurement would be needed to understand the nature of this mechanism.

Conclusions

The response of the CALICE highly granular hadronic calorimeter (AHCAL) to muons in the energy range between 6 GeV and 120 GeV was measured. The main results are summarized in the following points:

Energy dependence. The signal of muons is energy-dependent, because of the higher order electromagnetic effects which characterize the muon interaction with matter. The average energy deposited by a muon in the hadron calorimeter was measured as a function of the primary muon energy. The results show an increase of the average energy comparable with the Monte Carlo expectation.

Reconstruction of δ-rays. The higher order electromagnetic interactions of muons could be also directly measured. The high granularity of the AHCAL allows to identify the δ-rays produced along the ionization track. Hard knock-on electrons with energy above 5 GeV produced by a 120 GeV muon were measured. Their energy distribution was found consistent with the theoretical expectation for spin-1/2 particles.

Reconstruction of total energy loss by a muon. A parameterization of the dependence of the energy deposited in the absorber versus the energy measured in the sensitive layer was found. The total energy loss reconstructed in data agrees with the Monte Carlo expectation. The possibility of the reconstruction of the total energy with the allocation of the muon sampling fraction was also studied; in this case the total energy is reconstructed with a sizable bias and smearing due to the intrinsic Landau fluctuations of the energy deposited by muons.

The average energy loss by a 120 GeV muon in the AHCAL prototype was calculated as 512 MeV, much higher than the expected average total energy deposited by a minimum ionizing particle (404.25 MeV). The higher electromagnetic interactions of muons with matter affect significantly the average amount of energy deposited in the detector, making highly energetic muons very different than minimum ionizing particles.

Angular dependence. The dependence of the energy deposited by muons on the incidence angle was also measured. The variation of the energy deposited at an incidence angle α (ΔE_α) is found to depend on $cos(\alpha)$, as expected from geometrical considerations.

Moreover the measurement of the ionization energy deposited by pions in the AHCAL was performed. Ionization tracks of pions with energy ranging between 6 GeV and 80 GeV were analysed. The AHCAL is not capable to resolve the very small difference between the ionization energy loss of muons and pions at the energy considered in this study. The most probable value and the average signals of muons and pions are found identical.

Last but not least the probability of the emission of muons from the pion shower was measured. It was found to depend on the energy of the pions E_π according to the relation $P_\mu = (0.9 \pm 0.4_{stat} \pm 0.1_{syst}) \cdot 10^{-5} E_\pi$. Combining the results of this analysis with the DREAM and SPACAL results, a dependence of the probability of muon emission on the Z of the absorber of the hadron calorimeter was found. The value of P_μ measured in this analysis of the CALICE AHCAL ($Z = 26$, iron) is consistent with the results of the DREAM calorimeter ($Z = 29$,Copper), while the value obtained with the SPACAL calorimeter ($Z = 82$,lead) is almost 1 order of magnitude higher. The probability of the generation of muons in the hadron showers depends significantly on the number of mesons produced in the shower, which is expect to increase with the Z of the material.

These physics results can be also considered in the light of the proposed goals of the CALICE test beam which were outlined in chapter 5:

Physics performance of the AHCAL. The response of the AHCAL to electrons is 10% lower than to minimum ionizing particles. The e/mip ratio was measured as $(0.897 \pm 0.001_{stat} \pm 0.057_{syst})$. This quantity affects the final energy resolution of the hadronic calorimeter, as shown in section 5.2.

Moreover the identification and reconstruction of the δ-rays along the muon ionization tracks put in evidence also the excellent imaging capability of the detector.

Validation of Monte Carlo models for hadronic showers. The probability of muon emission of pion showers is found to have a very clean signature in the AHCAL/TCMT system. It could be hence used as additional observable for the validation of Monte Carlo models. However, more simulation studies and a reduction of the systematic uncertainties of the measurements are needed in order to have a better understanding of the results.

Technological feasibility. The muon signal can be collected with an efficiency of 95%, with a signal-to-noise ratio of about 10, well above the noise level. The most probable value of the muon signal (MIP) can be measured with a statistic precision of 1%. This feature depends on the operation of the Silicon Photomultiplier. In the laboratory tests which aimed at characterizing the photo detectors for the application to the Hadronic calorimeter a noise threshold at 0.5 MIPs was suggested in order to have a signal collection efficiency of 95% with a minimal noise. These values are in average confirmed in the prototype, establishing the possibility of building and operating a highly granular calorimeter based on the SiPM technology.

Calibration issues. The control of the response of the detector is also important. The muon signal is used to calibrate the cells of the hadronic calorimeter. In this analysis it is shown that the stability of the muon response depends on the temperature fluctuations. The muon signal is affected by an average systematic shift of about 10% in correspondence of a temperature variation of 4°. The observation that the ionization energy deposited by pions and muons is not different opens up the possibility to calibrate the detector using the charged pion segments in the hadronic shower. This approach is considered in an independent study in [189].

Combination of detectors The combination of the Hadronic Calorimeter and of the Tail Catcher Muon Tracker is an essential part of the analysis. The muons are identified and triggered using the information of the tail catcher. Moreover, the identification and reconstruction of muons escaping from a pion shower profits of the muon tracking ability of the tail catcher.

Finally it has to be outlined the impact of these experimental results on the more extended LDC/ILD detector project:

Identification of isolated muons. The experimental proof of the possibility of the identification of muon ionization tracks makes a highly granular calorimeter an extension of the tracker. In this respect the HCAL has a high potential in the connection between the tracks measured in the tracker and the energy deposited in the Tail Catcher. This feature is used also in this thesis, in Chapter 4, for the identification and reconstruction of the di-muon events in the study of SUSY.

Identification of muons within hadronic showers The measurement of the muons produced in the pion showers demonstrates that the good imaging performances of the AHCAL allow to identify ionization tracks also within a hadronic shower. This is possible with the combination of the AHCAL and the Tail Catcher information. This result can be interpreted as a first step for the experimental demonstration on real data that the combined analysis of the AHCAL and the Muon System would allow to identify muons within more complicated hadronic environment — e.g. dense jets.

Estimation of muon energy losses. In the LDC/ILC detector the momentum of muons is measured in the tracking system. However, in case the design of the muon chamber would provide also a spectrometer measurement of the muon momentum, the estimation of the energy losses by higher order electromagnetic interactions before the chambers is important. It was shown that such energy deposits can be reconstructed with precision with a parameterization of the correlation between visible energy and energy loss in the absorber material of the AHCAL.

Chapter 7

Conclusions and outlook

“They lived together in the ”Housetree”,
two spinster ladybirds prepared the breakfast everyday
while gossiping about this and that.
In this peaceful corner of the magic forest my story so ends”
— ibidem

The results presented in this thesis can be discussed according to the two main streams of the research program of the International Linear Collider (ILC). On one side the study of the neutralino system focuses on the physics potential of the ILC. On the other side the analysis of the experimental data refers to the R&D of the highly granular hadronic calorimeter developed for ILC. The common background of the two studies is the LDC/ILD detector design.

Study of the neutralino system

The neutralino system is analysed in the SPS1a$'$ mSUGRA SUSY scenario. In this specific point only the χ_1^0 and the χ_2^0 are light enough to be produced in pairs at a 500 GeV linear collider.

The χ_2^0 is studied in the process $e^+e^- \rightarrow \chi_1^0\chi_2^0 \rightarrow \chi_1^0\mu\tilde{\mu}_R$. The most important and original evidence of this study is that it is possible to find a clear signal from the χ_2^0 also in the continuum at a 500 GeV centre of mass energy. The traditionally referenced method for such measurement at ILC is in fact the scan at the $\chi_2^0\chi_2^0$ pair production threshold [92]. In this analysis it is shown that the mass of the χ_2^0 (183.89 GeV) can be determined with a relative statistical uncertainty of 0.75%; the uncertainty is comparable with the quoted value obtained with a threshold scan. The cross section of the process $e^+e^- \rightarrow \chi_1\chi_2 \rightarrow \chi_1\mu\tilde{\mu}_R$ is estimated at the 95% C.L. bound (3.75,5.57) fb after 4 years of operation, with the expected total luminosity of 500 fb^{-1}. The key-point of this result is that although the signal is very small, due to its specific kinematics, it is possible to find a combination of efficient cutting variables to enhance the significance of the signal over the background; at ILC the number of signal events will be compatible with a 5 σ observation of the χ_2^0 with a probability of 95% just after 2 years of operation.

The χ_1^0 is studied in the $e^+e^- \to \tilde{\mu}_L\tilde{\mu}_L \to \mu\mu\chi_1^0\chi_1^0$ process. The mass of the χ_1^0 (97.71 GeV) can be determined with a relative statistical uncertainty of 1.09%. An additional physics result of the analysis is the measurement of the properties of the $\tilde{\mu}_L$ sector. The mass of the $\tilde{\mu}_L$ (189.86 GeV) is estimated with a relative statistical uncertainty of 0.21%. The total number of events is largely above the 5σ evidence. Using an extended likelihood approach the cross section of this process (54.32 fb) can be estimated with a relative statistical uncertainty of 2.47% at a confidence level of 68%.

Analysis of experimental data: the muon response of the hadronic calorimeter

The sensitivity of the hadronic calorimeter to the energy losses of muons is studied. The muons in the range between 6 GeV and 120 GeV studied in this thesis loose energy mainly through ionization, emission of hard knock-on electrons, bremsstrahlung and radiative pair production [175]. The analysis shows that the AHCAL is not only sensitive to the ionization, which is the most significant component of the muon energy losses in matter, but also to the higher order radiative electromagnetic interactions. The energy dependence of the signal of the hadron calorimeter in response to muons from 6 GeV up to 120 GeV is measured and found in agreement with the Monte Carlo expectation. Moreover, the high granularity of the AHCAL allows to identify the δ-rays produced along the ionization track. Hard knock-on electrons with energy above 5 GeV produced by a 120 GeV muon are measured. Their energy distribution is found consistent with the theoretical expectation for spin-1/2 particles.

The AHCAL is also sensitive to the ionization signal traversing the detector at different angles. The dependence of the respomnse of the AHCAL to muons with incidence angles up to $28.3^\circ \pm 0.1^\circ$ is also measured and is found in agreement with the theoretical expectations.

The ionization is an essential component of the energy deposited by charged hadrons in the hadron showers. The measurement of the ionization energy deposited by pions in the AHCAL is performed. Ionization tracks of pions with energy ranging between 6 GeV and 80 GeV were analysed. The AHCAL is not capable to resolve the very small difference between the ionization energy loss of muons and pions at the energy considered in this study. The most probable value and the average signals of muons and pions are found identical.

Last but not least the probability of the emission of muons from the pion shower is measured. It is found to depend on the energy of the pions E_π according to the relation $P_\mu = (0.9 \pm 0.4_{stat} \pm 0.1_{syst}) \cdot 10^{-5} E_\pi$. Combining the results of this analysis with the DREAM [38] and SPACAL [166] results, the probability of muon emission from pion showers is found to increase with the Z of the absorber material of the calorimeter.

The design of the Highly granular Hadronic Calorimeter

The analysis of the response of the AHCAL to muons provides also the measurement of specific design features of the AHCAL, which is the main goal of the test beam program.

The response of the AHCAL to electrons is 10% lower than to minimum ionizing particles. The e/mip ratio is measured as $(0.897 \pm 0.001_{\mathrm{stat}} \pm 0.057_{\mathrm{syst}})$. This quantity affects the e/h ratio and consequently the energy resolution of the hadronic calorimeter.

An unique feature of the AHCAL is the high granularity. The identification and reconstruction of the δ-rays along the muon ionization tracks emphasizes the excellent imaging capability of the detector.

On the technical point of view, the muon signal can be collected with an efficiency of 95%, with a signal-to-noise ratio of about 10, well above the noise level. The most probable value of the muon signal (MIP) can be measured with a statistic precision of 1%. This feature depends on the operation of the Silicon Photomultiplier. In the laboratory tests which aimed at characterizing the photo detectors for the application to the Hadronic calorimeter a noise threshold at 0.5 MIPs was suggested in order to have a signal collection efficiency of 95% with a minimal noise. These values are in average confirmed in the prototype, establishing the possibility of building and operating a highly granular calorimeter based on the SiPM technology. The control of the response of the detector is also important. The muon signal is used to calibrate the cells of the hadronic calorimeter. In this analysis it is shown that the stability of the muon response depends on the temperature fluctuations. The muon signal is affected by an average systematic shift of about 10% in correspondence of a temperature variation of 4°.

Finally, the combination of the Hadronic Calorimeter and of the Tail Catcher Muon Tracker is an essential part of the analysis. The identification and reconstruction of muons escaping from a pion shower profits of the muon tracking ability of the AHCAL and of the tail catcher.

The LDC detector design

Both the study of the neutralino system and the analysis of the test beam data provide useful information about the design of the ILD/LDC detector for the International Linear Collider.

First, the tracking system shows an excellent performance. In the $e^+e^- \rightarrow \tilde{\mu}_L\tilde{\mu}_L$ process, the detector does not introduce any significant smearing to the kinematic edges of the energy distribution of the muons. The precision tracking is even more important in the analysis of the $\chi_1^0\chi_2^0$ pair production. In this case it allows to isolate the small features of the invariant mass spectrum, with a consequent precise measurement of the mass of the χ_2^0.

Second muons can be identified with a m.i.p. like track in the tracker and in the calorimeters, with a corresponding track in the muon chamber. It was shown that the detector has 95% muon detection efficiency in the muon momentum range of the signal processes. The identification of muons fails in the very forward region, because of lack of coverage in the proposed detector model. The sensitivity of the hadronic calorimeter to the muon ionization energy is experimentally proved in the analysis of the test beam data; it is hence demonstrated that the technological choice for the highly granular hadronic calorimeter is able to provide the information necessary for the muon identification.

Third the measurement of the muons produced in the pion showers demonstrates that the good imaging performance of the AHCAL allows to identify ionization tracks also in a complicated shower environment. This is possible with the combination of the AHCAL and the Tail Catcher information. This result can be interpreted as a first step for the experimental demonstration on real data that the combined analysis of the AHCAL and the Muon System would allow to identify muons within more complicated hadronic environment — e.g. dense jets.

Finally in the LDC/ILC detector the momentum of muons is measured in the tracking system. However, in case the design of the muon chamber would provide also a spectrometer measurement of the muon momentum, the estimation of the muon energy losses in higher order electromagnetic interactions before the chambers is important. It was shown that such energy deposits can be reconstructed with precision with a parameterization of the correlation between visible energy and energy loss in the absorber material of the AHCAL.

Outlook

The study of the neutralino system proposed in this thesis offers many opportunity for a more in-depth examination. The analysis is performed only in a single point of the mSUGRA SUSY parameter space; the statistical methods developed in this work can be used for the estimation of the sensitivity of ILC in a wider region of the parameters. Besides, the determination of the mass χ_1^0 can be performed also in the study of the $\tilde{\mu}_R\tilde{\mu}_R$ pair production; the results of these other channels can be combined to obtain a final quantification of the sensitivity of the International Linear Collider to the measurement of the χ_1^0. In 2009 the LHC will start to take data; the interplay between ILC and LHC in the study of the neutralino system offers interesting perspectives for future studies.

The analysis of the experimental data performed in this thesis provides the measurement of useful design parameters of the hadronic calorimeter and is the first step for the understanding of the response of the calorimeter to hadrons. The extracted e/mip ratio affects the e/h ratio and consequently the energy resolution of the detector. The measurement of the e/h ratio and of the energy resolution of the AHCAL in the analysis of the pion data collected in the test beam will complete the basic characterization of the response of the hadronic calorimeter to single particles. Furthermore, an important research field of the highly granular hadronic calorimetry is the validation of the hadronic shower Monte Carlo models; the probability of muon emission from a pion showers can be used as new experimental observable for this purpose.

List of Figures

List of Tables

Bibliography

[1] T. Behnke, C. Damerell, J. Jaros, and A. Miyamoto, *ILC Reference Design Report. Vol4: Detectors.* DESY, 2007.

[2] N. Phinney, T. Nobukazu, and N. Walker, *ILC Reference Design Report. Vol3: Accelerator.* DESY, 2007.

[3] A. Djouadi, J. Lykken, K. Monig, Y. Okada, M. Oreglia, and S. Yamashita, *ILC Reference Design Report. Vol2: Physics at the ILC.* DESY, 2007.

[4] F. Hasert and al., "Observation of neutrino-like interactions without muon or electron in the gargamelle neutrino experiment," *Nucl.Phys.B*, vol. 73, p. 1, 1974.

[5] K. Jakobs, "The physics results of the ua2 experiment," *Int.Journ.ofMod.Phys.A*, vol. 9, pp. 2903–2977, 1944.

[6] ALEPH Collaboration, Opal Collaboration, DELPHI Collaboration, L3 Collaboration, and SLD Collaboration, "Precision Electroweak Measurements on the Z resonance," *Phys.Rept*, vol. 427, no. 257, 2007.

[7] C. Adloff and al., "Measurement and QCD analysis of jet cross sections in deep-inelastic positron-proton collisions at $\sqrt{}$ of 300 GeV," *Eur.Phys.J.C*, vol. 19, p. 289, 2001.

[8] S. Checkanov and al., "Measurement of subjet multiplicities in neutral current deep inelastic scattering at HERA and determination of α_s," *Phys.Lett.B.*, vol. 558, p. 41, 2003.

[9] P. Higgs, "Broken symmetries and the masses of gauge bosons," *Phys.Rev.Lett.*, vol. 13, p. 508, 1964.

[10] P. Higgs, "Spontaneous symmetry breakdown without massless bosons," *Phys.Rev.*, vol. 145, p. 1156, 1966.

[11] D. Eisenstein and al., "Detection of the baryon acoustic peak in the large-scale correlation function of sdss luminous red galaxies," *ApJ*, 2004.

[12] N. Halverson, E. Leitch, and al., "Degree angular scale interferometer first results: a measurement of the cosmic microwave background angular power spectrum," *ApJ*, vol. 568, pp. 38–45, 2002.

[13] W. Hu and M. White, "Acoustic signatures in the cosmic microwave background," *ApJ*, vol. 471, pp. 30–51, 1996.

[14] U. Amaldi, W. de Boer, , and H. Furstenau, "Comparison of grand unified theories with electroweak and strong coupling constants measured at lep," *Phys.Lett.B*, vol. 260, p. 448, 1991.

[15] E. Gildener, “Gauge-symmetry hierarchies,” *Phys.RevD*, vol. 14, no. 16, 1976.

[16] J. Wess and B. Zumino, “Supergauge transformations in four dimensions,” *Nucl.Phys.B.*, vol. 70, p. 39, 1974.

[17] A. Salam and J. Strathdee, “Super-gauge transformations,” *Nucl.Phys.B.*, vol. 76, p. 477, 1974.

[18] B. Lee, C. Quigg, and H. Thacker, “Weak interactions at very high energy: the role of the Higgs Boson mass,” *Phys.Rev.D*, vol. 16, p. 1519, 1977.

[19] L. Alvarez-Gaume and al., “Review of Particle Physics,” *Phys.Lett.B*, vol. 667, 2008.

[20] CDF Collaboration and DO Collaboration, “Combined cdf and d0 upper limits on standard model higgs boson production at high mass (155-200 gev/c^2) with 3 fb^{-1} of data,” *arxiv:hep-ex/0808-0534*, 2008.

[21] ATLAS Collaboration, “ATLAS Technical Design Report,” *CERN*, vol. 9915, 1999.

[22] CMS Collaboration, “CMS Technical Proposal,” *CERN*, vol. 9438, 1994.

[23] R. Heuer, D. Miller, F. Richard, and P. Zerwas, *Tesla TDR PartIII: Physics at an* e^+e^- *Linear Collider*. DESY, 2001.

[24] G. Moortgat-Pick and al., “The role of polarized positrons and electrons in revealing fundamental interactions at the Linear Collider,” *hep-ph*, vol. 0507011, 2005.

[25] S. Choy, J. Kalinowsky, G. Moortgat-Pick, and P. Zerwas, “Analysis of the neutralino system in Supersymmetric theories - ADDENDUM,” *hep-ph*, vol. 0202039, 2008.

[26] S. Choy, J. Kalinowsky, G. Moortgat-Pick, and P. Zerwas, “Analysis of the neutralino system in Supersymmetric theories,” *Eur.Ohys.J. C*, vol. 22, pp. 563,579, 2001.

[27] A. Bartl, T. Kernreiter, and O. Kittel, “A CP asymmetry in $e^+e^- \to \chi_i^0\chi_j^0 \to \chi_j^0\tau\tilde{\tau}_k$,” *Phys.Lett.B*, vol. 578, pp. 341–348, 2004.

[28] N. Arkani-Hamed, H. Cheng, J. Feng, and L. Hall, “Probing Lepton Flavour Violation at Future Colliders,” *Phys.Rev.Lett.*, vol. 77, no. 10, p. 075004, 1996.

[29] P. Bethcle, K. Desch, W. Porod, and P. Wienemann, “Determination of MSSM parameters from LHC and ILC observables in a global fit,” *hep-ph*, vol. 0511006, 2005.

[30] M. Thompson, “Progress with particle flow calorimetry,” *arxiv:0709.1360v1*, 2007.

[31] M. Thompson, “Particle flow calorimetry at the International Linear Collider,” *Pramana-journal of physics*, vol. 69, no. 6, pp. 1101–1107, 2007.

[32] M. Thompson, “Calorimetry and Particle flow at the International Linear Collider,” *RAL HEP Forum*, 2006.

[33] M. Thompson, “Particle flow and ILD detector optimization studies,” 2° *ILD detector workshop*, 2008.

[34] P.Buzhan and al., “Silicon photomultiplier and its possible applications,” *Nucl.Instr.Methods*, vol. A504, p. 48, 2003.

[35] Z.Sadygov and al., “Super-sensitive avalanche silicon photodiode with surface transfer of charge carriers,” *Nucl.Instr.Methods*, vol. A504, p. 301, 2003.

[36] V.Saveliev and V.Golovin, “Novel type of avalanche photo-detector with geiger mode operation,” *Nucl.Instr.Methods*, vol. A447, pp. 486–490, 2003.

[37] R. Wigmans, *Calorimetry: Energy Measurement in Particle Physics.* Oxford University Press, 2000.

[38] D. Acosta and al., “On muon production and other leakage aspects,” *Nucl. Instr. and Met. A*, vol. 309, p. 143, 1991.

[39] A. Andresen and al., “Response of a uranium-scintillator calorimeter to electrons, pions and protons in the momentum range 0.510 gev/c,” *Nucl. Instr. and Met. A*, vol. 290, p. 95, 1990.

[40] T. Akesson and al., “Performance of the uranium/plastic scintillator calorimeter for the helios experiment at cern,” *Nucl. Instr. and Met. A*, vol. 262, p. 243, 1987.

[41] E. Bernardi and al., “Perfomance of a compensating lead-scintillator hadronic calorimeter,” *Nucl. Instr. and Met. A*, vol. 262, p. 229, 1987.

[42] D. Acosta and al., “Detection of muons with a lead/scintillating fiber calorimeter,” *Nucl. Instr. and Met. A*, vol. 320, p. 128, 1992.

[43] S. Weinberg and E. Gildner, “Symmetry breaking and scalar bosons,” *Phys.Rev.D*, vol. 13, no. 12, 1976.

[44] J. Valle, “Physics beyond the standard model,” *hep-ph9603307*, 1996.

[45] M. Peskin, “Beyond the standard model,” *Proceedings of the 1996 European School of High Energy Physics, Carry-le-Rouet,France*, 1997.

[46] J. Moffat, “Beyond the standard model,” *hep-ph/9802228*, 1998.

[47] M. Gaillard and B. Zumino, “Supersymmetry and superstring phenomenology,” *Eur.Phys.J.C*, 2008.

[48] J. Wess and J. Bagger, *Supersymmetry and Supergravity.* Princeton University Press, 1991.

[49] S. Weinberg, *Supersymmetry. The Quantum theory of fields, vol III.* Cambridge University Press, 2000.

[50] M. Plank, *The theory of heat radiation* . Dover Publications, 1959.

[51] A. Einstein, “Zur theorie der lichterzeugung und lichtabsorption,” *Ann. d. Phys.*, no. 325, p. 6, 1906.

[52] A. Compton, “A quantum theory of the scattering of x-rays by light elements,” *Phys. Rev.*, no. 21, p. 483, 1923.

[53] T. Lee and C. Yang, “Question of parity conservation in weak interactions,” *Phys. Rev.*, no. 104, p. 254, 1956.

[54] E. Ambler, R. Hayward, D. Hoppes, and R. Hudson, “Experimental test of parity conservation in beta decay,” *Phys.Rev.*, no. 105, p. 1413, 1957.

[55] S. Glashow, J. Iliopoulos, and L. Maiani, “Weak interactions with lepton-hadron symmetry,” *Phys.Rev.D*, vol. 2, p. 1285, 1970.

[56] S. Weinberg, “A model of leptons,” *Phys.Rev.Lett.*, vol. 19, p. 1264, 1967.

[57] A. Salam, *Elementary Particle Theory.* Svartholm, 1969.

[58] G. Arnison and al., “Experimental observation of isolated large transverse energy electrons with associated missing energy at $\sqrt{s} = 540$ gev,” *Phys. Lett.B*, no. 103, p. 122, 1983.

[59] D. Kazakov, “Beyond the Standard Model (In search of Supersymmetry),” *hep-ph/0012288*, 2002.

[60] “Lep design report,” *CERN-LEP/84-01*, 1984.

[61] “Slac linear collider conceptual design report,” *SLAC-R-229*, 1980.

[62] ALEPH Collaboration, Opal Collaboration, DELPHI Collaboration, L3 Collaboration, and SLD Collaboration, “Precision Electroweak Measurements and Constraints on the Standard Model,” *Parxiv:0712.0929*, 2007.

[63] P. Abreu and al., “A precise measurement of the z resonance parameters through its hadronic decays,” *Physics Letters B*, vol. 241, no. 3, pp. 435 – 448, 1990.

[64] D. Gross and F. Wilczek, “Asymptotically free gauge theories i,” *Phys.Rev.D*, vol. 8, p. 3633, 1973.

[65] Tevatron New Phenomena, Higgs working group, CDF Collaboration, and D0 Collaboration, “ Combined CDF and D0 Upper Limits on Standard Model Higgs Boson Production at High Mass (155-200 GeV/c2) with 3 fb-1 of data,” *Phys.Lett.B.*, vol. 558, p. 41, 2003.

[66] W. Marciano, G. Valenica, and S. Willenbrock, “Renormalization group-improved unitarity bounds on the Higgs boson and top quark masses,” *Phys.Rev.D*, vol. 40, 1989.

[67] P. Binetruy, *Supersymetry. Theory,experiment and cosmology.* Oxford University Press, 2006.

[68] V. Veltmann *Acta Phys. Pol. B*, vol. 12, p. 437, 1981.

[69] M. Kado and C. Tully, “Searches of Higgs Boson at LEP,” *Annu.Rev.Nucl.Part.Sci.*, vol. 52, 2002.

[70] ALEPH Collaboration, DELPHI Collaboration, L3 Collaboration, and OPAL Collaboration, “Searches for the Standard Model Higgs Boson at LEP,” *Physics Letters B*, vol. 565, 2003.

[71] D. Kazakov, “Supersymmetry as the nearest option beyond the standard model,” *Surveys in High Energy Physics*, vol. 3, no. 19, pp. 139–174, 2004.

[72] W. Hu and S. Dodelson, “Cosmic microwave background anisotropies,” *Ann.Rev.Astron.and Astrophys.*, 2002.

[73] W. Greiner, *Field Quantization.* Springer Verlag, 1994.

[74] M. Drees, R. Godbole, and P. Roy, *Theory and phenomenology of sparticles.* World Scientific Publishing, 2004.

[75] M. Peskin, “Supersymmetry in Elementary Particle Physics,” *hep-ph*, vol. 08011928, 2008.

[76] S. Dimopoulos and D. Sutter, “The supersymmetric flavor problem,” *Nucl.Phys.B*, vol. 452, p. 496, 1995.

[77] L. Hall, J. Lykken, and S. Weinberg, “Supergravity as the messenger of supersymmetry breaking,” *Phys.Rev.D*, vol. 27, p. 2359, 1983.

[78] S. Soni and H. Weldon, “Analysis of the supersymmetry breaking induced by n = 1 supergravity theories,” *Phys.Lett.B*, vol. 126, p. 215, 1983.

[79] M. Dine, N. Seiberg, and I. Affleck, “Dynamical supersymmetry breaking in four dimensions and its phenomenological implications,” *Nucl.Phys.B*, vol. 256, p. 557, 1985.

[80] H. Nilles, “Dynamical supersymmetry breaking in four dimensions and its phenomenological implications,” *Phys.Lett.B*, vol. 115, p. 193, 1982.

[81] A. Chamseddine, R. Arnowitt, and P. Nath, “Dynamical supersymmetry breaking in four dimensions and its phenomenological implications,” *Nucl.Phys.B*, vol. 227, p. 121, 1983.

[82] R. Barbieri, S. Ferrara, and C. Savoy, “Dynamical supersymmetry breaking in four dimensions and its phenomenological implications,” *Phys.Lett.B*, vol. 119, p. 343, 1982.

[83] N. Ohta, “Grand unified theories based on local supersymmetry,” *Prog.Theor.Phys.*, vol. 70, p. 542, 1983.

[84] A. Chamseddine, R. Arnowitt, and P. Nath, “Dynamical supersymmetry breaking in four dimensions and its phenomenological implications,” *Phys.Rev.Lett*, vol. 49, p. 970, 1983.

[85] M. Dine and A. Nelson, “Dynamical supersymmetry breaking in four dimensions and its phenomenological implications,” *Phys.Rev.D*, vol. 48, p. 1277, 1993.

[86] M. Dine, A. Nelson, and Y. Shirman, “Dynamical supersymmetry breaking in four dimensions and its phenomenological implications,” *Phys.Rev.D*, vol. 51, p. 1362, 1995.

[87] L. Randall and R. Sundrum, “Dynamical supersymmetry breaking in four dimensions and its phenomenological implications,” *Nucl.Phys.B*, vol. 557, p. 79, 1999.

[88] G. Giudice, M. Luty, and H. Murayama, “Dynamical supersymmetry breaking in four dimensions and its phenomenological implications,” *JHEP*, vol. 9812, p. 027, 1998.

[89] D. Kaplan, G. Kribs, and M. Schmaltz, “Dynamical supersymmetry breaking in four dimensions and its phenomenological implications,” *Phys.Rev.D*, vol. 62, p. 035010, 2000.

[90] Z. Chacko, M. Luty, and A. Nelson, “Dynamical supersymmetry breaking in four dimensions and its phenomenological implications,” *JHEP*, vol. 0001, p. 003, 2000.

[91] J. Aguilar-Saavedra and al., “Supersimmetry parameter analysis: SPA convention and project,” *Eur.Phys.J.C.*, vol. 46, pp. 43–60, 2006.

[92] LHC/LC Study Group, “Physics interplay of the lhc and the ilc,” *arXiv:hep-ph/0410364*, 2003.

[93] H. Baer, C. Balazs, A. Belyaev, and J. O’Farril, “Direct detection of dark matter in supersymmetric models,” *JCAP*, vol. 0309, p. 007, 2003.

[94] G. Degrassi, S. Heinemeyer, W. Hollik, P. Slavich, and G. Weiglein, “Towards high-precision predictions for the mssm higgs sector,” *Eur.Phys.J.C*, vol. 28, p. 133, 2003.

[95] S. Choy and al., “Reconstructing the chargino system at e^+e^- linear colliders,” *hep-ph/0002033*, 2000.

[96] A. T. odd asymmetry in neutralino production and decay, “Bartls,A. and Hesselbach,S. and Hohenwarter-Sodek,K. and Fraas,H. and Moortgat-Pick,G.,” *JHEP*, vol. 038, 2004.

[97] S. Choy, H. Song, and W. Song, “CP phases in correlated production and decay of neutralinos in the minimal supersymmetric standard model,” *Phys.Rev.D*, vol. 61, p. 075004, 2000.

[98] The OPAL collaboration, “Search for anomalous production of acoplanar di-lepton events in e^+e^- collisions at $\sqrt{s} = 183$ GeV and 189 GeV,” *Eur.Phys.J.C*, vol. 14, pp. 51–71, 2000.

[99] The OPAL collaboration, “Search for acoplanar lepton pair events in e^+e^- collisions at $\sqrt{s} = 161$ GeV, 172 GeV and 189 GeV ,” *Eur.Phys.J.C*, vol. 12, pp. 551–565, 2000.

[100] The OPAL collaboration, “Search for chargino and neutralino production at $\sqrt{s} = 192 - 209$ GeV at LEP,” *Eur.Phys.J.C*, vol. 12, pp. 551–565, 2000.

[101] The DELPHI collaboration, “Search for scalar fermions and long-lived scalar leptons at centre of mass energies of 130 GeV to 172 GeV,” *Eur.Phys.J.C*, vol. 6, pp. 385–401, 1999.

[102] The L3 collaboration, “Search for scalar leptons, charginos and neutralinos in e^+e^- collisions at $\sqrt{s} = 161 - 172$ GeV,” *Eur.Phys.J.C*, vol. 4, pp. 207–219, 1998.

[103] C. Benvenuti and al., “Films for superconducting accelerating cavities,” *Appl. Phys. Lett.*, vol. 45, p. 58, 1984.

[104] F. Furuta and al., “Experimental comparison at KEK of high gradient performance of different single cell superconducting cavity design,” *EPAC06*, 2006.

[105] R. Geng and al., “High gradient activities at Cornell: reentrant Cavities,” *SRF2005*, 2005.

[106] D. Schulte, “Guinea Pig,” *TESLA 97-08*, 1996.

[107] E. Accomando and al., “Physics with e^+e^- linear colliders,” *Phys. Rep.*, vol. 299, p. 1, 1998.

[108] H.Murayama and M. Peskin, “Physics opportunities at e^+e^- linear colliders,” *Ann. Rev. Nucl. Part. Sci.*, vol. 46, p. 553, 1996.

[109] D. Peralta, M. Martinez, and R. Miquel, “Top mass measurement at the $t\bar{t}$ threshold,” *Proc. of the International Workshop on Linear Colliders (LCWS99) Sitges*, 1999.

[110] I. Knowles and G. Lafferty, “Hadronization in z^0 decay,” *J.Phys.G*, vol. 23, p. 731, 1997.

[111] M. Green, S. Lloyd, P. Ratoff, and D. Ward, *Electron-positron Physics at the Z.* IoP Publishing, 1998.

[112] D. Gross and F. Wilczek, “The CDFII Detector — Technical design report,” *FERMILAB-Pub-96/390-E*, 1996.

[113] T. Abe and al., “SiD Detector Outline Document,” *http://www.ilcldc.org/documents/dod*, 2006.

[114] K. Abe and al, “GLD Detector Outline Document,” *physics/0607154*, 2006.

[115] P. Le Du and al., “Detector Outline Document for the 4^{th} concept detector,” *http://www.4thconcept.org/4doc.pdf*, 2006.

[116] D. Kiseilewska and al, “Detector Outline Document for the Large Detector Concept,” *http://www.ilcldc.org/documents/dod*, 2006.

[117] BTeV Collaboration, “The BTeV Pixel Detector,” *Nucl. Instr. and Meth. A*, vol. 446, pp. 235–239, 2000.

[118] F. Sauli, “GEM: A New Concept for Electron Amplification in Gas Detectors,” *Nucl. Instr. and Meth. A*, vol. 386, p. 531, 1997.

[119] Y. Giomataris and al., “Micromegas: A High Granularity Position Sensitive Gaseous Detector for High Particle Flux Environments,” *Nucl. Instr. and Meth. A*, vol. 376, p. 29, 1996.

[120] T. Behnke, S. Bertolucci, R. Heuer, and R. Settles, *Tesla TDR PartIV: A detector for TESLA.* DESY, 2001.

[121] V.Saveliev and V.Golovin, “Silicon avalanche photodiodes on the base of metal-resistor-semiconductor (mrs) structure,” *Nucl.Instr.Methods*, vol. A442, p. 223, 2003.

[122] I. Hinchliffe, F. Paige, M. SHapiro, J. Soderqvist, and W. Yao, “Precision SUSY measurements at LHC,” *hep-ph*, vol. 9610544, 1996.

[123] S. Martin, “A Supersymmetry Primer,” *hep-ph*, vol. 9709356, 2006.

[124] P. Bethcle, K. Desch, and P. Wienemann, “FITTINO, a program for determining MSSM parameters from collider observables using an iterative method,” *hep-ph*, vol. 0412012, 2005.

[125] K. Desch, “ILC potential of the χ_2^0 mass measurement in the di-τ channel,” *Talk at ECFADESY workshop. Prague November*, 2002.

[126] R. Hagedorn, *Relativistic Kinematics.* W.A.Nenjamin,INC., 1964.

[127] E. Byckling and K. Kajantia, *Particle Kinematics.* John Wiley and Sons, 1973.

[128] W. Porod, "Spheno, a program for calculating supersymmetric spectra, SUSY particle decays and SUSY particle production at e^+e^- colliders," *LC-TOOL-2001-03*, 2001.

[129] W. Kilian, T. Ohl, and J. Reuter, "WHIZARD: Simulating Multi-Particle Processes at LHC and ILC," *arXiv: 0708.4233 [hep-ph]*, 2007.

[130] W. Kilian, T. Ohl, and J. Reuter, "O'Mega: An Optimizing matrix element generator," *LC-TOOL-2001-040-rev, arXiv: hep-ph/0102195-rev.*, 2001.

[131] W. Kilian, "WHIZARD Manual 1.0," *LC-TOOL-2001-039, http://www-flc.desy.de/lcnotes/.*

[132] J. Allison, "Geant 4 - A Simulation Toolkit," *Nuclear Physics News*, vol. 17, no. 20, 2002.

[133] "MOKKA web page," *http://polzope.in2p3.fr:8081/MOKKA.*

[134] "MARLIN web page," *http://ilcsoft.desy.de/portal/softwarepackages/marlin/.*

[135] "MarlinReco web page," *http://ilcsoft.desy.de/portal/softwarepackages/marlinreco/.*

[136] A. Freitas and D. Miller, "Pair Production of Smuons and Selectrons Near Threshold in e+ e- and e- e- Collisions," *Eur.Phys.J. C*, vol. 21, pp. 361–368, 2001.

[137] R. Dalitz, "On the analysis of τ-Meson Data and the nature of the τ Meson," *Phil. Mag.*, vol. 44, p. 1068, 1953.

[138] E. Fabbri, "A study of the τ Meson decay," *Il nuovo cimento*, vol. 11, no. 5, p. 479, 1954.

[139] S. Choy, B. Chung, J. Kalinowsky, Y. Kim, and K. Rolbiecki, "Analysis of the neutralino system in three-body leptonic decays of neutralinos," *Eur.Phys.J. C*, vol. 46, pp. 511–520, 2006.

[140] G. Cowan, *Statistical Data Analysis* . Oxford University Press, 2002.

[141] S. Bityukov, "On the signal significance in the presence of Systematic and statistical uncertainties," *hep-ph/0207130*, 2002.

[142] S. Bityukov and N. Krasnikov, "Uncertainties and Discovery potential in planned experiments," *hep-ph/0204326*, 2002.

[143] S. Bityukov and N. Krasnikov, "On the observability of a signal above background," *Nucl.Inst.Meth.A*, vol. 453, pp. 518–524, 2000.

[144] S. Bityukov and N. Krasnikov, "New physics discovery potential in new physics experiments," *Mod.Phys.Lett.A*, vol. 13, no. 40, pp. 3235–3249, 2000.

[145] A. Read, "Modified frequentist analysis of search results (The CL_s method)," *Advanced Statistical Techniques in Particle Physics - proceedings*, 2002.

[146] C. Fabjan and F. Giannotti, "Calorimetry for particle physics," *Review of modern physics*, vol. 75, pp. 1243–1286, 2003.

[147] U. Amaldi, “Fluctuations in calorimetry measurements,” *Physica Scripta*, vol. 23, pp. 409–424, 1981.

[148] A. Ferrari and P. Sala, “The physics of high energy reactions,” *Proceedings of the Workshop on Nuclear Reacttions Data and Nuclear Reactors Physics, Design and Safety*, 15 April—17 May 1996.

[149] R. Wigmans, “On the energy resolution of uranium and other hadron calorimeters,” *Nuclear Instruments and Methods in Physics Research A*, vol. 259, pp. 389–429, Sept. 1987.

[150] D. Green, *The Physics of Particle Detectors*. Cambridge University Press, 2000.

[151] T. A. Gabriel, D. E. Groom, P. K. Job, N. V. Mokhov, and G. R. Stevenson, “Energy dependence of hadronic activity,” *Nuclear Instruments and Methods in Physics Research A*, vol. 338, pp. 336–347, Jan. 1994.

[152] D. Groom, “Energy flow in a hadronic cascade: Application to hadron calorimetry,” *Nuclear Instruments and Methods A*, 2006.

[153] I. Ivantchenko, W. Leltchouck, and W. Seligman, “Methods of hadronic shower energy classification in GEANT4.” Talk given at the Atlas LaR Week (2004).

[154] H. Martyn, “Detection of long-lived staus and gravitinos at the ILC,” *Proceedings of the International Linear Collider Workshop*, p. 201, 2007.

[155] “CALICE Web Site,” *http://llr.in2p3.fr/activites/physique/flc/calice.html.*

[156] The CALICE collaboration, “Response of the CALICE Si-W Electromagnetic Calorimeter Physics Prototype to Electrons,” *submitted to Nucl.Instr. and Meth. A*, 2008.

[157] S. Blin, “Dedicated very front-end electronics for an ILC prototype hadronic calorimeter with SiPM readout,” *LC-DET-2006-007*, 2006.

[158] M. Groll, *Construction and commissioning of a hadronic test-beam calorimeter to validate the particle flow concept at the ILC.* PhD thesis, Hamburg University, 2007.

[159] CALICE SIPM collaboration, “Status report on silicon photomultiplier development and its applications,” *Nucl.Instr.Methods A*, vol. 563, p. 368, 2006.

[160] CALICE Collaboration, “Electron data with the CALICE tile AHCAL prototype at the CERN test-beam ,” *CAN-011*, 2007.

[161] V. Andreev and al., “A high-granularity scintillator calorimeter readout with silicon photomultipliers,” *Nucl.Instr.Methods A*, vol. 540, p. 368, 2005.

[162] Hamamatsu, “Multi-pixel photon counter, datasheet,” *www.hamamatsu.com*, 2006.

[163] N. D’Ascenzo and al., “Study of micro pixel photon counters for a high granularity scintillator-based hadron calorimeter,” *DESY 07-196*, 2007.

[164] N.D’Ascenzo and al., “Application of the micro pixel photon counter to hadron calorimetry and pet,” *Il Nuovo Cimento*, vol. 30C, p. 463, 2007.

[165] Z. Ajaltouni and et al., “Response of the ATLAS Tile Calorimeter Prototype to Muons,” *Nucl. Instr. and Meth. A*, vol. 388, pp. 64–78, 1997.

[166] N. Akchurin and al., “Muon detection with a dual-readout calorimeter,” *Nucl. Instr. and Meth. A*, vol. 533, pp. 305–321, 2004.

[167] M. Catanesi and al., “Hadron, Electron and muon response of a uranium-scintillator calorimeter,” *Nucl. Instr. and Meth. A*, vol. 260, pp. 43–54, 1987.

[168] J. Backen and al., “Study of a bgo calorimeter using electron and hadron beams from 1 to 50 gev,” *Nucl. Instr. and Met. A*, vol. 228, p. 294, 1985.

[169] J. Backen and al., “Performance of a prototype bgo calorimeter in an electron beam from 2 to 50 gev,” *Nucl. Instr. and Met. A*, vol. 254, p. 535, 1987.

[170] B. Rossi, *High Energy Particles.* Prentice Hall, 1954.

[171] D. Kotov and S. Kelner, “Muon energy loss to pair production,” *Sov.J.Nucl.Phys.*, vol. 7, no. 2, p. 237, 1968.

[172] S. Kelner, “Pair production in collisions between Muons and atomic Electrons,” *Phys.Atom.Nucl.*, vol. 61, no. 3, p. 448, 1998.

[173] L. Bezrukov and E. Bugaev, “Nucleon shadowing effects in photonuclear interactions,” *Sov.J.Nucl.Phys.*, vol. 33, no. 5, p. 635, 1981.

[174] D. Caldwell and al., “Measurement of shadowing in photon-nucleus total cross sections from 20 to 185 GeV,” *Phys.Rev.Lett.*, vol. 42, no. 9, p. 553, 1979.

[175] W. Lohmann, R. Kopp, and R. Voss, “Energy loss of muons in the energy range 1-GeV to 10000-GeV,” *CERN 85-03.*

[176] E. Berger and al., “The measurement of energy loss of 150 GeV positive muons in iron with the TILECAL prototype,” *Z.Phys.C*, vol. 73, p. 455, 1997.

[177] P. Amaral and al., “A precise measurement of 180 GeV muon energy losses in iron,” *Eur.Phys.J. C*, vol. 20, p. 487, 2001.

[178] M. Schein and P. Gill, “Burst frequency as a function of energy,” *Rev.Mod.Phys.*, vol. 11, p. 267, 1939.

[179] R. Christy and S. Kusaka, “Burst production by mesotrons,” *Phys.Rev.*, vol. 59, p. 414, 1941.

[180] H. Corben and J. Schwinger, “The electromagnetic properties of mesotrons,” *Phys.Rev.*, vol. 58, p. 953, 1940.

[181] “LCIO web page,” *http://ilcsoft.desy.de/portal/softwarepackages/lcio/.*

[182] CALICE Collaboration, “Electron data with the CALICE tile AHCAL prototype at the CERN test-beam ,” *CAN-010*, 2008.

[183] CALICE Collaboration, “Electron data with the CALICE tile AHCAL prototype at the CERN test-beam — Effect of the temperature correction,” *CAN-010a*, 2008.

[184] CALICE Collaboration, “Preliminary results from hadron shower data with the CALICE tile AHCAL prototype ,” *CAN-003*, 2007.

[185] CALICE Collaboration, “Pion data with the CALICE tile AHCAL prototype at the CERN test-beam ,” *CAN-011*, 2008.

[186] CALICE Collaboration, “Preliminary study of the combined response of the CALICE calorimeter prototypes to pion beams ,” *CAN-004*, 2007.

[187] CALICE Collaboration, “Response of the CALICE Si-W ECAL Physics Prototype to Electrons ,” *CAN-008*, 2008.

[188] D. Lopez Mateos and al., “A parametrerization of the energy loss of muons in the atlas tracking geometry,” *ATLAS Note*, 2008.

[189] CALICE Collaboration, “Track Segments in Hadronic Showers in the Analogue Scintillator Tile HCAL ,” *CAN-013*, 2008.

Acknowledgements

I would like to thank my supervisor, Dr. Erika Garutti, who guided me in these three years of research and study. I would like also to thank the referees of my dissertation and disputation, Prof. Dr. J. Mnich, Prof. Dr. P. Schleper and J.Prof. Dr. J.Haller.

I thank Dr. Felix Sefkow and Dr. Ties Behnke for the possibility they gave me to perform my studies within the FLC group. I am thankful to all the members of the HCAL and of the ILD optimization groups. I would like to thank in particular Philip Betchle who supervisioned me in the study of the neutralino system. How can I forget then the collegues who shared with me the office in these last three years? I thank Beni Lutzt, Niels Meyer and Sebastian Richter for their patience. I thank Nanda Wattimena who initiated me to the ice-skating, or better to the *falling-on-the-ice* and Daniela Kaefer, my *tanzenpartnerin*.

I thank Prof. Dr. W.Hansen and Prof. Dr. A. Liechtenstein for the opportunity they gave me to teach at the University of Hamburg. I am grateful to the good discussions with the students of the Physik II excercise groups in SS 2008 and I hope that they will soon be involved in particle physics.

Many are the older friends who helped me to grow up as a physicist and as a men. I would like to thank in particular Prof. Dr. V. Saveliev and Prof. Dr. G. Gorini for the interesting chats about physics and about life.

There is also a group of close friends which I would like to remember here. I shared with them my emotions in these last three years. Among them I thank the *conconsole* Peppino Tropea, Gigliola Raffa, Antonellina Iannuso, the *vicina* Sara Comparato, the *ragioniere* Alessio Bonato and the JugendPfarrer Johannes Zehe.

My parents, my lovely sister Arianna and my little brother Francesco are for sure part of these three years. Together with them, Franca, Walter, Aldo, Granma Lucia and Grandpa Basso were a warm and welcoming support in the good and bad times.

But the careful reader of my thesis will have now, at the end, one question. Who is the Princess Camomilla? She is my Princess, my beautiful Daniela. Without her, without the desire of building a family together, without the continous sharing of life, dreams and energy, the pages of my studies would barely have sense.